



Multiscale methodology for vulnerability assessment of masonry structures

Maryam Tabbakhha

► To cite this version:

Maryam Tabbakhha. Multiscale methodology for vulnerability assessment of masonry structures. Other. Ecole Centrale Paris, 2013. English. NNT : 2013ECAP0032 . tel-00905526

HAL Id: tel-00905526

<https://theses.hal.science/tel-00905526>

Submitted on 18 Nov 2013

HAL is a multi-disciplinary open access archive for the deposit and dissemination of scientific research documents, whether they are published or not. The documents may come from teaching and research institutions in France or abroad, or from public or private research centers.

L'archive ouverte pluridisciplinaire **HAL**, est destinée au dépôt et à la diffusion de documents scientifiques de niveau recherche, publiés ou non, émanant des établissements d'enseignement et de recherche français ou étrangers, des laboratoires publics ou privés.



**ÉCOLE CENTRALE DES ARTS
ET MANUFACTURES
«ÉCOLE CENTRALE PARIS »**

THÈSE

présentée par
Maryam Tabbakhha

pour l'obtention du
GRADE DE DOCTEUR

Spécialité : Modélisation Numérique en Génie Civil

Laboratoire d'accueil : Laboratoire MSSMat, Mécanique des Sols, Structures et Matériaux

SUJET : Méthodologie multi-échelle pour évaluer la vulnérabilité des structures en maçonnerie

soutenue le : 14 mai 2013

devant un jury composé de :

Gregg Brandow	Président
Luc Davenne	Rapporteur
Hassan Moghaddam	Rapporteur
John A. Ochsendorf	Examineur
Fernando Lopez-Caballero	Examineur
Arezou Modaressi	Directrice de thèse

2013ECAP0032

Change is the end result of all true learning.

-Leo Buscaglia

Abstract

The aim of this thesis is to develop numerical models for evaluating the vulnerability of unreinforced masonry construction under different types of loading. Therefore, the behavior of unreinforced masonry panels under monotonic loading in both macro- and micro- scales is studied. Simulating the nonlinear behavior of the masonry wall in pre and post-peak regions and capturing its failure mechanism is the main focus of this study. First, the masonry wall in the panel is substituted by two simple bars using the so-called macro-element strategy and a tri-linear behavior is proposed to assess the ultimate strength of the wall as well as its response before and after peak. The lack of information about the failure mechanism of the masonry wall and relation between the failure mechanism and mechanical properties of the bar elements in this type of modeling lead to another description of this structure namely micro-modeling strategy. In this strategy, units and mortars are modeled separately and all inelastic behavior of the masonry wall is supposed to happen in mortars. Hence, special attention is paid to development of a reliable description of material properties for these elements using an accurate constitutive law.

Three dimensional representation of a masonry wall in this work enhances the capability of existing methods to predict the masonry behavior under both in-plane and out-of-plane loadings. Firstly, failure envelopes including tension cut-off and the Mohr-Coulomb yield surface are assigned to interface elements in GEFDyn finite element software. Then, the elastoplastic constitutive law is improved by adding a compression cap to the yield surfaces in order to include compressive failure of masonry in the interface element. In the new model, softening behavior for tensile and compressive strength as well as cohesion of mortar is considered. The ability of both models to reproduce the pre- and post-peak behavior of the masonry wall is verified by comparing the numerical results with experimental data. The importance of defining the compression failure of masonry by limiting the shear strength of the wall with its compressive strength is shown by comparing the obtained results with those of a real test. The results showed that the second model is capable to simulate the behavior of masonry wall with a good accuracy. Then, the effect of initial stresses and geometrical properties of the wall such as opening and aspect ratio and material properties of the mortar like its cohesion, tensile strength and compressive strength, on lateral strength and failure mechanism of the masonry walls are demonstrated. Moreover, in order to comprehend failure characteristics damage indexes based on the total length of cracks in different rows and columns of mortars are introduced and compared for different configurations.

The lengths of sliding in horizontal mortars and opening in vertical ones are the most important

parameters that control the behavior of the wall. Finally, the relation between different cracking profiles and contributing material properties are summarized into a table. The applicability of the 3D model is also demonstrated in simulating the behavior of masonry walls under out-of-plane loads. The crack patterns and load-displacement paths of a wall under this type of loading, using different boundary conditions, initial loading and mortar's cohesion are studied and compared together. Obtained results indicate high dependency of the results to these parameters. Finally, the effects of the surrounding walls on performance of each individual wall and that of the set are demonstrated through the analysis of the behavior of two perpendicular walls under different loading configurations.

Keywords: Unreinforced masonry walls, macro modeling, micro modeling, in-plane loading, out of plane loading, failure mechanism, opening, aspect ratio.

Acknowledgements

It is with immense gratitude that I acknowledge the great support, help, and patience of my advisor Professor Arezou Modaressi. I consider it an honor to work with her at Ecole Centrale Paris. Her advice on both research as well as my personal life have been invaluable.

It gives me great pleasure in acknowledging the support and help of Professor Gregg Brandow at USC civil engineering department. Many interesting and good-spirited discussions relating to this research helped me a lot.

I would like to thanks the other members of thesis committee: Prof. Luc Davenne, Prof. Hassan Moghaddam and Prof. John A Ochsendorf. I am indebted to Prof. Luc Davenne and Prof. Alessandro Mandolini for accepting the reviewing of manuscript.

I place on the record, my sincere gratitude to Dr. Bardet for his kind help. I also appreciate the help provided by Dr. Fernando Lopez-Caballero at Ecole Centrale Paris. I always admire his point of view to scientific subjects. I would like to thank my colleagues, Anna Gaspar, Luis Berenguer Todo-Bom, Sahar Hemmati, Cristian Nieto, Tammam Hammad and Ghizlaine Benosman who supported me during my work at Ecole Centrale Paris.

I appreciate all the kind help and support of my friends and family, especially my dear brother, sister, and in-laws. I would like to deeply thank my dearest parents for their everlasting patience, support, and encouragements throughout my life.

Finally, I would like to acknowledge the most important person in my life, my husband, Hamid, for all love, love, and love. I dedicate this dissertation to him with love.

Contents

Abstract	i
Acknowledgements	iii
	Page
Contents	1
List of Figures	6
List of Tables	17
1 Introduction	18
1.1 Introduction	19
1.2 Objectives of study	20
2 Literature review	23
2.1 Introduction	24
2.2 Macro modeling of infill masonry frames	26
2.3 Micro modeling of masonry walls	31
2.4 Modeling of masonry under cyclic loads	36
2.5 Conclusion	43
3 Macro modeling	44
3.1 Introduction	45

3.2	Behavior of infill frames	46
3.3	Macro element of code TREMURI	49
3.4	Experiments conducted at CSTB	50
3.5	Numerical modeling of masonry	51
3.5.1	FEMA 356 proposed strut model	53
3.5.2	Calibrated model proposed by Hashemi [46]	56
3.5.3	Mostafaei and Kabeyasawa model [76]	57
3.6	Tri-linear proposed model	61
3.6.1	Validation of proposed model, CSTB test	61
3.6.2	Comparing the obtained results using different models	62
3.6.3	Validation of proposed model, Vermeltfoort test	64
3.7	Conclusion	65
4	Micro modeling : in plane loading	67
4.1	Introduction	68
4.2	Masonry failure mechanisms	68
4.3	Numerical modeling of masonry wall	70
4.3.1	Interface element formulations	72
4.4	Simple yield surface for interface elements (Model I)	73
4.4.1	Numerical Validation	77
4.4.2	Wall with opening	86
4.4.3	Influence of aspect ratio	88
4.4.4	Cyclic behavior of masonry walls	93
4.4.5	Conclusion and perspective	98
4.5	Multi-surface yield function for interface elements (Model II)	99
4.5.1	Properties of composite yield surface	99
4.5.2	Numerical validation for Model II	107
4.5.3	Effect of compression cap's slope θ	113

4.6	Aspect ratio effect	118
4.7	Parametric study	129
4.7.1	Cohesion of mortars	129
4.7.2	Tensile strength of mortars	134
4.7.3	Compression strength of masonry	137
4.7.4	Initial normal load	138
4.7.5	Captured crack patterns	142
4.8	Conclusion	146
5	Micro modeling: out of plane loading	148
5.1	Introduction	149
5.2	Behavior of a wall under out-of-plane displacements	151
5.2.1	Case A	152
5.2.2	Parametric study on Case A	154
5.2.3	Case B	166
5.2.4	Parametric study on Case B	169
5.3	Behavior of two walls under out-of-plane Loads	179
5.3.1	Series 1: Top nodes of Wall 1 move in x direction	180
5.3.2	Parametric study on Series 1: displacement applied to Wall 1	184
5.3.3	Series 1: roof's movement simulation	189
5.3.4	Series 2: roof movement simulation	195
5.4	Conclusion	203
6	Conclusion	205
6.1	Summary and conclusion	206
6.2	Perspective and future work	208
7	Appendixes	209

A	Macro models formulations	210
B	Parametric study using micro model	213
8	Bibliography	228

List of Figures

1.1	Collapse in unreinforced masonry building (a) Westmorland California [102] (b) Port-au-Prince, Haiti [45]	20
2.1	(a) Micro modeling approach to model infilled frame (b) macro modeling strategy for representing infilled frame [88], [52]	26
2.2	Different Modeling strategies for masonry structures (a) masonry sample (b) detailed micro-modeling (c) simplified micro-modeling (d) macro-modeling	27
2.3	(a) Single strut model suggested by Stafford-Smith [1966] [99] (b) six-strut model proposed by Chrysostom [1991] [21]	27
2.4	(a) Strut model by [30] (b) trilinear relations: stress-strain relation and typical force-deformation relation for struts proposed by El-Dakhakhni et al. [2003] [30] .	28
2.5	Force-displacement envelope curve of the equivalent strut, Decanini et al.[2004] [27]	29
2.6	(a) Multi-strut model (b) variation of the strut area proposed by Crisafulli et al. [2007] [24]	29
2.7	Three-dimensional SAT model of URM infill wall proposed by Hashemi et al.[2007] [46]	30
2.8	Plastic concentrator model proposed by Puglisi et al.[2009] (a) Infill panel with plastic concentrator (b) force-displacement diagram with plastic concentrator [88]	30
2.9	(a) Macro model used for simulating masonry infill panel by [92] (b) force-displacement diagram representing nonlinear behavior of masonry under monotonic loading, proposed by Rodrigues et al. [2010] [92]	31
2.10	Failure surface considered in Page [1987] [82] and Riddington et al. [1990] [91] studies, respectively	32
2.11	(a) Yield surface used in Lourenco et al. [1983] [59] (b) hyperbolic yield criterion proposed by Lotfi et al. [1994] modelings [57]	34

2.12	Proposed multisurface yield function by Lourenco et al. [1997] [61]	34
2.13	(a) Yield function for interface elements (b) hyperbolic asperity model by Gi- ambanco et al. [2001] [40]	35
2.14	Three linear yield surface of interface element by Sutcliffe et al. [2001] [101]	36
2.15	(a) Single masonry unit (b) piecewise linear yield surface used by Chaimoon et al. [2007] [17]	37
2.16	Schematic representation of masonry wall modeled by equivalent frame model (a) Belmouden et al. [2009] [9] (b) Bayer et al. [2012] [11]	38
2.17	Response of the mortar joint model (a) tensile stress (b) shear strain superimposed on constant compressive stress and (c) cyclic shearing strains in Gambarotta et al. [1997] studies [37]	39
2.18	Limit strength domain for (a) composite model by Gambarotta et al. [1997] [37] (b) continuum model proposed by Gambarotta et al. [1997] [37]	39
2.19	Motion of auxiliary yield function proposed by Oliveira et al. [2004] in tension and compression [80]	40
2.20	Scheme of an irregular masonry defined by four rigid elements [14]	41
2.21	Hysteretic behavior of the axial (left) and shear (right) connecting springs used in Casolo et al. [2007] model [14]	41
2.22	Cyclic stress-strain relationship for unloading-reloading stages, initial loading in (a) tension (b) compression and (c) shear proposed by Karapitta et al. [2011] [51]	42
3.1	Formation of diagonal strut [23]	46
3.2	Corner Crushing failure (CC)	47
3.3	Diagonal Compression failure (DC)	47
3.4	Sliding Shear failure (SS)	48
3.5	Diagonal Cracking failure (DCK)	49
3.6	Frame Failure (FF)	49
3.7	CSTB test set-up [31]	51
3.8	Blocks and joints properties	51
3.9	Masonry wall properties and results of experiments	52
3.10	Crack propagation, load displacement diagram, block prototype and utilization percentage	52

3.11	Diagonal equivalent model of masonry	52
3.12	Masonry strut material model recommended by FEMA 356	55
3.13	(a) Material stress-strain curve (b) force-displacement diagram using FEMA 356 strut model	55
3.14	Masonry strut material model proposed by Hashemi et al. [2007] [46]	56
3.15	(a) Material stress-strain curve (b) force-displacement diagram using calibrated strut model	57
3.16	Force-displacement envelope for conventional masonry infill walls proposed by Mostafaei et al. [2004] [76]	58
3.17	(a) Material stress-strain curve (b) force-displacement diagram using Mostafaei and Kabasaki [76] strut model	60
3.18	Shear force-displacement curve proposed for diagonal struts	61
3.19	(a) Material stress-strain curve used in model (b) load-displacement curve of CSTB test using trilinear proposed model	62
3.20	Numerical simulation of shear base force and top displacement curve in an infilled frame under monotonic loading using different methods	63
3.21	(a) Tested wall by Vermeltfoort et al. [85] (b) load-displacement diagram	64
3.22	(a) Stress-strain curve of material (b) load-displacement curve obtained for trilinear proposed model used for Vermeltfoort test [85]	65
4.1	Masonry failure mechanisms: (a) joint tensile cracking (b) joint slipping (c) unit direct tensile cracking (d) unit diagonal tensile cracking (e) masonry crushing . . .	69
4.2	Failure modes for masonry walls subjected to in-plane loads (a) diagonal tensile failure (b) sliding shear failure (c) bending failure (crushing of masonry) [96] . . .	70
4.3	GEFdyn 3D solid element with eight integration points	71
4.4	GEFdyn zero thickness interface element [79]	71
4.5	Potential crack planes in the middle of units are modeled by zero-thickness inter- face element	72
4.6	Simple yield surface for interface elements	74
4.7	Relation between normal and shear stresses and displacements in interface element, left and right figures respectively	74
4.8	Coulomb friction law, definition of dilatancy angle [60]	75

4.9	Experimental test (a) first: Vertical loading (b) second: Horizontal loading [60]	78
4.10	Experimental crack pattern after loading [60]	79
4.11	GEFDyn model geometry and elements	79
4.12	Different categories of interface elements used for modeling masonry wall	80
4.13	Deformed shape of masonry wall at $d = 2\text{ mm}$ model I	82
4.14	Load-Displacement diagram for model I	83
4.15	Stress diagrams in the masonry wall bricks $d = 0.11\text{ mm}$ for model I	83
4.16	Stress diagrams in the masonry wall bricks $d = 2\text{ mm}$ for model I	84
4.17	Crack pattern in the masonry wall at $d = 2\text{ mm}$	85
4.18	Wall with central opening tested by Raijmakers and Vermentfoort [1993] [86]	86
4.19	Experimental crack patterns for different tests [60]	87
4.20	Deformed shape of the wall with opening result from simulation for model I	87
4.21	Load displacement diagram of experiment and numerical model for model I	88
4.22	Crack pattern in the masonry wall with opening $d = 2\text{ mm}$ for model I	89
4.23	Deformed shape, pushover curve and crack pattern in the masonry wall for aspect ratios less than 1 at $d = 2\text{ mm}$ for model I	90
4.24	load-displacement diagram for different aspect ratios $H/L < 1$ for model I	91
4.25	Deformed shape, pushover curve and crack pattern in the masonry wall for aspect ratios greater than 1 at $d = 2\text{ mm}$ for model I	92
4.26	load-displacement diagram for different aspect ratios $H/L > 1$ for model I	93
4.27	One cycle displacement	94
4.28	(a) Deformed shape (b) load-displacement curve in the masonry wall for one cycle loading	94
4.29	Crack pattern in different elements of the wall for one cycle loading at final step $d = 0\text{ mm}$	95
4.30	Multiple cycles displacement	96
4.31	(a) Deformed shape (b) load-displacement curve in the masonry wall for multiple cycles loading	96
4.32	Crack pattern in different elements of the wall for multiple cycles loading at final step $d = 0\text{ mm}$	97

4.33	Comparison between load-displacement curves from cyclic to monotonic loading . . .	98
4.34	Shear behavior of masonry, experimental results by Van der Pluijm (1993)[86] for different confinement stresses, with $C_0 = 0.87[N/mm^2]$; $\tan(\phi_0) = 1.01$; $\tan(\phi_0) =$ 0.73 ; $GII = 0.0580.13 * \sigma[Nmm/mm^2]$ [86]	100
4.35	(a) Deformed shape (b) stress-strain curve of masonry in shear	101
4.36	Tensile behavior, experimental results from Van der Pluijm (1992)[85], with $F_t0 =$ $0.30[N/mm^2]$ and $GI = 0.012[Nmm/mm^2]$	101
4.37	(a) Deformed shape (b) stress-strain curve of masonry in direct tension	102
4.38	Composite yield function for 3D masonry wall configuration used in this study . .	103
4.39	(a) Variation of compression cap with respect to F_c (b) Comparison between com- pression cap used in this study and that of given by Lourenco in 2D [60]	104
4.40	Wall deformation under monotonic loading for model II in Plane XZ	108
4.41	Load displacement diagram for model II	109
4.42	Profile of cracks at (a) local peak $d = 1.1mm$ (b) local drop $d = 1.3mm$	109
4.43	Horizontal forces which are carried out by each brick, composite yield surface . . .	110
4.44	Comparison between numerical modeling results for yield function with and with- out compression cap for model II and model I, respectively	111
4.45	Profile of cracking for interface elements for model II at $d = 4mm$	111
4.46	Stress distribution at (a) $d = 1mm$ (b) $d = 2mm$ (c) $d = 4mm$	112
4.47	Profile of cracking in the wall with different θ	113
4.48	Pushover curve for the wall with different θ	114
4.49	Results of analysis at displacement of $1mm$	114
4.50	Results of analysis at displacement of $2mm$	115
4.51	Results of analysis at displacement of $20mm$	115
4.52	Load displacement curve for (a) model II (b) comparison between model I and model II	116
4.53	Results of analysis at displacement of $3mm$	116
4.54	Total deformed shape (a) model II (b) model I	117
4.55	Profile of cracking for wall with opening at $d = 20mm$	117
4.56	Results for wall with $AS = 0.5$ ($H = 0.5H_0$) model II	118

4.57	Load-displacement curves for wall using models I and II, $AS = 0.5$ ($H = 0.5H_0$)	119
4.58	Results for wall with $AS = 2/3$ ($L = 1.5L_0$) model II	119
4.59	Load-displacement curves for wall using models I and II, $AS = 2/3$ ($L = 1.5L_0$)	120
4.60	Results for wall with $AS = 0.5$ ($L = 2L_0$) model II	121
4.61	Load-displacement curves for wall using models I and II, $AS = 0.5$ ($L = 2L_0$)	121
4.62	Load-displacement diagram for different aspect ratios $H/L < 1$	122
4.63	Results for wall with $AS = 2$ ($L = 0.5L_0$) model II	123
4.64	Load-displacement curves for wall using models I and II, $AS = 2$ ($L = 0.5L_0$)	124
4.65	Results for wall with $AS = 1.5$ ($H = 1.5H_0$) model II	124
4.66	Load-displacement curves for wall using models I and II, $AS = 1.5$ ($H = 1.5H_0$)	125
4.67	Results for wall with $AS = 2$ ($H = 2H_0$) model II	126
4.68	Load-displacement curves for wall using models I and II, $AS = 2$ ($H = 2H_0$)	126
4.69	load-displacement diagram for different aspect ratios $H/L > 1$	128
4.70	Deformed shapes and crack patterns in the walls with different mortars' cohesion at $d = 4mm$	130
4.71	Pushover curves for the walls with different cohesion	131
4.72	Numerating rows and columns in the wall	132
4.73	Length of cracks in different types of elements for walls with different cohesion at $d = 2mm$	133
4.74	Deformed shapes and crack patterns in the walls with different tensile strengths at $d = 4mm$	135
4.75	Pushover curves for the walls with different tensile strengths	135
4.76	Length of cracks in different types of elements for walls with different tensile strengths at $d = 2mm$	136
4.77	Deformed shapes and crack patterns in the walls with different compressive strengths at $d = 4mm$	137
4.78	Pushover curves for the walls with different compressive strengths	138
4.79	Length of cracks in different types of elements for walls with different compressive strengths at $d = 2mm$	139

4.80	Deformed shapes and crack patterns in the walls with different initial normal stresses at $d = 4mm$	140
4.81	Pushover curve for the wall with different σ_n	141
4.82	Length of cracks in different types of elements for walls with different initial vertical stresses at $d = 2mm$	143
5.1	(a) Failure of masonry wall, Haiti earthquake (b) Out-of-plane collapse of masonry wall, Champerico, Guatemala	149
5.2	(a) Damage of a rural masonry building at Yukar Demirci Village, Turkey [16](b) Failure of a rural masonry building in Palu, Turkey [16]	150
5.3	Studied walls subjected to out of plane displacement	151
5.4	(a), (b) Deformed shape (c) total crack pattern in the wall, Case A, at $d_{top} = 2mm$	152
5.5	Lateral displacement vs. horizontal loads in y direction, Case A	153
5.6	Cracks on the wall (a) at $d = 0.91mm$ (b) at $d = 1.03mm$, Case A	153
5.7	Stress distribution in bricks at $d = 2mm$ for Case A	154
5.8	Crack pattern in the masonry wall $d = 2mm$, Case A	155
5.9	Cracking profile for the walls with different mortar's cohesion	156
5.10	Effect of mortar's cohesion on pushover curve	157
5.11	Crack pattern (a) before and (b) after stepped cracks for wall with $C = 3.5e4Pa$	157
5.12	Length of different types of cracks in different interface elements at rows and columns of walls with different C , Case A	159
5.13	Total crack pattern for walls with different σ_{n0}	160
5.14	Influence of initial normal stress on the behavior of the wall	161
5.15	Length of different types of cracks in different interface elements at rows and columns of walls with different σ_{n0} , Case A	163
5.16	Profile of cracking for walls with different compressive strength for masonry	164
5.17	Influence of masonry compressive strength on the behavior of wall	164
5.18	Length of different types of cracks in different interface elements at rows and columns of walls with different F_{c0} , Case A	165
5.19	(a), (b) Deformation of wall (c) cracking profile of the wall, Case B	167

5.20	(a) Pushover curve for out-of-plane displacement (b) Pushover for in-plane and out-of-plane displacement	168
5.21	Crack pattern in the masonry wall $d = 1.5mm$, Case B	168
5.22	Deformation and cracking profile for different C_0 , Case B	170
5.23	Load displacement curve for different C_0 , Case B	170
5.24	Length of different types of cracks in different interface elements at rows and columns of walls with different C , Case B	171
5.25	Deformation and cracks profile in Case B with different σ_{n0}	173
5.26	Load displacement curve for different σ_{n0} , Case B	174
5.27	Length of different types of cracks in different interface elements at rows and columns of walls with different σ_{n0} , Case B	175
5.28	Deformation and crack pattern for wall with different F_{c0}	176
5.29	Pushover curve for wall with different F_{c0} , Case B	177
5.30	Length of different types of cracks in different interface elements at rows and columns of walls with different F_{c0} , Case B	178
5.31	Series 1: two perpendicular walls ($1 \times 1 \times 0.1$) subjected to out-of-plane loads	179
5.32	Series 2: two perpendicular walls ($1 \times 1 \times 0.1$ and $1.5 \times 1 \times 0.1$) subjected to out-of-plane loads	180
5.33	Deformation of the set, top nodes of Wall 1 move in x direction, Series 1	181
5.34	Load-displacement curve for the Series 1, Wall 1 moves in x direction	182
5.35	Crack pattern of the set before and after stiffness reduction in Wall 2, Series 1 . . .	183
5.36	Crack pattern of Wall 1 at local peak and drop, Series 1	183
5.37	Crack pattern in the masonry walls $d = 2mm$, Series 1	184
5.38	Deformation and crack pattern for Series 1 with different C_0 , displacements are applied to Wall 1	185
5.39	Pushover curve for the wall 1 in the set with $C_0 = 1e5Pa$	186
5.40	Pushover curve for the case $C_0 = 7.0e5Pa$, Series 1, Wall 1 loaded in x direction .	186
5.41	Minor principal stress (a) $d = 1.54$ (b) $d = 1.72$	187
5.42	Pushover curve for different C_0 , Series 1, Wall 1 loaded in x direction	187

5.43	Deformation and crack pattern for Series 1 with different σ_{n0} , displacements are applied to Wall 1	188
5.44	Pushover curve for different σ_{n0} , Series 1, Wall 1 loaded in x direction	189
5.45	Deformation in different planes, Series 1, $d = 2mm$, all top nodes move in x direction	190
5.46	Crack's pattern for Series 1 (a) Wall 1 subjected to u_x (b) Walls 1 and 2 subjected to u_x	191
5.47	Load displacement curves for Series 1 (a) all top nodes are loaded in x direction (b) comparison between two cases: Series 1, all nodes loaded and Wall 1 top nodes are loaded in x direction	191
5.48	Deformation in different planes, Series 1, $d = 2mm$, all top nodes move in y direction	192
5.49	Load displacement curve for Series 1 (a) all top nodes are loaded in y direction (b) comparison between two cases: Series 1, all nodes move in x direction and all nodes move in y direction	193
5.50	Load displacement curve comparison: (a) walls subjected to in-plane displacements (b) walls are subjected to out-of-plane displacements	193
5.51	Deformation and total crack pattern for walls subjected to 0.05 degree rotation, Series 1	194
5.52	Lateral load-displacement curves of walls in (a) x direction (b) y direction, Series 1, 0.05 degree rotation	195
5.53	Crack pattern in the masonry walls ,Series 1, roof rotates 0.05 degree	196
5.54	Deformation in different planes, Series 2, all top nodes move $d = 2mm$ in x direction	197
5.55	Total cracks pattern, all top nodes move $2mm$ in x direction (a) Series 2 (b) Series 1	198
5.56	Load displacement curve, all top nodes move $2mm$ in x direction (a) Series 2 (b) comparison between Series 2 and Series 1	198
5.57	Deformation in different planes, Series 2, all top nodes move $d = 2mm$ in y direction	199
5.58	Total cracks pattern, all top nodes move $2mm$ in y direction (a) Series 2 (b) Series 1	200
5.59	Load displacement curve, all top nodes move $2mm$ in y direction (a) Series 2 (b) comparison between Series 2 and Series 1	200
5.60	Deformation and total crack pattern for walls whose supposed roof is subjected to 0.05 degree of rotation, Series 2	200
5.61	Lateral load-displacement curves of walls in (a) x direction (b) y direction, Series 2, 0.05 degree rotation	201

5.62 Crack pattern in the masonry walls, Series 2, 0.05 rotation	202
B.1 Shear wall results for $\beta = 15^\circ$	213
B.2 Stress distribution in bricks d=4mm for $\beta = 15^\circ$	214
B.3 Shear wall results for $\beta = 32.80^\circ$	215
B.4 Stress distribution in bricks d=4mm for $\beta = 30^\circ$	215
B.5 Shear wall results for $\beta = 67^\circ$	216
B.6 Stress distribution in bricks d=4mm for $\beta = 67^\circ$	216
B.7 Shear wall results for $\beta = 75^\circ$	217
B.8 Stress distribution in bricks d=4mm for $\beta = 75^\circ$	217
B.9 Profile of cracking in the wall with different β	218
B.10 Pushover curve for the wall with different β	219
B.11 Shear wall results for $GI = 8N/m^2$	219
B.12 Shear wall results for $GI = 13N/m^2$	219
B.13 Shear wall results for $GI = 23N/m^2$	220
B.14 Shear wall results for $GI = 33N/m^2$	220
B.15 Pushover curve for the wall with different GI	221
B.16 Profile of cracking in the wall with different GI	221
B.17 Shear wall results for $GII = 9.25N/m^2$	222
B.18 Shear wall results for $GII = 1.25E1N/m^2$	222
B.19 Shear wall results for $GII = 1.25E3N/m^2$	223
B.20 Shear wall results for $GII = 1.25E4N/m^2$	223
B.21 Pushover curve for the wall with different GII	224
B.22 Profile of cracking in the wall with different GII	224
B.23 Shear wall results for $GIII = 1E2N/m^2$	225
B.24 Shear wall results for $GIII = 4E3N/m^2$	225
B.25 Shear wall results for $GIII = 7.5E3N/m^2$	226
B.26 Shear wall results for $GIII = 1E4N/m^2$	226

B.27 Pushover curve for the wall with different $GIII$	226
B.28 Profile of cracking in the wall with different $GIII$	227

List of Tables

3.1	Properties of equivalent struts models tested	63
4.1	Elastic properties of bricks and mortar used in the model [60]	81
4.2	Inelastic properties of joints [60]	81
4.3	Properties of the potential brick cracks [60]	81
4.4	Inelastic properties for the horizontal and vertical interface elements for model II .	108
4.5	Brick-middle interface element properties for model II	108
5.1	Inelastic properties for the horizontal and vertical interface elements	152
5.2	The crack profile for the damaged walls, Case A	166
5.3	The crack profile for the damaged walls, Case B	177

Chapter 1

Introduction

1.1 Introduction

Masonry construction was one of the first types of structures erected by ancient civilizations which is still being used in different parts of the world. Simplicity of construction procedure, availability of the constituent materials, aesthetic, durability, easy maintenance, fire protection, and insulation properties of masonry structures have made it popular throughout history. Masonry walls are used as load-bearing and infill panels in low and medium/high rise buildings respectively. High structural strength under gravity loads and significant stiffness of masonry under lateral loads have drawn attention of structural engineers to examine their structural behavior. However, the research development and practice in the industry on masonry structures have not been as advanced as concrete and steel. The reason lies behind complex composition and behavior of masonry structures. Masonry is composed of units (i.e. brick and concrete) and mortar, which have distinct material properties. Unit and mortar constitute a composite structure, exhibiting a complex behavior which is not easy to predict. Conducted research on masonry structures has been very limited, compared to concrete and steel. Therefore, there is a great need for further investigation and development of computational tools and methods to assess the behavior of such structures at different scales.

Masonry structures are home to a large population of the world, especially in the developing countries. Failure of masonry structures under earthquake and wind loads, result in fatal catastrophes frequently. The heavy masonry walls do not sway with the earthquake motion and exhibit brittle behavior, resulting in crack propagation and collapse under cyclic loading. Moreover, victims of natural disasters that live in masonry structures, get buried under heavy weight of masonry wall, which may cause immediate death or hinder search and rescue operations. Hence, evaluating the vulnerability of masonry is a key issue in risk analysis. Vulnerability can be expressed as a degree of loss of an element at risk or set of elements at risk, due to the occurrence of a natural or technological phenomenon. Two key factors can be identified as essential basis of all methods of calculating vulnerability: a robust assessment of aggression hazard (earthquake, wind, flood, drought) and an appropriate model for calculating structural damage.

Various methods are currently used to determine the vulnerability of infrastructure, individual structures and economic or social factors related to risk posed by a hazard. These methods aim to find the level of damage induced in each element at risk for a given hazard level. The choice of the appropriate method to use depends on the size of the project, the quantity and quality of data and resources. If post-event observations and experts' opinion constitute the methods used for groups of buildings, analytical simplified models and detailed analysis of structures are convenient for individual buildings.

In earthquake engineering, a more sophisticated concept, called "Performance Based Design" has been developed in recent years. This approach reveals the need to define the status of a structure in its response to seismic excitation by a level of performance which is close to the

meaning of ultimate limit states and service widely used in France and abroad. The effective use of a method based on the performance of the structure requires the definition of progressive degrees of damage related to the function of a particular system in the diagnostic approach. The objective of a damage computation is therefore to evaluate the loss of stiffness of the structure based on a sufficiently detailed analysis and to estimate the characteristics of vulnerability for a given level of earthquake or other type of aggression.

Moreover, numerous important historic sites and structures are exposed to the same aggressions while being deteriorated and often poorly maintained. In addition to the evaluation of their performance, it is important to analyze rehabilitation solutions and remedial actions for existing buildings.



(a)



(b)

Figure 1.1: Collapse in unreinforced masonry building (a) Westmorland California [102] (b) Port-au-Prince, Haiti [45]

1.2 Objectives of study

This study focuses on nonlinear analysis of unreinforced masonry construction using multiscale modeling. The behavior of masonry structure under monotonic loading is investigated using finite element tools in both macro- and micro- levels. First, the overall behavior of masonry infills and their response is evaluated using macro modeling strategy in which the infill panel is substituted by two struts. As this approach necessitates experimental data from full scale tests which are not always available due to their high cost and important number of parameters to explore, a numerical approach is used to develop a virtual panel -testing simulator. This sim-

ulator is based on a Finite Elements 3D micro-modeling strategy in which bricks and mortars are modeled individually. Not only the failure mechanisms of masonry walls with different geometries and material properties can be assessed by this approach but also both in-plane and out-of-plane loadings can be taken into account. The main objectives of this study are:

to develop a simple and suitable constitutive law for macro models, capable to represent the behavior of masonry infill walls in post-peak regime,

to verify and develop an accurate micro-model in 3D which is able to predict the behavior of masonry wall before and after damage and give a deep insight of failure mechanisms of unreinforced masonry walls under in-plane loading. The developed constitutive law should be able to predict different failure modes and ultimate sustainable loads of the masonry with a reasonable agreement with experimental data,

to investigate the relation between failure mechanism of the wall and geometrical and material properties of masonry walls,

to introduce damage indexes which illustrate failure mechanisms of masonry structures under monotonic loads,

to find a relation between material properties and cracking profile in the wall,

to predict the behavior of masonry walls under out of plane loads, considering the effect of boundary condition and geometrical configurations on response of masonry structures.

In Chapter 2, a general overview of different strategies which have been implemented for numerical modeling of masonry construction are reviewed. First, the research development on modeling masonry infill panels using simple macro elements and the associated constitutive laws are summarized. Then, characterization of micro-modeling of masonry walls discussed. In this method, units and mortars are modeled separately using solid and interface elements. In this strategy, bricks are supposed to remain unchanged and all non linearity is assumed to happen in the mortars. Hence, defining an appropriate constitutive law which is able to reproduce different types of failure in this composite material is the main issue of this strategy. Therefore, different failure envelopes which have been implemented by researchers in addition to the advantages and disadvantages of each model are discussed. Then, the other types of models which have been used to predict the behavior of masonry wall under cyclic loading are presented.

Chapter 3 deals with the numerical modeling of masonry infill panels using macro elements. In this chapter, different failure mechanisms of an infill masonry panel are studied. Then an experimental test which has been carried out by CSTB (Centre Scientifique et Technique du Batiment) [31] is modeled using four different techniques from the literature and the deficiency of each model is discussed. Afterward, a tri-linear constitutive model to represent masonry infill wall under monotonic loading is proposed and validated by reproducing the results of two

different experimental tests. Since this type of modeling can just reproduce overall behavior of the wall and is not able to predict the failure mechanisms of walls with different geometrical and material properties, a more accurate model is suggested to be developed for capturing failure characteristics of unreinforced masonry walls.

Chapter 4 introduces a 3D model of unreinforced masonry wall in which units and mortars are represented separately. In this chapter, the performance of masonry walls under in-plane loads is studied using the numerical tool. The nonlinear behavior of a masonry wall is concentrated in the mortars which are modeled using interface elements. First, a simple model which includes tension and shear failure of the joints is used. The deficiencies of the model is verified by comparing the numerical results with experimental data. Then, a more realistic model which comprehends tension, shear and compression failure of masonry is developed. In this model, shear strength of the wall is limited by compression strength of masonry through a straight line. Hence, multisurface yield function comprises tension cut-off, a Mohr-coulomb friction law and a linear compression cap. The softening behavior for tensile strength, cohesion, and compressive strength of masonry is considered. Validation of the model is proved by comparing the obtained numerical results with experimental evidence available in the literature. The importance of considering compression cap in the yield surface is demonstrated by comparing the obtained results of the first and second models. The effect of opening, aspect ratio and material properties on formed failure mechanism of the wall are studied here. Moreover, the length of cracks in different rows and columns of mortars is measured to introduce a damage index associated with different types of failure mechanisms.

Chapter 5 is allocated to study of the behavior of masonry walls under out-of-plane loading. In this chapter first, two masonry walls with different boundary conditions are subjected to out-of-plane loading. The failure mechanism, crack's profile and ultimate strength of the walls are compared and the behavior of masonry wall under this kind of loading is analyzed. A parametric study has been carried out to find the relation between different material properties and damage indexes. Then, two perpendicular walls are modeled and subjected to uniform displacements in x and y directions and rotation. Analysis of the behavior of a set of walls gives a more accurate insight about the difference between in-plane and out-of-plane strength of the walls and assesses the influence of surrounding walls on total performance of a structure. Finally the influence of the size of constituent walls on general behavior of the system is pursued. The manuscript ends with a general conclusion and perspective giving some proposition for future work.

Chapter 2

Literature review

2.1 Introduction

Masonry is the art of building construction with units which are bounded together by the mortar. The simulation of such constructions is difficult because they are composed of two different materials with distinct directional properties such as units (clay bricks, concretes or stone) and mortar. Anisotropic behavior of bricks, dimensions of unit and mortar, aspect ratio, arrangement of bed and head joints, properties of unit mortar interface bond and quality of working, among others are some factors that make masonry modeling difficult. The reliability of numerical modeling highly depends on extracting correct mechanical properties of masonry components from experimental data as well as an accurate definition of boundary conditions and geometry of structure.

Masonry walls are implemented in structural systems in two different circumstances: as infill in steel or reinforced frame structures or as main load bearing element in masonry constructions. In the first system, masonry wall is surrounded by beam and columns and whenever the system is subjected to different loads, interaction between infill and frame would be important. Experimental results show that masonry existence has a significant influence on the behavior of structural system especially under seismic loading. Therefore, masonry stiffness, strength, seismic behavior as well as its interaction with surrounding frame should be considered to have an accurate estimation of these systems. But in the second system, the behavior of masonry components namely units and mortars and their interactions are important. For assessing the behavior of masonry wall in each of these two systems, depending on the desired simplicity, level of accuracy and application field [93], two finite element modeling strategies are used to investigate the behavior of masonry constructions which are namely macro modeling and micro modeling approaches (Figure 2.1 and Figure 2.2).

Macro modeling approach used to simulate the behavior of infill masonry frames is based on representation of an infill by either a single or multiple compressive equivalent diagonal strut, see Figure 2.1(b) or an equivalent orthotropic continuous model. The main purpose of such simplified modeling is that it takes into account global behavior of a structural system without modeling all components and all possible local failure modes. This strategy is based on physical understanding of infilled frame's behavior so a few elements are chosen to represent the overall behavior of the system. Using an equivalent diagonal bar was the first time proposed by Poliakov [1957] [87]. He suggested that a panel can be replaced by a diagonal strut in compression. Holmes [1961] [48] adopted his suggestion and replaced the infill with an equivalent pin-jointed diagonal strut with the same material and the same thickness as the infill. Later, many researchers improved the model. The behavior of infill masonry frames have been studied by changing diagonal strut model's variation such as using single or multiple diagonal struts, [99], [10], [97], material properties namely the elastic behavior of diagonal bar [66], [55] and inelastic behavior of equivalent strut [89], [92].

When masonry wall is simulated by macro modeling strategy, the properties of units, mortar and interface between mortar and bricks are smeared out in one continuum isotropic or an-isotropic material with a relation between average masonry stress and strain. A complete macro model can reproduce an orthotropic material with different tensile and compressive strengths along the material axes as well as different inelastic behavior for each material axis [63]. A great number of studies have used homogenization technique to identify an appropriate constitutive law including main information related to behavior of composite material [83], [104] and [105]. In this method behavior of composite in elastic and inelastic regions is obtained from mechanical characteristics of its components namely blocks and mortar joints and the geometry of the assemblage [12]. This modeling strategy is applicable when the dimension of a structure is large enough so that the relationship between average stress and average strain is acceptable [17].

On the other hand, in micro-model strategy, Figure 2.1(a), for simulating infill frames' behavior, the structure is divided into different types of elements, including brick, mortar, interface between brick and mortar, interface between masonry panel and frame and the frame elements. Hence, in a micro model representing masonry, surrounding frame and infill wall components are established using a numerical method such as finite element method (FEM) or discrete element method (DEM). Then, the behavior of structural system is assessed in detail and all the possible failure mechanisms can be reproduced [100], [73]. Intensive computational effort is the limitation of this strategy that makes the implementation of this strategy for analysis of large structures, difficult. The first finite element approach to model infill frames was suggested by Mallick et al [1967], [1971] [71], [72], defining an appropriate interface element to take into account the slip between frame and infill. Different works have been done using different techniques to evaluate behavior of infill in terms of micro-modeling [56], [4], [26]. Generally, infill walls were represented by 4 or 8-node rectangular elements and frames by beam elements and in some of the models, interaction between frame and models was simulated by interface elements [52]. In spite of its accuracy, this method is not useful for modeling of practical cases such as multi-bay or multistory structures. This type of modeling is very useful for calibrating simplified modeling parameters.

Micro modeling is probably the best way to understand the failure mechanism of masonry constructions. In this method bricks and mortars are modeled separately. Depending on the accuracy of the model, two different types of this approach are implemented: detailed-micro modeling and simplified micro-modeling. In detailed approach units and mortars are represented by solid continuum elements while interface between brick and mortar are represented by discontinuous interface elements which are planes of failure and slipping. In this type of modeling, for taking into account brittle behavior of blocks and non-linearity of joints, a finite element model with very fine mesh is required, Ignatakis et al. [1989] [49]. The accuracy of modeling is very high but the calculation time is the main issue with this method [35]. In the second approach, bricks are modeled by solid elements whereas the properties of mortar and interface between mortar and units are lumped to the discontinuous interface elements. This model is normally used to capture basic failure modes of masonry during loading and local behavior of each component. Because of complexity of modeling, this approach is efficient for small size models and not useful

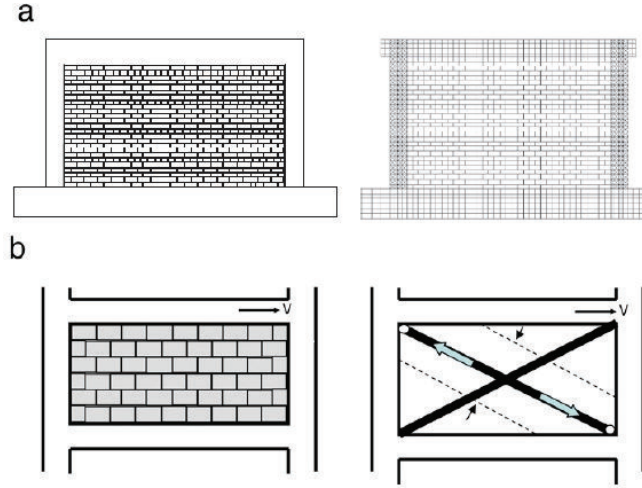


Figure 2.1: (a) Micro modeling approach to model infilled frame (b) macro modeling strategy for representing infilled frame [88], [52]

for modeling of large structures because of large number of elements and cost of calculation.

2.2 Macro modeling of infill masonry frames

Considerable amount of research work has been done on implementation of macro-modeling strategy considering plasticity theory to assess the behavior of masonry wall subjected to monotonic and cyclic loads. This approach is applied for numerical modeling of large scale structures in which global behavior of the structure is important. Disadvantages of this method includes the inability to produce different failure modes and need for comprehensive experimental data to determine the properties of equivalent material.

Macro-modeling strategy for infill masonry frame implements a single global structural member, composed most often of equivalent diagonal struts instead of masonry panel. Infill masonry at high lateral load deforms in shear mode while surrounding frame represents deformation in flexural mode. So, to model the composite action between infill and frame, researchers have suggested that a diagonal strut with appropriate geometry and material characteristic is substituted with infill masonry. This method called equivalent diagonal strut approach: Holmes [1963] [48], Stafford-Smith [1966] [99], Chrysostomou [2002] [21], El-Dakhakhni et al. [2003] [30].

Stafford-Smith [1966] [99] modeled infill panel using an equivalent pin-joint strut. Based on experimental data from a large series of tests on masonry infill frames, he suggested a range

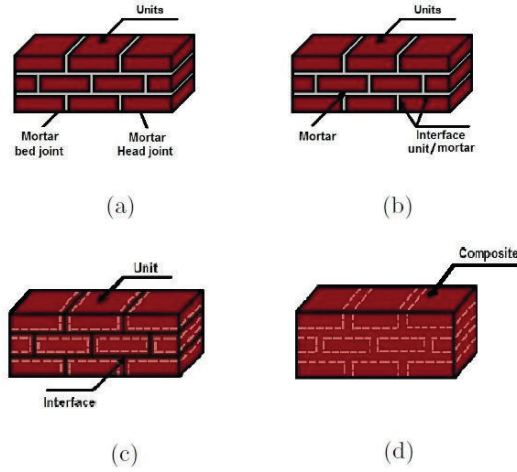


Figure 2.2: Different Modeling strategies for masonry structures (a) masonry sample (b) detailed micro-modeling (c) simplified micro-modeling (d) macro-modeling

for the ratio of width to diagonal length of masonry. So the infill replaced by a diagonal bar whose width depended on relative stiffness between frame and infill. Chrysostom [1991] [21] and Chrysostom [2002] [22] assigned three compression only inclined struts in each diagonal direction instead of infill masonry whose behavior was defined by strength envelope and equation of hysteresis loop. Off-diagonal struts which represented interaction between infill masonry panel and frame were positioned in critical locations along the frame members. Stiffness and strength degradation of masonry infills were considered in their model. By considering three struts, the interaction between infill and the surrounding frame is accounted for which has an important role in the performance of infilled frame.

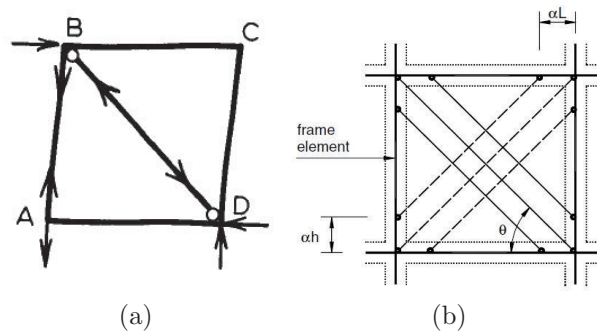


Figure 2.3: (a) Single strut model suggested by Stafford-Smith [1966] [99] (b) six-strut model proposed by Chrysostom [1991] [21]

El-Dakhakhni et al. [2003] [30] also modeled infill by three struts. They proposed a simple method for estimating the lateral stiffness and lateral load capacity of infilled masonry steel frames which crushes in the corners as well as the internal force in steel frame member. Nonlinear behavior of both masonry infill (crushing) and steel frame (formation of plastic hinges) were accounted by this method. In their method three struts one diagonal and two off-diagonal are substituted masonry infill whose force-displacement diagram was based on orthotropic behavior of masonry infill. A simplified trilinear stress-strain relation was accounted for masonry infill, Figure 2.4(b). Similar load displacement diagram was also used for modeling frame member's behavior.

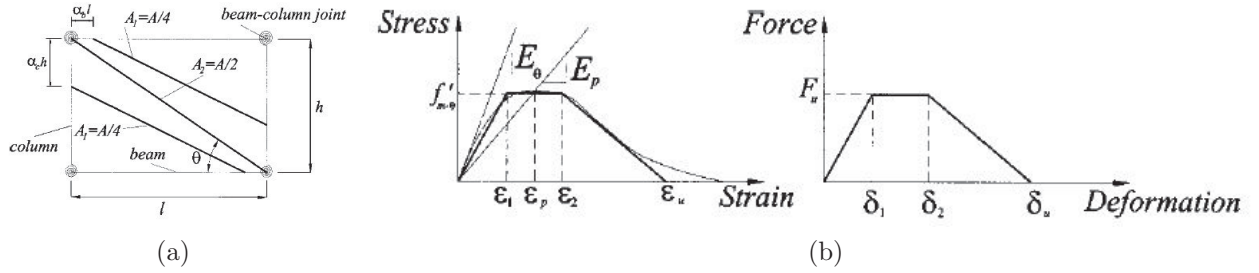


Figure 2.4: (a) Strut model by [30] (b) trilinear relations: stress-strain relation and typical force-deformation relation for struts proposed by El-Dakhakhni et al. [2003] [30]

For modeling the multi-story frame with infilled masonry, Decanini et al. [2004] [27] replaced each panel by two struts which were inactive in tension and just worked in compression. However combination of both struts provides a resistance against lateral loads. Hysteresis model which was adopted for masonry panel is shown in Figure 2.5. The influence of mechanical characteristic of infill was investigated by using different types of masonry with different strengths. Based on the results of studies, they showed that the global nonlinear seismic behavior of masonry infill frames can be obtained by using simple model which combines a shear type model with equivalent strut elements.

Crisafulli et al. [2007] [24] developed a macro model based on mutli-strut formulation. A 4-node panel element which connected to the frame at beam-column joints was implemented to take into account compressive and shear behavior of masonry separately. Two parallel struts and a shear spring in each direction were used for taking into consideration the infill stiffness and masonry's strength. The configuration of model considers the lateral stiffness of the panel and the strength of masonry during shear failure or tension diagonal failure. As the contact length between panel and the frame decreased by load increment and cracks formed in the masonry infill, the area of equivalent strut supposed to decrease by increment of lateral displacement on the system, Figure 2.6(b). The model was able to reproduce different shear failures which were observed for masonry infills. The model was also suitable to use in large structural frames. The main limitation of this model is that as panel element was connected to frame in beam-column

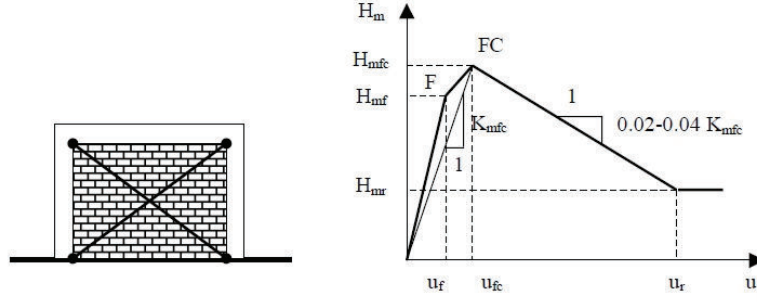


Figure 2.5: Force-displacement envelope curve of the equivalent strut, Decanini et al.[2004] [27]

joints, the bending moment and shear forces of the frame could not be obtained.

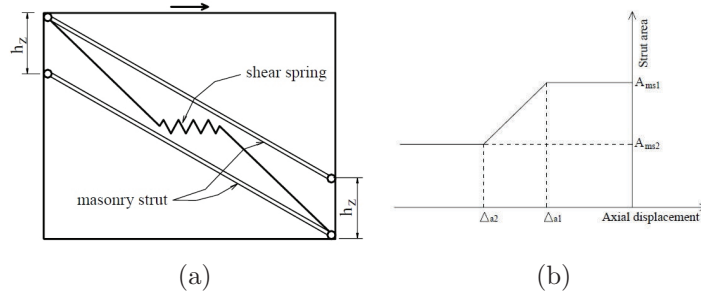


Figure 2.6: (a) Multi-strut model (b) variation of the strut area proposed by Crisafulli et al. [2007] [24]

The previous models had 2 dimension configurations, so they were not capable to take into account the out-of-plane behavior of masonry. Hashemi et al. [2007] [46] developed a 3D model in which interaction between frame and panel as well as in-plane and out of plane behavior of infill were taken into account. A three-dimensional strut and tie model that takes into account both in-plane and out of plane strength of infill under bi-directional loading was used. The model was composed of eight compression-only struts which were connected together with a tension-only link element at the center of the infill panel. Results have shown that existence of in-plane forces cause decrease in out-of-plane capacity of infill whereas out-of plane forces also decrease in-plane capacity of infilled frame.

Puglisi et al. [2009] [88] showed that the conventional equivalent strut does not correspond to the real behavior of wall. The real infill is a unique element but the strut model strategy replaces masonry by two independent bars. So, a simple modification in diagonal strut system was proposed so that to consider coupling between two bars. A plastic concentrator was included at intersection of the bars to capture inelastic behavior of the wall. It also links the two bars to account for the transfer of forces between them. Presence of plastic concentrator gives a more

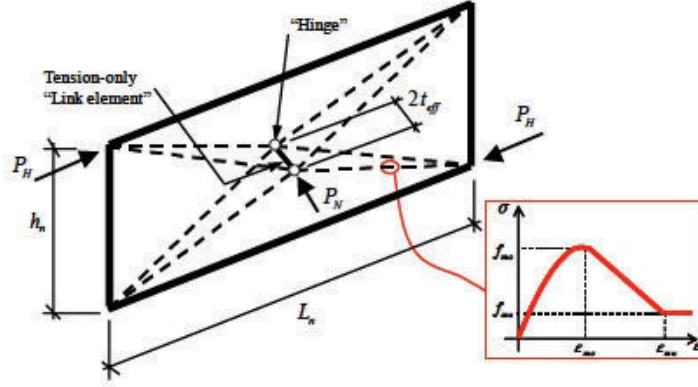


Figure 2.7: Three-dimensional SAT model of URM infill wall proposed by Hashemi et al.[2007] [46]

realistic representation of infill frame's behavior shown in Figure 2.8.

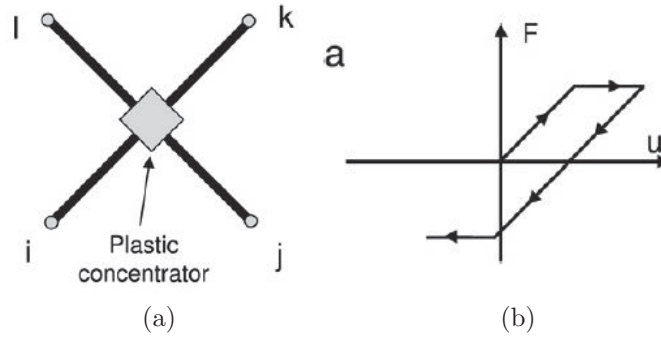


Figure 2.8: Plastic concentrator model proposed by Puglisi et al.[2009] (a) Infill panel with plastic concentrator (b) force-displacement diagram with plastic concentrator [88]

Rodrigues et al. [2010] [92] have developed an equivalent bi-diagonal compression strut model to evaluate the behavior of masonry infill walls which were subjected to cyclic loads. As damage on panel in one direction affects its behavior in the other direction, the interaction between frame and masonry infill in two directions was considered in the proposed model. Therefore, their model could capture more accurate global response and energy dissipation during loading. Masonry infill was modeled by four support strut elements with rigid behavior and a central strut element. Nonlinear hysteresis behavior of masonry was concentrated in the central strut element which had purely tensile or compressive nature. Different rules were implemented in hysteresis procedure to model loading, unloading and reloading. Stiffness and strength degradation as well as pinching effect also were considered in the model.

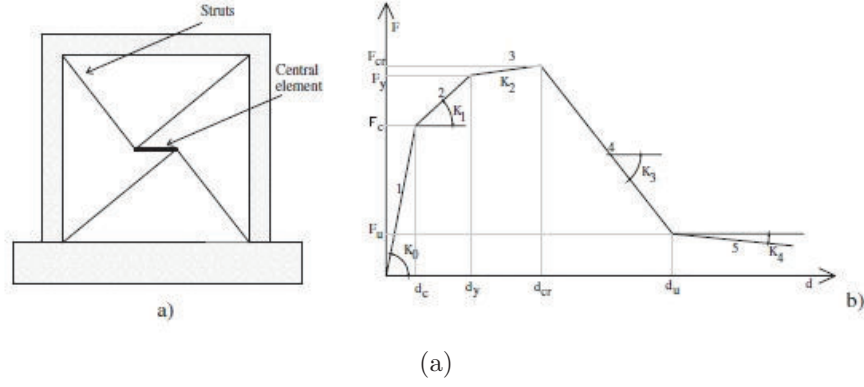


Figure 2.9: (a) Macro model used for simulating masonry infill panel by [92] (b) force-displacement diagram representing nonlinear behavior of masonry under monotonic loading, proposed by Rodrigues et al. [2010] [92]

2.3 Micro modeling of masonry walls

A lot of research has been done by using simplified micro modeling to investigate behavior of masonry wall under different load condition. Different researchers have developed different models to elaborate performance of masonry wall under monotonic and seismic loading. Most of research has been done to investigate the in-plane nonlinear behavior of masonry and is studied in 2 dimensions. Therefore, these models are unable to reproduce the out of plane behavior of the wall. As one of the most critical issues about the performance of the unreinforced masonry construction against seismic loading is its out-of plane behavior and great damage which may happen because of its reaction, a real and accurate model must be able to model both in plane and out of plane behavior of the wall simultaneously under monotonic and cyclic loading.

Page [1978] [82], was the first one who used micro-modeling strategy to investigate in-plane behavior of clay masonry. Brick element supposed to be elastic linear whereas nonlinear behavior of masonry occurred in mortars which were modeled by linkage elements. Low tensile strength, shear strength depending upon degree of present compression stress, nonlinear deformation for tension and shear and high compression strength were the characteristics of linkage elements. The failure criterion in tension was a linear failure envelope while a bi-linear failure criterion was used for shear, see Figure 2.10(a). If tensile or shear failure criterion was violated, failure occurs in the joint. His model was capable to reproduce nonlinear behavior of masonry and local joint failure. Softening behavior for compression was taken into account by changing shear stiffness depending on present compressive stress. Test on deep masonry beam under vertical load was used to validate numerical analysis. Stress distribution was captured but the failure load could not be evaluated because no failure was considered for brick.

Another simple micro-model was proposed by Chiostri et al. [1989] [19], in which bricks were

assumed to be elastic isotrop and gap-elements were used to model mortars. These gap elements were opened progressively due to tension failure of masonry. Tangent stiffness matrix also was changed because of geometrical non linearity. Gap condition means when gap elements open or close or when material behaves nonlinear. In their study analytical response highly depended on the position of gap elements and there were some free parameters which were chosen to reproduce experimental results. Sliding of bed joint could be seen and the bricks were not involved in their model.

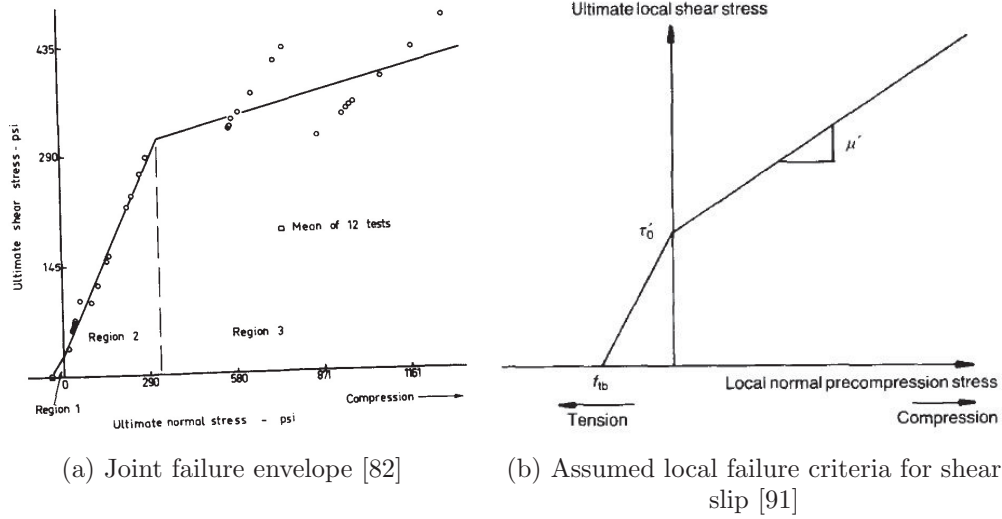


Figure 2.10: Failure surface considered in Page [1987] [82] and Riddington et al. [1990] [91] studies, respectively

Riddington et al. [1990] [91] proposed a more complex model in which bricks, mortars and interface between mortars and bricks modeled separately. Bricks and mortars assumed to remain linear elastic and they are modeled by plane stress elements. In their model, bricks and mortars are connected together by interface elements. Interface elements initially had a high stiffness in both normal and shear directions and in each iteration. They were checked if they reached tension or shear failures or not. In their hypothesis shear failure was different in different levels of precompression stresses. For precompression more than $2N/mm^2$ shear failure initiated by joint slip while for values more than 2, shear failure initiated by tensile failure within the mortar. A complex procedure was used to simulate tensile failure in tension. Interface elements were removed when tension cracks appeared in the model and shear stiffness was assigned to zero in case of shear sliding.

Lourenco et al. [1993] [59] considered gradual softening behavior after crack or slip in the model. They proposed a model which includes continuum elements as brick either elastic linear or with Von-Misses plasticity to capture compression failure in bricks and line interface elements as a plane of weakness where shear and tension damage were assumed to take place in. Softening

behavior was considered for tension and shear in interface elements. Failure surface for interface consisted of two parts: parabolic tension cut-off for tension part and Coulomb failure envelope for shear with softening behavior for cohesion. A first model with elastic behavior for bricks was considered. The model was capable to show crack pattern and qualitative behavior of the experiment but as brick crushing was not taken into account after diagonal cracking load continued to increase with displacement increment. Then Von-Misses criterion for brick crushing was added into the model and analysis showed compression in bricks was limited but calculated failure load was still too high. They concluded that there is no relevant difference between the parabolic criterion and tension cut-off and dilatancy angle has a great influence on behavior of wall.

Masonry units were modeled using smeared crack elements and mortars were represented by interface element in Lotfi et al. [1994] [57] finite element model. The dilatancy which was observed in experiments was modeled using a dilatant interface element for mortars. In this model, the dilatancy decreased by normal stress increment and the rate of dilatancy reduced by increasing the cumulative tangential displacements. Tension and compression failures of units were obtained by using Von-Misses plasticity model in combination of Rankine tension cut-off failure surface. A three-parameter hyperbolic yield function was considered for interface element to reproduce initiation and propagation of fracture in mortar under combination of normal and shear stresses, Figure 2.11(b). This yield function was used to provide smooth transaction between Mohr-Coulomb criterion considered for shear failure and tension cut-off assigned for tension failure. Softening behavior for shear-tension as well as in tension-compression was considered for mortars and units respectively. The comparison between experimental and analytical model showed that failure mode, ductility and crack pattern provided well, the load carrying capacity of masonry evaluated well but under higher normal loads, there was some discrepancy at the final stage of loading because of deficiency of smeared crack model and uncertainty in material parameters for mortar joints.

A sophisticated micro-model was developed by Lourenco et al. [1997] [61] which considered compression failure of masonry. In their model, bricks were assumed to remain elastic whereas a multisurface yield surface including all failure mechanisms in masonry was considered for mortars via zero thickness interface elements. Multisurface yield failure consisted of tension cut-off envelope for tension, Mohr-Coulomb failure criterion for shear and a cap for compression. Moreover an interface element was suggested in the middle of bricks as potential crack plane to capture tension failure of bricks. The main characteristic of the model was cap envelope which limited combination of shear and compression stress in the element. By adding this limitation, unit diagonal tension as well as masonry crushing was included in the model. Softening behavior was also considered for tension, shear and compression. There was a good agreement between experimental data and computational analysis in term of capturing load-displacement diagram in both pre-peak and post-peak regions.

To study the effect of dilatancy of material and roughness of contact, Giambanco et al. [2001]

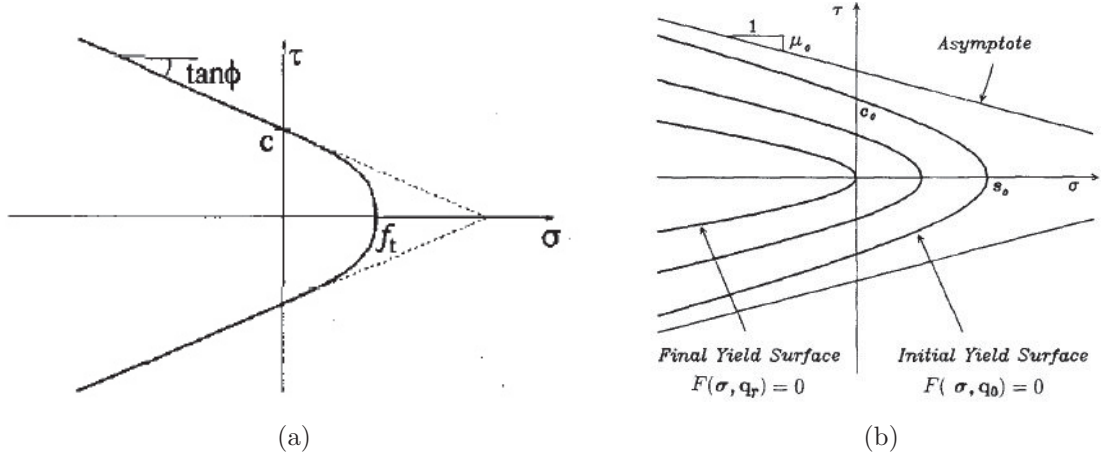


Figure 2.11: (a) Yield surface used in Lourenco et al. [1983] [59] (b) hyperbolic yield criterion proposed by Lotfi et al. [1994] modelings [57]

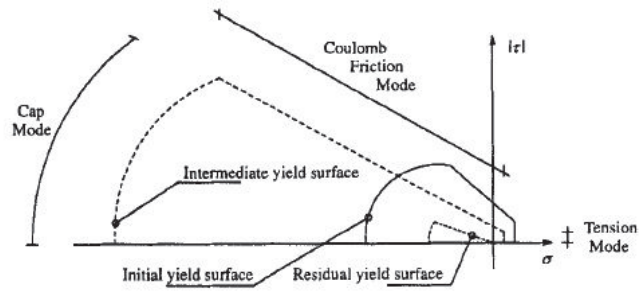


Figure 2.12: Proposed multisurface yield function by Lourenco et al. [1997] [61]

[40] implemented a micro-model for masonry with fully elastic bricks and inelastic interface to predict the behavior of mortar joints in masonry structures. A material dilatancy parameter and the geometrical dilatancy related to roughness of contact were introduced into the model to study effect of roughness at structural level. Moreover a bilinear yield function comprising Mohr-Coulomb criterion for shear and tension cut-off was adopted to evaluate the shape of contact during sliding and cohesion loss process. The compression failure of material did not take into account in their model. Softening behavior was assumed for cohesion and tensile strength. The roughness of surface was also taken into account to describe the change of surface shape during sliding and loss of cohesion. So, the angle α (Figure 2.13(b)) was added to friction angle in shear yield function formulation. This angle depends on the configuration of contact surface and cohesion loss during the loading. It was shown that the roughness of contact surfaces and its evolution have a great influence on failure mode, crack pattern, ductility and post peak branch of load-displacement diagram. In case with no roughness the cracks appeared just at top and bottom of the wall and there was a clear difference between load displacement curves in post-peak region while a good agreement was obtained between results of experiments and analytical model with asperity in term of crack pattern. They concluded that introduction of brick crushing and/or joint compaction will establish the limit load.

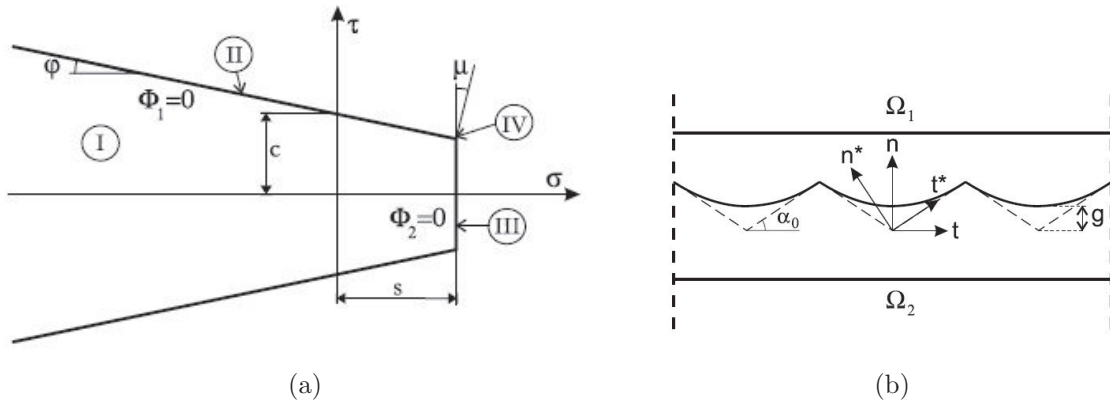


Figure 2.13: (a) Yield function for interface elements (b) hyperbolic asperity model by Giambanco et al. [2001] [40]

Lower bond limit analysis is an alternative to conventional finite element method for elaborating collapse load of masonry structures. Sutcliffe et al. [2001] [101] developed a new technique for calculating the lower bond limit load to investigate the behavior of masonry wall under in-plane loading. Two assumptions were made to use this method: first, the materials were assumed to be perfect-plastic, flow rule was associated with no strain hardening or softening and second, all changes in geometry of structure and deformations were negligible. In order to prevent nonlinear restrictions, linear yield surfaces were used for brick and mortars. Two separate yield function were defined for bricks and mortars. Bricks were supposed to be isotropic and homogeneous with Mohr-Coulomb yield failure curve applicable to considering tensile failure of units. A tri-linear yield surface composed of tension cut-off for tensile failure, Mohr-Coulomb for shear failure and

a linear approximation of cap model of Lourenco et al. [1997] [61] for compression failure also was assumed for mortars, Figure 2.14. In their study softening behavior was not taken into account. Two examples were used to investigate the effectiveness of results. They showed that the model can capture collapse load with good agreement to experimental data, but the failure mode and crack patterns could not be achieved by their model.

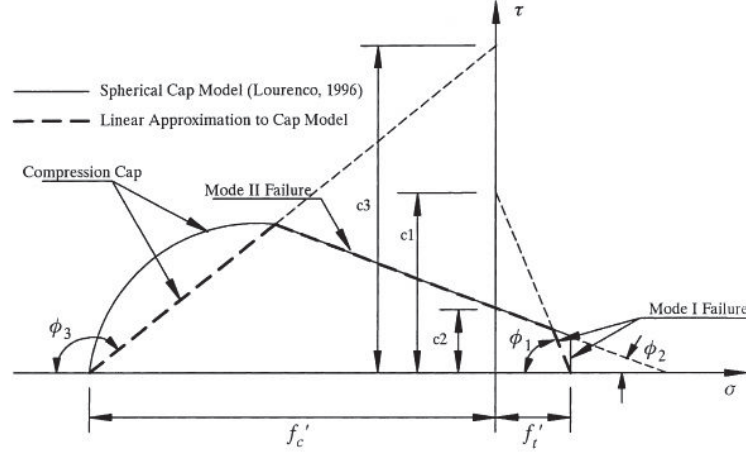


Figure 2.14: Three linear yield surface of interface element by Sutcliffe et al. [2001] [101]

Chaimoon et al. [2007] [17] discretized bricks by triangular finite element units which were surrounded by interface elements as shown in Figure 2.15(a). The interior interface elements represented brick interface while exterior ones around perimeter used to simulate horizontal and vertical mortars. Bricks were supposed to remain linear elastic whereas all nonlinear behavior of masonry assigned to interior and exterior horizontal and vertical interfaces. A multisurface yield function composed of tension cut-off, Mohr-Coulomb criterion for shear and a linear cap model was considered for mortar interface elements. They proposed an equation to compute the slope of the compression cap. Shear failure in addition to tension failure of bricks assessed by assigning a failure surface composed of Mohr-Coulomb envelope and the tension cut-off to interior interface elements. Fracture of unreinforced masonry wall was captured by defining a single branch softening curve for tension and shear as well as a single branch softening curve with a residual level for compression for mortar interface elements. The suggested model was capable to reproduce experimental evidence well.

2.4 Modeling of masonry under cyclic loads

All the researches explained above, study the in-plane behavior of unreinforced masonry shear wall under monotonic loading using micro modeling strategy. Due to the complexity of be-

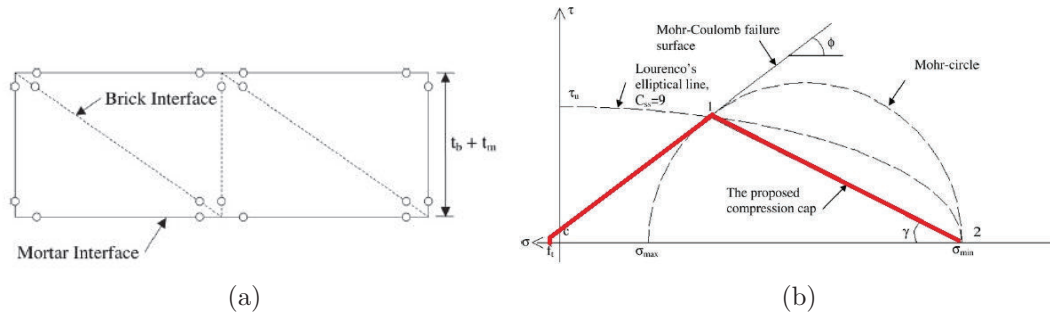


Figure 2.15: (a) Single masonry unit (b) piecewise linear yield surface used by Chaimoon et al. [2007] [17]

havior of masonry under cyclic loading few studies on the behavior of these constructions are available. Nonlinear behavior of masonry under monotonic loads consists of cracking, crushing, sliding, tension and compression and shear softening behavior but there are some other complex behaviors which should be predicted for masonry model under cyclic loading. Reloading and unloading rules, stiffness degradation in tensile and compressive regimes, energy dissipation at each cycle and between cycles, crack closure in compression and plastic strain at zero stress level are the other parameters which should be considered in masonry constitutive laws in case of cyclic loading so the extension of monotonic constitutive model to cyclic one is very intricate. Different strategies and models were used to evaluate the behavior of such construction under cyclic loading. Marco modeling, micro modeling and equivalent frame systems are the strategies which have been proposed by different researchers to assess these phenomena.

Using equivalent frame system to investigate the seismic behavior of masonry has been explored long time ago. Different researchers have used this method to carry pushover analysis and assess the behavior of such construction. In this system, masonry wall is discretized by piers and spandrels which are modeled using 2 node macro element, considering nonlinear behavior of material by defining an appropriate constitutive law. The shear and compression failure modes are considered in the model. Researchers have shown that this model can obtain overall behavior of masonry building in a reasonable fashion [50], [69], [9] and [90]. Different strategies have provided to overcome the limitation of this method such as defining the reduced stiffness of the masonry, the compatibility between the walls and connecting transverse members, and then it was extended to analysis of 3D systems [70] too.

Gambarotta et al. [1997] [37] used a composite model to reproduce the behavior of masonry shear walls under in-plane cyclic loads. They applied a constitutive model which takes into account the damage of mortars together with brick and mortar interface decohesion due to opening and frictional sliding. Bricks were modeled by isoparametric elements which were connected by interface elements. Friction of mortars was limited by definition of a friction limit and their damage by introducing the damage conditions as shown in Figure 2.18(a). The brittle behavior

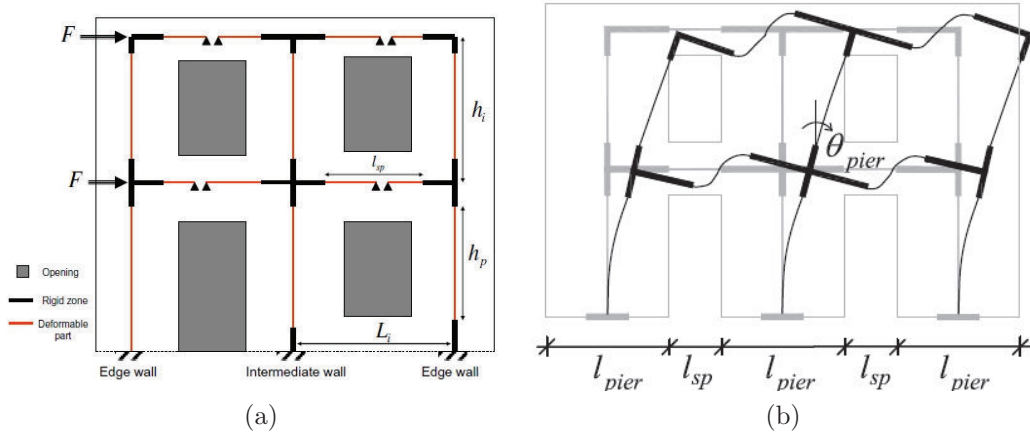


Figure 2.16: Schematic representation of masonry wall modeled by equivalent frame model (a) Belmouden et al. [2009] [9] (b) Bayer et al. [2012] [11]

in tension, energy dissipation due to friction, and stiffness degradation under compression were the characteristics of mortar joint model. Softening behavior was assumed for tensile and shear in mortar joint. Constitutive law for bricks was composed of two parts: Elastic part and post-elastic region. In post-elastic region the tensile fracture of bricks and compressive failure of masonry were reproduced. Tension failure of brick were captured by putting the interface elements in the middle of bricks while an elastic limit condition based on Von-Mises criterion assumed for brick to predict compression failure of masonry as a consequence of different transverse deformation in brick and mortar joints. Figure 2.17 shows the model response to tensile and shear strains as well as cyclic shearing strains. The model was validated by simulating two experimental tests. It was shown that the proposed model was capable to reproduce the stiffness of walls and capture the maximum lateral load as well as the hysteresis behavior of wall during cyclic loading. Different failure mechanisms also were distinguished separately. By the way the proposed model was complicated for modeling the large masonry walls with opening.

Gambarotta et al. [1997] [38] then extended their model [37] to evaluate cyclic behavior of masonry by using a continuum model in which masonry wall was made of two layers, bed joint and brick and head joint. A constitutive formulation based on homogenization process was applied to the bricks. Decohesion and slipping was assumed for bed mortar interface while damage and failure of brick were considered for bricks and head joints. Model was improved by considering compressive strength of masonry and shear strength of brick see Figure 2.18(b). The model was successfully implemented to analyse the behavior of large masonry structures with opening. Numerical calculations showed that model can reproduce damage distribution and cyclic behavior of structures well.

Oliveira et al. [2004] [80] extended the cap model constitutive law for interface in monotonic

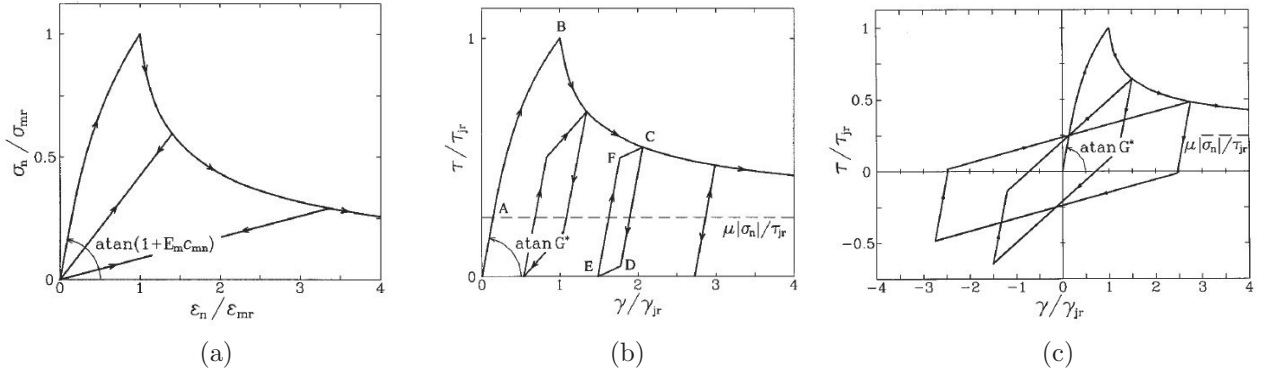


Figure 2.17: Response of the mortar joint model (a) tensile stress (b) shear strain superimposed on constant compressive stress and (c) cyclic shearing strains in Gambarotta et al. [1997] studies [37]

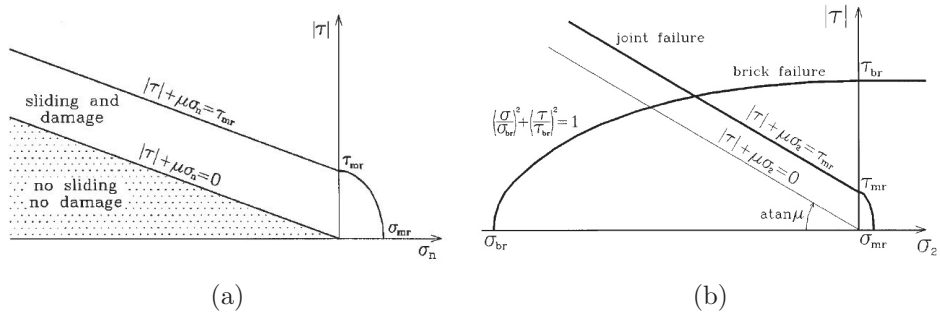


Figure 2.18: Limit strength domain for (a) composite model by Gambarotta et al. [1997] [37] (b) continuum model proposed by Gambarotta et al. [1997] [37]

loading, proposed by Lourenco et al. [1997] [61] by adding two new auxiliary yield surfaces based on incremental theory of plasticity to reproduce cyclic behavior of masonry wall. These yield surfaces were used to model unloading/reloading behavior of wall by including stiffness degradation during each unloading/reloading cycle and between cycles. Their motion was controlled by a mix hardening laws. Each time that stress reversal took place, new unloading surfaces became active and they were deactivated when unloading surface reached monotonic envelope toward which it moved. The accuracy of their model was assessed by making comparison to experimental data. The numerical results have shown that the model was capable to reproduce the main feature of cyclic behavior of masonry wall, namely stiffness degradation, energy dissipation and deformed patterns. The research indicated that geometric asymmetric have a great influence in the performance of a wall against cyclic loads. But a premature numerical failure prevented the model to predict the behavior of low height walls.

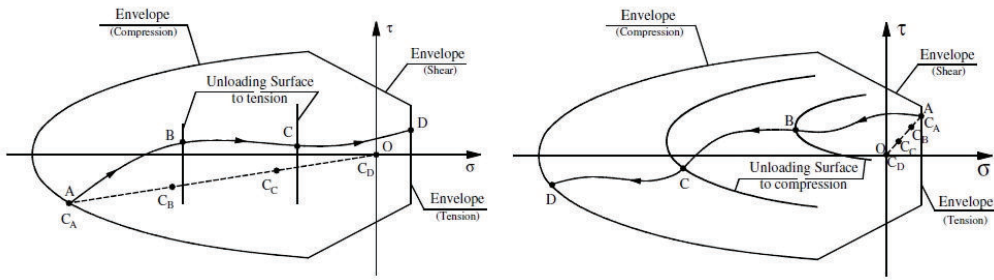


Figure 2.19: Motion of auxiliary yield function proposed by Oliveira et al. [2004] in tension and compression [80]

Casolo et al. [2007] [14] implemented the rigid body spring model to simulate in-plane behavior of masonry under cyclic actions. Discrete model, collection of plane quadrilateral rigid elements which were connected by 2, normal springs and one shear spring, were considered in their study. Specific separate constitutive law involving hysteresis behavior under axial and shear deformations was assigned to elements so that to reproduce post-elastic behavior such as mechanical deterioration and hysteresis energy dissipation. Coulomb-like law also was adopted to relate strength of shear spring to vertical axial loads.

This approach is effective for time history analysis of large masonry structures and reduces computational effort significantly. Constitutive law for individual springs was provided to satisfy following assumption for masonry: low strength, brittle response and rapid mechanical degradation in tension, exhibition of maximum bearing capacity with limited ductility, progressive mechanical degradation and energy dissipation after peak in compression and dependence to normal stresses and significant energy dissipation for repeated cycles in shear. They showed adoption of a discrete model consisted of rigid body and spring to model behavior of masonry under cyclic loading has some advantage in term of simplicity over a continuum model especially for defining the degradation of material under cyclic loads. The proposed model deals with

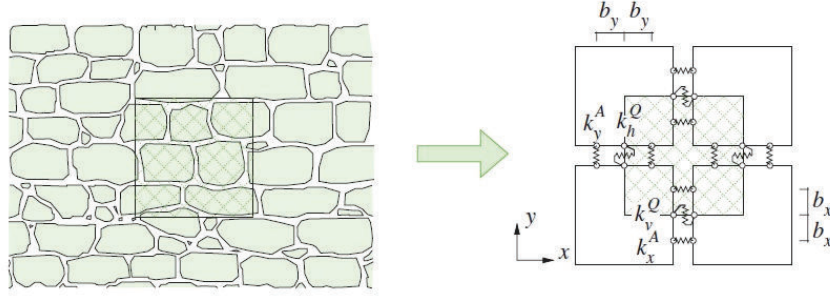


Figure 2.20: Scheme of an irregular masonry defined by four rigid elements [14]

uniaxial stress state at once so less computational effort needs to do for dynamical analysis of masonry.

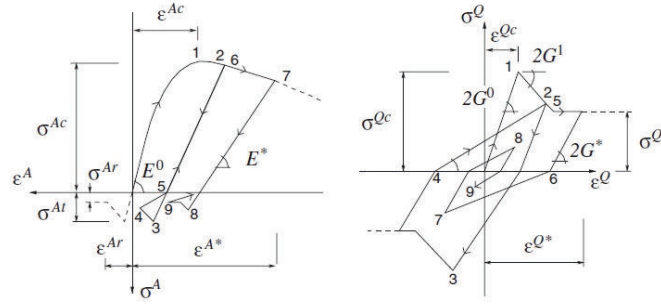


Figure 2.21: Hysteretic behavior of the axial (left) and shear (right) connecting springs used in Casolo et al. [2007] model [14]

Karapitta et al. [2011] [51] developed a smeared crack constitutive model to investigate the behavior of unreinforced masonry under monotonic and cyclic in-plane loading. Macro-modeling approach was considered in their study since masonry was supposed to be homogeneous with different strengths along and normal to bed joints and cracks are smeared over the areas of finite elements. Three constitutive laws for describing tension, shear and compression damage based on uni-axial stress and equivalent total strain were implemented in the model. The stiffness degradation depending on direction of loading, unloading and reloading was evaluated in the analysis. Tensile and shear stress strain curves were composed of linear elastic and softening regions, whereas linear elastic, strain hardening and strain softening were characterized for compression in masonry.

The proposed unloading-reloading regimes considered for tension, compression and shear were shown in Figure 2.22. Results showed that model is capable to predict the most important charac-

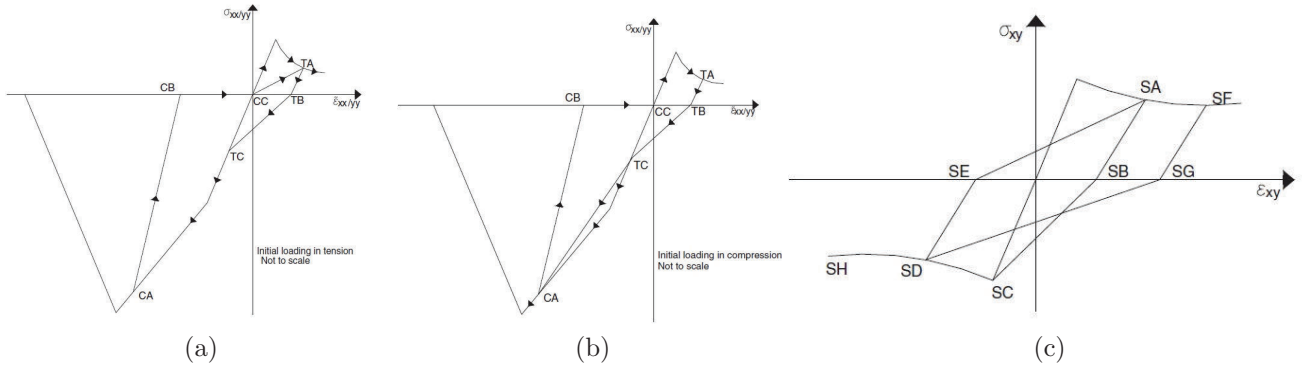


Figure 2.22: Cyclic stress-strain relationship for unloading-reloading stages, initial loading in (a) tension (b) compression and (c) shear proposed by Karapitta et al. [2011] [51]

teristics of masonry subjected to cyclic loading such as hysteresis behavior, stiffness degradation and energy dissipation. Some improvements such as dependence of shear to compression, considering effect of Poisson ratio and coupling of tension and compression damage were proposed by authors.

In this study the behavior of masonry as infill and as shear wall will be investigated in scale of macro and micro, respectively. At first, the behavior of infill masonry panels is studied by macro-modeling strategy. In macro element modeling, two compression-only struts elements are representing masonry. The results of monotonic loading experiments on masonry infill panels which have been done by CSTB (Centre Scientifique et Technique du Btiment) are used to calibrate the diagonal strut's characteristics. In this approach, having knowledge about the behavior and failure modes of the wall is very necessary for calibrating model parameters.

As laboratory tests are costly and their results highly depend on condition of tests, micro-modeling strategy is used to evaluate behavior of masonry wall under different types of loading, wall's dimensions and mechanical properties. In second part, mechanical properties of bricks and joints are considered separately. Masonry wall is modeled in 3D using solid elements as bricks whereas mortars are modeled using zero-thickness interface elements. A constitutive law is defined for material so that to simulate the behavior of masonry shear wall. Numerical results are validated by making a comparison with experimental data carried out by Rajmakers and Vermeltfoort [1992] [85], Vermeltfoort Rajmakers [1993] [86] and CUR [1994] [25]. In third part, the behavior of masonry wall under out-of-plane loads is investigated. A masonry wall and two perpendicular walls are subjected to out-of-plane loads and their failure mechanisms are studied. Finally, the micro-model is improved to reproduce the response of masonry walls under cyclic loading.

2.5 Conclusion

The development of numerical modeling of masonry structures using macro and micro model strategies has been reviewed in this chapter. The accuracy of models to assess the nonlinear behavior of masonry infills using the macro elements with different geometries and mechanical properties has been evaluated. Moreover, different constitutive laws proposed by several researchers for interface element representing nonlinear behavior of masonry wall have been appraised. Studying the development of different strategies for modeling masonry construction and considering their advantages and disadvantages in this chapter, gave a good insight about the more important parameters which should be considered in the modeling and enable the author to propose the more convenient models for representing masonry in both macro and micro levels.

Chapter 3

Macro modeling

3.1 Introduction

Steel or reinforced concrete frames with masonry panels are one of the most popular types of constructions in seismic regions all over the world especially in residential and commercial buildings. Masonry panels typically consist of brick, clay tile or concrete blocks and mortars and are constructed between beam and columns of a frame. These panels are used for interior partitioning as well as exterior enclosure. They are not considered as structural elements in design process, so their stiffness and strength are ignored whereas global response of infill frames can significantly be affected by presence of infill.

Masonry wall increases the stiffness and strength of infilled frame so its performance is not the same as bare frames. Increasing the rigidity of a system will change the natural frequency of the structure therefore the applied load on structure may increase or decrease dramatically depending on the seismic spectrum values at the closeness of the bare structure natural period. Therefore masonry panel increases stiffness and strength of structural system and introduces more modes of failure mechanism associated with wall failure and wall-frame interaction. Existence of masonry infill also can change redistribution of stresses that can make unpredictable damage along frames.

A lot of research activities including experimental or analytical works have been done to investigate the behavior of infill masonry panel on frames and its influence on performance of structural system. The simplest and more practical way to simulate behavior of infilled frames has been done by macro modeling. In this strategy, masonry infill is replaced by a single or multiple compression-only diagonal struts with appropriate geometrical and mechanical characteristics. In this section, first, different failure mechanisms of infilled frames are discussed briefly. Then, the results of CSTB tests [31] are presented and the equivalent strut model is identified to model masonry infill. Three different methods which are used in literature are selected to calibrate the characteristic of equivalent diagonal strut. Then a trilinear model is proposed as constitutive law to simulate masonry behavior. The methods are:

- FEMA 356 model [34]
- Calibrated model proposed by Hashemi and Mosalam [2007] [46]
- Mostafaei and Kabeyasawa model [2004] [76]
- Tri-linear proposed model

The details of each model will be discussed in the following sections.

3.2 Behavior of infill frames

Modeling of the behavior of infill wall is a very complex issue due to important role of interaction between infill and masonry on performance of this construction. In most cases, when in-plane lateral loads are applied at one top of an infill frame, a diagonal truss-formed strut is formed from top loaded corner to the opposite bottom corner to resist it. In moderate loads, the infill separates from surrounding frame at non-integrated parts and in the opposite direction infill acts as diagonal, Figure 3.1. As load increases, depending on mechanical properties of infill and frame and their interaction, failure occurs finally either in infill or frame.

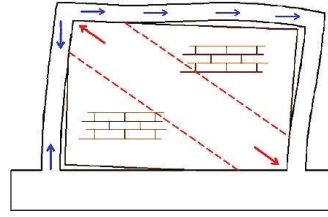


Figure 3.1: Formation of diagonal strut [23]

Tension failure in windward column or shear failure in columns or beams are the most common types of fracture in the frame. If frame has sufficient strength to prevent these failures, load increment causes failure in infill masonry. For infill frames made of concrete, failure is initiated by cracking along diagonal compression and ends to collapse by crushing or crushing near loaded corners. The same phenomenon appears in masonry made of brick in addition to an alternative possibility of shear failure along mortar joints. Different failure modes for infill masonry frames can be classified into five distinct modes [5]:

- Corner crushing: This type of failure is associated with the crushing of infill at least at one loaded corner. This failure happens when masonry infill has low compressive strength. Corner crushing failure is frequently observed.
- Diagonal compression: This mode of failure is represented by crushing the infill within its central region. It can be seen in infill with high slenderness ratio that experiences out-of-plane buckling instability under in-plane loading. This type of failure occurs rarely in practical panels because in these cases, infill thickness is designed to satisfy acoustic isolation and fire protection requirement. Inertial forces in out of plane direction of wall also can cause this type of failure. The combined effect of in-plane and out-of-plane loading decrease strength of the wall in both in-plane and out-of-plane directions which increases the probability of wall failure in both directions [77].
- Sliding shear: This failure happens in panels with weak mortar joints in comparison to the masonry units as well as in panels with low to medium aspect ratio whose shear stress

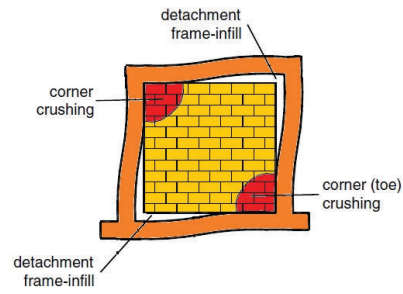


Figure 3.2: Corner Crushing failure (CC)

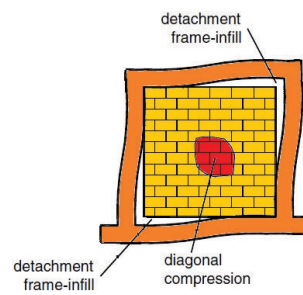


Figure 3.3: Diagonal Compression failure (DC)

dominates its normal stress. Horizontal sliding along bed joints is the characteristic of this type of failure. This type of failure is widely seen.

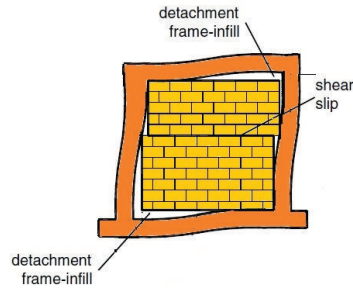


Figure 3.4: Sliding Shear failure (SS)

- Diagonal cracking: Is in the form of a diagonal crack which connects the top loaded corner to bottom opposite corner. This type of failure is experienced in frames with weak joints and infill with high compressive strength or in weak frames. Some researches do not consider this phenomenon as failure mode because the infill carries additional load after diagonal cracks.

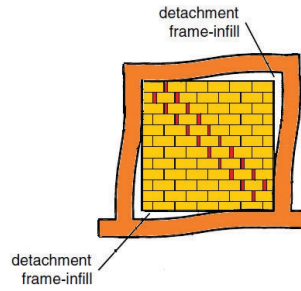


Figure 3.5: Diagonal Cracking failure (DCK)

- Frame failure: When infill panel has high compressive strength, applied load is carried out by infill and transferred to surrounding frame and causes failure in columns. If in design process the effect of strong infill on surrounding frame is not considered, this type of failure is inevitable. This failure mode may also associate with frame with weak joints.

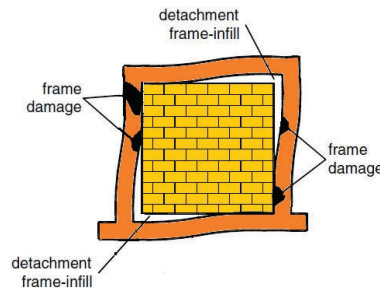


Figure 3.6: Frame Failure (FF)

It should be noted that the first two modes of failure namely corner crushing and shear sliding are important in practical point of view.

3.3 Macro element of code TREMURI

Lagomarsino et al. [2004] [54] developed a model based on a macro mechanical element representative of the in-plane behavior masonry panels to simulate the cyclic and dynamic responses of masonry wall as well as entire buildings. They performed several types of analysis such as pushing progressive, incremental non-linear, incremental dynamic and modal, using a finite element code developed at DICAT (Dipartimento di Ingegneria delle Costruzioni dell'Ambiente e del Territorio, University of Genoa). The results of these analyzes were compared with those

obtained by quasi-static tests on a prototype of a masonry building on a real scale (Magenes and Calvi [1997] [68]). In addition, Calderini and Lagomarsino [2006] [?] developed a damage model for numerical analysis of historical masonry buildings. Masonry is considered as a composite material manufactured by assembling bricks periodic orthogonal joints connected by mortar. Masonry is considered as a composite material constructed by regular assembling of bricks which are connected by mortars.

Masonry elements subjected to dynamic actions have two distinct behavior in the plane of the wall: the slipping due to shear, cracking due to shear and bending. These two main failure modes have been confirmed by actual observations after earthquakes and experimental tests performed on masonry walls. Most frequently failure mode for these structures is formed by the diagonal cracks due to shear forces. This failure mechanism is developed as a combination of vertical and horizontal loads when the major principal stresses in the wall become greater than the tensile strength of the masonry. The flexural strength of a panel in masonry is conditioned by the crushing of the compressed portion.

The macro-element proposed by Gambarotta and Lagomarsino [1996] [39] allows, using a reduced number of degrees of freedom to represent the two main failure modes of masonry structures: shear (taking into account the friction) and flexion. This approach is the main feature of macro element used in the calculation software TREMURI. Using internal variables, this model takes into account the development of damage to the interior of the element, by the deterioration of rigidity and decrease in resistance. The main simplifying assumptions of the method are the following: the structural elements are the walls and floors (or vaults). The floors are considered as rigid elements plans. The behavior of floors in bending and out of plane behavior of walls are not taken into account (out of plane behavior of the walls is considered negligible compared to the in plane behavior). TREMURI model is used as the base model to perform preliminary analysis and to verify the developed macro-element in this work. A post-processor damage has also been developed in this context.

3.4 Experiments conducted at CSTB

At first step, the results of CSTB tests are used to define and calibrate the numerical model. Figure 3.7 shows the test set-up which was used to apply lateral in-plane loads on masonry panel. Two types of loading were available: monotonic and cyclic. Force was applied to the corner of the panel and transferred through its length by a hamlet whose connection with the rest of the wall is badly identified. In addition, confinement was provided by tendons which were located on both sides of the wall. Tension of tendons was not measured.

These tests were conducted using 37 walls, corresponding to 11 different categories of construction. Before each test, dimensional control and simple compression test were performed on blocks. The results of CSTB tests for wall number 3 are used as input data. The properties of

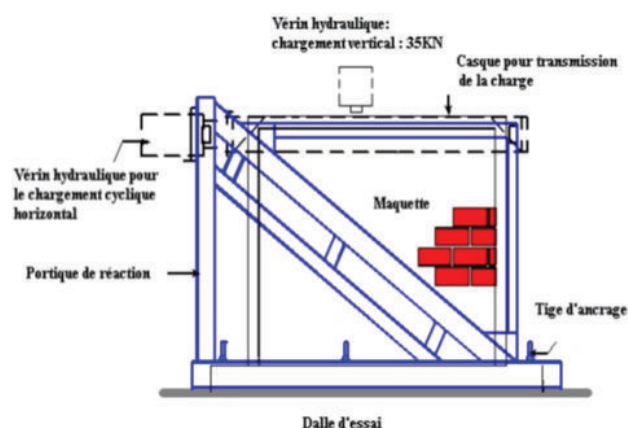


Figure 3.7: CSTB test set-up [31]

blocks, mortar and wall are summarized in Figure 3.8 whereas load displacement diagram and crack pattern are drawn in Figure 3.9.

N° d'essai	Nom de dossier	blocs			Joints			
		type	Dimensions H×L×e (cm)	Résistance En compression (MPa)	Horizontaux	Verticaux (*)	Résistance En flexion (Mpa)	Résistance En compression (Mpa)
1	ER 55390518 Partie I	Blocs creux en béton	20×50×20	bloc poteau 7 Bloc courant 9,3	mortier	remplis	4,37	17,9
2						--	--	--
3						Non remplis	--	--
4						--	--	--
5		Blocs creux en béton	20×50×20	Bloc courant 9,3	mortier	remplis	4,37	17,9
6						--	--	--
7						Non remplis	--	--
8						--	--	--
9						remplis	--	--

Figure 3.8: Blocks and joints properties

3.5 Numerical modeling of masonry

As shown in Figure 3.11, the masonry wall is replaced by two diagonal struts. So the section area obtained in each method is divided by 2 for each strut. A 2D model of the frame is developed whose beam and columns have concrete rectangular sections.

N° d'essai	Dim du mur H×L(m)	chainages	Nature d'essai	résultats			
				Charge élastique (KN)	Déplacement élastique (mm)	Charge max (KN)	Déplacement max (mm)
1	2,6×3,71	Verticaux : Blocs poteaux 4HA10 cadre10×10 Horizontal : Coffre 4HA10 Cadre8×12	Statique	182	0,59	+534	+4,09
2			Alterné	-178 +217	-0,84 +0,93	+570 -553	+2,88 -5,07
3			Statique	175	0,83	+364	+415
4			Alterné	-276 +237	-1,82 +1,45	+361 -400	+3,46 -4,68

Figure 3.9: Masonry wall properties and results of experiments

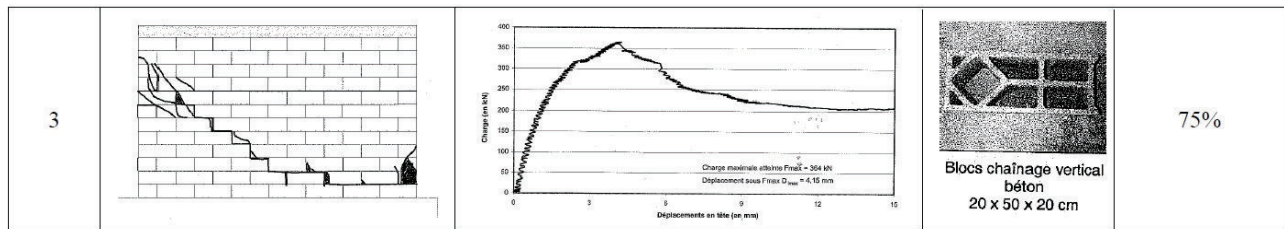


Figure 3.10: Crack propagation, load displacement diagram, block prototype and utilization percentage

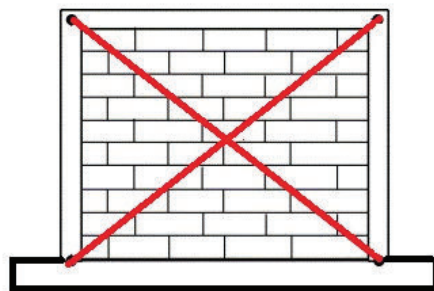


Figure 3.11: Diagonal equivalent model of masonry

Structural elements are beam and columns with nonlinear hysteresis bending moment-end rotation characteristics. Diagonal struts are represented by bar elements with non-linear behavior. The geometrical and mechanical properties of each bar are determined using the methodology described for each model. The modulus of elasticity of masonry, the compressive strength of the blocks and the shear strength of mortar joint are the main parameters. The monotonic displacement is imposed to the top corner of the frame. The same displacements are imposed to the two top nodes in the model because of integrity action of the wall. The symmetric stress-strain curve with same resistance in tension and compression is proposed to model as masonry material property.

As mentioned before, the geometrical and mechanical characteristics of struts are obtained by 4 different methods and the results of numerical analysis are compared to experimental data to gain an insight how much the accuracy of each model is. First, strut characteristics will be obtained by FEMA 356 [34] formulation as described in the following section.

3.5.1 FEMA 356 proposed strut model

According to FEMA 356 [34] provision, an infill can be replaced by a single diagonal strut whose thickness and modulus of elasticity are the same as the infill ones. In the proposed model, the section of strut is equal to the thickness of strut times the strut width a which is calculated by Equation A.1.

$$a = 0.175(\lambda \cdot h_{col})^{-0.4} \cdot r_{inf} \quad (3.1)$$

Where:

$$\lambda = \left[\frac{E_{me} \cdot t_{inf} \cdot \sin(2\theta)}{4 \cdot E_{fe} \cdot I_{col} \cdot h_{inf}} \right]^{0.25} \quad (3.2)$$

$$\theta = \arctan(h_{inf}/l_{inf}) \quad (3.3)$$

In above formulations, h_{col} is the column height between centerlines of the beams, r_{inf} is the diagonal length of infill panel, E_{me} is the expected modulus of elasticity of infill wall material, t_{inf} is the thickness of infill panel and equivalent strut, θ is the angle whose tangent is the infill height-to-length aspect ratio which is calculated by Equation 3.4, E_{fe} is the expected modulus of elasticity of frame material, I_{col} is the moment of inertia of columns around the axis perpendicular to the loading direction and h_{inf} is the height of infill wall. As the modulus of elasticity of infill material was not measured, the proposed equation by UBC code (Section 2106.2.12.1 1997 UBC) is used:

$$E_m = 750 \cdot f'_m < 3000 \text{ksi} \quad (3.4)$$

Hence, the compression strength of the masonry prism is needed for calculating the modulus of the modulus of elasticity of masonry infill. f'_m is determined by the equation recommended by

Paulay and Priestly [1992] [84]:

$$f'_m = \frac{f'_{cb} (f'_{tb} + \alpha \cdot f'_j)}{U_u (f'_{tb} + \alpha \cdot f'_{cb})} \quad (3.5)$$

Where: $\alpha = \frac{j}{4.1 \times h_b}$ and U_u is stress non uniformity coefficient and is equal to 1.5. f'_{cb} is compression strength of brick and is equal to $9.3MPa$, f'_{tb} is tension strength of brick and may be determined for solid brick [84] as $0.1 f'_{cb} = 93MPa$, f'_j is mortar compression strength and is equal to $17.9MPa$, j is mortar joint thickness which is assumed $15mm$ and h_b is the height of masonry unit and is equal to $20cm$. Parameters are calculated as: $\alpha = 0.0183$, $f'_m = 7.09MPa$, $E_m = 5325MPa$, $\lambda = 2.881$ and $a = 0.344m$. The calculations are represented in detail in Appendix A. The expected in-plane shear strength of the unreinforced masonry infill wall is given by Equation A.6:

$$V_{ine} = A_n \cdot f_{vie} \quad (3.6)$$

$$A_n = t_{inf} \cdot l_{inf} \quad (3.7)$$

$$f_{vie} = \nu_{me} = 0.75 \left[\nu_{ts} + \frac{P_{CE}}{A_n} \right] \quad (3.8)$$

Where f_{vie} is expected shear strength of masonry infill, ν_{ts} is the average bed-joint shear strength, P_{CE} is the expected gravity compressive force applied on the URM infill wall and A_n is the area of net mortared section of the masonry infill wall and is equal to $A_n = 0.743m^2$. As there is no information about shear strength of the joints and applied normal stress on it, a value is supposed for shear strength of masonry infill. $\nu_{ts} + \frac{P_{CE}}{A_n}$ is assumed to be $620kPa$, $\nu_{me} = 496kPa$, $V_{ine} = 368.03kN$.

FEMA 356 provisions, provide a maximum nonlinear drift ratio d which is correspond to the sudden loss of the lateral strength of the unreinforced masonry walls in nonlinear analysis. The value of drift is is determined depending on the height of the infill, aspect ratio and frame to infill shear strength ratio. To define the value of ultimate strain for masonry material ϵ_{mu} shown in Figure 3.12, the value of maximum nonlinear drift ratio is used. Based on FEMA Table 7-9 for the wall aspect ratio equal to 1.43 and the frame to infill strength ratio less than 0.7, the maximum nonlinear drift ratio is obtained: $d = 0.35\%$

$$\beta < 0.7 \Rightarrow l_{inf}/h_{inf} = 3.71/2.6 = 1.43 \Rightarrow d = 0.35\%$$

Using above calculated parameters, the material and geometric properties of the proposed diagonal strut model, namely the area of the diagonal struts A_{strut} , yield strength of masonry f_{my} , its corresponding strain ϵ_{my} and ultimate strain of masonry can be calculated as:

$$A_{strut} = t_{inf} \cdot a \quad (3.9)$$

$$f_{my} = \frac{V_{ine}}{A_{strut}} \cdot \frac{r_{inf}}{l_{inf}} \quad (3.10)$$

$$\epsilon_{my} = \frac{f_{my}}{E_{me}} \quad (3.11)$$

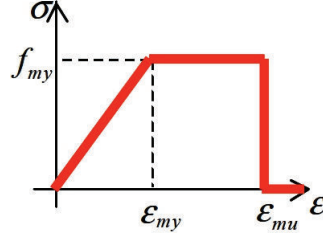


Figure 3.12: Masonry strut material model recommended by FEMA 356

$$\epsilon_{mu} = d \cdot \frac{h_{inf} \cdot l_{inf}}{r_{inf}^2} \quad (3.12)$$

By substituting the value of each parameter in above formulation, the proposed stress-strain curve for material and the strut's area are obtained as: $A_{strut} = 0.0688m^2$, $f_{my} = 6.51MPa$, $\epsilon_{my} = 0.0012$, $\epsilon_{mu} = 0.001645$.

Here, 2 diagonal struts are used for simulating masonry infill. The area proposed by FEMA, is divided by two and its value is allocated to each diagonal bar. Displacements are imposed to the top corners of the frame. The value of displacements increases monotonically from zero to $2cm$ in both two top nodes of frame and here the total displacement is $4cm$. Relation between top displacements versus base shear of diagonal struts is acquired. Figure 3.13(a) shows the strain-stress curve which is defined as material properties of struts.

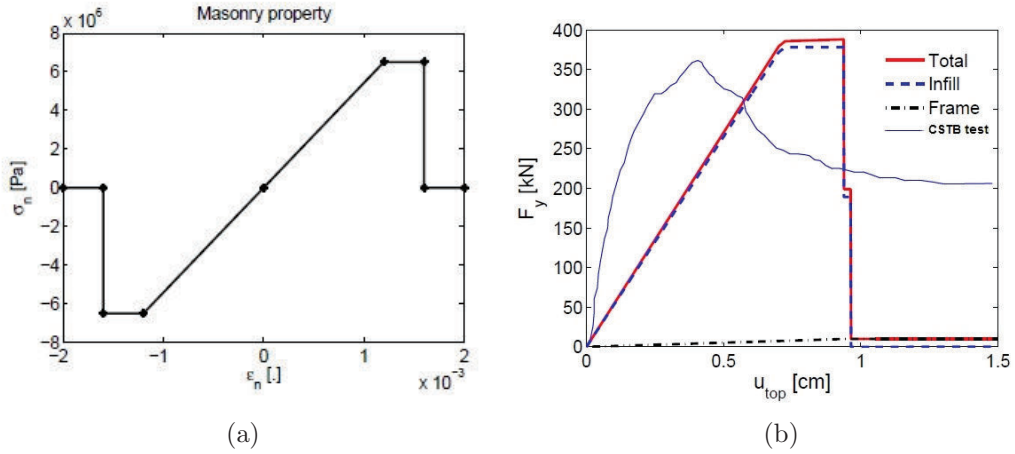


Figure 3.13: (a) Material stress-strain curve (b) force-displacement diagram using FEMA 356 strut model

The Figure 3.13(b) demonstrates pushover curve of the wall. As shown in this figure, black dashed line is the response of the frame, the blue dashed one is the response of the masonry

wall (diagonal struts) and the red one is the total response of the system which is obtained from summation of infill and frame responses. The solid blue line is the response of CSTB test number 3. As can be seen in Figure 3.13(b) the FEMA 356 model overestimates the shear strength of the system and could not be able to predict the residual strength of the system. It should be noted that the values of normal stress and bed joint shear strength were not available and the assumed values may have led to overestimating the ultimate strength. Initial stiffness of masonry infill which is calculated by FEMA formulations is very lower than that of the experiment. This is maybe due to underestimating some parameters like modulus of elasticity of masonry. This parameter was calculated based on UBC code. According to FEMA 356 formulations, nonlinear behavior of the wall is perfect plastic and after a certain displacement, the infill masonry panel exhibits no strength in shear and collapse. Figure 3.13(b) shows that this assumption is highly conservative and wall carries out considerable amount of shear stress in plastic region.

3.5.2 Calibrated model proposed by Hashemi [46]

As the results calibrated by FEMA 356 were not satisfactory, another methodology which proposed by Hashemi et al. [2007] [46] is used. The calibrated model is based on compression material properties namely maximum compressive strength of masonry f'_m which is obtained from uniaxial compression test on masonry wall and a parabolic stress-strain curve with linear softening. In this modeling, the parameters of strut model are calibrated to be in accordance with the observed load-displacement curve of experimental results. Masonry infill strength V_{ine} , its corresponding lateral drift Δ_y , the residual strength V_{res} and its corresponding lateral displacement Δ_{res} are obtained from the base shear-displacement curve of wall 3, see Figure 3.8. Material model for calibrated model is shown in Figure 3.14. As shown in this figure, the residual resistance of masonry is taken into account.

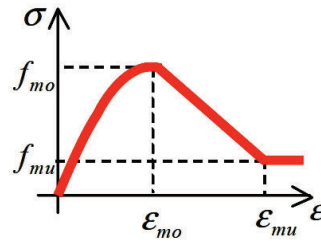


Figure 3.14: Masonry strut material model proposed by Hashemi et al. [2007] [46]

$$A_{strut} = \frac{V_{inf}}{f'_m} \quad (3.13)$$

$$\epsilon_{mo} = \frac{l_{inf}}{r_{inf}^2} \cdot \Delta_y \quad (3.14)$$

$$f_{mu} = \frac{V_{res}}{A_{strut}} \quad (3.15)$$

$$\epsilon_{mu} = \frac{l_{inf}}{r_{inf}^2} \cdot \Delta_{res} \quad (3.16)$$

By substituting the value of each parameters the area of strut model as well as material model are calculated: $A_{strut} = 0.0508m^2$, $\epsilon_{mo} = 6.25 \times 10^{-4}$, $f_{mu} = 2.87MPa$, $\epsilon_{mu} = 0.0014$ and $f'_m = f'_{mo} = 7.09MPa$. The material property and obtained pushover curve of structure are shown in Figure 3.15(a) and Figure 3.15(b). The detailed computations are represented in Appendix A.

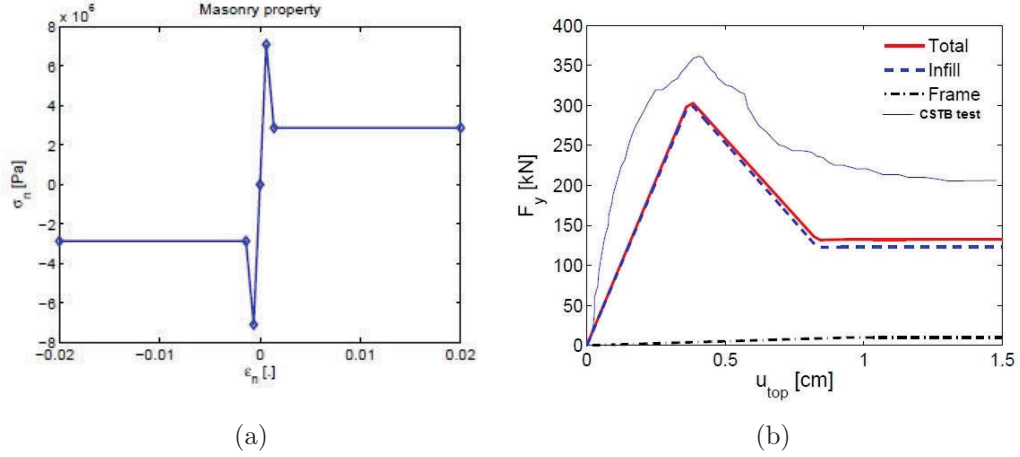


Figure 3.15: (a) Material stress-strain curve (b) force-displacement diagram using calibrated strut model

Push-over curve obtained from calibrated model formulation has a more realistic shape in plastic region respecting the FEMA 356 one. But difference between calculated maximum load and that obtained from the test is still high. The maximum normal stress in the strut assumed to be equal to the compressive strength of masonry. The area of struts is computed based on the ratio of shear strength of masonry infill in yield point and compressive strength of masonry and thus the modulus of elasticity of masonry in this case is approximately 2 times greater than those of FEMA 356. This method can predict the total schema of masonry behavior well, but underestimates the strength of the structure in both elastic and plastic regions. Hence, these equations underestimate the response of the masonry wall. By the way, the formulation is based on the pushover curve results which can be obtained from experiment data. Hence to calculate the model's parameters, we need to run the test but the aim of numerical modeling is to calculate the response of structure without performing the experiment.

3.5.3 Mostafaei and Kabeyasawa model [76]

In this section constitutive law for material is based on the formulation of Mostafaei et al. [2004]. Figure 3.16 shows the force-displacement curve which is applied to the masonry infill panel. In

this study like others masonry is replaced by two struts and their combination in two opposite directions produces the lateral stiffness of the wall. The section of bar elements is determined based on FEMA 356 formulations. Shear strength at assumed yielding point V_y , shear strength at maximum point V_m as well as post-peak residual shear strength V_p and their corresponding displacements, U_y , U_m and U_p are the main parameters of this trilinear envelope. α in the curve represents the ratio of stiffness after yielding to the initial stiffness. The difference of this method with those of FEMA 356 and calibrated is that in this case, maximum strength of masonry is determined based on the minimum of compression failure and sliding shear failure values of masonry wall. Then, yield strength of the wall and its corresponding displacement are determined based on the geometry of Figure 3.16. The plastic strength of the masonry wall and its corresponding displacement are calculated based on some assumptions. Finally, forces and displacements are converted to stress and strain and applied to the bar elements.

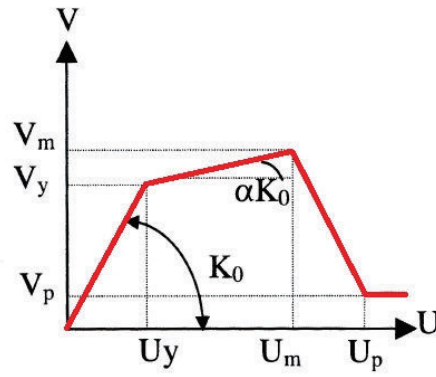


Figure 3.16: Force-displacement envelope for conventional masonry infill walls proposed by Mostafaei et al. [2004] [76]

Maximum lateral strength V_m is estimated based on sliding shear and compression failures. The other parameters are calculated based on following equations. According to ACI 530-88 recommendations, maximum shear strength obtained from sliding shear and compression failure is limited to $0.814MPa$ [2]. The corresponding shear strength should not exceed this value. Shear failure strength of diagonal strut in compression failure can be calculated from the following equation based on Stafford-Smith et al. [1969] [98] study:

$$\frac{V_c}{t.l_m} = a.t.f'_m \cdot \frac{\cos\theta}{t.l_m} \quad (3.17)$$

Thus: $\frac{V_c}{t.l_m} = 0.44MPa$. Maximum shear strength of infill in shear sliding failure mechanism is calculated as:

$$\frac{V_f}{t.l_m} = \frac{\tau_0}{(1 - \mu \cdot \tan\theta)} \quad (3.18)$$

Where τ_0 is cohesive capacity of the mortar beds and it ranges typically between 0.098 and 1.4MPa and may be assumed typically as $\tau_0 = 0.04.f'_m$ [84] and μ is sliding friction coefficient along the bed joints and is determined based on Chen et al. [2003] [18] results as:

$$\mu = 0.654 + 0.000515f'_j \quad (3.19)$$

Where f'_j is the mortar block compression strength. Based on these formulations, the sliding shear failure mechanism can be obtained as: $\frac{V_f}{t.l_m} = 0.5306MPa$. Therefore, the corresponding shear strength is calculated as the minimum of sliding and compression diagonal strength: $V_m = 0.44 \times 0.2 \times 3.71 = 0.326MN$. The maximum displacement corresponding to the maximum lateral force is estimated by Equation 3.20, Mandan et al. [1992] [65]:

$$U_m = \frac{\epsilon'_m \cdot d_m}{\cos\theta} \quad (3.20)$$

In this equation ϵ'_m is the masonry compression strain corresponding the maximum compression stress: $\epsilon'_m = 1.33 \times 10^{-3}$ and d_m is the diagonal strut length. So the value of maximum lateral displacement is calculated as: $U_m = 0.0074m$. The initial stiffness K_0 can be obtained by Madan et al. [1992] [65] formulation:

$$K_0 = 2 \cdot \left(\frac{V_m}{U_m} \right) \quad (3.21)$$

The lateral yielding force V_y and its correspond displacement U_y may be calculated from the geometry as shown in Figure 3.16, α supposed to be 0.2.

$$V_y = \frac{V_m - \alpha \cdot K_0 \cdot U_m}{1 - \alpha} \quad (3.22)$$

$$U_y = \frac{V_y}{K_0} \quad (3.23)$$

The parameters are calculated as: $K_0 = 89.19MN/m$, $V_y = 0.2475MN$, $U_y = \frac{0.2475}{89.19} = 0.0028m$. The U_p and V_p are calculated so that the line connecting the peak of the envelope and the point (U_p, V_p) passes through the 80% post-peak point [76]. Therefore:

$$V_p = 0.3V_m \quad (3.24)$$

$$U_p = 3.5(0.015h_m - U_m) + U_m \quad (3.25)$$

$V_p = 0.099MN$, $U_p = 0.118m$. In this method the area of the strut is determined according to FEMA 356 formulation so: $A_{strut} = 0.069m^2$. The proposed stress-strain envelope is obtained by:

$$\sigma_m = \frac{V_m}{A_{strut} \cdot \cos(\alpha)} \quad (3.26)$$

$$\sigma_y = \frac{V_y}{A_{strut} \cdot \cos(\alpha)} \quad (3.27)$$

$$\sigma_p = \frac{V_p}{A_{strut} \cdot \cos(\alpha)} \quad (3.28)$$

$$\alpha = \tan^{-1}(2.7/4.21) = 0.5703 \text{ rad}, l_d = \sqrt{2.7^2 + 4.21^2} = 5.256m.$$

$$\epsilon_m = \frac{U_m \cdot \cos(\alpha)}{l_d} \quad (3.29)$$

$$\epsilon_y = \frac{U_y \cdot \cos(\alpha)}{l_d} \quad (3.30)$$

$$\epsilon_p = \frac{U_p \cdot \cos(\alpha)}{l_d} \quad (3.31)$$

So, $\sigma_m = 5.68MPa$, $\sigma_y = 4.26MPa$, $\sigma_p = 1.7MPa$, $\epsilon_m = 0.0012$, $\epsilon_y = 0.000484$, $\epsilon_p = 0.0018$. Material model is shown in Figure 3.17(a). Pushover curved obtained by this method is also shown in Figure 3.17(a).

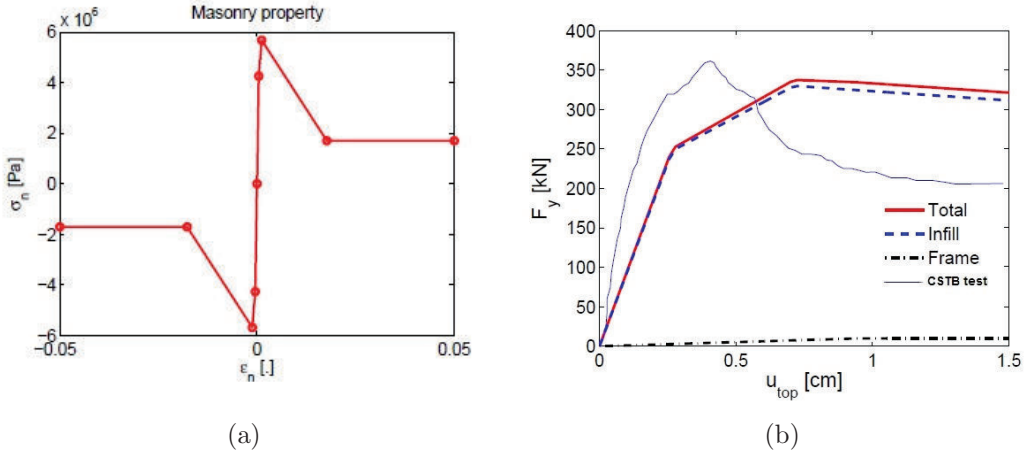


Figure 3.17: (a) Material stress-strain curve (b) force-displacement diagram using Mostafaei and Kabasaki [76] strut model

The performance curve shows that this model is able to predict the value of maximum shear resistance of system better than previous methods but it overestimates the correspond displacement of this point. The accuracy of this model is more than the two described before. The stiffness of this model like that of FEMA 356 and calibrated model is underestimated. In this method, the stiffness of the wall is calculated based on shear strength of the masonry and its corresponding displacement which is determined from its compressive strength. Since the value of compressive strength was not available and obtained through Equation A.5, the stiffness of wall may have been underestimated. The plastic response of the wall is overestimated using this method. That's because of the plastic region formulations.

3.6 Tri-linear proposed model

In this section, a tri-linear model for describing the material properties of replaced struts is proposed. The model is validated by simulating two experimental tests on masonry walls which have been done by CSTB [31] and Vermeltfoort [1992] [85]. In first part, the formulation is implemented to model CSTB test and the results of four cases are compared. Then, the proposed force-displacement curve is applied to model another experiment which has been done by Vermeltfoort [1992] [85].

In this method, the area of strut element is determined by FEMA 356 formulations. The maximum shear strength of masonry is distinguished as the shear sliding strength of the masonry wall. V_y and its corresponding displacement are determined based on proposed material envelope as shown in Figure 3.18. In this method, V_p is assumed to be 50% of maximum shear strength and U_p is determined to be in accordance with the slope of the third line of proposed curve as shown in Figure 3.18. The same slope in second and third line of shear force-displacement curve is assumed.

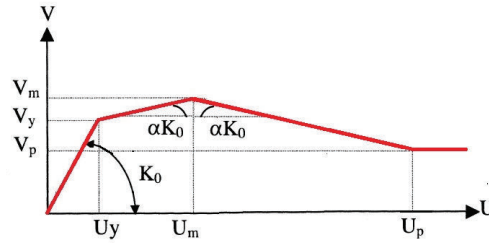


Figure 3.18: Shear force-displacement curve proposed for diagonal struts

Since in numerical modeling the stiffness of the wall was underestimated, a new formulation is used for calculation of this parameter. Masonry modulus of elasticity in this section is calculated by MSJC [2008] [78] (MSJC Sec. 1.8.2.1.1 for concrete-unit masonry) formulations for concrete-units masonry, Equation 3.32. Thus in this case the value of modulus of elasticity is greater than previous models.

$$E_m = 900.f'_m \quad (3.32)$$

3.6.1 Validation of proposed model, CSTB test

In this section, the proposed model is used to simulate the experimental test of CSTB. The proposed stress-strain curve and the numerical results are described in Figure 3.19(a) and Figure 3.19(b) respectively. The compression strength of masonry is calculated using Equa-

tion A.5 like previous cases. The calculations are described in detail in Appendix A. The parameters are computed: $E_m = 6.36 \times 10^9 Pa$, $\lambda = 3.226$, $a = 0.3287m$, $A_{strut} = 0.0657m^2$, $V_m = V_{ini} = 0.33MN$, $U_m = 0.0047m$, $K_0 = 143.6MN/m$, $V_y = 0.244MN$, $U_y = 0.0018m$, $V_p = 0.165MN$, $U_p = 0.0106m$, $\sigma_m = 6.65MPa$, $\sigma_y = 4.99MPa$, $\sigma_p = 3.33MPa$, $\epsilon_m = 0.00075$, $\epsilon_y = 0.000288$ and $\epsilon_p = 0.0017$. Figure 3.19(a) shows the material stress-strain curve for proposed model.

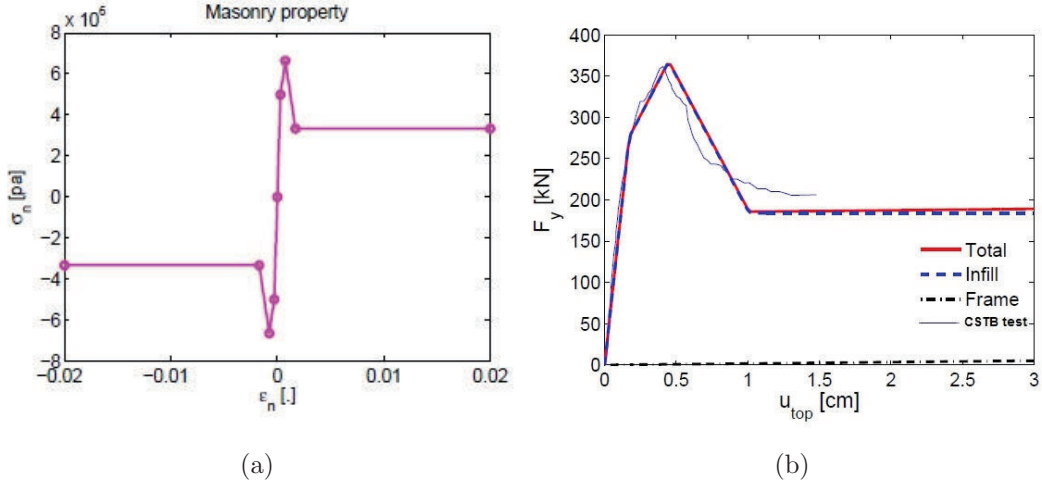


Figure 3.19: (a) Material stress-strain curve used in model (b) load-displacement curve of CSTB test using trilinear proposed model

Total base shear-displacement response of structure for frame, infill wall and summation of them is shown in Figure 3.19(b). As shown in this figure, this method estimates the behavior of the structure very well in terms of nonlinear post-peak behavior and assessing the ultimate shear strength of the wall. The compression strength is considered the same as FEMA 356 model and modulus of elasticity is changed here. Comparison of this model with the other methods shows the important role of modulus of elasticity of masonry E_m , the area of struts and shear strength of masonry in determining the response of structure. The differences of this model and those of Mostafaei [76] are modulus of elasticity of masonry, the slope of the third line of curve and plastic stress of masonry. In elastic region the elastic modulus of masonry is different for the last two cases and the proposed model assessed the stiffness of the wall very well. Thus, for the concrete blocks, the formulation which proposed by MSJC [2008] [78] is more reliable.

3.6.2 Comparing the obtained results using different models

In this section, the properties of each model are summarized in Table 3.1 to compare better the results. The computed load-displacement curves in addition to tested one are drawn in Figure 3.20.

Table 3.1: Properties of equivalent struts models tested

	FEMA 356 model	Calibrated model	Mostafaei model	Proposed model
$A_{strut}[m^2]$	0.0345	0.0254	0.0345	0.0323
$E_m[MPa]$	5.3×10^3	11.3×10^3	5.3×10^3	6.36×10^3
$f'_m[MPa]$	7.09	7.09	7.09	7.09
$\sigma_y[MPa]$	6.51	-	4.26	4.99
$\epsilon_y[MPa]$	0.0012	-	0.00048	0.00029
$\sigma_m[MPa]$	6.51	7.09	5.68	6.65
$\epsilon_m[MPa]$	0.00165	0.000625	0.0012	0.00075
$\sigma_p[MPa]$	0	2.87	1.7	3.33
$\epsilon_p[MPa]$	0.00165	0.0014	0.0018	0.0017

Comparing the properties of different models shows that both area of strut and modulus of elasticity are important. For example the modulus of elasticity in calibrated model is two times greater than those of Mostafaei but since the section of bars is different for these two models, the same initial stiffness was obtained for both models. Determining post-peak region and plastic strength of the wall helps to have more reliable information about the performance of the wall under loads. In this study, the $V_p = 0.5V_m$ was proposed and a good agreement between computational model and experimental data was found.

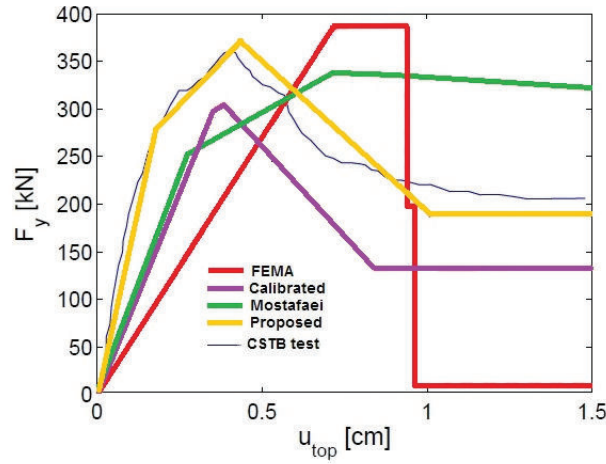


Figure 3.20: Numerical simulation of shear base force and top displacement curve in an infilled frame under monotonic loading using different methods

3.6.3 Validation of proposed model, Vermeltfoort test

In this section, the wall which was experimented by Vermeltfoort [1992] [85] Vermeltfoort and Raijmakers [1993] [86] and CUR [1994] [25] is modeled using bar elements. The tri-linear proposed model is used to simulate the behavior of this masonry shear wall. The shear wall has a width of 990[mm] and height of 1000[mm] and thickness of 10[mm]. The wall shape as well as force-displacement curve are shown in Figure 3.21.

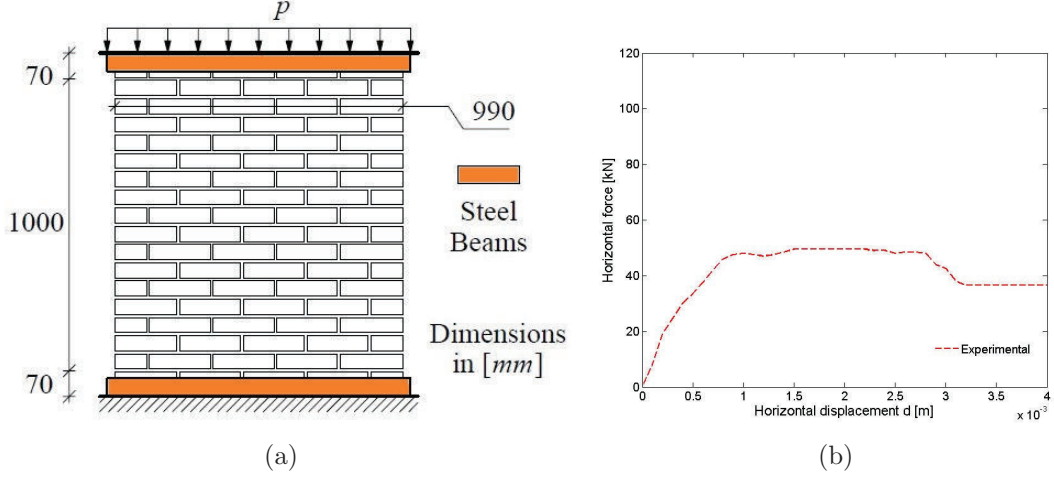


Figure 3.21: (a) Tested wall by Vermeltfoort et al. [85] (b) load-displacement diagram

In the macro-modeling strategy, the wall is replaced by two diagonal struts. The section of struts is calculated based on FEMA formulations. A steel frame with rectangular section equal to $5 \times 10 \text{ cm}^2$, is supposed to surround the infill masonry. The modulus of elasticity of beams and columns are supposed to be the same as that of CSTB. Hence, the area of struts is calculated as: $\lambda = 9.5 \Rightarrow a = 0.097 \text{ m} \Rightarrow A_{strut} = a.t = 0.1 \times 0.097 \cong 0.01 \text{ m}^2$. The cohesion of mortars, initial normal stress on the wall, compression failure of masonry together by friction angel are known and are equal to $C = 3.5e5 \text{ Pa}$, $\sigma_{n0} = 3e5 \text{ Pa}$, $f'_m = 10.5e6 \text{ Pa}$ and $\phi = 36.9^\circ$. The maximum shear sliding force of the wall can be computed by Equation 3.33:

$$V_m = V_{ini} = C + \sigma_{n0} \cdot \tan(\phi) \cdot t_{inf} \cdot l_{inf} \quad (3.33)$$

So the parameters are calculated as: $V_m = 5.4e4 \text{ Pa}$, $E_m = 900 \cdot f'_m = 9.45 \text{ GPa}$, $\epsilon'_m = \frac{f'_m}{E_m} = 0.001$, $\theta = \text{atan}(1/0.99) = 45.3^\circ$, $U_m = \frac{\epsilon'_m \cdot d_m}{\cos(\theta)} = 0.002 \text{ m}$, $K_0 = 2 \times (\frac{5.4e4}{0.002} = 54 \text{ MPa}$, $V_y = \frac{5.4e4 - 0.2 \times 54 \times 10^6 \times 0.002}{1 - 0.2} = 40500 \text{ Pa}$, $U_y = \frac{40500}{54 \times 10^6} = 0.0007 \text{ m}$, $V_p = 0.5 \times 5.4 \times 10^4 = 27000 \text{ Pa}$, $U_p = \frac{27000}{0.2 \times 54 \times 10^6} + 0.002 = 0.0045 \text{ m}$. The yield, maximum and plastic stresses in addition to their corresponding displacements are:

$$\sigma_y = 5.7MPa, \sigma_m = 7.6MPa, \sigma_p = 3.9MPa, \epsilon_y = 0.00034, \epsilon_m = 0.001, \epsilon_p = 0.0023.$$

The stress-strain curve of struts is shown in Figure 3.22(a) whereas Figure 3.22(b) represents the comparison between experimental data and computational results. Figure 3.22(b) shows the proposed macro model can reproduce the load-displacement curve of tested wall very well. There is a very good agreement between initial stiffness, ultimate shear strength and post-peak response of the wall obtained from computational model and experimental evidence.

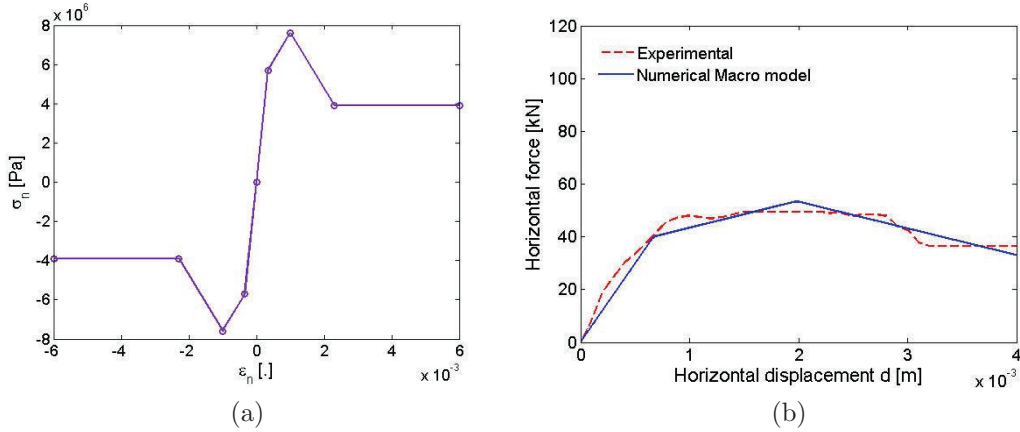


Figure 3.22: (a) Stress-strain curve of material (b) load-displacement curve obtained for trilinear proposed model used for Vermeltfoort test [85]

Using macro-model strategy, the masonry wall is replaced by two strut elements. The struts have the same properties in compression and tension. The properties of proposed model are calculated based on Figure 3.18 and corresponding equations. The ultimate shear strength of the wall is determined by this method but there is no other information about the formed cracks in the wall and the failure mechanism of the wall which are very important to know.

3.7 Conclusion

In this section, the masonry wall was modeled using macro-modeling strategy. In this method, the infill masonry is replaced with two diagonal struts. First, the masonry wall which was tested by CSTB [31] was modeled using two bar elements. The material and geometrical properties of the bar elements were calculated using three different methods from the literature: FEMA356 [34], calibrated model proposed by Hashemi et al. [2007] [46] and Mostafaei et al. [2007] [76]). Then a tri-linear model was suggested and successfully reproduced the experimental results. Then the proposed model was used to simulate the response of a shear wall which was subjected to monotonic loading by Vermeltfoort [1992] [85] Vermeltfoort and Raijmakers [1993] [86] and

CUR [1994] [25]). The computational results show that the trilinear model is able to properly assess the response of the masonry walls. However, data relating to the compressive strength of the masonry, the shear strength of the bed joints, the vertical load acting on the wall are necessary.

The trilinear proposed model, with its basic assumptions, is more suitable to simulate the behavior of infill panels. Rotation is not considered in this macro model so the flexural behavior of masonry panel cannot be simulated by this model. On the other hand, knowing the mechanism of failure is the main issue of researches on masonry structures and macro-modeling strategy as presented here is not capable to give any information about that. Therefore, in next sections, the behavior of masonry wall in detail using micro-models will be studied. Failure mechanism of the masonry wall will be assessed using different models considering different geometry and material characteristics.

Chapter 4

Micro modeling : in plane loading

4.1 Introduction

Unreinforced masonry wall (URM) term is devoted to masonry wall which contains no reinforcement. These types of walls are used in exterior walls to bear the loads or in interior wall to separate the volumes. Traditionally, URM using clay brick has been implemented to resist against different loads in low rise construction almost all over the world. Even today, buildings using unreinforced masonry wall are constructed in many areas because of its durability, resistance against fire, simplicity to construct and low construction cost but they have poor performance under seismic loads. Therefore, special attention has been given to evaluate their performance under different conditions by many researchers either by experimental tests or numerical models to allow more reliable use of masonry.

As masonry walls are composed of two different materials with their own special characteristics, the prediction of their performance under different load conditions, different geometries and different material characteristics are very difficult. To get a comprehensive insight into the behavior of these walls, a large number of laboratory tests involving various conditions are required. As, obtaining accurate responses from laboratory tests is costly and time consuming and needs precise testing instruments, sophisticated numerical tools have been developed to investigate the behavior of these complex constructions. As described before, one of the main approaches used to simulate the behavior of masonry walls is micro modeling strategy. Micro models try to describe the behavior of masonry in detail and capture local failure of each component and catch final failure mechanism of the wall. Thus, mortars and bricks and their interfaces are modeled separately using appropriate constitutive laws.

In this section attention will be given to micro modeling of the unreinforced masonry wall in 3D configuration. The model is composed of unit elements (bricks), which are considered as solid and rigid elements, and interface elements (mortars) as potential crack planes. Mortars are considered as weakness planes of wall so that interface elements control nonlinear behavior of masonry wall whereas bricks remain elastic. First, possible failure modes of masonry are studied. Then, a simple constitutive law is implemented for the interface to simulate reaction of wall under monotonic loading. Afterward, the computational model is improved to take into account all failure mechanisms of the wall. The effect of opening, aspect ratio and properties of mortars on behavior of masonry walls are also investigated in this chapter.

4.2 Masonry failure mechanisms

The basic types of failure mechanisms in masonry wall are characterized as unit failure mechanism, joint failure mechanism and combined mechanisms involving joints and units. Five different failure mechanisms are allocated to masonry as: tension failure of bricks, tension failure of joints,

shear failure of joints diagonal tensile failure of unit and crushing failure of masonry. Figure 4.1 shows these phenomena: cracking of the units in direct tension is dealt with unit's failure, cracking of the joints and sliding of the bed or head joints (at low value of normal stress) are considered as joint's failure and diagonal tensile cracking which is happened under sufficient normal stress and masonry crushing are identified as combined failure mechanisms [60].

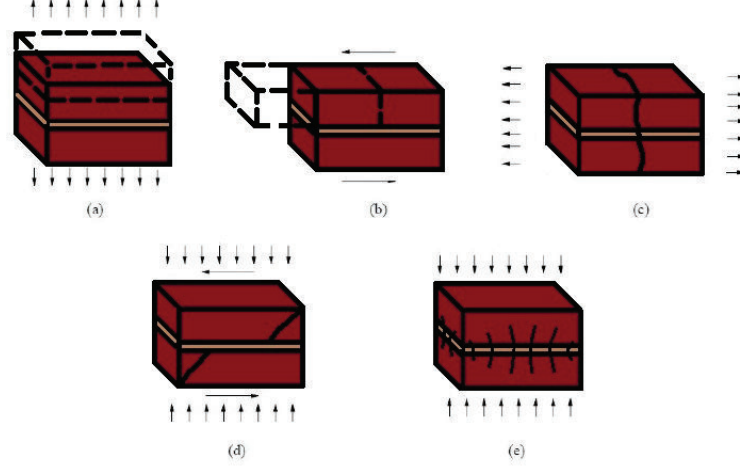


Figure 4.1: Masonry failure mechanisms: (a) joint tensile cracking (b) joint slipping (c) unit direct tensile cracking (d) unit diagonal tensile cracking (e) masonry crushing

It is worthy to note that geometry of the wall has a very important role in causing different failure mechanisms. Depending on the geometry, three different mechanisms are distinguished as failure of unreinforced masonry walls:

- Diagonal tensile failure: When the wall is subjected to high normal compressive loads and significant horizontal force is applied to the wall. This type of failure is the most common mode of failure in shear masonry walls. It usually happens for the wall with aspect ratio of 1, but it can also occur in a panel with higher aspect ratio (which is defined as the ratio of height and length of the wall, H/L) when high vertical loads also are applied to the wall. Diagonal crack pattern happens when the principal tensile stress in the mortar exceeds the tensile strength of joints.
- Sliding shear failure: This type of failure is predominant for the wall with high lateral loads and low normal stresses. When there is no sufficient compression to produce higher shear strength and the cohesion of mortar is not enough to resist lateral loads, bed joints slide and failure of wall happens. This type of failure generally happens in walls with low aspect ratio, for example $H/L = 1/1.5$ and often in walls with $H/L = 1/1$ depending on the characteristics of their components.

- **Crushing failure:** Crushing of masonry at the toes of wall occurs usually due to rocking deformation whenever masonry has high shear strength and is subjected to low lateral displacement. This mode of failure is most common for the walls with aspect ratio higher than one, for example $H/L = 1.5/1$. In the cases with low vertical loads, the wall can rock like a rigid body and finally experience crushing failure.

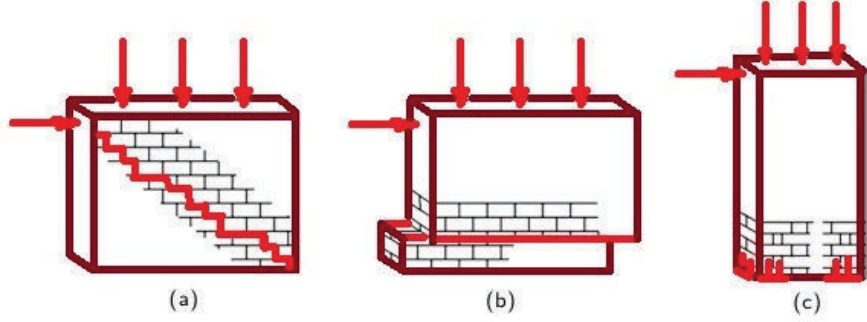


Figure 4.2: Failure modes for masonry walls subjected to in-plane loads (a) diagonal tensile failure (b) sliding shear failure (c) bending failure (crushing of masonry) [96]

As aspect ratio of the wall can cause a specific mode of failure, its influence on the behavior of masonry wall is discussed in this chapter using micro model of masonry.

The aim of this study is to capture all failure mechanisms of masonry walls with different geometrical and material properties under in-plane loading and to find the most important parameters which influence the behavior of masonry wall. Pushover curve and crack's profile of each analysis are drawn to compare results better.

4.3 Numerical modeling of masonry wall

GEFDyn Software [7], is used for modeling masonry walls and for pre and post processing of results, SDTools (Structural dynamic toolbox) software is implemented [94]. GEFDyn can be used for 3D or 2D analysis of structures and geo-structures under static or dynamic loading in linear and non-linear domain taking into account coupling of mechanical, hydraulic and thermal phenomena. It is developed for geotechnical problems with numerous non-linear rheological constitutive laws dedicated to geo-materials and specially the soil and its interaction with structures [7]. SDTools specializes in providing open and extensible MATLAB based solutions in experimental modal analysis and finite element modeling for vibration problems [94]. In this study, the masonry wall is simulated using micro-model strategy which considers bricks and interface between mortars and bricks separately. The results of numerical modeling are validated comparing

the obtained results with available experimental data.

For modeling of masonry wall, two types of elements are used. 3D solid elements for bricks and interface elements for mortars which are shown in Figure 4.3 and Figure 4.4, respectively. Interface elements also are implemented in the middle of brick to capture tensile failure of bricks. Isotropic Hexagonal iso-parametric continuum element (3D Solid volume) with Mohr-coulomb failure criterion is used to represent bricks. The material characteristics of solid elements are chosen somehow to restrict brick's behavior in elastic domain. Each brick is modeled using two solid elements and an interface element between the solids, see Figure 4.5. So, the tension failure of the brick is reproduces by an interface element.

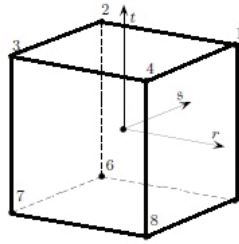


Figure 4.3: GEFdyn 3D solid element with eight integration points

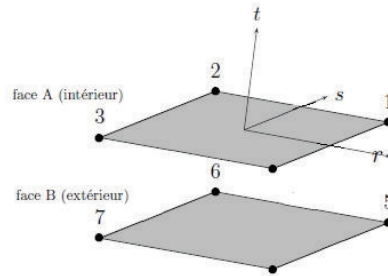


Figure 4.4: GEFdyn zero thickness interface element [79]

The behavior of mortars and tension failure of bricks are represented by interface elements. This type of element permits discontinuity in displacement field. The behavior of this element is written in terms of stress and relative displacement across interface element. 2D eight nodes interface element used in this modeling is shown in Figure 4.4. Interface element formulations are described in the following section.

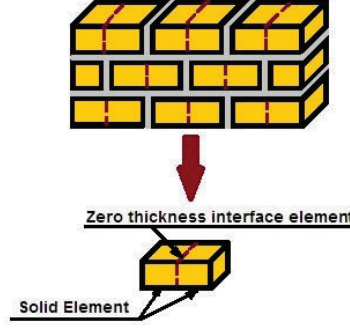


Figure 4.5: Potential crack planes in the middle of units are modeled by zero-thickness interface element

4.3.1 Interface element formulations

In finite element modeling, the interaction between two bodies can be described by [40]:

- Link element: connects two opposite nodes of element in contact [47]
- Thin element: continuum finite element with very fine thickness [43]
- Zero thickness interface element: allows displacement discontinuity between contacted nodes [60]

Interface element was first used by Goodman et al. [1968] [41] to describe discontinuity in rock masses and Page [1978] [82] was the first one who implemented interface element in modeling masonry walls. In this study, properties of mortar and interaction between units and mortars are lumped into interface element so they are source of nonlinearity in the model. An artificial thickness is considered for interface in this study to define stress state of element. The behavior of interface element is described by a relation between stresses and relative displacements between two opposite points of an element.

Interface field:

In interface element, \vec{n} is normal vector from surface 1 to surface 2.

Displacement jump:

Displacement which is read in interface element is the difference between displacements of surface 2 and surface 1.

$$[u] = [u_2] - [u_1] \quad (4.1)$$

Normal and tangential components of displacement are defined as:

$$[u_n] = [\underline{u}] \cdot \underline{n} \quad (4.2)$$

$$[\underline{u}_T] = [\underline{u}] - [u_n] \cdot \underline{n} \quad (4.3)$$

$$|u_T| = \sqrt{[u_s]^2 + [u_t]^2} \quad (4.4)$$

Where u_s and u_t are the sliding components in the plane of interface.

Stress components:

Normal and tangential components of stress vector read as below:

$$\sigma_n = \underline{n} \cdot \underline{\underline{\sigma}} \cdot \underline{n} \quad (4.5)$$

$$\underline{\underline{\sigma}}_T = \underline{\underline{\sigma}} \cdot \underline{n} - \sigma_n \cdot \underline{n} \quad (4.6)$$

$$\sigma_T = (\sigma_t^2 + \sigma_s^2)^{1/2} \quad (4.7)$$

Stress vector always remains continue between interface element and the two solids even when there is opening under principle of action and reaction. Therefore, there are only discontinuities in displacement field.

4.4 Simple yield surface for interface elements (Model I)

In this section the constitutive law which is implemented for the interface elements is described. In Model I, all tension and shear failures has been assumed to take place in interface elements. Hence, the yield function is composed of a opening criterion and the plasticity criterion for describing the tension and shear behavior of masonry joints. Figure 4.6 represents the composite yield surface which is used in model I. As shown in this figure, the yield function is given for a 3D configuration. This yield function consists of two parts: A straight tension cut-off condition for simulating opening of cracks as well as tension failure of the mortars and the Mohr-Coulomb failure criterion for capturing the sliding of the joints and shear failure of mortars under compressive normal stresses.

The behavior of interface element under normal stress and shear stress is shown in this Figure 4.7. As shown in figure, no softening behavior is considered for masonry in this model in tension and shear. No degradation is allowed in cohesion and friction angel of interface material. Whenever shear stress reaches yield value, it behaves nonlinear and shear-displacement relation obeys perfect plastic theory.

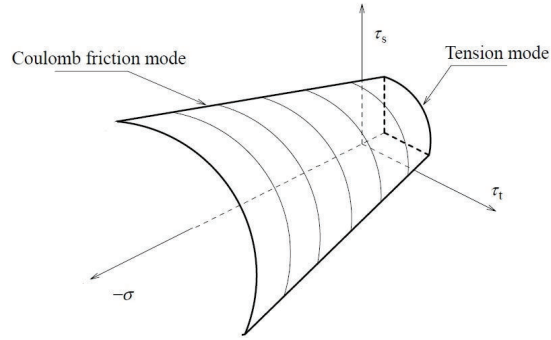


Figure 4.6: Simple yield surface for interface elements

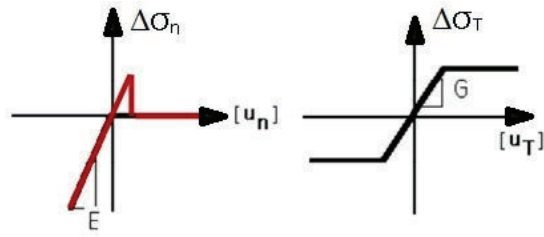


Figure 4.7: Relation between normal and shear stresses and displacements in interface element, left and right figures respectively

The Mohr-Coulomb failure criterion is written in the context of non-associated plasticity. The yield function read:

$$f_1 = \sqrt{\sigma_t^2 + \sigma_s^2} + \sigma_n \cdot \tan \phi - C \quad (4.8)$$

Where C and ϕ are cohesion and friction angel of joint respectively. The dilatancy angle defines as the ratio of plastic opening of interface over sliding of interface. The dilatancy angle is a function of relative plastic shear displacement and normal confining stress. By increasing the values of these two quantities, the dilatancy angle tends to be zero. This phenomenon is confirmed by experiments.

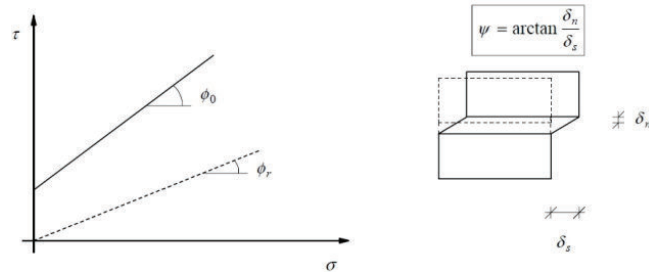


Figure 4.8: Coulomb friction law, definition of dilatancy angle [60]

The potential function which specifies the direction of plastic flow g_1 is represented in Equation 4.9:

$$g_1 = \sqrt{\sigma_t^2 + \sigma_s^2} + \sigma_n \cdot \tan \psi \quad (4.9)$$

In tension region, whenever displacement in the element overpasses a certain value, the interface element opens and tension, shear and compression stresses in element become zero. This certain value called artificial interface thickness, e which actually is yield displacement. There is no limitation for compression stress in the interface element and it is calculated by multiplying relative displacement times the modulus of elasticity of interface element. The formulations related to the behavior of interface element in tension are represented below:

- No interpenetration between two solids:
 $[u_n] \geq -e \Rightarrow \sigma \cdot n = E \cdot \Delta u_n$
- Detachment and free surface:
 $[u_n] > e \Rightarrow \sigma \cdot n = 0$
- Contact and compression:
 $[u_n] < e \Rightarrow \sigma \cdot n = E \cdot \Delta u_n$

Where e is thickness of interface element and F_t is tensile strength of mortars:

$$e = \frac{F_t}{E} \quad (4.10)$$

Hence:

$$f_2 = 0 \text{ if } \sigma_n > 0 \& [u_n] > e \quad (4.11)$$

In elasto-plastic approach total displacement's increment in interface element can be decomposed into an elastic part and a plastic part:

$$[\partial_t u_t] = [\partial_t u_t^e] + [\partial_t u_t^p] \quad (4.12)$$

$$[\partial_t u_s] = [\partial_t u_s^e] + [\partial_t u_s^p] \quad (4.13)$$

$$[\partial_t u_n] = [\partial_t u_n^e] + [\partial_t u_n^p] \quad (4.14)$$

Increment of stress vector depends on relative elastic displacement as shown in Equation 4.15, Equation 4.16 and Equation 4.17 where G and E are shear and normal elastic rigidities of the interface.

$$[\partial_t \sigma_t] = G_t [\partial_t u_t^e] = G_t ([\partial_t u_t] - [\partial_t u_t^p]) \quad (4.15)$$

$$[\partial_t \sigma_s] = G_s [\partial_t u_s^e] = G_s ([\partial_t u_s] - [\partial_t u_s^p]) \quad (4.16)$$

$$[\partial_t \sigma_n] = E [\partial_t u_n^e] = E ([\partial_t u_n] - [\partial_t u_n^p]) \quad (4.17)$$

We have associated flow rules, therefore for each failure mechanism, the plastic displacement in the element obtained as:

Mechanism 1 : shear

$$[\partial_t u_t^p] = \lambda_1 \cdot \frac{\partial g_1}{\partial \sigma_t} = \lambda_1 \cdot \frac{\sigma_t}{|\sigma_T|} \quad (4.18)$$

$$[\partial_t u_s^p] = \lambda_1 \cdot \frac{\partial g_1}{\partial \sigma_s} = \lambda_1 \cdot \frac{\sigma_s}{|\sigma_T|} \quad (4.19)$$

$$[\partial_t u_n^p] = \lambda_1 \cdot \frac{\partial f_1}{\partial \sigma_n} = \lambda_1 \cdot \tan \psi \quad (4.20)$$

In above formulation, ψ is supposed to be zero in interface elements in this study. λ is plastic multiplier and calculated by Equation 4.21.

Mechanism 2 : tension or compression

$f_2 = 0$ if $\sigma_n > 0$

No limitation and yield function is considered for compression $\sigma_n < 0$

Shear mechanism is active when: $f_1 = 0$, $\dot{f}_1 = 0$:

$$\dot{f}_1 = 0 \Rightarrow G \cdot \frac{\sigma_s}{\sigma_T} [\partial_t u_s - \lambda_1 \frac{\sigma_s}{\sigma_T}] + \frac{\sigma_t}{\sigma_T} [\partial_t u_t - \lambda_1 \frac{\sigma_t}{\sigma_T}] + E \cdot \tan\phi [\partial_t u_n - \lambda_1 \tan\psi] = 0$$

$$\lambda_1 = G (\sigma_T \cdot [\partial_t u_T] / |\sigma_T| + E [\partial_t u_n] \tan\phi / (G + E \tan\phi \tan\psi) = 0 \quad (4.21)$$

Given λ_1 , increment of stresses can be calculated in interface elements from the following equations.

$$\partial_t \sigma_t = G_t [\partial_t u_t - \lambda_1 \sigma_t / |\sigma_T|] \quad (4.22)$$

$$\partial_t \sigma_s = G_s [\partial_t u_s - \lambda_1 \sigma_s / |\sigma_T|] \quad (4.23)$$

$$\partial_t \sigma_n = E [\partial_t u_n - \lambda_1 \tan\psi] \quad (4.24)$$

4.4.1 Numerical Validation

In micro modeling strategy mechanical properties of different constituents involved and the behavior, geometry and material property of each component define the global behavior of structure while in the other models such as continuous approach or macro-element strategy the identification of parameters needs a good understanding of the overall behavior of infill or wall that is very difficult to achieve. Therefore, the approach of using numerical simulations instead of laboratory tests can be interesting.

The micro-modeling strategy for masonry wall is validated by a comparison between GEFDyn results and experimental results available in the literature. The results are compared to shear wall tests carried out in the Netherlands at 1992 [85], [86] and [25]. This experimental data is used because of the availability of most of the parameters, which are necessary to characterize in micro model.

It should be noted that multiple experiments for masonry walls with the same settings may lead to different results [60]. This is due to variabilities and uncertainties which may occur both in the material properties or test condition. The main objective of this study is to demonstrate the ability of the numerical model to reproduce the main features of the wall behavior that were observed in the tests and not just an exact simulation of experimental results. A large number of

parameters for material properties, boundary conditions and geometrical properties are necessary to develop an accurate model that fits the experimental results.

Model geometry and loading

Two types of walls were considered in the masonry shear wall tests that were carried out by CUR [1994][25], Raijmakers and Vermeltfoort [1992][85] and Vermeltfoort and Raijmakers[1993][86]. One type is a continuous masonry wall and the other one is the wall with central opening. As described in Figure 4.9, first, the vertical precompression was applied to the wall. Then, a horizontal monotonically increased displacement was imposed at the top of the wall whereas the top and bottom boundaries were kept horizontal and vertical movement at the top of the wall was precluded. The shear walls have a width of 990[mm] and height of 1000 [mm] built up with 18 horizontal rows and 16 horizontal active courses and 2 courses that are clamped in steel beams.

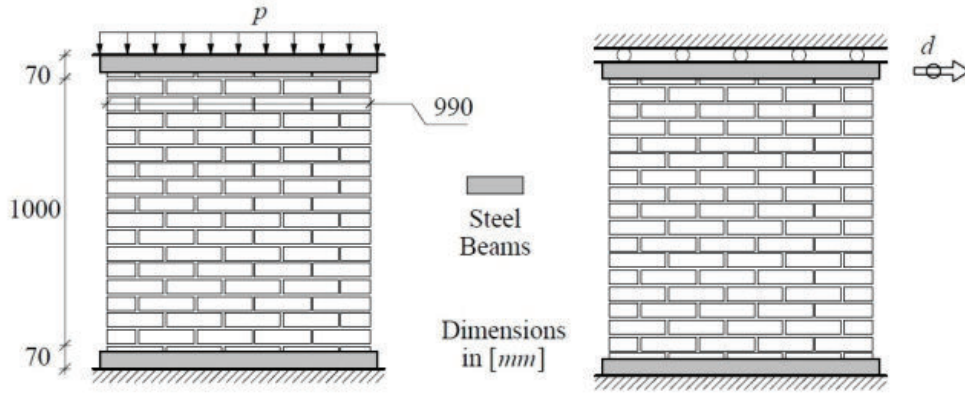


Figure 4.9: Experimental test (a) first: Vertical loading (b) second: Horizontal loading [60]

The walls were made of wire-cut solid clay bricks with dimensions $210 \times 52 \times 100$ [mm³] and 10 [mm] thick mortar prepared with a volumetric cement: lime: sand ratio of 1: 2: 9 [60]. As mentioned above, different vertical pre-compression forces p were uniformly distributed on the wall before applying horizontal displacement. Experimental crack pattern for two walls with the same geometry, mechanical properties and initial vertical stress $p = 0.3$ [N/mm²] are shown in Figure 4.10. As demonstrated in this figure, total behavior of the walls are similar but are not exactly the same. Walls J4D and J5D experienced horizontal tensile crack at the left top and right bottom of the wall at the earliest loading stage, but diagonal stepped cracks caused the failure in the wall. Crack in the bricks and crushing at the toes were also observed in the wall.

The GEFDyn model of the wall using 18×9 3D solid elements, 153 horizontal and 144 vertical (72 represent mortar and 72 represent brick-middle) interface elements is shown in Figure 4.11.

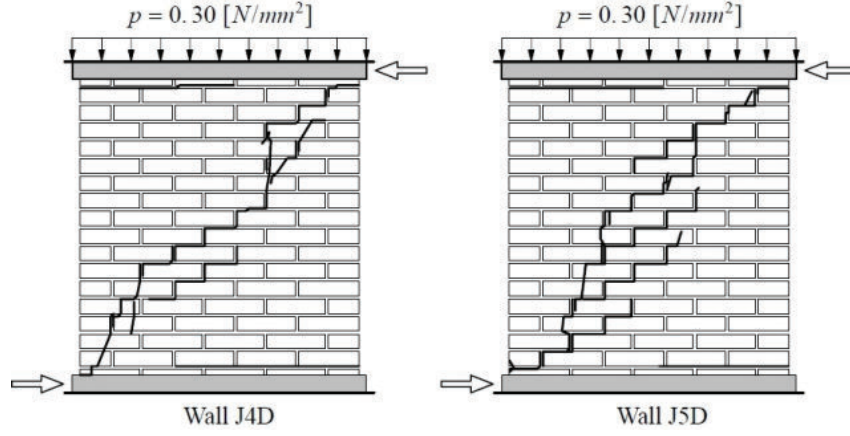


Figure 4.10: Experimental crack pattern after loading [60]

Figure 4.12 also represents the arrangement of units, horizontal and vertical interfaces as well as interfaces in the middle of bricks.

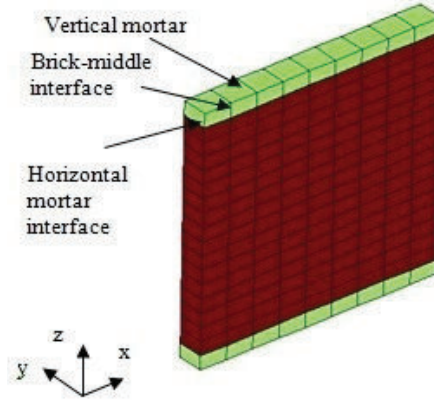


Figure 4.11: GEFDyn model geometry and elements

Boundary conditions

The steel beams are not modeled here but the top nodes of the wall are fixed in z direction and the movement of nodes at the base is prevented in all directions.

$$u_x = d, u_y = 0, u_z = 0 \text{ for } z = z_{max}$$

$$u_x = 0, u_y = 0, u_z = 0 \text{ for } z = 0$$



Figure 4.12: Different categories of interface elements used for modeling masonry wall

Material properties

As mentioned before, interface element allows discontinuities in displacement and its behavior is defined by an equation between stress vector and relative displacement. Equation 4.25 demonstrates the relation between displacement and stress in interface element:

$$\sigma = D.\epsilon \quad (4.25)$$

Where $D = \{E_{interface}, G_{sinterface}, G_{tinterface}\}$. As mortars are assumed to be isotropic, $G_{sinterface} = G_{tinterface}$. The elastic stiffness matrix D can be calculated from the properties of units, mortars and the thickness of mortars. In this analysis, the bricks are supposed to remain elastic and their properties do not change. So, according to uniform stress distribution and serial chain connection between components, the elastic stiffness matrix D defines as [60]:

$$E_{interface} = \frac{E_u \cdot E_m}{h_m(E_u - E_m)} \quad (4.26)$$

$$G_{interface} = \frac{G_u \cdot G_m}{h_m(G_u - G_m)} \quad (4.27)$$

Where h_m is the actual thickness of mortar in tested wall, E_u and E_m are Young's moduli and G_u and G_m are shear moduli of unit and mortar respectively. Multi-surface yield surface which composed of Mohr-Coulomb shear failure and tension cut-off failure, Figure 4.6 is considered as interface element failure criterion.

The properties of bricks and mortars are given in Table 4.1. These properties are obtained from the results of tension, compression and shear experimental samples. As the modulus of elasticity of the brick is much higher than those of mortar, the bricks remain elastic and mortars act as the plane of weakness. Therefore, the nonlinear characteristic of the wall is concentrated in interface elements.

Nonlinear properties of interface elements are given in Table 4.2. The friction angle, measured by $\tan\phi$, is assumed constant, i.e. $\tan\phi = 0.75$; $\phi = 36.9^\circ$. This is the (residual) value obtained by Vander Pluijm (1993) [86]. The dilatancy angle that is measured by $\tan\psi$ is assumed to be equal to zero. Results from Van der Pluijm(1993) studies indicate that a normal confining pressure

Table 4.1: Elastic properties of bricks and mortar used in the model [60]

Brick		Mortar	
E	ν	$E_{interface}$	$G_{interface}$
16700 MPa	0.15	82 GPa/m	36 GPa/m

between 1.0 to 2.0 [N/mm²] is enough to yield dilatancy angle to zero [60].

Table 4.2: Inelastic properties of joints [60]

Tension	Shear			Thickness
f_t	C	$\tan\phi$	$\tan\psi$	e
0.25 MPa	0.35 MPa	36.9°	0	3e-6 [m]

According to Figure 4.7, when the displacement exceeds element's thickness, the interface element will be opened. The opening in the interface elements is because of tension failure, so the thickness of interface elements is calculated as the ratio between tension strength and modulus of elasticity of interface as in Equation 4.10 and reads:

$$e = \frac{f_t}{E} = \frac{2.5 \times 10^5}{8.2e9} = 3e - 6$$

An elastic dummy stiffness is allocated to interface element in the middle of bricks and its artificial thickness is calculated based on bricks properties. f_t and E here are the tension strength of brick and dummy modulus of elasticity of the interface element located in the middle of bricks.

$$e = \frac{f_t}{E} = \frac{2 \times 10^6}{1e15} = 2e - 9$$

Table 4.3: Properties of the potential brick cracks [60]

$E_{Brick-middle}$	$G_{Brick-middle}$	f_t
1.0e6 [MPa]	1.0e6 GPa/m	2.0 MPa

Cracking profile

The cracking pattern obtained for an initial vertical pressure of 300 kPa and 2 mm horizontal displacement at the top of the panel is given in Figure 4.13. Note that horizontal displacement is applied to all top nodes.

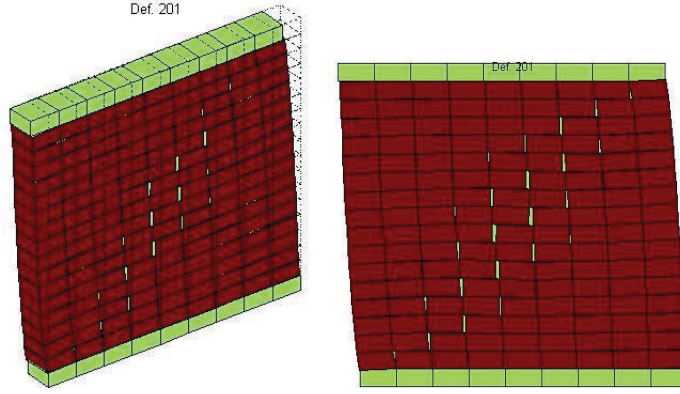


Figure 4.13: Deformed shape of masonry wall at $d = 2 \text{ mm}$ model I

As shown in Figure 4.13, the model is capable to reproduce stepped diagonal crack. Some brick middle interfaces as well as vertical mortar interfaces are opened due to tension failure. Dots represents undeformed shape of wall in the left figure. Push-over curve is calculated and compared to the experimentally obtained result, see Figure 4.14. There are two curves for experimental tests: greater one belongs to Wall J5D and smaller one represents total lateral forces at the base of Wall J4D, see Figure 4.10. Horizontal forces of all base nodes are summed at each step to represent base shear in the wall. As shown in this figure, there is a good agreement between experimental evidences and numerical results. The initial stiffness of the wall, elastic behavior of the wall and yield value are reproduced well. There is a drop in push over curve at $d = 1.1 \text{ mm}$ because of formation of diagonal cracks in the wall. When diagonal cracks appear in the wall, vertical elements in that region open and do not sustain normal and shear stresses and suddenly the wall loses a lot of strength. But, there is difference between pushover curve and experimental data after $d = 1.5 \text{ mm}$ and base shear rises by displacement increment. This difference comes from this fact that the compression failure is not considered in the model.

The contours of normal and shear stresses in different planes as well as major principal stress and minor principal stress of the bricks at earliest steps ($d = 0.11 \text{ mm}$) and the last step of loading ($d = 2 \text{ mm}$) are shown in Figure 4.15 and Figure 4.16.

The whole process can be understood from these figures. As shown in Figure 4.15 due to difference between stiffness of mortars and bricks a diagonal strut parallel to the diagonal of the wall

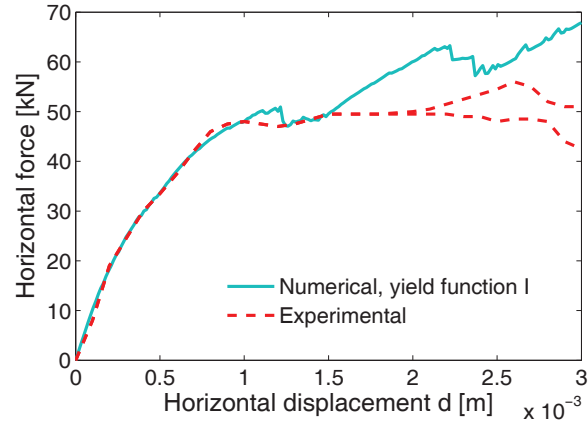


Figure 4.14: Load-Displacement diagram for model I

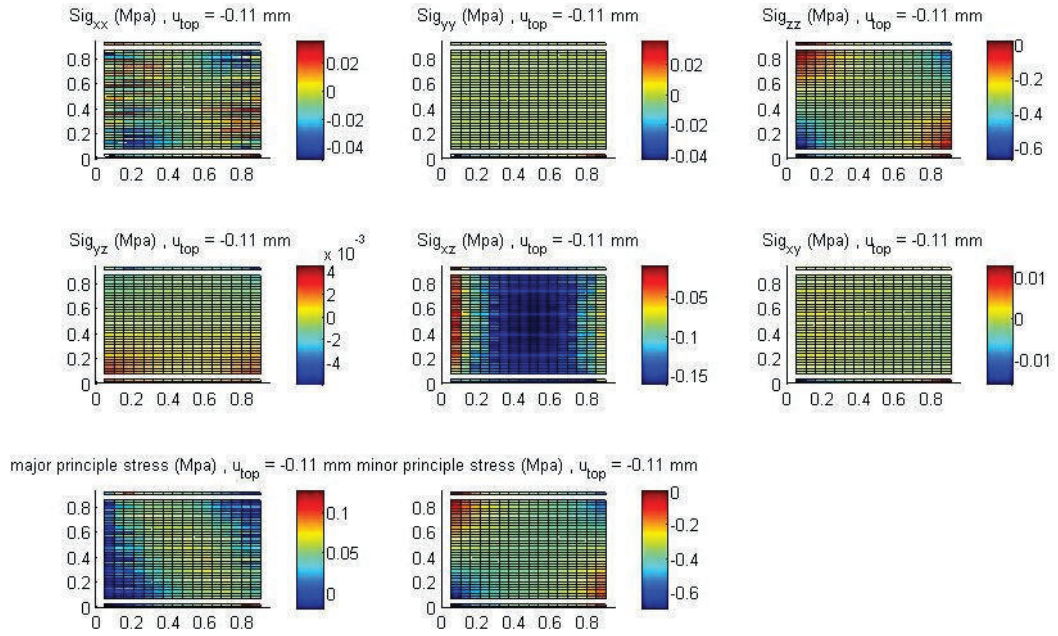


Figure 4.15: Stress diagrams in the masonry wall bricks $d = 0.11$ mm for model I

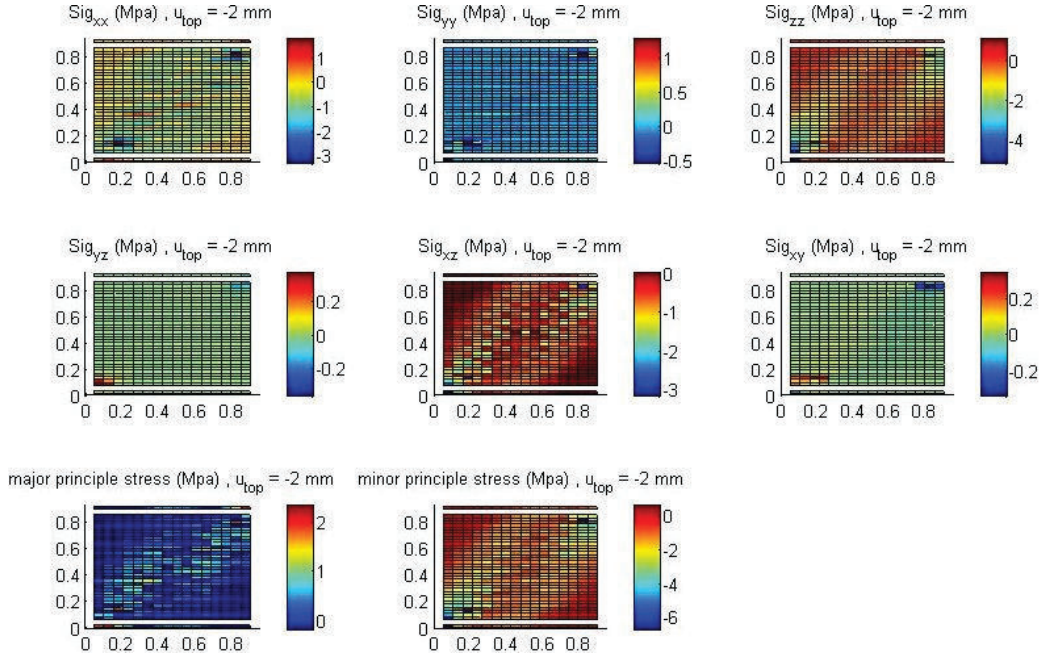


Figure 4.16: Stress diagrams in the masonry wall bricks $d = 2mm$ for model I

can be distinguished in major principal stress planes from left top to right bottom corners. Minor principal stress figure demonstrates that the left bottom and right top corners of the wall suffer maximum compression stress and crushing failure in the bricks will happen there, if these values exceed the compressive strength of the wall. If the stress in major principal stress plane exceeds tension strength, tension failure happens. In the same way, if minor principle stress in a point exceeds compression strength of brick, crushing failure would be imminent. Then, by increasing lateral displacement, shear and compression stresses in elements augment and the orientation of major principal stress changes and becomes reversed. As shown in the figure, the major principle stresses are along a diagonal, so that in these locations, tension failure happened. Thus, interface elements in correspondence to the direction of major principal stresses fail in tension and make such crack pattern in the wall.

In Figure 4.17, different failure mechanisms as well as their corresponding cracks in horizontal interface, vertical interface and brick middle interface are presented. Shear failure in interface elements is demonstrated by sliding in element whereas opening of interface element represents tension failure in that element. Moreover, opening of brick-middle interface illustrates tension failure in the bricks.

By paying attention to Figure 4.17(b) it reveals that there is sliding failure at top left and bottom right of the wall, but the diagonal pattern cracks are greater so they are predominant. Figure 4.17(c) and Figure 4.17(d) show tensile failure in the vertical mortar as well as tensile

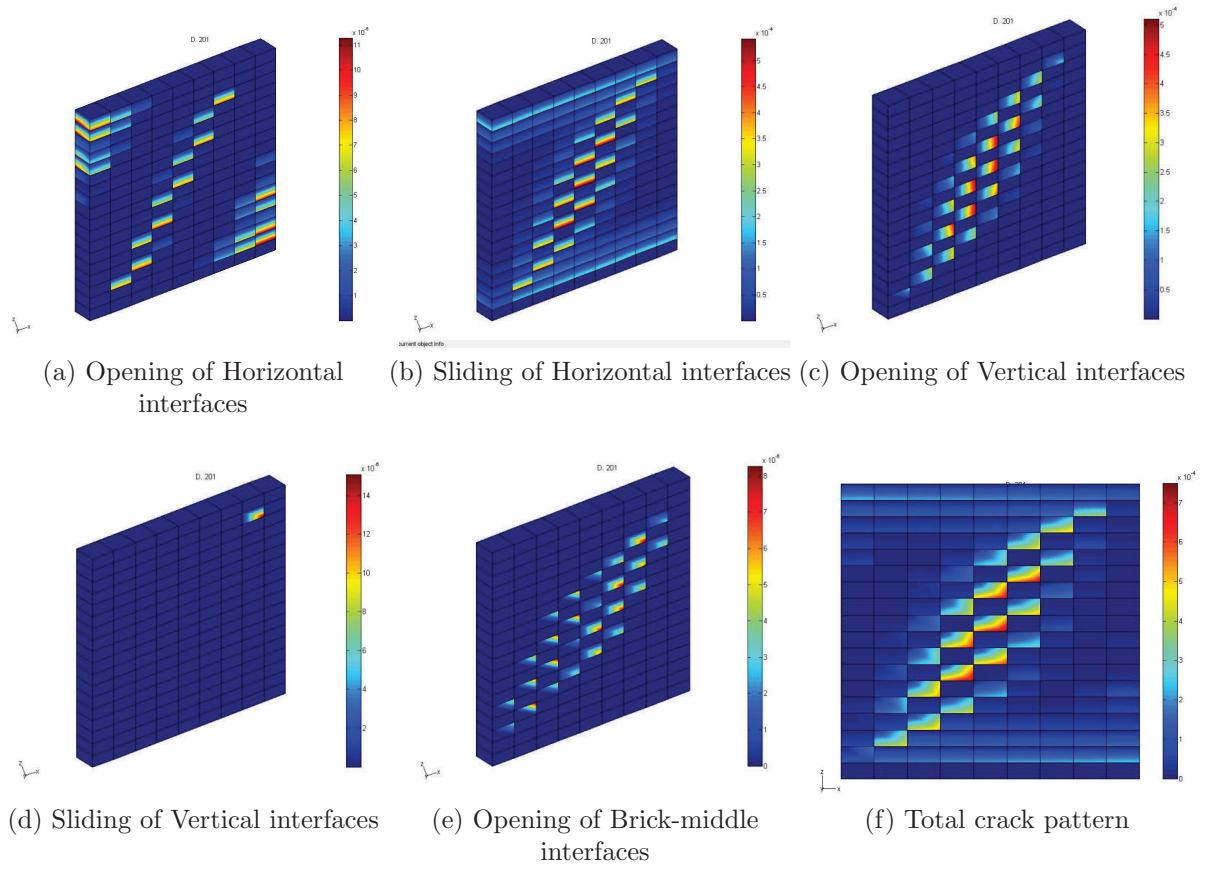


Figure 4.17: Crack pattern in the masonry wall at $d = 2mm$

failure in the bricks. Except one element, no vertical interface experiences shear failure. Figure 4.17(a) also illustrates the opening in horizontal interfaces which are located at two corners plus diagonal direction. The total crack pattern also is shown in Figure 4.17 (e).

4.4.2 Wall with opening

In this section the wall with central opening which was subjected to a monotonic loading by Raijmakers and Vermentlfoort [1993] [86] is modeled and validated. Figure 4.18 shows the experiment's wall which was tested and subjected to vertical pre-compression equal to $0.3 [N/mm^2]$. The material properties and dimension of the wall is the same as the one without opening. The central opening creates two weak piers and forces the struts to be developed around the opening.

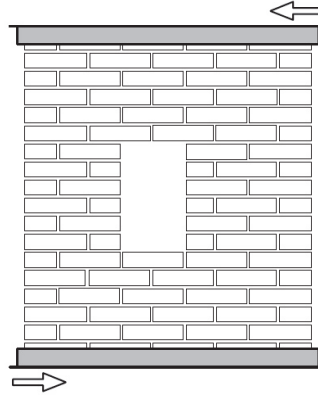


Figure 4.18: Wall with central opening tested by Raijmakers and Vermentlfoort [1993] [86]

Figure 4.19 shows the crack pattern of the two walls with the same properties. Diagonal stepped cracks are developed at two sides of the central opening. Tensile cracks also can be found at top and bottom of left and right small piers respectively. Finally top left and bottom right toes fail because of crushing.

Deformed shape and cracking pattern of wall result from numerical modeling are illustrated in Figure 4.20 and Figure 4.22. Diagonal cracks around the opening are reproduced well, see Figure 4.20. Dots represent undeformed shape of the wall before loading.

Force displacement diagram of the model is drawn in Figure 4.21 and compared with experimental results. It should be first noted that difference between load displacement of walls J2G and J3G is originated from different crack propagations. As shown in Figure 4.19 diagonal cracks are not experienced in the wall J3G as in the wall J2G, so wall J3G fails sooner and its collapse load is 20% lower than that of wall J2G. The response of walls in terms of load-displacement and total

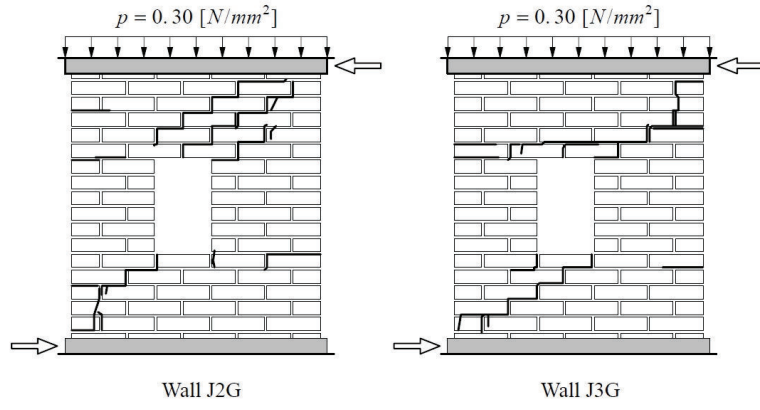


Figure 4.19: Experimental crack patterns for different tests [60]

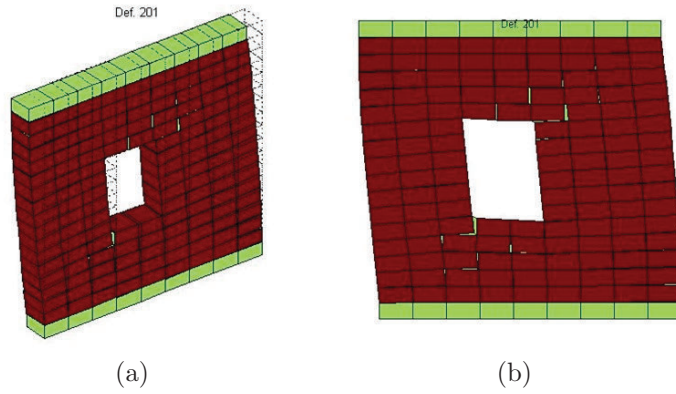


Figure 4.20: Deformed shape of the wall with opening result from simulation for model I

crack pattern are different for the same walls. This difference comes from the scatter properties of material and small number of bricks constituted the wall. Failure mechanism in wall J2G is bending failure and the wall withstand higher lateral strength while in right wall (wall J3G) an early sliding of the mortars at top of the opening is the reason of failure and lower load-displacement curve is obtained for this wall. The absence of limitation for compressive strength of masonry and no definition for crushing failure of masonry cause the great difference between pushover curves of experiment and the model. Hence, in order to have an accurate model a limit for compression strength should be defined. This limit should also controls the shear strength in the masonry wall. Tension failure in the bricks as well as sliding and opening of the mortars are shown in detail in Figure 4.22.

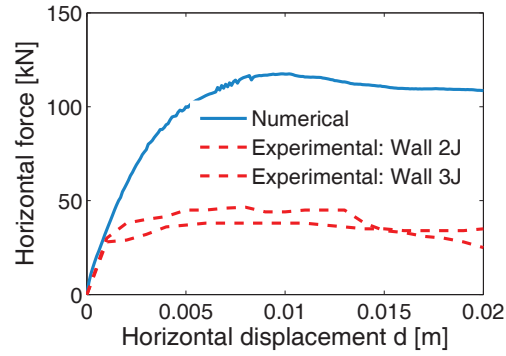


Figure 4.21: Load displacement diagram of experiment and numerical model for model I

4.4.3 Influence of aspect ratio

A parametric study by varying the height H and width L of the wall shows different patterns of cracking. The ratio H/L made an important change in the push-over curve, the fracture mechanisms and subsequently crack patterns of the wall. In this section, two series of wall with aspect ratio less than 1 and more than 1 are studied. Therefore, the length of the wall is multiplied by 0.5, 1.5 and 2. The same values are used to multiply by the height of wall. The following sections demonstrate the results of numerical modeling for aspect ratio less than 1 and greater than 1.

(a) Aspect ratio less than 1

Pushover curve and total crack pattern of the walls with aspect ratio less than 1, are summarized in Figure 4.23. Please note that the experimental curve is that of the wall J4D and is only put in the figure to give a reference for comparison.

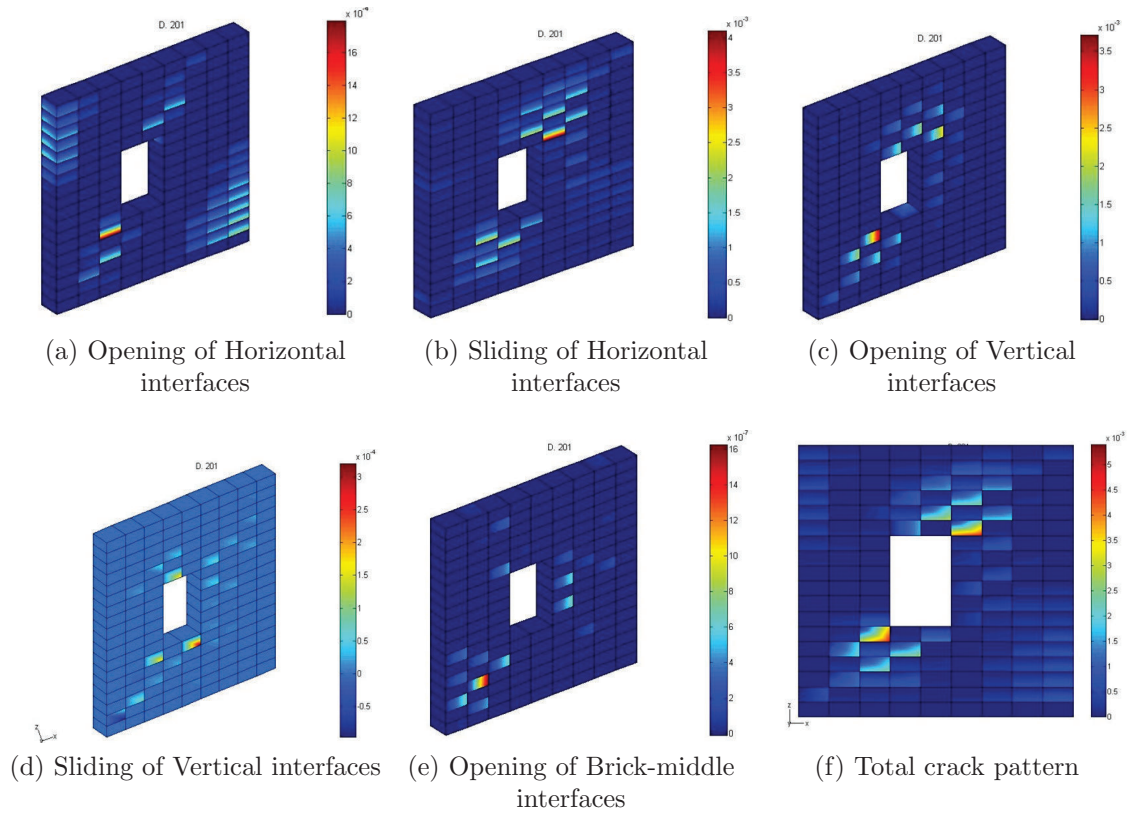


Figure 4.22: Crack pattern in the masonry wall with opening $d = 2mm$ for model I

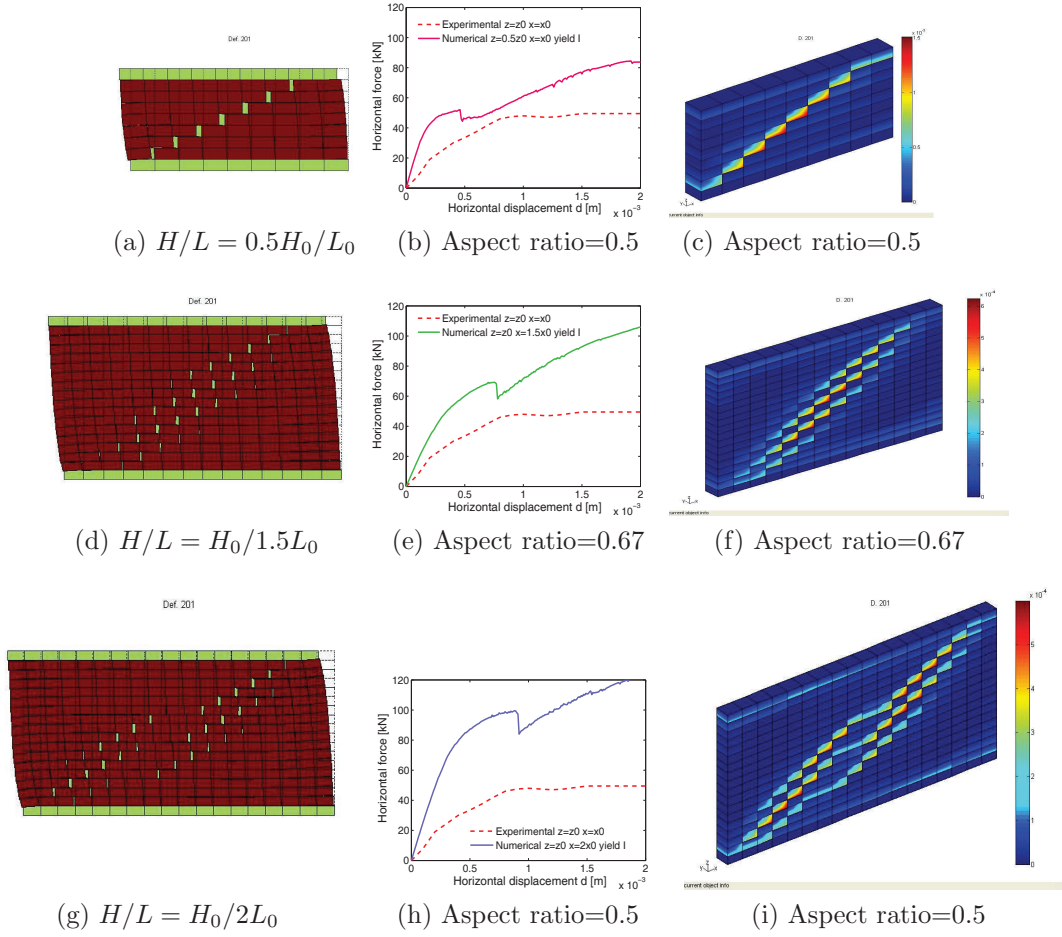


Figure 4.23: Deformed shape, pushover curve and crack pattern in the masonry wall for aspect ratios less than 1 at $d = 2mm$ for model I

For the case H/L equal to one or less than one, the diagonal crack pattern can be found but the start and final points of the cracks depends on the length of the wall. By paying attention to the push-over curves it can be understood that the stiffness of the wall is augmented by increasing the length of elements. The jump observed in push over curves is due to tension failure initiation in the joints and loss of continuity between elements. As can be seen in push over curve, the shear strength is increased infinitely, because no limitation is assumed for compression strength in the mortar elements. In some cases, the failure of the wall is because of crushing failure of the corners, but in this section the model is not capable to capture the compressive failure neither in bricks and nor in mortars. The push over curves and normalized push over of these cases are shown in Figure 4.24 to have an accurate comparison.

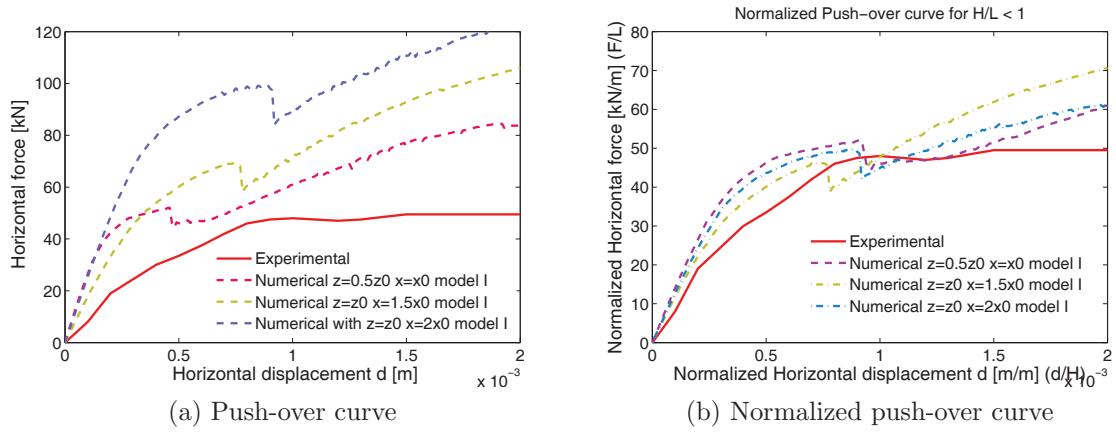


Figure 4.24: load-displacement diagram for different aspect ratios $H/L < 1$ for model I

As can be seen in the Figure 4.24, total tendency of the push over curve is the same. For the wall with the same aspect ratio, case $z = 0.5z_0$ and $x = 2x_0$, the longer wall bears much greater loads while both curves have the same stiffness. In normalized push over curve as shown, for the same aspect ratio, the wall with lower length has a little more strength. As a conclusion, by increasing the aspect ratio, the stiffness and maximum shear strength increase. The cracking configuration is highly dependent on this ratio. For the case H/L equal to unity or less, the crack is diagonally in a way, but the starting point and end point of the crack depend on the length of the wall.

(b) Aspect ratio greater than 1

In this part the results of modeling for three walls with aspect ratios greater than one are presented. The first case belongs to the wall whose length is divided by 2, so it has aspect ratio equal to 2. To make a good comparison of results different cases are gathered in Figure 4.25.

For a ratio greater than 1, the failure mechanism is because of brick crushing. The crack on the edges of the panel is dominant, but the diagonal is not clear. As there is no limit for compression

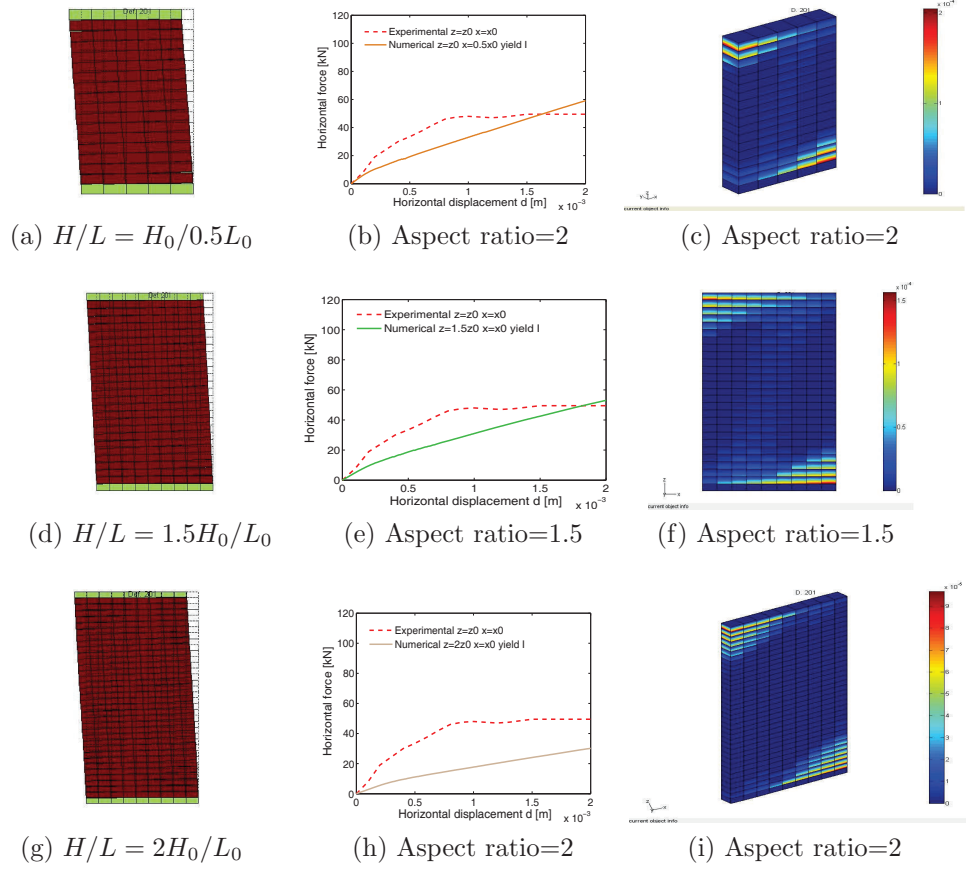


Figure 4.25: Deformed shape, pushover curve and crack pattern in the masonry wall for aspect ratios greater than 1 at $d = 2mm$ for model I

for mortars in this study, the push over curves increase with load increment and collapse load can not be distinguished here. Figure 4.26 shows push over curves and normalized push over curves for aspect ratio greater than 1.

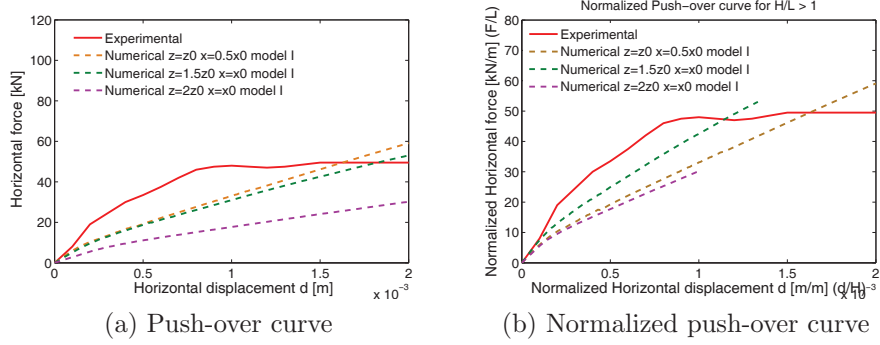


Figure 4.26: load-displacement diagram for different aspect ratios $H/L > 1$ for model I

In normalized curve it can be found that walls with the same aspect ratio have the same pushover curve and sustain the same lateral load. Wall's stiffness has inverse relation with wall's aspect ratio. As can be seen in Figure 4.26(a) wall with aspect ratio equal to 1.5 is stiffer than walls with aspect ratio equal to 2. Overturning moment has greater value for higher wall and that causes earlier compression failure in the wall.

The results show that the aspect ratio (H/L) has a great influence on its resistance against different loads and thus on the failure mode of the wall. For the ratio greater than 1, the mechanism of grinding of bricks would be predominant, so compression failure of the toes is the predominant failure mode of the masonry. For the case with the ratio below 1, depending on normal stress and loading, horizontal sliding of the mortar would be the main mechanism of failure, but for the case with a rate approximately equal to 1, the diagonal tension is predominant.

4.4.4 Cyclic behavior of masonry walls

In this section, the masonry wall without opening which was tested by Raijmakers and Vermeltoft (1992) and Vermeltoft and Raijmakers (1993) is subjected to two types of cyclic loading in order to study the behavior of masonry subjected to earthquakes. Two types of cyclic loading are applied to the masonry wall in order to find the capability of model to capture different phenomena and failure mechanisms. The maximum amplitude of applied displacements is 2 mm. In a first test just one cycle is applied to the wall and maximum displacement is reached in primary loading and then the cycle performs whereas in the second test, the maximum displacement is reached after five cycles during which the displacement amplitude augments gradually. The characteristics of loading and the wall's response will be discussed in the following.

(a) One cycle loading

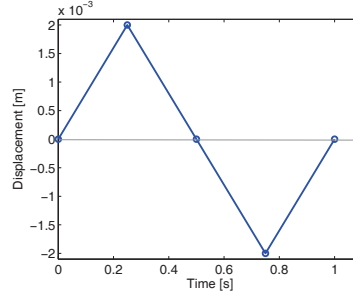


Figure 4.27: One cycle displacement

In first part, the wall is subjected to a one cycle loading-unloading displacement as shown in Figure 4.27. The horizontal displacements are imposed gradually to the top of the wall up to $d = 2mm$. Afterward, the wall is unloaded down to $d = -2mm$ and finally displacements are gradually increased to zero $d = 0mm$. The total diagonal crack after loading and the obtained load-displacement curve are shown in Figure 4.28. The local drifts at $d = 0.0015mm$ and $d = -0.0005mm$ represent the formation of diagonal crack pattern in the wall in different directions. Since there is no limitation for compression in this model, the carried out shear strength in negative displacements is higher than positive displacements. In this case two diagonal cross crack pattern are developed in the wall due to cyclic movement. The cracks which are raised from first positive cycle are greater than the cracks originated from the second cycle.

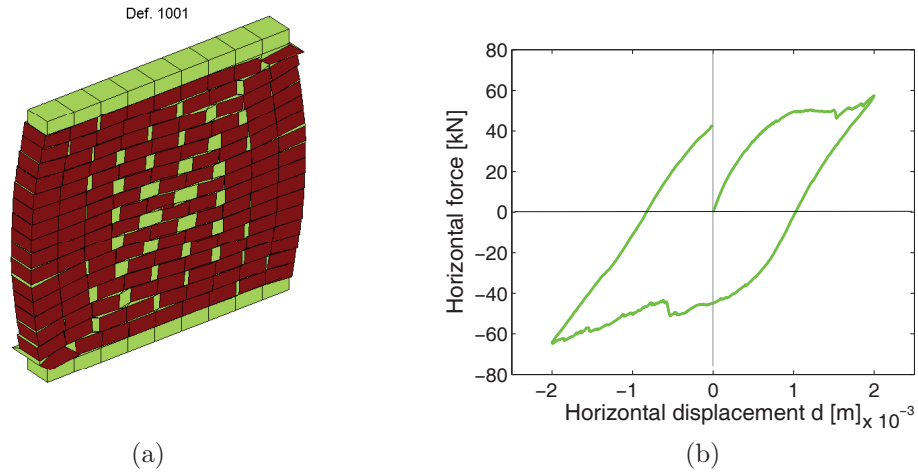


Figure 4.28: (a) Deformed shape (b) load-displacement curve in the masonry wall for one cycle loading

The cracks due to sliding and opening of horizontal elements, the cracks due to tension failure of bricks and total crack pattern after loading are shown in Figure 4.28. As cyclic displacements

are applied to the wall, two series of stepped cracks in wall's diagonals are formed. The length of cracks at the center of the wall is more than the other parts.

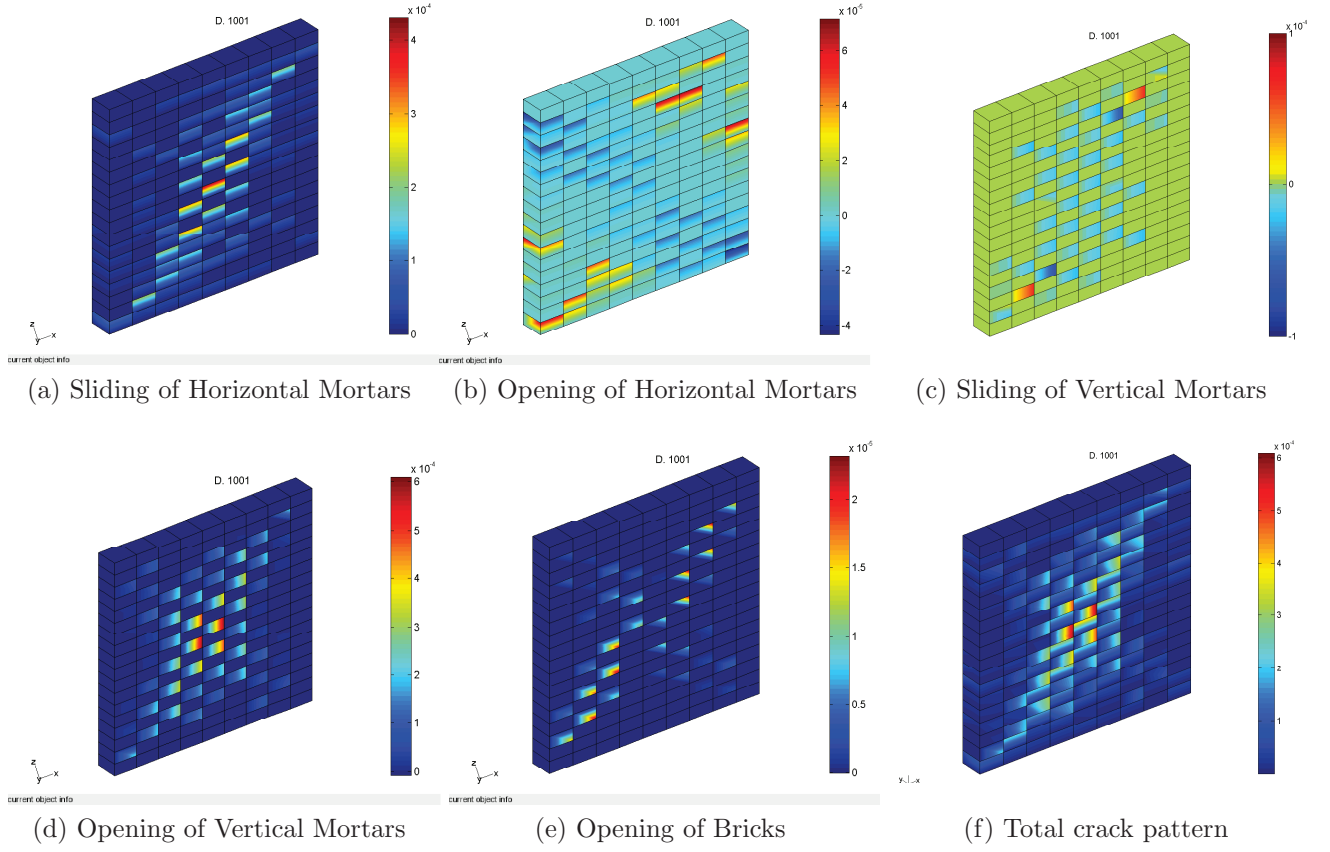


Figure 4.29: Crack pattern in different elements of the wall for one cycle loading at final step $d = 0mm$

(b) Multiple cycles loading

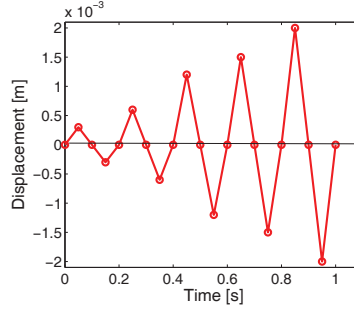


Figure 4.30: Multiple cycles displacement

In this part, the displacements $d = \pm 2mm$ are applied gradually to the wall through five cycles. The amplitude of displacements are $\pm 0.0003mm$, $\pm 0.0006mm$, $\pm 0.0012mm$, $\pm 0.0015mm$ and $\pm 0.002mm$ respectively as shown in Figure 4.30. The deformed shape and load-displacement curve at final step $d = 0mm$ are displayed in Figure 4.31.

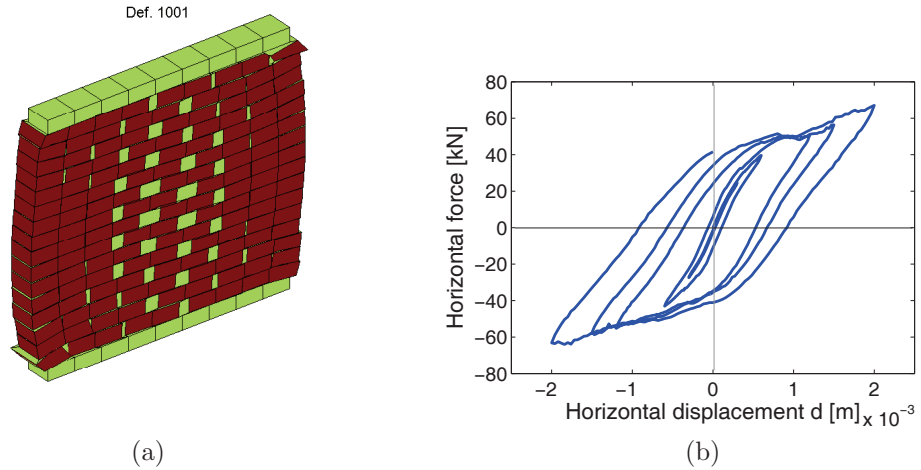


Figure 4.31: (a) Deformed shape (b) load-displacement curve in the masonry wall for multiple cycles loading

As can be seen in the Figure 4.31, the crack pattern is different from the first one. In the second case, the failure is important in the middle of the wall and a rupture can be distinguished over there. This failure is because of opening of vertical mortars. The obtained load-displacement curve shows that as no degradation was assumed for the model, stiffness of the wall is not changed during loading and as the compression failure is not captured in the wall, base shear increases with displacement increment. From result depicted above it can be concluded that the number of cycles has an important influence in the failure mode of the masonry shear wall. The length of

cracks and their location on the wall for different interface elements after loading are represented in Figure 4.32.

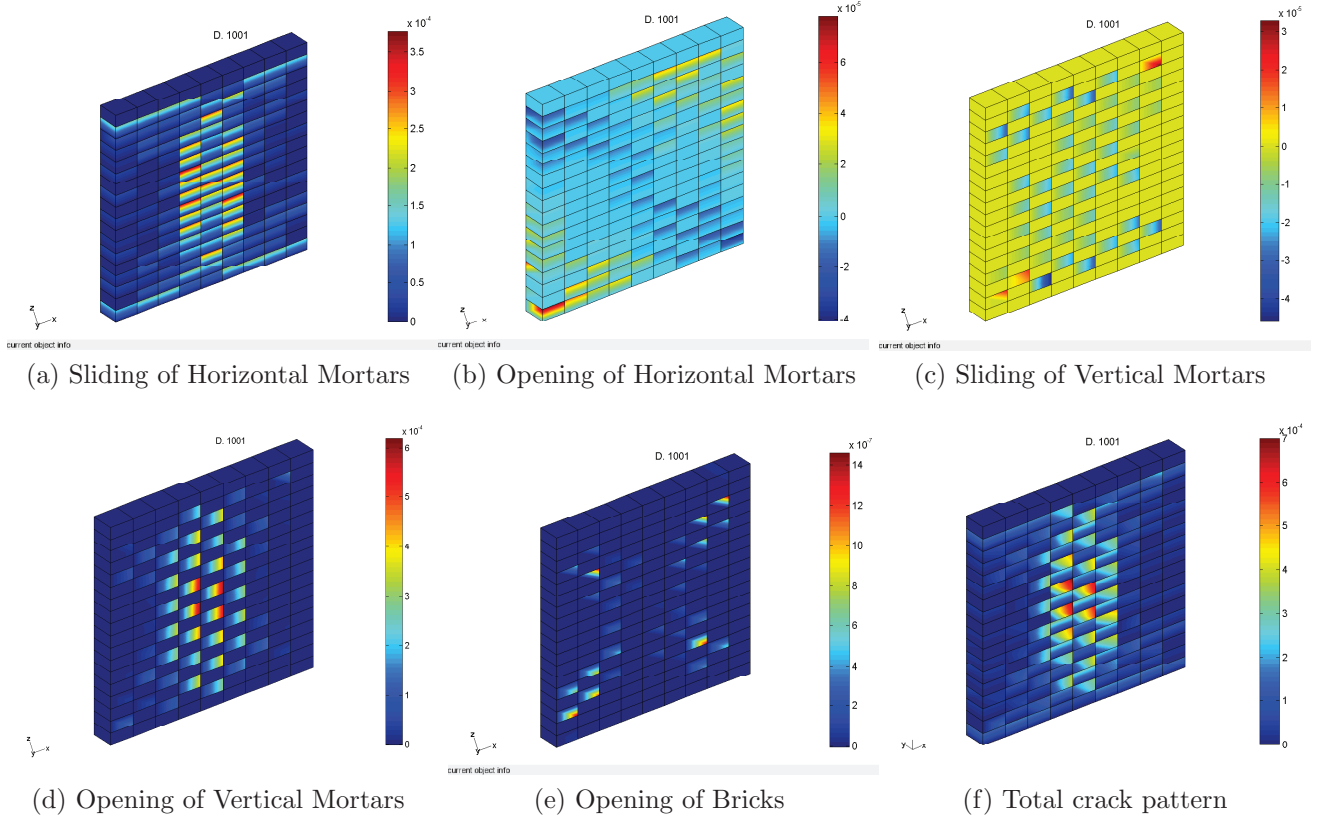


Figure 4.32: Crack pattern in different elements of the wall for multiple cycles loading at final step $d = 0mm$

Figure 4.33 shows different load displacement curves obtained from numerical modeling for one cycle and multiple cycles loading and experimental data from monotonic loading. As shown in this figure, model I is not able to predict the cyclic response of the wall. The reduction of wall's stiffness because of loading-unloading process and cyclic loading as well as maximum lateral strength of the wall could not be captured in this model.

In the absence of the degradation phenomenon in the modeling of material behavior, results show that even if the envelope curves of load-displacement are similar, failure mechanisms and cracking pattern are different because redistribution of loads in both cases are not the same. It is found that the loading history plays an essential role on the map of cracks. The model still needs improvement in terms of reduction in the cohesion and rigidity to the rate of degradation during cyclic loading in order to take into account the material damage. Moreover, in addition to refining compression cap and softening behavior for material's strength, the reduction of modulus

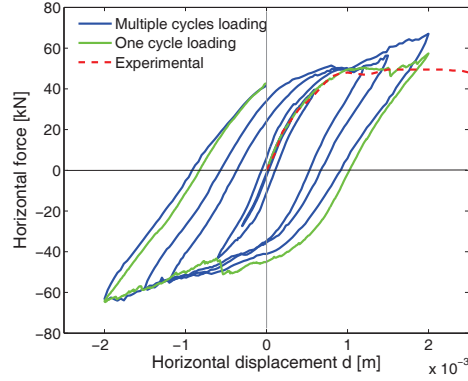


Figure 4.33: Comparison between load-displacement curves from cyclic to monotonic loading

of elasticity with initiating plastic displacement will be added to the model in order to take into account the stiffness degradation of the wall during cyclic loading.

4.4.5 Conclusion and perspective

The results show that the 3D model of this study successfully simulated the behavior of masonry wall. Numerical model was validated with comparing its response to experimental data. In GEFDyn masonry model, bricks are modeled using solid elements and mortars are represented with interface elements. A Mohr-coulomb yield function with tension cut-off is considered for interface element as material property and bricks are supposed to remain elastic. A potential crack plane is considered in the middle of bricks using interface element to simulate tensile failure of bricks. Crack pattern is captured very well and push over curve shows that the model is capable of producing initial stiffness of the wall and its behavior to first steps of non-linearity. As no limitation was supposed for compression failure of the joints and bricks and no softening for shear and tension behavior of the mortars, the load increased with displacement increment and shear stress was raised by compression augmentation. These lacks in the model cause a great difference between load-displacement diagrams of the wall with opening. Thus, the model will be developed in the next section to take into account softening behavior and compression failure in the masonry.

Some simulations were made to capture the effect of cyclic loading on the masonry wall and the number of cycles. It was found that the loading history plays a role in the map of cracks. The model still requires improvement in terms of reduction in the cohesion and rigidity based on the rate of degradation during cyclic loading to take account of material damage.

4.5 Multi-surface yield function for interface elements (Model II)

In previous section, the masonry wall was simulated using micro-modeling strategy in which bricks and mortars are modeled separately. Bricks were modeled by solid elements while mortars were represented by interface element. A simple yield surface considering tension failure and shear sliding failure of the mortars was assumed for vertical and horizontal interface elements. The micro model was validated by comparing its response with the experimental data available in the literature [85], [86]. The obtained results of numerical modeling show that the crack pattern was captured well but compression failure was not taken into account. As there is no limitation considered for compression stress in the mortars, shear stress increased by compressive stress increment according to Mohr-Coulomb criterion so that in the load displacement curve, a considerable difference between the ultimate load of numerical model and experimental evidence was observed. Thus the previous model could not take into account the ultimate strength of masonry.

In this section, the micro model is improved. The softening behavior is considered in shear and tension stress-strain curve. Moreover, a linear compression cap is added to the previous yield surface to capture compression failure of the wall. Therefore, in this section a multi-surface constitutive law composed of tension cut-off, Mohr-Coulomb and linear cap representing tension, shear and compression failure of the mortars is used. The idea of compression cap was the first time introduced by Drucker-Prager [1957] [28] in soil mechanics. First time, Lourenco [1996] [60] added a composite compression cap to the yield surface of interfaces in modeling masonry walls using micro-modeling strategy. In this section, a simplified compression cap is introduced and used to capture compression failure of the wall. Then parametric study will be done and the effect of each model parameter on the behavior of wall will be investigated. Then the failure mechanism of walls with different aspect ratios is investigated. Moreover, the behavior of wall with central opening is also simulated.

4.5.1 Properties of composite yield surface

Three types of failure are considered for mortars i.e. interface elements: tension failure, shear failure and compression failure. Associated flow rule is considered for tension whereas non associated flow rule is used for shear and compression. Different types of failure and their yield function formulation are described and discussed in the following sections:

Mohr-Coulomb shear criterion

Mohr-Coulomb criterion is used for defining the shear yield threshold. In this section, softening behavior is assumed for cohesion. The yield function according to Equation 4.8 reads:

$$f_1 = \sqrt{(\sigma_s)^2 + (\sigma_t)^2} + \sigma_n \cdot \tan \phi - C \quad (4.28)$$

Where:

$$C = C_0 \cdot \exp(C_0 \cdot |\gamma^p| / GII) \quad (4.29)$$

$$\gamma^p = \sqrt{[u_s^p]^2 + [u_t^p]^2} \quad (4.30)$$

In the above equations, C_0 is the initial cohesion of interface, ϕ is friction angle, $[u_s^p]$ and $[u_t^p]$ are the shear plastic displacements in s and t directions respectively. GII is fracture energy of mode II. Figure 4.34, represents the results of direct shear tests which have been done by Pluijm et al. [1993] [86]. The solid curve which is defined by exponential function can match with experimental data well. Thus, in this formulation, the softening behavior of masonry is controlled by shear plastic displacement.

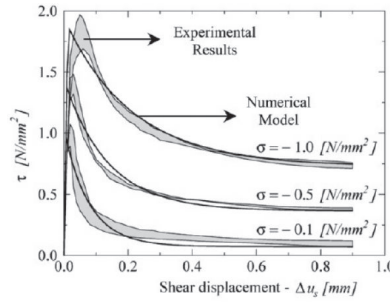


Figure 4.34: Shear behavior of masonry, experimental results by Van der Pluijm (1993)[86] for different confinement stresses, with $C_0 = 0.87[N/mm^2]$; $\tan(\phi_0) = 1.01$; $\tan(\phi_0) = 0.73$; $GII = 0.0580.13 * \sigma[Nmm/mm^2]$ [86]

A non-associated flow rule is considered for shear in mortar interface. In Equation 4.31, ψ is dilatancy angle. The potential function for shear is unchanged and defined as:

$$g_1 = \sqrt{(\sigma_s)^2 + (\sigma_t)^2} + \sigma_n \cdot \tan \psi \quad (4.31)$$

A lateral displacement is applied to two bricks with horizontal mortar to investigate the accuracy of formulations. There is a good accuracy between numerical modeling and actual behavior of specimen and softening behavior of mortar is reproduced well. The results are shown in

Figure 4.35.

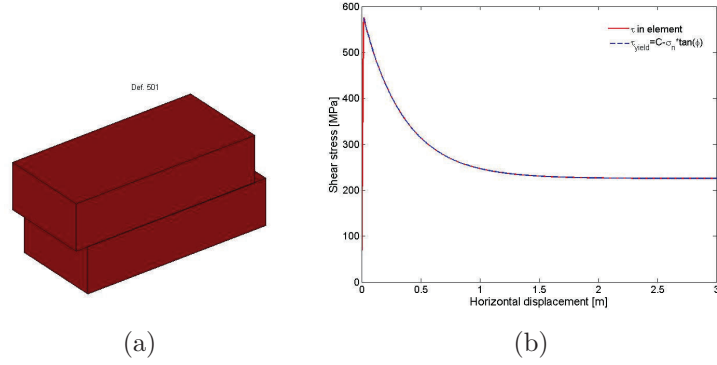


Figure 4.35: (a) Deformed shape (b) stress-strain curve of masonry in shear

Tension failure

A softening curve according to the Van der Pluijm [85] results of direct tension experiment for masonry, is assumed for tensile strength of mortars, see Figure 4.36. In Equation 4.32, F_{t0} and GI are tensile strength and mode I fracture energy of joints respectively and $[u_n^p]$ is the relative plastic normal displacement of interface element.

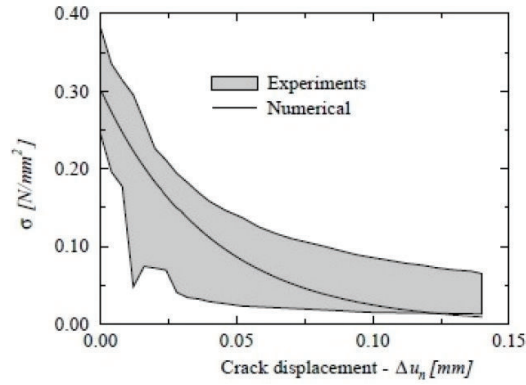


Figure 4.36: Tensile behavior, experimental results from Van der Pluijm (1992)[85], with $F_{t0} = 0.30[N/mm^2]$ and $GI = 0.012[Nmm/mm^2]$

$$F_t = F_{t0} \cdot \exp(-F_{t0}/GI \cdot < [u_n^p]^+ >) \quad (4.32)$$

Where:

$$\begin{aligned} \langle x \rangle^+ &= x \text{ if } x \geq 0 \\ \langle x \rangle^+ &= 0 \text{ if } x < 0 \end{aligned}$$

Yield function for tension is defined as:

$$f_2 = \sigma_n - F_t \quad (4.33)$$

Associated flow rule is considered for this mechanism. Moreover, e_{open} is defined in the model so that when interface displacement exceeds this value, the interface element will open and tension, shear and compression stresses become zero. A simple direct tension test is done in order to investigate the accuracy of modeling. The results show the accuracy of formulations and the similarity of the softening branch in stress-strain curve with the real behavior of bricks and mortars in tension.

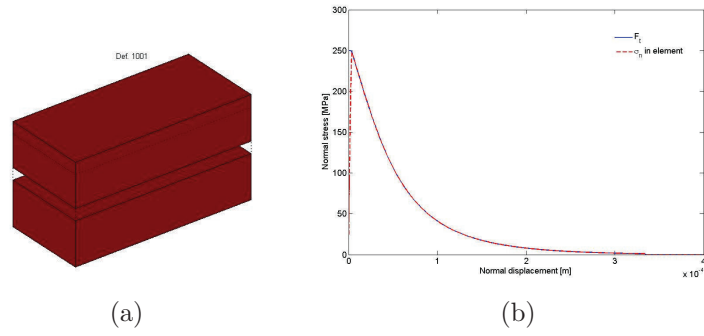


Figure 4.37: (a) Deformed shape (b) stress-strain curve of masonry in direct tension

Compression failure criterion

Compression failure is added to the interface element formulation. Compressive strength of mortar is assumed to vary with normal plastic displacement which is expressed by an exponential function.

$$F_c = F_{c0} \cdot \exp(F_{c0}/GIII \cdot \langle [u_n^p]^- \rangle) \quad (4.34)$$

Where:

$$\begin{aligned} \langle x \rangle^- &= 0 \text{ if } x > 0 \\ \langle x \rangle^- &= x \text{ if } x \leq 0 \end{aligned}$$

In Equation 4.34, F_{c0} is the initial compressive strength of masonry, $[u_n^p]$ is the plastic normal relative displacement and G_{III} is fracture energy of mode III failure. In this study, to reproduce crushing of masonry and diagonal shear failure, the combination of compression and shear stresses is limited. As mentioned in literature review, this strategy has been used in 2D by some of researchers [101], [17]. So the new yield function is introduced to limit shear by compression increment in interface element. Yield function is introduced:

$$f_3 = \sqrt{(\sigma_s)^2 + (\sigma_t)^2} - \sigma_n \cdot \tan \theta - F_c \cdot \tan \theta \quad (4.35)$$

In Equation 4.35, F_c is given in Equation 4.34 and θ is the new parameter which represents the slope of compression cap, shown in Figure 4.38.

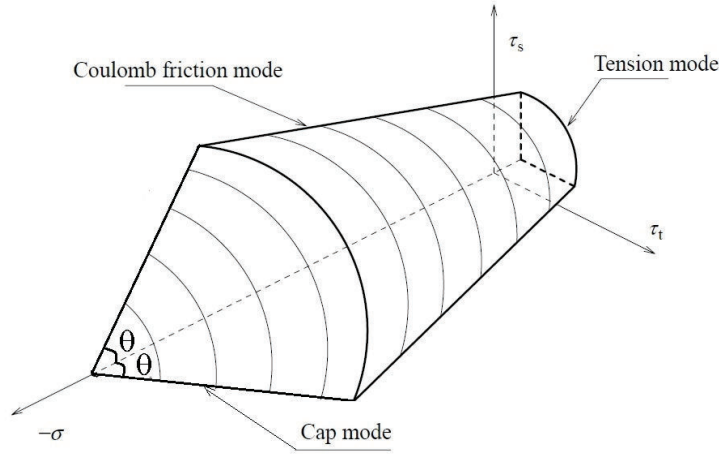


Figure 4.38: Composite yield function for 3D masonry wall configuration used in this study

The compressive cap conversion with respect to compressive strength is shown schematically in Figure 4.39(a). The comparison between proposed ellipsoid compression cap for two values for C_{ss} which were proposed by Lourenco [1996] [60] and the linear compression cap used in this study is shown in Figure 4.39(b).

A non-associated flow rule is considered for compression. The potential function is read in Equation 4.36. β is also a new parameter of the model and represents the direction of plastic deformations. The variation of θ and β are also investigated in the following sections and Appendix B respectively.

$$g_3 = \sqrt{(\sigma_s)^2 + (\sigma_t)^2} - \sigma_n \cdot \tan \beta \quad (4.36)$$

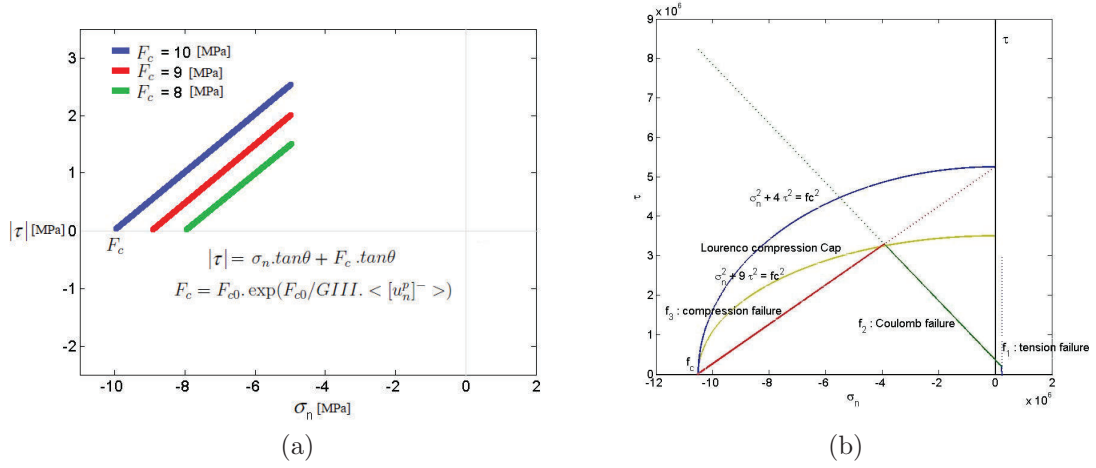


Figure 4.39: (a) Variation of compression cap with respect to F_c (b) Comparison between compression cap used in this study and that of given by Lourenco in 2D [60]

It has worth to note again that u_s , u_t and u_n are the jump of displacements in different directions.

Composite yield function corners

The coupling between shear and tension as well as shear and compression are considered in the model. The coupling between them happens in the intersection of Mohr-Coulomb shear criterion and tension cut-off as well as Mohr-Coulomb and compression cap.

(a) Shear and tension are active:

Tension and shear mechanisms are active when : $f_2 = 0$, $\dot{f}_2 = 0$ and $f_1 = 0$, $\dot{f}_1 = 0$ so:

$$f_1 = \sqrt{\sigma_s^2 + \sigma_t^2} + \sigma_n \cdot \tan(\phi) - C_0 \cdot \exp(-C_0/GII \cdot |\gamma^p|) = 0$$

$$\dot{f}_1 = \partial f_1 / \partial \sigma_s \cdot \dot{\sigma}_s + \partial f_1 / \partial \sigma_t \cdot \dot{\sigma}_t + \partial f_1 / \partial \sigma_n \cdot \dot{\sigma}_n + \partial f_1 / \partial u_s^p \cdot \dot{u}_s^p + \partial f_1 / \partial u_t^p \cdot \dot{u}_t^p = 0$$

$$f_2 = \sigma_n - F_{t0} \cdot \exp(-F_{t0}/GI < [u_n^p]^+ >)$$

$$\dot{f}_2 = \partial f_2 / \partial \sigma_n \cdot \dot{\sigma}_n + \partial f_2 / \partial [u_n^p] \cdot \dot{[u_n^p]}$$

$$[u_n]^p = \sum_k [u_n]^p; [\dot{u}_s]^p = \sum_k [\dot{u}_s]^p; [\dot{u}_t]^p = \sum_k [\dot{u}_t]^p$$

Where k denotes the number of active mechanism.

$$|\tau| = \sqrt{(\sigma_s)^2 + (\sigma_t)^2}$$

$$[u_n]^p = \lambda_1 \cdot \partial g_1 / \partial \sigma_n + \lambda_2 \cdot \partial f_2 / \partial \sigma_n = \lambda_1 \cdot \tan(\psi) + \lambda_2$$

$$[u_s]^p = \lambda_1 \cdot \partial g_1 / \partial \sigma_s + \lambda_2 \cdot \partial f_2 / \partial \sigma_s = \lambda_1 \cdot \frac{\sigma_s}{|\tau|}$$

$$[u_t]^p = \lambda_1 \cdot \partial g_1 / \partial \sigma_t + \lambda_2 \cdot \partial f_2 / \partial \sigma_t = \lambda_1 \cdot \frac{\sigma_t}{|\tau|}$$

The consistency condition of active mechanisms can be written as:

$$\mathbf{A} : \dot{f}_1 = 0 \Rightarrow \frac{\sigma_s}{|\tau|} \cdot G \cdot [u_s - \lambda_1 \cdot \frac{\sigma_s}{|\tau|}] + \frac{\sigma_t}{|\tau|} \cdot G \cdot [u_t - \lambda_1 \cdot \frac{\sigma_t}{|\tau|}] + E \cdot \tan(\phi) \cdot [u_n - \lambda_1 \cdot \tan(\psi) - \lambda_2] + C_0^2 / GII \cdot \exp(-C_0 / GII \cdot |\gamma^p|) \cdot \frac{u_t^p}{|\gamma^p|} \cdot \lambda_1 \cdot \frac{\sigma_t}{|\tau|} = 0$$

$$G \left[\frac{\sigma_s}{|\tau|} \cdot u_s + \frac{\sigma_t}{|\tau|} \cdot u_t \right] + E \cdot \tan(\phi) \cdot u_n = \lambda_1 \cdot \left[G \frac{\sigma_s^2}{|\tau|^2} + G \frac{\sigma_t^2}{|\tau|^2} + E \tan(\phi) \tan(\psi) - C_0^2 / GII \cdot \exp(-C_0 / GII \cdot |\gamma^p|) \cdot \left[\frac{u_s^p}{|\gamma^p|} \frac{\sigma_s}{|\tau|} + \frac{u_t^p}{|\gamma^p|} \cdot \frac{\sigma_t}{|\tau|} \right] \right] + \lambda_2 [E \cdot \tan(\phi)]$$

$$G \left[\frac{\sigma_s}{|\tau|} \cdot u_s + \frac{\sigma_t}{|\tau|} \cdot u_t \right] + E \tan(\phi) u_n = \lambda_1 \cdot h_{11} + \lambda_2 \cdot h_{12}$$

With:

$$h_{11} = G + E \tan(\phi) \tan(\psi) - C_0^2 / GII \cdot \exp(-C_0 / GII \cdot |\gamma^p|) \cdot \left[\frac{u_s^p}{|\gamma^p|} \frac{\sigma_s}{|\tau|} + \frac{u_t^p}{|\gamma^p|} \cdot \frac{\sigma_t}{|\tau|} \right]$$

$$h_{12} = E \tan(\phi)$$

$$\mathbf{B} : \dot{f}_2 = 0 \Rightarrow E [u_n - \lambda_1 \tan(\psi) - \lambda_2] + F_{t0}^2 / GI \cdot \exp(-F_{t0} / GI \cdot u_n^p) [\lambda_1 \tan(\psi) + \lambda_2] = 0$$

$$E u_n = \lambda_1 [E \tan(\psi) - F_{t0}^2 / GI \cdot \exp(-F_{t0} / GI \cdot u_n^p) \cdot \tan(\psi)] + \lambda_2 [E - F_{t0}^2 / GI \cdot \exp(-F_{t0} / GI \cdot u_n^p)]$$

$$E u_n = \lambda_1 \cdot h_{21} + \lambda_2 \cdot h_{22}$$

$$h_{21} = E \tan(\psi) - F_{t0}^2 / GI \cdot \exp(-F_{t0} / GI \cdot u_n^p) \cdot \tan(\psi)$$

$$h_{22} = E - F_{t0}^2/GI \cdot \exp(-F_{t0}/GI \cdot u_n^p)$$

Therefore, there are two equations with two unknowns, namely λ_1 and λ_2 . The unknowns are calculated based on these two equations. By having the unknowns, $[u_n]^p$, $[u_s]^p$ and $[u_t]^p$, the stresses can be calculated based on the following equations :

$$\dot{\sigma}_n = E(\dot{u}_n - \dot{u}_n^p) \quad (4.37)$$

$$\dot{\sigma}_s = G(\dot{u}_s - \dot{u}_s^p) \quad (4.38)$$

$$\dot{\sigma}_t = G(\dot{u}_t - \dot{u}_t^p) \quad (4.39)$$

(b) Shear and compression are active:

Compression and shear mechanisms are active when : $f_3 = 0$, $\dot{f}_3 = 0$ and $f_1 = 0$, $\dot{f}_1 = 0$. Hence:

$$f_1 = \sqrt{\sigma_s^2 + \sigma_t^2} + \sigma_n \cdot \tan(\phi) - C_0 \cdot \exp(-C_0/GII \cdot |\gamma_p|) = 0$$

$$\dot{f}_1 = \partial f_1 / \partial \sigma_s \cdot \dot{\sigma}_s + \partial f_1 / \partial \sigma_t \cdot \dot{\sigma}_t + \partial f_1 / \partial \sigma_n \cdot \dot{\sigma}_n + \partial f_1 / \partial u_s^p \cdot \dot{u}_s^p + \partial f_1 / \partial u_t^p \cdot \dot{u}_t^p = 0$$

$$f_3 = |\tau| - \sigma_n \cdot \tan(\theta) - F_{c0} \cdot \exp(F_{c0}/GIII \cdot < [u_n^p]^- >) \cdot \tan(\theta)$$

$$\dot{f}_3 = \partial f_3 / \partial \sigma_s \cdot \dot{\sigma}_s + \partial f_3 / \partial \sigma_t \cdot \dot{\sigma}_t + \partial f_3 / \partial \sigma_n \cdot \dot{\sigma}_n + \partial f_3 / \partial u_n^p \cdot \dot{u}_n^p = 0$$

$$[u_n]^p = \lambda_1 \cdot \partial g_1 / \partial \sigma_n + \lambda_3 \cdot \partial g_3 / \partial \sigma_n = \lambda_1 \cdot \tan(\psi) - \lambda_3 \cdot \tan(\beta)$$

$$[u_s]^p = \lambda_1 \cdot \partial g_1 / \partial \sigma_s + \lambda_3 \cdot \partial g_3 / \partial \sigma_s = \lambda_1 \cdot \frac{\sigma_s}{|\tau|} + \lambda_3 \cdot \frac{\sigma_s}{|\tau|}$$

$$[u_t]^p = \lambda_1 \cdot \partial g_1 / \partial \sigma_t + \lambda_3 \cdot \partial g_3 / \partial \sigma_t = \lambda_1 \cdot \frac{\sigma_t}{|\tau|} + \lambda_3 \cdot \frac{\sigma_t}{|\tau|}$$

$$\mathbf{A} : \dot{f}_1 = 0 \Rightarrow \frac{\sigma_s}{|\tau|} \cdot G \cdot [\dot{u}_s - \lambda_1 \cdot \frac{\sigma_s}{|\tau|} - \lambda_3 \cdot \frac{\sigma_s}{|\tau|}] + \frac{\sigma_t}{|\tau|} \cdot G \cdot [\dot{u}_t - \lambda_1 \cdot \frac{\sigma_t}{|\tau|} - \lambda_3 \cdot \frac{\sigma_t}{|\tau|}] + E \cdot \tan(\phi) \cdot [\dot{u}_n - \lambda_1 \cdot \tan(\psi) + \lambda_3 \cdot \tan(\beta)] + C_0^2 / GII \cdot \exp(-C_0 / GII \cdot |\gamma^p|) \cdot \frac{u_s^p}{|\gamma^p|} \cdot [\lambda_1 \cdot \frac{\sigma_s}{|\tau|} + \lambda_3 \cdot \frac{\sigma_s}{|\tau|}] + C_0^2 / GII \cdot \exp(-C_0 / GII \cdot |\gamma^p|) \cdot \frac{u_t^p}{|\gamma^p|} \cdot [\lambda_1 \cdot \frac{\sigma_t}{|\tau|} + \lambda_3 \cdot \frac{\sigma_t}{|\tau|}] = 0$$

$$G \left[\frac{\sigma_s}{|\tau|} \cdot \dot{u}_s + \frac{\sigma_t}{|\tau|} \cdot \dot{u}_t \right] + E \cdot \tan(\phi) \cdot \dot{u}_n = \lambda_1 \cdot [G \frac{\sigma_s^2}{|\tau|^2} + G \frac{\sigma_t^2}{|\tau|^2} + E \tan(\phi) \tan(\psi) - C_0^2 / GII \cdot \exp(-C_0 / GII \cdot |\gamma^p|) \cdot [\frac{u_s^p}{|\gamma^p|} \frac{\sigma_s}{|\tau|} + \frac{u_t^p}{|\gamma^p|} \frac{\sigma_t}{|\tau|}]] + \lambda_3 [G \frac{\sigma_s^2}{|\tau|^2} + G \frac{\sigma_t^2}{|\tau|^2} + E \tan(\phi) \tan(\beta) - C_0^2 / GII \cdot \exp(-C_0 / GII \cdot |\gamma^p|) \cdot [\frac{u_s^p}{|\gamma^p|} \frac{\sigma_s}{|\tau|} + \frac{u_t^p}{|\gamma^p|} \frac{\sigma_t}{|\tau|}]] = 0$$

$$G[\frac{\sigma_s}{|\tau|} \cdot \dot{u}_s + \frac{\sigma_t}{|\tau|} \cdot \dot{u}_t] + E \tan(\phi) \dot{u}_n = \lambda_1 \cdot h_{11} + \lambda_3 \cdot h_{13}$$

$$h_{11} = G + E \tan(\phi) \tan(\psi) - C_0^2 / GII \cdot \exp(-C_0 / GII \cdot |\gamma^p|) \cdot [\frac{u_s^p}{|\gamma^p|} \frac{\sigma_s}{|\tau|} + \frac{u_t^p}{|\gamma^p|} \frac{\sigma_t}{|\tau|}]$$

$$h_{13} = G - E \tan(\phi) \tan(\beta) - C_0^2 / GII \cdot \exp(-C_0 / GII \cdot |\gamma^p|) \cdot [\frac{u_s^p}{|\gamma^p|} \frac{\sigma_s}{|\tau|} + \frac{u_t^p}{|\gamma^p|} \frac{\sigma_t}{|\tau|}]$$

$$\mathbf{B} : \dot{f}_3 = 0 \Rightarrow \frac{\sigma_s}{|\tau|} \cdot G \cdot [\dot{u}_s - \lambda_1 \cdot \frac{\sigma_s}{|\tau|} - \lambda_3 \cdot \frac{\sigma_s}{|\tau|}] + \frac{\sigma_t}{|\tau|} \cdot G \cdot [\dot{u}_t - \lambda_1 \cdot \frac{\sigma_t}{|\tau|} - \lambda_3 \cdot \frac{\sigma_t}{|\tau|}] - E \cdot \tan(\theta) \cdot [\dot{u}_n - \lambda_1 \cdot \tan(\psi) + \lambda_3 \cdot \tan(\beta)] - F c_0^2 / GIII \cdot \exp(F_{c0} / GIII \cdot u_n^p) \cdot \tan(\theta) [\lambda_1 \tan(\psi) - \lambda_3 \tan(\beta)] = 0$$

$$G[\frac{\sigma_s}{|\tau|} \cdot \dot{u}_s + \frac{\sigma_t}{|\tau|} \cdot \dot{u}_t] - E \cdot \tan(\theta) \cdot \dot{u}_n = \lambda_1 \cdot [G \frac{\sigma_s^2}{|\tau|^2} + G \frac{\sigma_t^2}{|\tau|^2} - E \tan(\theta) \tan(\psi) + F_{c0}^2 / GIII \cdot \exp(F_{c0} / GIII \cdot u_n^p) \cdot \tan(\theta) \tan(\psi) - \lambda_3 [G \frac{\sigma_s^2}{|\tau|^2} + G \frac{\sigma_t^2}{|\tau|^2} + E \tan(\theta) \tan(\psi) - F_{c0}^2 / GIII \cdot \exp(F_{c0} / GIII \cdot u_n^p) \cdot \tan(\theta) \tan(\beta)]]$$

$$G[\frac{\sigma_s}{|\tau|} \cdot \dot{u}_s + \frac{\sigma_t}{|\tau|} \cdot \dot{u}_t] - E \tan(\theta) \dot{u}_n = \lambda_1 \cdot h_{31} + \lambda_3 \cdot h_{33}$$

$$h_{31} = G - E \tan(\theta) \tan(\psi) + F_{c0}^2 / GIII \cdot \exp(F_{c0} / GIII \cdot u_n^p) \cdot \tan(\theta) \tan(\psi)$$

$$h_{33} = G + E \tan(\theta) \tan(\beta) - F_{c0}^2 / GIII \cdot \exp(F_{c0} / GIII \cdot u_n^p) \cdot \tan(\theta) \tan(\beta)$$

By calculating λ_1 and λ_3 , $[\dot{u}_n]^p$, $[\dot{u}_s]^p$ and $[\dot{u}_t]^p$ are calculated and then stresses are obtained from Equation 4.37, Equation 4.38 and Equation 4.39.

4.5.2 Numerical validation for Model II

In this section, the numerical analysis is repeated while new yield functions are used for interface elements. The difference between this model and the previous one is that the compression failure is taken into account in this model by limiting the shear stress with compressive strength increment. In order to impose this limitation some new parameters are added into the model such as: f_{t0} , GI , f_{c0} , $GIII$, GII , θ and β . Table 4.4 and Table 4.5 show the values which are used for horizontal and vertical interface elements and brick-middle interfaces respectively. Modulus of elasticity and shear modulus of brick interface element and its thickness is the same as the one in the model I. In Table 4.4, C_0 represents initial cohesion of mortars. For first try, θ is given: $\theta = 45 - \phi/3$ then the effect of this parameter will be studied. The horizontal displacement is applied to the wall similar to the model I. Initial normal stress on the wall is $\sigma_n = 0.3 MPa$. Elastic properties of mortars and bricks are given in Table 4.1.

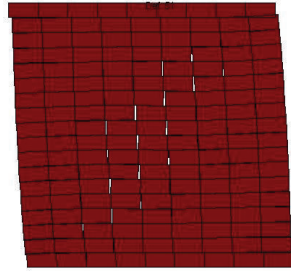
Here, non associated flow rule is considered for compression so $\beta = 45^\circ$. The effect of β on

Table 4.4: Inelastic properties for the horizontal and vertical interface elements for model II

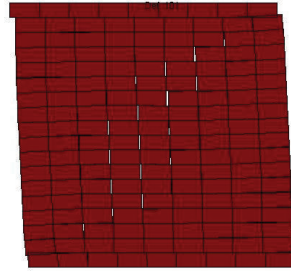
Tension		Shear				Compression				Thickness
f_{t0}	GI	C_0	ϕ	ψ	GII	f_{c0}	$GIII$	θ	β	e
0.25 MPa	18 Pa.m	0.35 MPa	36.9°	0°	125 Pa.m	10.5 MPa	5e3 Pa.m	32.7°	45°	3e-6 [m]

Table 4.5: Brick-middle interface element properties for model II

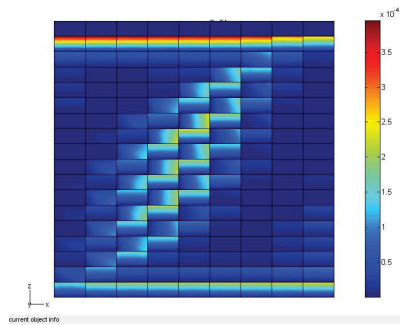
Tension		Shear				Compression				Thickness
f_{t0}	GI	C_0	ϕ	ψ	GII	f_{c0}	$GIII$	θ	β	e
2 MPa	80 Pa.m	2.8 MPa	45°	45°	50 Pa.m	1e15 MPa	1e15 Pa.m	45°	0	2e-9 [m]



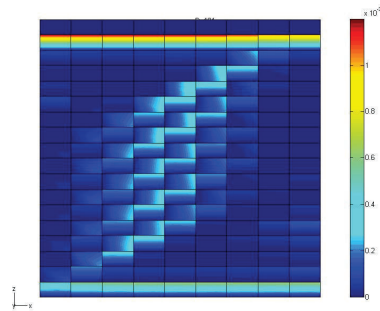
(a) Wall deformation at d=2mm



(b) Wall deformation at d=4mm



(c) Total crack pattern at d=2mm



(d) Total crack pattern at d=2mm

Figure 4.40: Wall deformation under monotonic loading for model II in Plane XZ

performance of masonry wall is studied in Appendix B. Crack pattern for $d = 2mm$ and $d = 4mm$ are shown in Figure 4.40. As shown in this figure, sliding of top and bottom rows as well as diagonal cracks are produced well in this model. Horizontal mortars at top right and bottom left of the wall open whereas the top left and bottom right ones are crushed. According to this figure, the cracking pattern reproduces well by using composite yield function for interface elements.

Push over curve for the model II is shown in Figure 4.41 and compared to the experimental

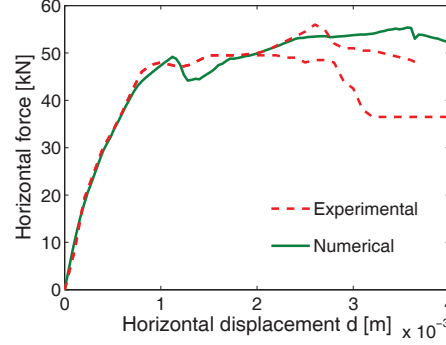


Figure 4.41: Load displacement diagram for model II

results. As illustrated in this figure, there is a good agreement between experimental data and numerical results. At $d = 1.12mm$ a sudden drop is observed in pushover curve. This drop is because of formation of diagonal cracks in the vertical mortars which is accompanied by tension failure in the bricks. As a result, at this point a lot of energy is released in the wall. By opening of vertical interfaces, all stresses at these interfaces are set to zero which makes a numerical load drop in the model. The cracking profile before and after the sudden drop is shown in Figure 4.42.

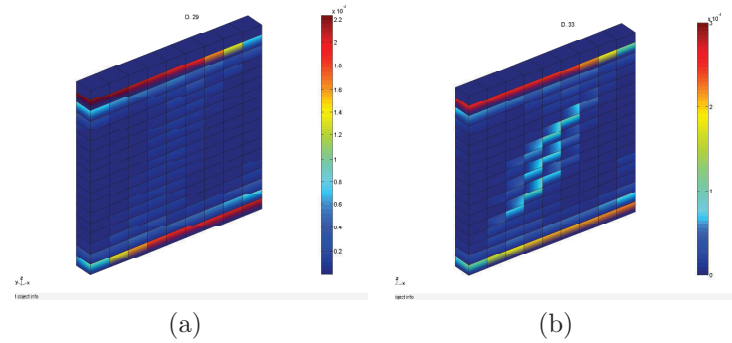


Figure 4.42: Profile of cracks at (a) local peak $d = 1.1mm$ (b) local drop $d = 1.3mm$

Figure 4.43 shows the summation of horizontal force at the base of each brick. The horizontal force of the wall in y label of pushover curve is the summation of all horizontal forces at the base of the wall. This figure shows the contribution of each brick in horizontal strength of the wall. The color of bricks and the corresponding pushover curve is the same. As shown in this figure,

the lateral strength of the wall is mainly carried out by the bricks at the bottom left corner. The drop in the curves is associated with the formation of diagonal cracks in the wall. The horizontal interfaces at the right bottom of the wall sustain no lateral load because they open at earlier steps and cannot withstand stresses.

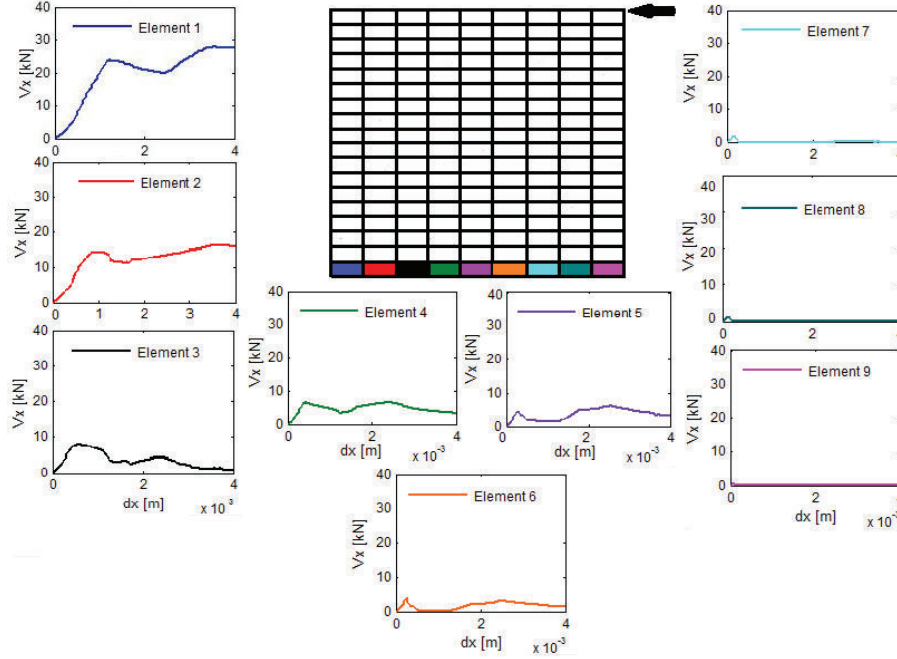


Figure 4.43: Horizontal forces which are carried out by each brick, composite yield surface

Moreover, the comparison between this model using compression cap and the first model with no limit for compression is shown in Figure 4.44. Results show the new model is capable to assess the ultimate strength of masonry shear wall. So after imposing certain deformations, the shear stress instead of increasing with compression stress, will decrease with compression stress increment.

Detailed crack pattern, namely the sliding and opening of horizontal and vertical interfaces in addition to tension failure of brick-middle interfaces are illustrated in Figure 4.45. According to Figure 4.45(g) bricks which are located at diagonal of wall experience tension failure. Horizontal mortars open mainly at the top left and bottom corners of the wall Figure 4.45(b) but some of horizontal elements in diagonal region are also opened due to opening of vertical elements Figure 4.45(d). Horizontal elements at the top and bottom rows of the wall as well as those in diagonal of the wall slide as shown in Figure 4.45(c). Sliding of vertical interfaces also is shown in Figure 4.45(e).

Distributed stresses in the wall namely shear in xy plane, minor principal stresses and major principle stresses at different displacements are illustrated in Figure 4.46. At $d = 1mm$ before

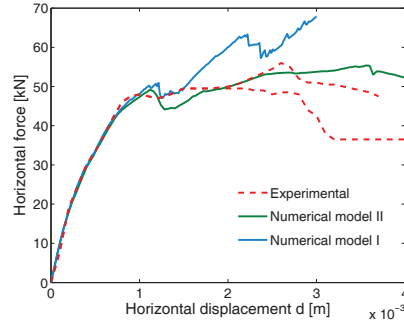


Figure 4.44: Comparison between numerical modeling results for yield function with and without compression cap for model II and model I, respectively

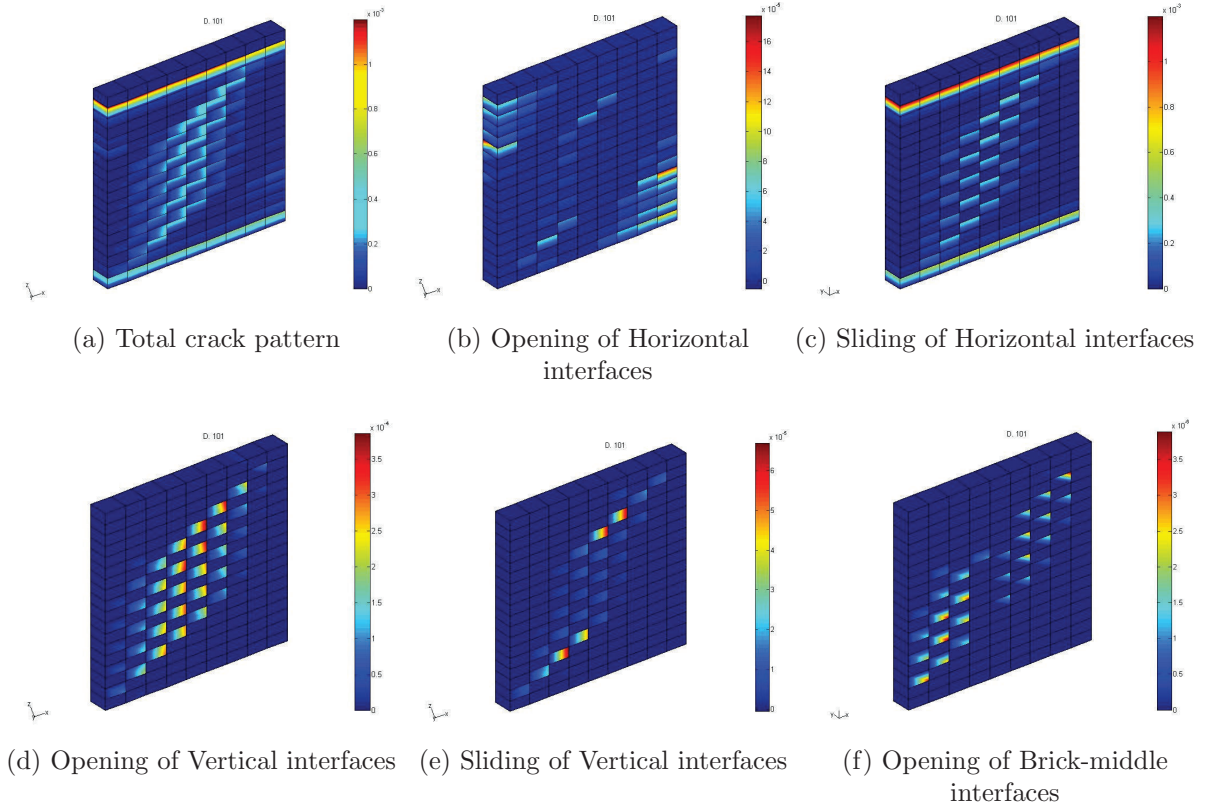


Figure 4.45: Profile of cracking for interface elements for model II at $d = 4mm$

formation of diagonal cracks in the wall maximum and minimum principal stresses and shear stresses lie on diagonal strut. After initiation of diagonal cracks, these cracks change the orientation of compressive strength. Hence, two distinct struts at each sides of diagonal cracks are formed as shown in Figure 4.46(a) and (b) for $d = 2mm$ and $d = 4mm$. The region with high shear stresses which represents the location of sliding elements are shown in left figures. Wherever the tension stress in vertical interface elements passes the tensile strength of mortar $f_{t0} = 0.25MPa$, they open and fail in tension whereas bricks-middle interface elements open when major principal stress violates tensile strength of bricks $f_{t0} = 2MPa$. As illustrated in this figure, horizontal elements at top left and bottom right corners of the wall crush because of high level of compression stress over there.

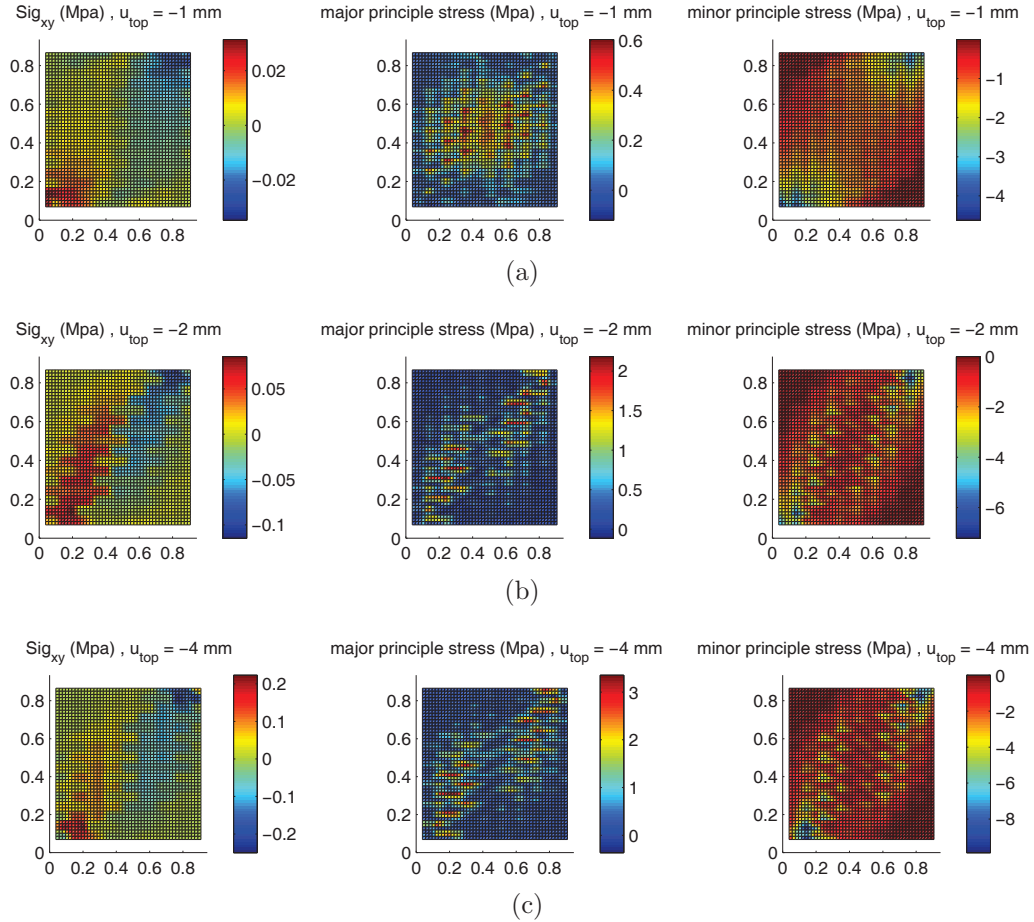


Figure 4.46: Stress distribution at (a) $d = 1mm$ (b) $d = 2mm$ (c) $d = 4mm$

4.5.3 Effect of compression cap's slope θ

In this section two other values are used for the slope of compression cap. In the first case θ is considered to be $\theta = 25^\circ$ which is associated with $\theta = 45 - \phi/1.85$. The middle one is based on the equation: $\theta = 45 - \phi/3$ and in the last one the slope is $\theta = 90^\circ$. The total crack patterns are shown in Figure 4.47 while the pushover curves are compared in Figure 4.48.

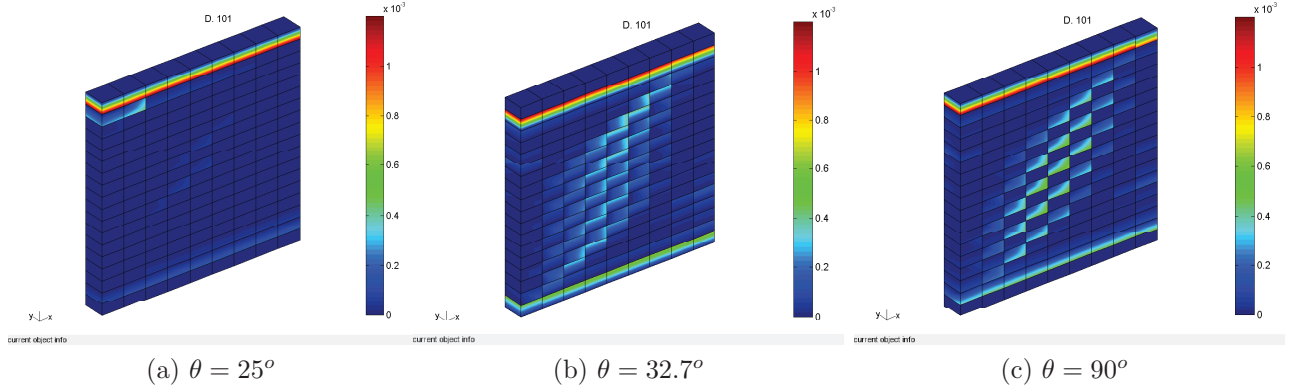


Figure 4.47: Profile of cracking in the wall with different θ

In wall with $\theta = 29^\circ$ the wall fails sooner than for $\theta = 32.7^\circ$. In this case right after formation of diagonal cracks in the wall, the horizontal mortars in the corner crush and loose their shear strength too. In this case the top horizontal mortars undergo sliding shear failure and the wall exhibits brittle behavior. Increasing the θ postpones the reduction of shear failure by increasing normal stress for the walls with the same compression strength. Instead the wall with $\theta = 45 - \phi/3 = 32.7^\circ$ sustains more lateral load and experiences diagonal cracking pattern and finally fails in compression. The wall corners are the location of compressive failure. There is a good agreement between the results of computational modeling and experimental data using this formulation. $\theta = 90$ is associated with the composite yield surface with compression cut-off. In this case shear stress do not decrease with the increment of compression stress in the failure envelope and at $\sigma_n = Fc$, shear stress in the interface element becomes zero. The results show although that the crack profiles are similar but pushover curves considerably diverge. Hence, the formulation used in this study with $\theta = 45 - \phi/3$ is an appropriate equation which reproduces results similar to experimental evidence.

Behavior of masonry wall with opening

In this section, the behavior of wall with opening is investigated using new model. The behavior of wall with opening was studied using model I before. As shown before, the numerical model was not capable to reproduce the maximum load which is withstood by the wall. In this section,

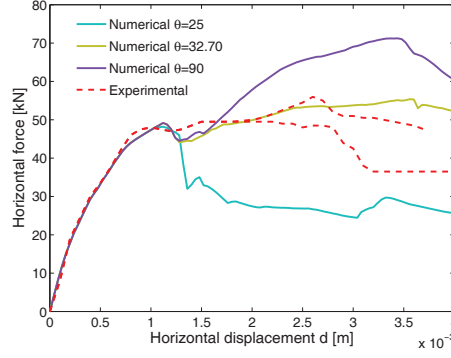


Figure 4.48: Pushover curve for the wall with different θ

softening behavior for shear, tension and compression is considered in the model. In addition, a compression cap is added to yield function to control the limit of shear and compression and to capture the compression failure of the wall. First, the deformed shape and crack pattern of the wall with opening in different displacements are illustrated in Figure 4.49, Figure 4.50 and Figure 4.51.

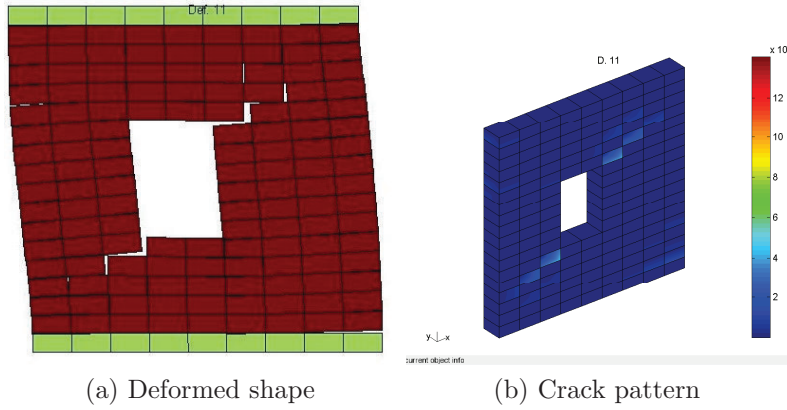


Figure 4.49: Results of analysis at displacement of $1mm$

As can be seen in Figure 4.49, diagonal stepped cracks initiate from the top right and bottom right corners of the opening. At this point some of horizontal elements on bottom right and top left of the wall and small piers open slightly. By increasing the applied displacements, previous cracks open more and their length increases. Thus at $d = 2mm$ as initial diagonal pattern cannot develop to the compressed toes, two other diagonal cracks parallel to previous ones are developed to the wall's corners. As shown in Figure 4.50, the horizontal mortars located at the top of left and the bottom right of the small piers fail in tension and open and force the adjacent horizontal elements to close and sustain compression loads.

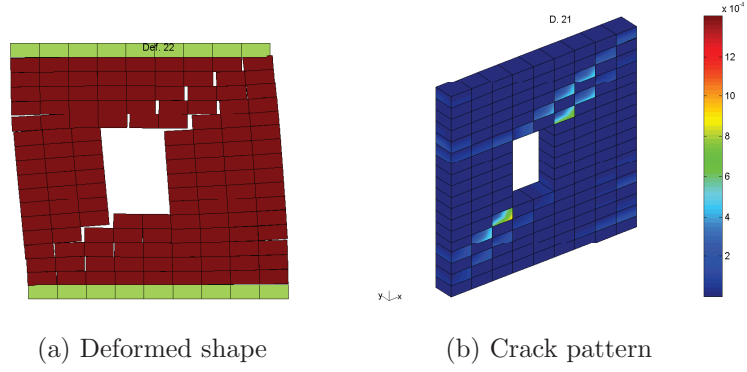


Figure 4.50: Results of analysis at displacement of $2mm$

Under increasing displacements horizontal mortars at top left of small pier slip, the horizontal mortars at top and bottom of wall crush and some of diagonal cracks which were formed initially close and become inactive. Finally at displacements equal to $d = 20mm$, the diagonal cracks become predominant, wall toes are crushed, horizontal cracks developed in small piers and they fail due to bending. Sliding and opening of horizontal and vertical interface elements as well as opening of brick-middle interfaces are shown in Figure 4.51.

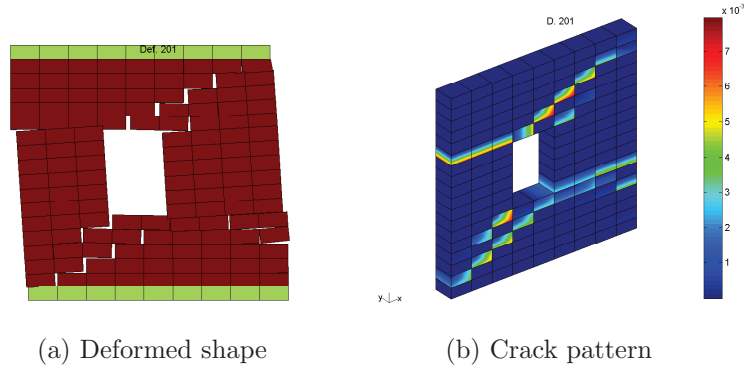


Figure 4.51: Results of analysis at displacement of $20mm$

Pushover curve for wall using model II is displayed in Figure 4.52(a). There is a good agreement between load displacement curve from computational effort and those obtained by experimental test. Hence, the model is capable to reproduce maximum lateral strength of the wall. The lateral load carried out by the wall decreases a lot after $d = 3mm$ and that is because of slipping of horizontal mortars at the top and bottom of left and right small piers. The deformed shape and profile of cracks at this displacement are shown in Figure 4.53. In Figure 4.52(b) the obtained load-displacement curve from model using model I and model II are compared. This figure shows the importance of considering compression cap and softening behavior to have an accurate result.

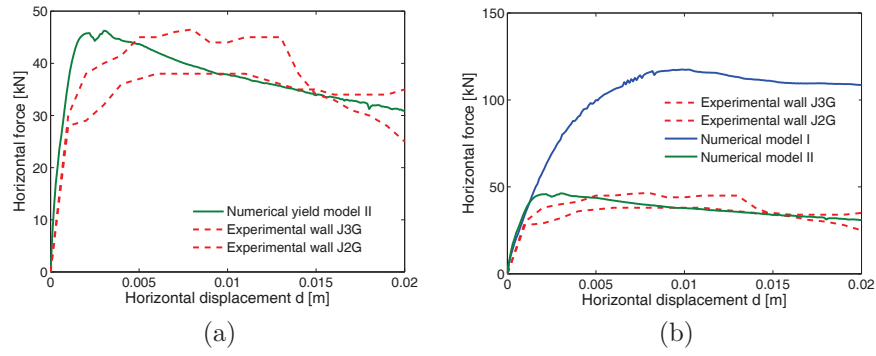


Figure 4.52: Load displacement curve for (a) model II (b) comparison between model I and model II

The previous yield function could not capture the bending failure of the piers. Studies showed that the compression failure as well as softening behavior for tension strength and cohesion of mortars should be considered to assess the ultimate strength of the wall correctly.

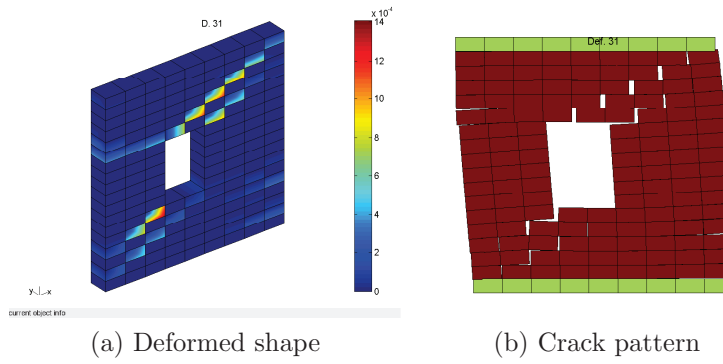
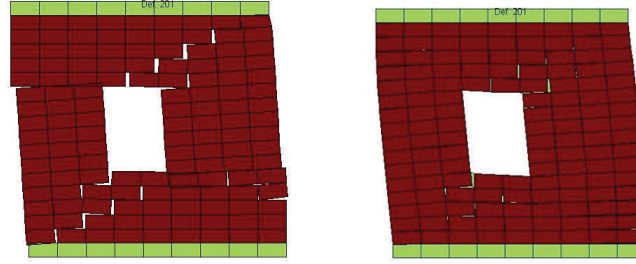


Figure 4.53: Results of analysis at displacement of $3mm$



(a)

(b)

Figure 4.54: Total deformed shape (a) model II (b) model I

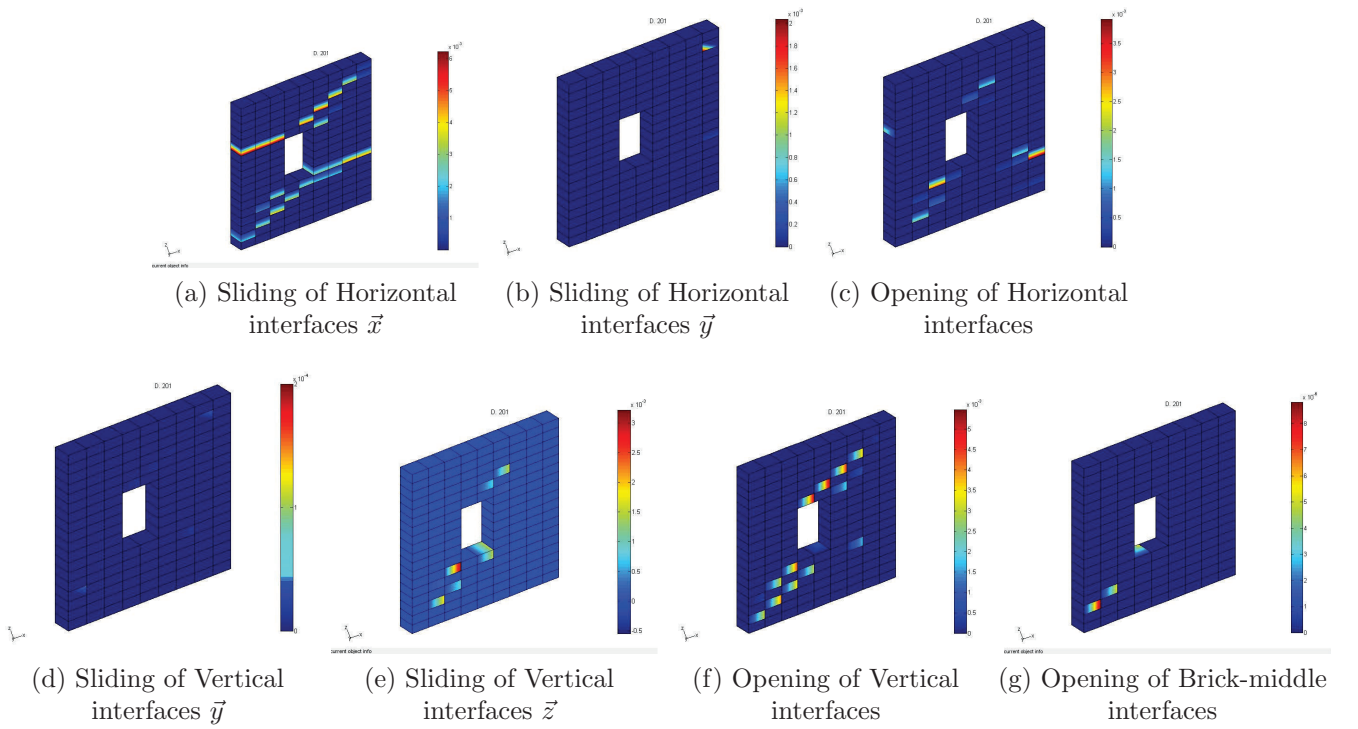


Figure 4.55: Profile of cracking for wall with opening at $d = 20mm$

4.6 Aspect ratio effect

In this section, the behavior of masonry shear walls with different aspect ratios namely lower than 1 and greater than 1, will be analyzed. The combined yield function consisting in compression cap is used for modeling of these walls. For each case, the total crack pattern, pushover curve and deformed shape are illustrated. Then pushover curves resulted from model I and model II will be compared. It should note that in all cases the initial compressive stresses equal to $p = 0.3MPa$ imposed to the wall before applying horizontal displacements.

(a) Aspect ratio less than 1

This category contains three different walls. In the first case, the walls height is divided by 2 whereas for second and third cases the length of wall is multiplied by 1.5 and 2. Therefore, two different aspect ratios for masonry wall namely 0.5 and 0.67 are studied. The results of first case are illustrated in Figure 4.56.

(a) $H/L = 0.5H_0/L_0$, $As = 0.5$

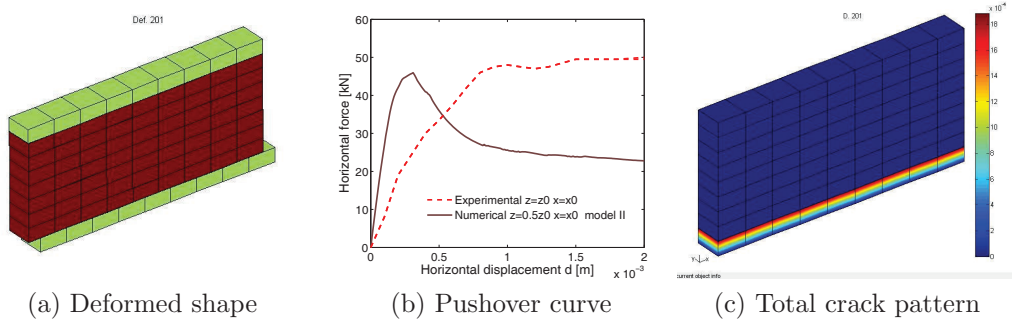


Figure 4.56: Results for wall with AS = 0.5 ($H = 0.5H_0$) model II

Deformed shape shows that all horizontal mortars on the first row slide. In this case as softening behavior is considered for cohesion of mortars, the shear strength of the mortars decreases by raising displacements and as a result horizontal elements experience shear sliding failure very soon. Thus, wall loses its strength under lateral displacements and in each step loses its cohesion and therefore more plastic shear displacement is undergone by the wall. As the height of the wall is divided by 2 the weight of the wall reduces and thus normal stress on the wall decreases. Therefore, the level of confinement is not sufficient to prohibit the shear sliding failure of the wall. As shown in pushover curve Figure 4.56(b), the wall with demi-height, AS (aspect ratio)=0.5 is stiffer than tested wall with AS=1 but at $d = 0.3mm$ the wall with AS=0.5 slips on its first row and its lateral strength decreases significantly.

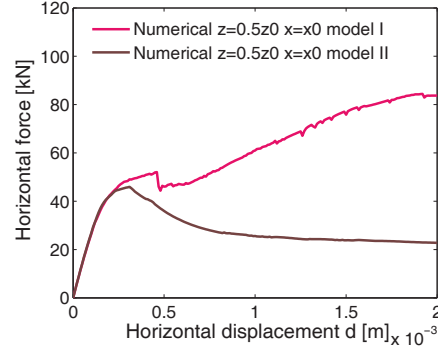


Figure 4.57: Load-displacement curves for wall using models I and II, $AS = 0.5$ ($H = 0.5H_0$)

Comparing pushover curve of two yield functions demonstrates that since model I cannot capture the reduction of mortar's cohesion, its lateral strength increases under incremental displacements. Since the results of model II are validated by comparing experimental evidence, the obtained pushover curve using this model is reliable.

(b) $H/L = H_0/1.5L_0$, $AS = 2/3$

The aspect ratio of this wall is less than 1 and is equal to $2/3$. This wall also is stiffer than the wall with aspect ratio equal to 1. Moreover, maximum shear load carried out by this wall is much greater than the other one. The wall slides and loses its strength in the lowest row of wall as shown in Figure 4.58. First, the corners of wall fail in tension and open. Then at $d = 0.69mm$ sliding shear failure is observed at all horizontal mortars in the first row and after that point the lateral strength which is carried out by the wall decreases considerably. Similar to previous case, reducing cohesion of mortar exponentially by plastic relative shear displacement and insufficient normal stress cause sliding shear failure in the wall. As shown in Figure 4.58(b), wall with $L = 1.5L_0$ sustains less strength than wall with $L = L_0$ after $d = 0.93mm$ because of its failure.

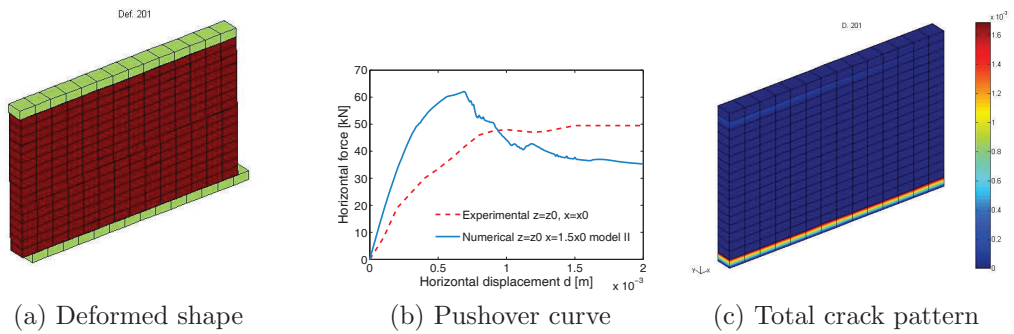


Figure 4.58: Results for wall with $AS = 2/3$ ($L = 1.5L_0$) model II

The softening behavior of mortar's cohesion and consequently decreasing shear strength of the wall cause sliding shear failure before formation of diagonal cracks in the wall. The previous yield function was not capable to reproduce this phenomenon so its results were not trustworthy. Pushover curves using different methodologies are compared in Figure 4.59. The local jump in pushover curve using model I corresponds to formation of diagonal zigzag cracks in the wall.

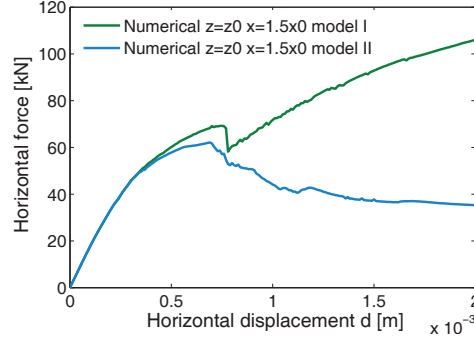


Figure 4.59: Load-displacement curves for wall using models I and II, $AS = 2/3$ ($L = 1.5L_0$)

(c) $H/L = H_0/2L_0$, $AS = 0.5$

The wall's length is multiplied by 2 in this case. Hence, the wall has aspect ratio equal to 0.5. Similar to previous cases, sliding of the wall in the lowest rows of mortars is the reason of the wall's failure and softening behavior of cohesion causes such failure. The normal stress on the wall also is insufficient to prevent sliding shear failure of mortars. Lateral load-displacement curve is shown in Figure 4.61(b). According to this figure, the initial stiffness and the maximum shear strength of the wall are about two times greater than the wall with aspect ratio 1. Sliding shear failure happens at displacement equal to $d = 0.64mm$ and reduces lateral strength of the wall significantly.

The load displacement diagrams using model I and model II are shown in Figure 4.61 to emphasize the importance of considering accurate yield function on predicting strength of the wall. As illustrated in this figure wall slides before formation of observed diagonal cracks in the results of model I (local drop in pushover curve). Sufficient normal stress on the wall may prevent sliding shear failure of the wall and causes the wall to carry out greater lateral loads.

Obtained pushover curves for different cases are drawn in the same figure to have a better comparison. The obtained force-displacement curve for the walls with aspect ratio less than 1 are shown in Figure 4.62(a). Same aspect ratio can be obtained for two walls with different dimensions. For example $AS=0.5$ may correspond to the wall whose height is divided by 2 or the wall whose length is multiplied by 2. As illustrated in Figure 4.62(a), all three walls are stiffer

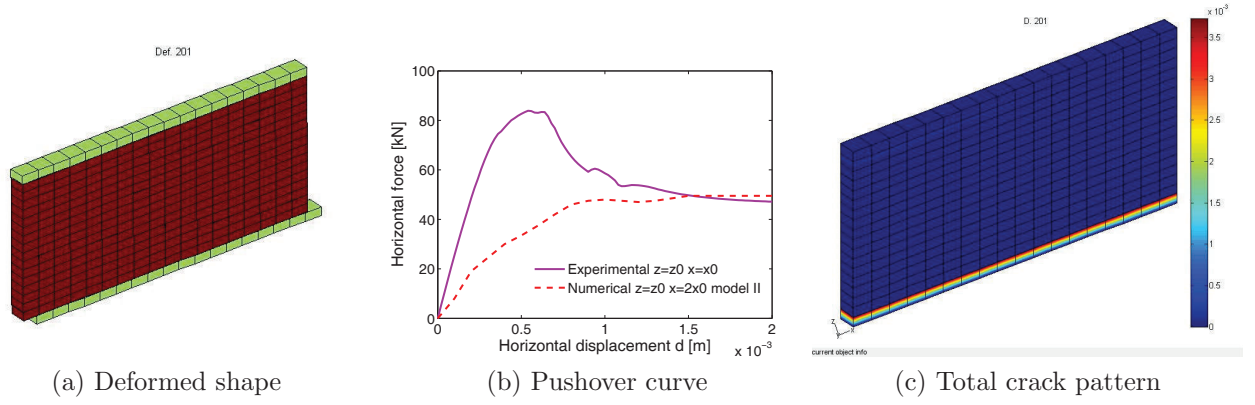


Figure 4.60: Results for wall with $AS = 0.5$ ($L = 2L_0$) model II

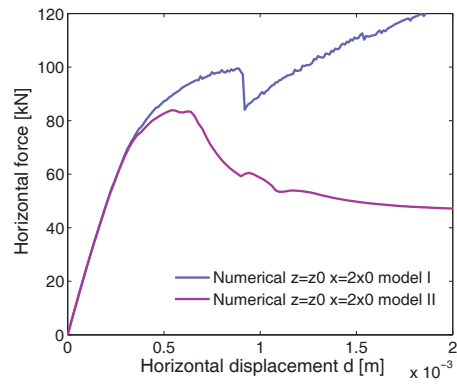


Figure 4.61: Load-displacement curves for wall using models I and II, $AS = 0.5$ ($L = 2L_0$)

than the wall with aspect ratio equal to 1. Moreover, walls with lower aspect ratio ($AS=0.5$) has the same initial stiffness and are stiffer than another wall with aspect ratio equal to 0.67 ($AS=2/3$). As shown in this figure, for same aspect ratio, wall with greater dimension carries out greater lateral loads. By the way, all three cases exhibit brittle behavior and their lateral strength decreases considerably due to sliding shear failure of horizontal mortars in the first row.

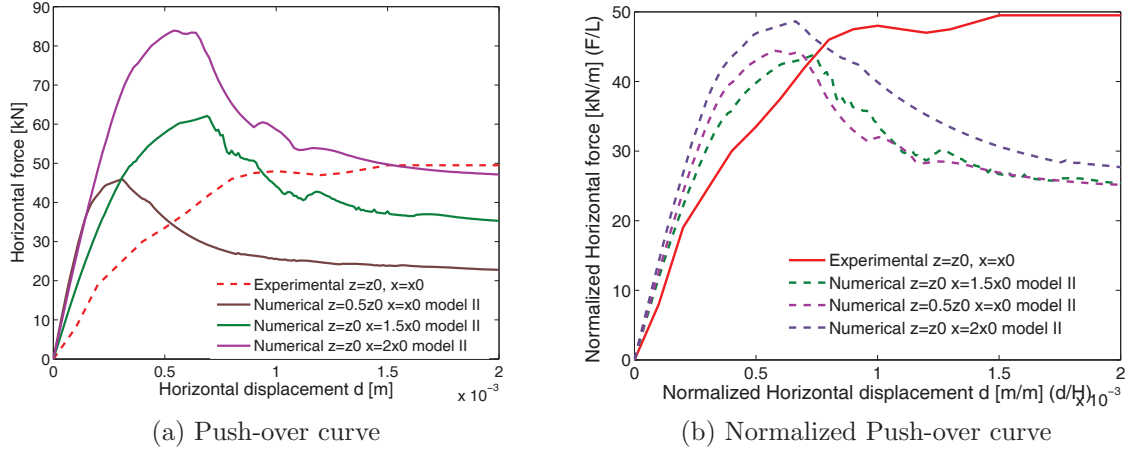


Figure 4.62: Load-displacement diagram for different aspect ratios $H/L < 1$

To make a better comparison, pushover curves are normalized. Hence, the obtained horizontal force is divided by its length and applied displacement to the wall is divided to the wall's length. The results are shown in Figure 4.62(b). As shown in this figure, wall with aspect ratio less than 1 are stiffer than wall with $AS=1$. Walls with lower aspect ratio withstand greater lateral strength. Moreover, for the wall with the same aspect ratio, wall with larger dimensions is stronger than another one. These walls have the brittle failure and at larger displacements exhibit much lower lateral strength than the wall with aspect ratio equal to 1.

By comparing the obtained results using model II and model I it is found that neglecting the softening behavior of cohesion in mortars may lead to the wrong results and obtaining wrong failure mechanism for the walls with aspect ratios less than 1. If sliding of the wall at the highest and lowest rows of mortars is prevented by using mortars with higher cohesion or applying sufficient vertical load to prevent such failure, diagonal cracks may appear in the wall and wall carries out much greater loads according to the response of model I. Another important parameter is the maximum length of cracks in the elements. The maximum length which is formed in the wall is 1.88 mm for first item with $AS=0.5$ ($H = 0.5H_0$) while its value is 1.67 mm and 1.7 mm for the wall with $AS=2/3$ ($L = 1.5L_0$) and $AS=0.5$ ($L = 2L_0$) respectively. Thus, for the wall with lower dimension, the length of cracks is higher than other walls with aspect ratio less than 1.

(b) Aspect ratio greater than 1

To create the wall with aspect ratio more than one, the wall's length is divided by 2 for a case and for the others the height of wall is multiplied by 1.5 and 2. Deformed shape, pushover curve and total crack pattern are shown for each case.

(a) $H/L = H_0/0.5L_0, AS = 2$

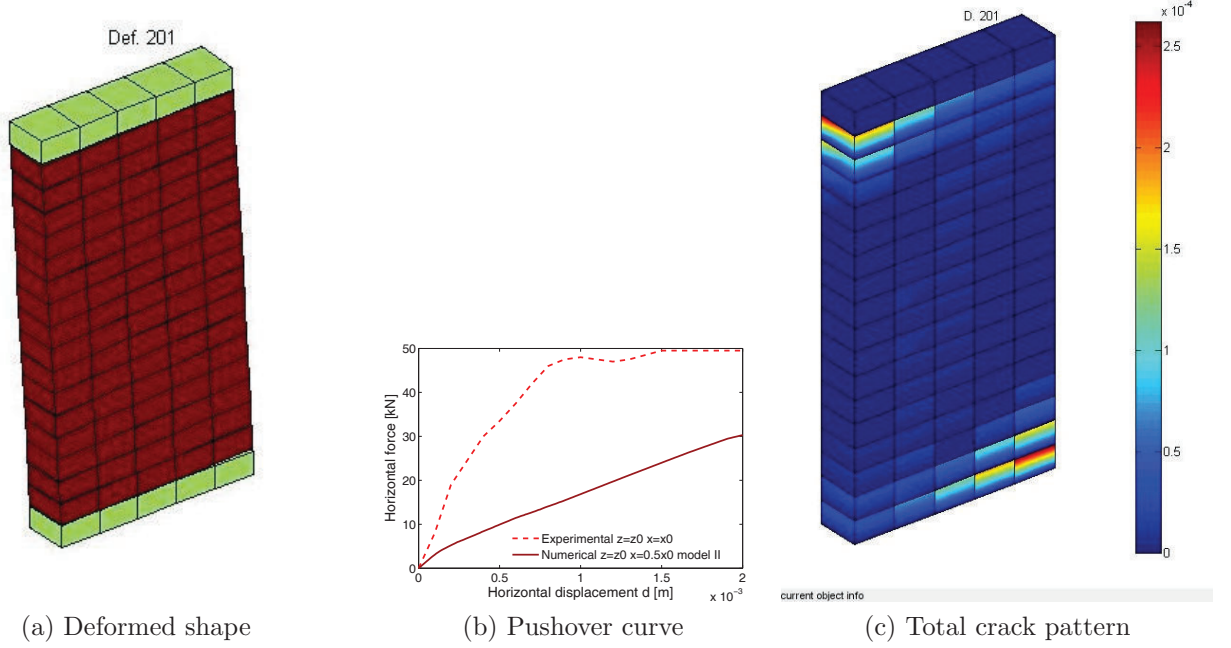


Figure 4.63: Results for wall with $AS = 2$ ($L = 0.5L_0$) model II

The same cracking pattern is obtained for the wall using models I and II. The reproduced initial stiffness for both yield functions is the same and is lower than that of wall with aspect ratio equal to 1. Comparison between pushover curves in Figure 4.64 shows that the same load-displacement curve is assessed by using models I and II until $d = 2mm$. No crushing failure takes place in wall corners up to this displacement. The initial stiffness of this wall is changed at $d = 0.17mm$ due to separation of the wall's corners from the wall due to opening of the horizontal joints. At this point wall loses its integrity so its stiffness decreases.

The horizontal mortars in the top left and bottom corners of the wall fail in tension and shear and no diagonal cracks appear in the wall with such properties as shown in Figure 4.63(c). The wall top right and bottom left are compressed but the normal stress in the wall is not enough to cause compression failure in the element.

(b) $H/L = 1.5H_0/L_0, AS = 1.5$

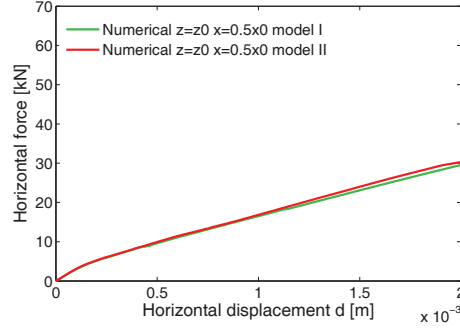


Figure 4.64: Load-displacement curves for wall using models I and II, $AS = 2$ ($L = 0.5L_0$)

In this paragraph, the performance of the wall with aspect ratio equal to 1.5 is studied. Wall is loaded up to $d = 4mm$ gradually. The deformed shape, pushover curve and total crack pattern are shown in Figure 4.65. As illustrated in this figure horizontal mortars at top and bottom rows as well as some elements in the next rows slide and open. Obtained deformed shapes using model II and model I are similar until $d = 2mm$. Figure 4.65(b) shows that the initial stiffness of the wall with aspect ratio greater than 1 is lower than that of the wall with aspect ratio equal to 1.

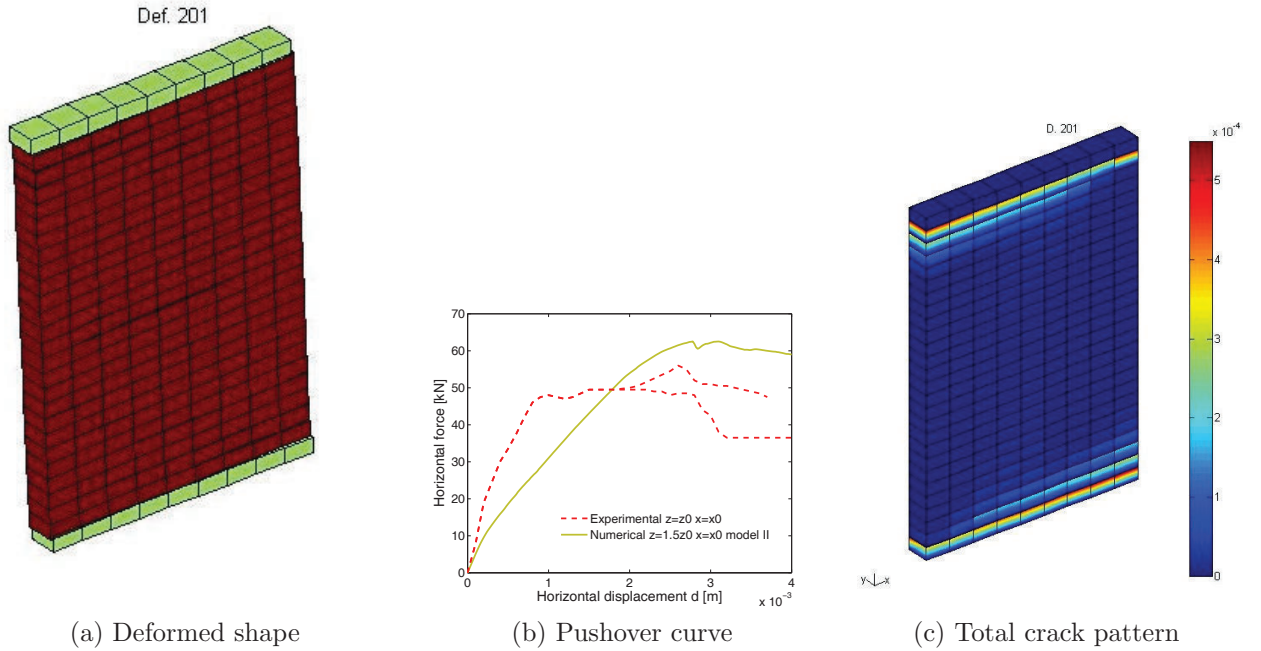


Figure 4.65: Results for wall with $AS = 1.5$ ($H = 1.5H_0$) model II

The load-displacement curve is explained as following. The initial stiffness of the wall first decreases at $d = 0.24mm$. At this point, horizontal elements at the top left and bottom right of the wall open and do not carry out any stress. Then, horizontal element at top left and bottom right of the wall begin to crash due to high normal stress and consequently their shear strength decreases by normal stress increment as shown in Figure 4.65 at $d = 2.67mm$. The previous model (model I) was not capable to reproduce such phenomenon. Thus, if the wall was analyzed using model I, the lateral load increased by normal stress increment after $d = 2.67mm$ and crashing of horizontal elements was not captured.

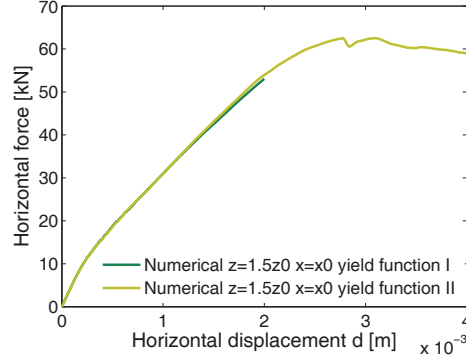


Figure 4.66: Load-displacement curves for wall using models I and II, $AS = 1.5$ ($H = 1.5H_0$)

Obtained load-displacement curves using model I and model II are compared at Figure 4.66. The curves are the same using either of yield functions up to $2mm$. Since compression failure happens at $d = 2.67mm$ in some of horizontal mortars and as maximum displacement which was applied to the wall in previous study was $d = 2mm$, it can be concluded that the results before compression failure are the same but after that, previous model cannot reproduce the actual behavior of the wall.

(c) $H/L = 2H_0/L_0$, $AS = 2$

In this case, the wall's height is multiplied by 2 and $d = 2mm$ displacement is gradually applied to the top nodes of the wall. Deformed shape, pushover curve and crack pattern are shown in Figure 4.67. Similar to previous cases, the mortars at top left and bottom right of the wall fail in shear and tension and thus slide and open. Diagonal cracks were not observed in the wall. According to pushover curve, no crushing happens in this wall up to $d = 2mm$. In this case, stiffness of the wall changes at $d = 0.3mm$ because of tension failure of horizontal mortars at the corners. The stiffness of the wall in this case also is much lower than the stiffness of wall with aspect ratio equal to 1 and that is because of decreasing the shear section of the wall, see Figure 4.67(b). The pushover curves for model I and model II are the same as explained before, see Figure 4.68.

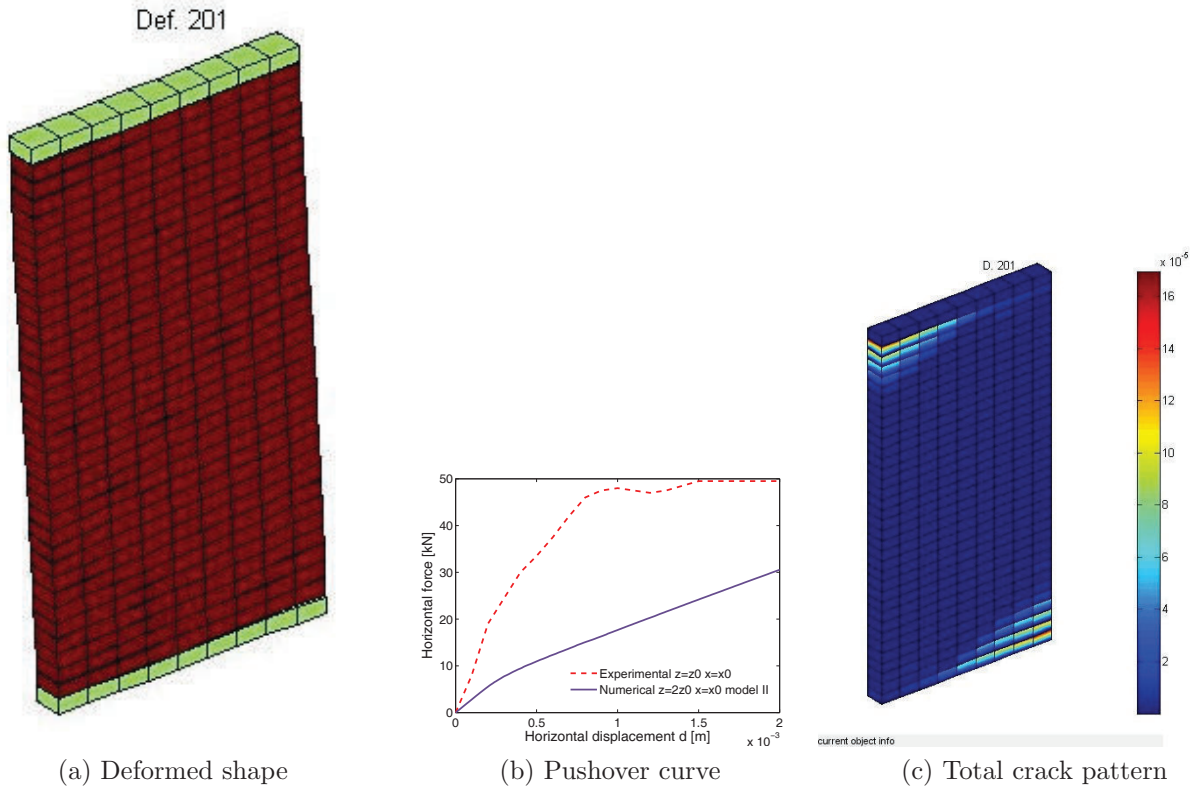


Figure 4.67: Results for wall with $AS = 2$ ($H = 2H_0$) model II

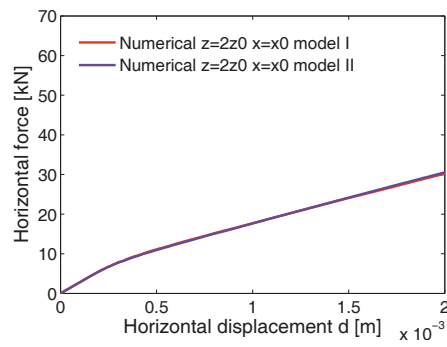
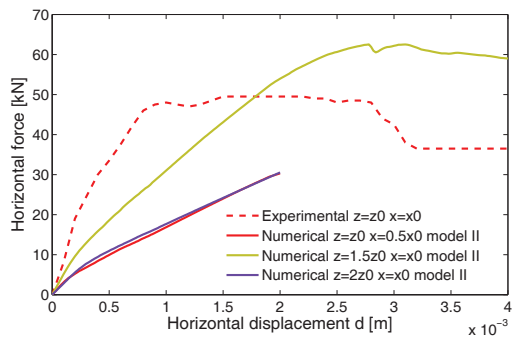


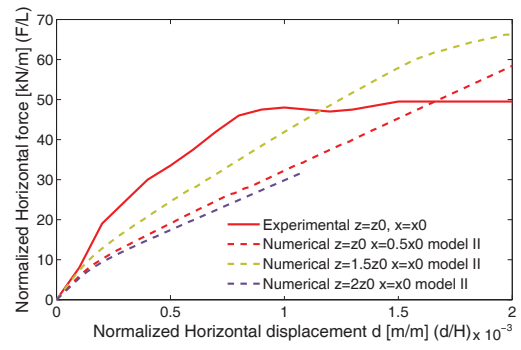
Figure 4.68: Load-displacement curves for wall using models I and II, $AS = 2$ ($H = 2H_0$)

The pushover curves for different cases with aspect ratio greater than 1 are drawn in a same figure to be compared together and with that of the wall with aspect ratio equal to 1, Figure 4.69(a). As explained before, whenever plastic displacements initiate in the interface element, the slope of pushover curve changes and for all of these cases, the opening and sliding of horizontal mortars in the corners cause change of stiffness at earlier steps. According to results of Figure 4.69(a), walls with aspect ratio greater than 1, have lower stiffness than walls with aspect ratio equal to 1 and the stiffness decreases with aspect ratio increment. For example wall with aspect ratio =1.5 have larger stiffness and sustain larger lateral loads than wall with aspect ratio = 2. Walls with the same aspect ratio have the same load-displacement curve but horizontal mortars in wall with lower dimension open and slide sooner. It's worth to know that the wall with aspect ratio equal to 1.5 carries out larger lateral load than wall with aspect ratio equal to 1 at larger displacements (after $d = 1.7mm$ to $d = 4mm$) although its stiffness is much lower than that of with $AS_{\zeta}1$ because the failure mechanisms are different in these case. It behaves in flexion while in the other case shear mechanism prevails. For the wall with $AS=1$ the main reason of wall's damage is formation of diagonal cracks in the wall which is together with crushing of some horizontal elements at the corner while for wall with $AS_{\zeta}1$, no zigzag cracks appear in the wall and wall fails due to crushing of horizontal elements at the corners. It should be noted that the walls with $AS=2$ are loaded up to $d = 2mm$ and the crushing failure does not happen in the wall up to this displacement. It is shown that the model can capture crushing failure of horizontal mortars for $AS=1.5$ which were loaded up to $d = 4mm$ while previous model was not able to reproduced that.

Figure 4.69(b) shows normalized pushover curve for different cases. As shown in labels, the horizontal force is divided by wall's length whereas displacement applied to the wall is divided by the height of the wall to find the strength of the wall regardless its dimensions. As shown in this figure, the initial stiffness and lateral strength of the walls decrease by aspect ratio increment. For the walls with the same aspect ratio, wall with greater dimensions carries out lower normalized lateral strength. The maximum length of crack in the wall with $AS=2$ and $L = 0.5L_0$ is 0.26 mm at $d = 2mm$, for the wall with $AS=1.5$ this parameter is 0.22 mm and for the wall with $AS=2$ and $H = 2H_0$, it is 0.16 mm. Thus, by increasing the dimension of wall the length of opening and sliding of horizontal mortars decreases. For the wall with the same aspect ratio, the normal stress on the lower mortars is greater for the one with larger dimension because of its weight, so those elements open and slide less than another one.



(a) Push-over curve



(b) Normalized Push-over curve

Figure 4.69: load-displacement diagram for different aspect ratios $H/L > 1$

4.7 Parametric study

In this section, effect of different parameters on the response of the model will be studied in order to have a better idea about the influence of each parameter on behavior of the wall and to find the most critical parameters, which change greatly the wall's performance. The aim of this study is to reproduce different failure mechanism of masonry wall and to find the reason of such failure. Hence, some parameters in horizontal and vertical interfaces are changed in order to investigate the variation in the wall's behavior. These parameters are: the cohesion C_0 , tensile strength f_{t0} , compression strength f_{c0} , normal stress on the wall σ_{n0} and slope of shear-compression part of yield function θ . Moreover, influence of fracture energy of modes I, II and III namely GI , GII and $GIII$ are studied in Appendix B. Finally the influence of normal stress on the walls will be studied. In this section, four values are chosen for each parameter and results are compared to the original one.

4.7.1 Cohesion of mortars

Four different values are chosen for C to investigate the wall's behavior under monotonic loading: $C_0 = 9.5e4Pa$, $C_0 = 1.5e5Pa$, $C_0 = 5.5e5Pa$ and $C_0 = 7.5e5Pa$ whereas the tested wall has $C_0 = 3.5e5Pa$. Therefore, the performance of these five cases can be compared here in terms of deformed shape, load-displacement curve and profile of cracks. In order to have a better comparison the same scale is used for the length of cracks. Deformed shape and crack pattern related to each case are illustrated in Figure 4.70.

As can be seen in this figure, for walls with lower values of cohesion for mortar, sliding shear failure happens at two other rows in addition to top and bottom horizontal mortars. Diagonal cracks are also formed in the wall in these cases. In the cases with $C_0 = 9.5E04Pa$ and $C_0 = 1.5E05Pa$, first mortars at the corners of the wall open and slide. Then, diagonal cracks appear in the wall and after that zigzag cracks cause sliding failure at the horizontal mortars next to them as shown in Figure 4.70. The difference between walls with $C_0 = 9.5E04Pa$ and $C_0 = 1.5E05Pa$ is that for the first one as the cohesion of mortars is lower than the second one, the top row of mortars slides more and the length of cracks in two additional rows is lower than another one. By increasing the cohesion of mortar for the wall with $C_0 = 3.5E05Pa$ the sliding failure of middle rows disappears and diagonal crack patterns become predominant. Moreover in this case, horizontal mortars at the top and bottom of the wall slide and open. As shown in Figure 4.70(h) and (j) for the wall with high cohesion, no diagonal cracks are formed in the wall and walls fail due to shear sliding failure of top horizontal mortars. The length of cracks and their distribution in the wall decrease for the wall with $C_0 = 7.5E05Pa$ rather than the wall with $C_0 = 5.5E05Pa$. Horizontal mortars at the lower row in the wall slide more than the other ones.

By comparing the load-displacement curves and paying attention to failure of the walls, it can be

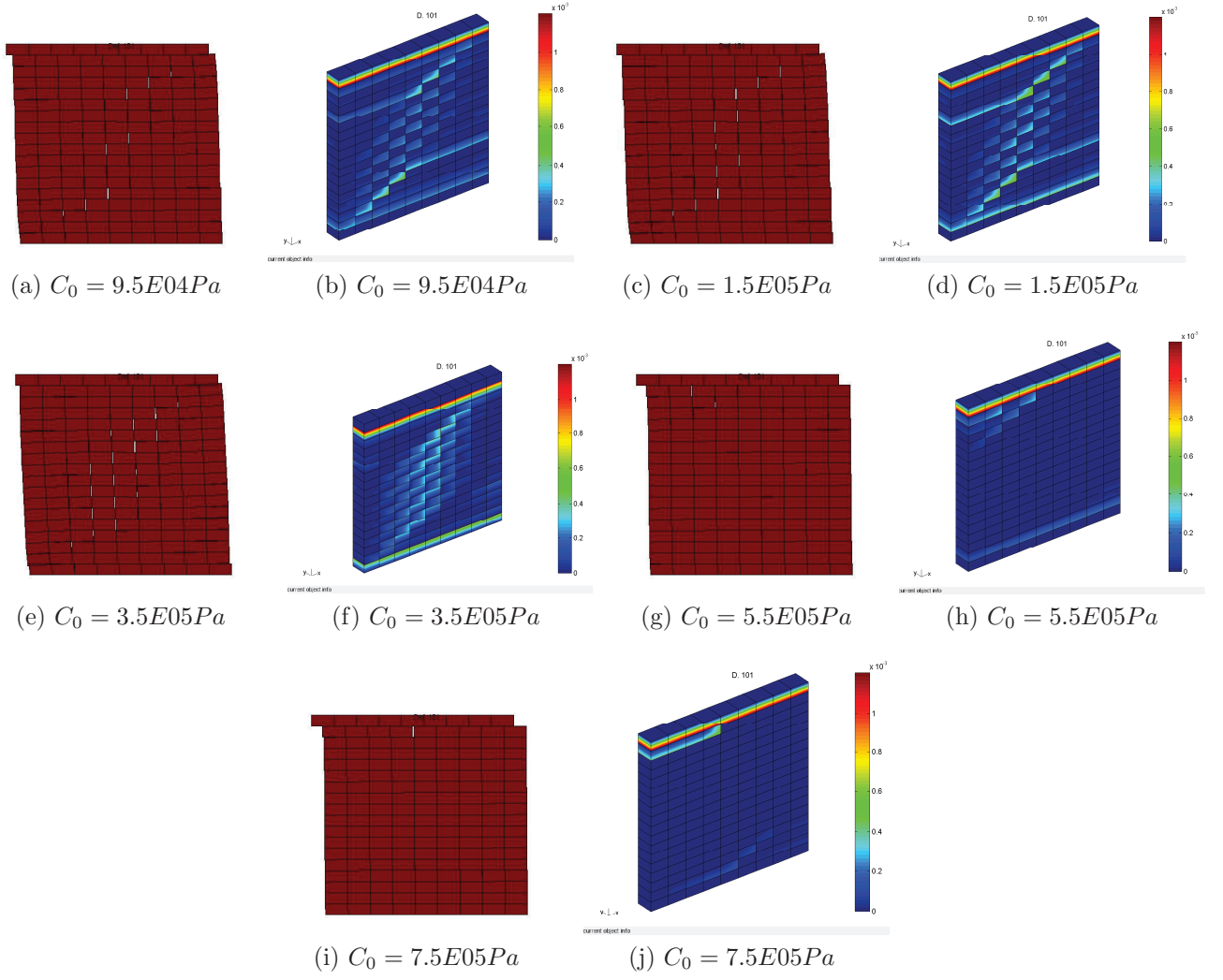


Figure 4.70: Deformed shapes and crack patterns in the walls with different mortars' cohesion at $d = 4mm$

assessed that although increasing the cohesion of mortars enables the wall to undergo higher shear stresses but for the walls with high cohesion brittleness of the wall also increases. The significant drift in pushover curves of walls with $C_0 = 5.5E05Pa$ and $C_0 = 7.5E05Pa$ corresponds to the sliding shear failure of top horizontal mortars. The first reduction in stiffness of the walls with $C_0 = 9.5E04Pa$ and $C_0 = 1.5E05Pa$ corresponds to formation of diagonal cracks in the wall while the sliding shear failure of mortars adjacent to diagonal cracks causes the reduction of shear strength of the wall after $d = 1.6mm$ and $d = 1.8mm$ respectively. Hence, it should be noted that although the increment of cohesion increases the lateral strength of the wall but it may increase the brittleness of masonry wall under specific condition and the type of failure cannot be guessed easily.

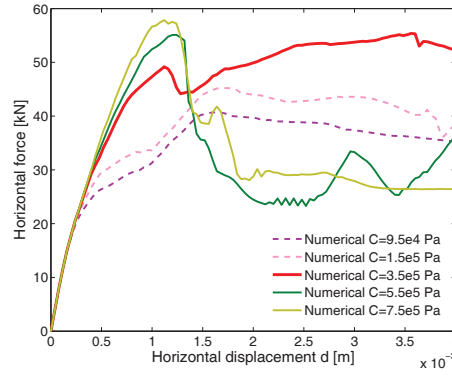


Figure 4.71: Pushover curves for the walls with different cohesion

As shown in Figure 4.72, the wall is composed of 17 rows and 8 columns. To find the pattern of cracks and find its relation to the material properties, the length of cracks in horizontal elements in each row as well as vertical elements and brick-middle elements in each column are summed and compared. The yellow lines illustrate the location of brick-middle interfaces in each column which dark lines correspond to the mortars. Sliding and opening of horizontal and vertical cracks are demonstrated separately. Then, for example, the length of sliding cracks in all horizontal interfaces are summed and compared in a separate figure.

Figure 4.73 shows the length of cracks in different types of elements at $d = 2mm$. According to Figure 4.73(a) the length of sliding cracks at the top rows are greater than the other ones in all cases. In the middle rows, sliding of cracks decreases with cohesion increment. This figure shows that for two walls with lower cohesion, the length of cracks in different rows are more similar and the maximums belong to rows 1, 5, 13 and 17. According to Figure 4.73(b), the horizontal mortars near to the edges of the wall open more than the others and that opening is greater at the bottom rows because of overturning moment. The opening of horizontal interfaces first increases by cohesion increment but for two great ones its value decreases.

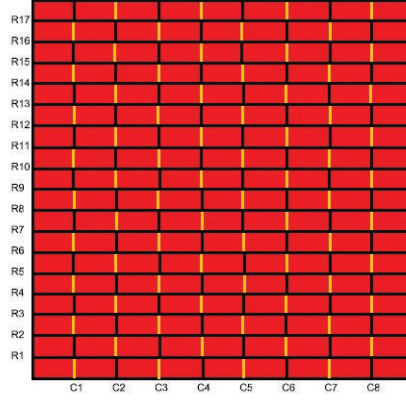
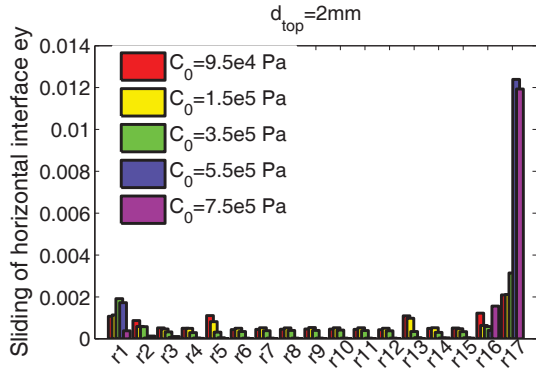
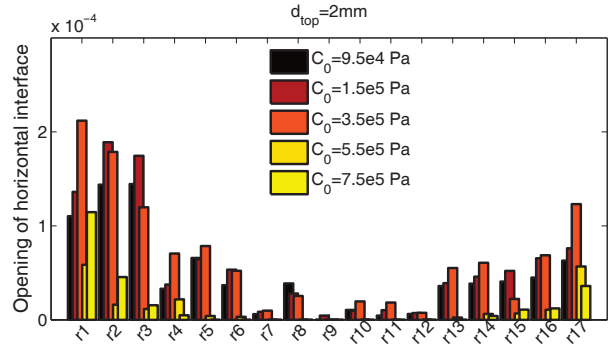


Figure 4.72: Numerating rows and columns in the wall

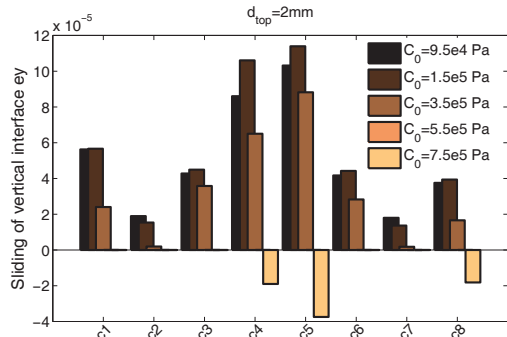
Sliding of vertical elements is larger at the middle columns for different cases. The distribution of sliding of vertical mortars can represent formation of diagonal cracks in the wall. The walls with $C_0 = 9.5e04Pa$, $C_0 = 1.5e05Pa$ and $C_0 = 3.5e05Pa$ which have normal distribution, experience diagonal cracks. Length of sliding cracks in vertical elements in the walls with higher cohesion decreases, see Figure 4.73(c). Figure 4.73(d) represents the length of opening in vertical mortars. As explained before, as the distribution of opening cracks in three first cases is approximately normal, diagonal cracks have formed in the wall. The length of opening decreases with cohesion increment. The opening of vertical elements in $C_0 = 1.5e05Pa$ is greater than for $C_0 = 9.5e04Pa$ because as explained before, the top horizontal mortars slide less and instead vertical interfaces open more. The bricks at the edges fail more in tension in cases with lower cohesion. Moreover, the length of opening reduces with cohesion increment and for the walls with $C_0 = 5.5e05Pa$ and $C_0 = 7.5e05Pa$ no bricks in the wall fail in tension. Sliding of horizontal elements together with opening of vertical elements cause failure in the walls with lower cohesion whereas high total length of sliding cracks in horizontal elements in walls with greater cohesion represents brittle failure in the wall.



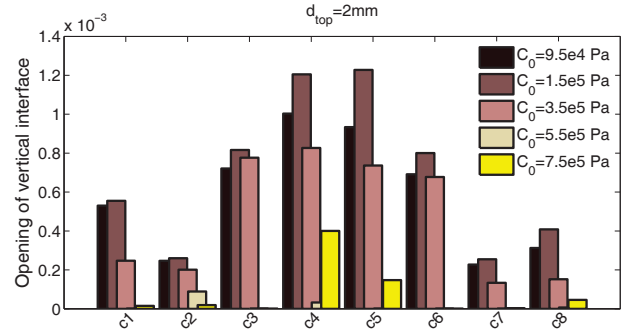
(a) Sliding of horizontal mortars



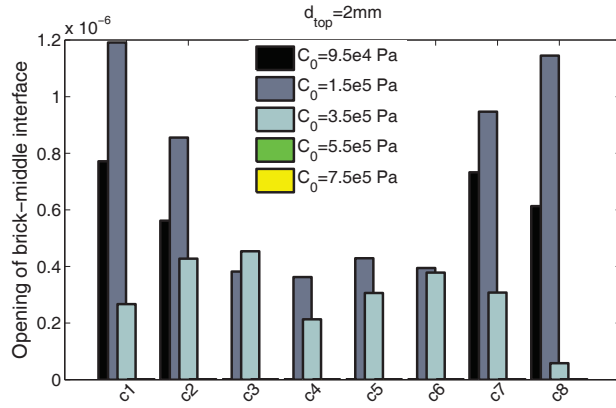
(b) Opening of horizontal mortars



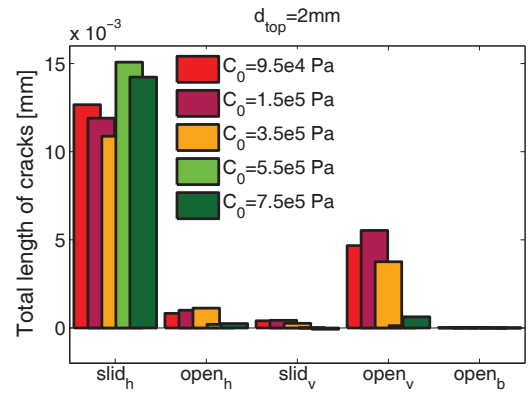
(c) Sliding of vertical mortars



(d) Opening of vertical mortars



(e) Opening of brick interfaces



(f) Total length of cracks

Figure 4.73: Length of cracks in different types of elements for walls with different cohesion at $d = 2mm$

4.7.2 Tensile strength of mortars

Five different values for tensile strength of mortars have been studied: $50kPa$, $85kPa$, $200kPa$, $450kPa$ and $650kPa$. According to the results of modeling which are shown in Figure 4.76, by decreasing tensile strength of mortars for case with $f_{t0} = 5E04Pa$ more horizontal mortars fail in tension and failure happens sooner. Hence, the horizontal mortars in the top of wall lose their strength very soon and suffer sliding shear failure. The load displacement curve shows the wall undergoes less shear strength. In second case, the tensile strength of mortars increases to $f_{t0} = 8.5E04Pa$. Figures 4.76(c) and (d) show that sliding of the horizontal joints as well as opening of vertical joints at the bottom left of the wall cause failure in the wall. In this case vertical mortars open sooner and their length of opening is greater and their opening causes sliding shear failure at the adjacent horizontal mortars. The first drop in pushover curve at $d = 0.9mm$ corresponds to the formation of diagonal cracks in the wall whereas at $d = 2.88mm$ wall loses its lateral strength significantly due to sliding shear failure of horizontal mortars at the bottom part of the wall.

In the walls with higher tensile strength with $f_{t0} = 4.5E05Pa$ and $f_{t0} = 5.5E05Pa$, high tensile strength of mortars prevents tension failure of mortars and their opening. Since failure happens at weakest planes, top row and bottom row of mortars undergo sliding shear failure in these two cases respectively. It should be noted that just increasing a parameter does not always lead to a better response and increasing tensile strength of mortars highly may cause the brittle failure in the wall. Figure 4.75 represents the load-displacement curves for wall with different tensile strengths for the mortars. By increasing the tensile strength for first three cases the lateral strength of the wall increases whereas for the other cases sliding shear failure of a row of mortar causes brittle behavior of masonry wall.

As shown in Figure 4.76, except walls with $f_{t0} = 8.5e4Pa$ and $f_{t0} = 2.5e5Pa$ the other walls undergo sliding shear failure at the top or bottom rows of mortars. Opening of horizontal mortars at the wall's edges are greater than the middle of wall. Horizontal mortars in walls with sliding shear failure open less than the other walls. The normal distribution of opening and sliding of vertical mortars in walls with $f_{t0} = 8.5e4Pa$ and $f_{t0} = 2.5e5Pa$ represent formation of diagonal cracks in the walls. Bricks also do not fail in tension in walls with sliding shear failure as shown in Figure 4.76. The tension failure of bricks decreases by increasing tensile strength of the mortars. Finally, Figure 4.76(f) shows that walls with higher opening length in vertical mortars and sliding of horizontal mortars react better under monotonic loads. Cracks are distributed more smoothly in walls with higher lateral strength while the cracks are concentrated in specific elements in walls with brittle behavior.

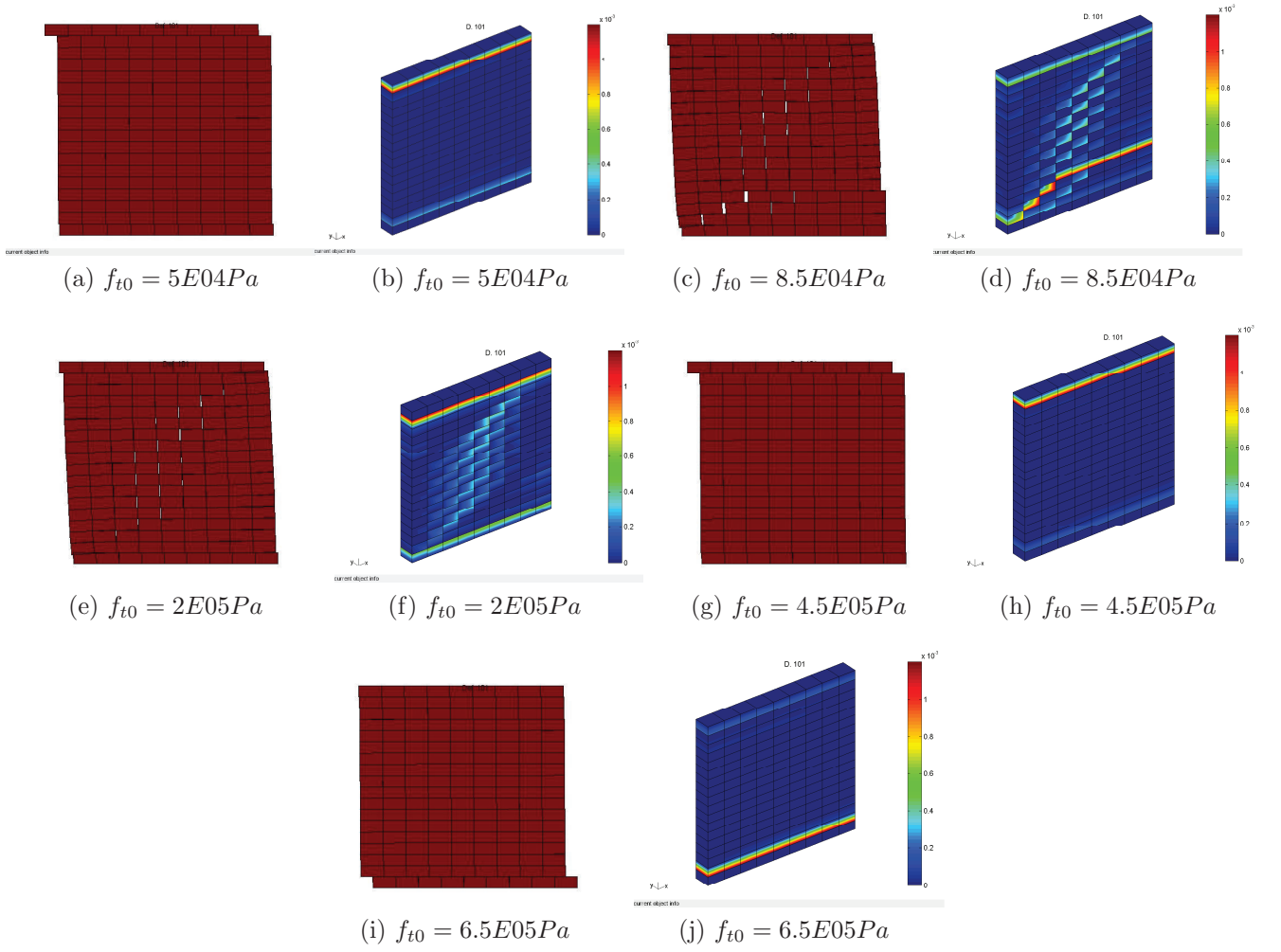


Figure 4.74: Deformed shapes and crack patterns in the walls with different tensile strengths at $d = 4mm$

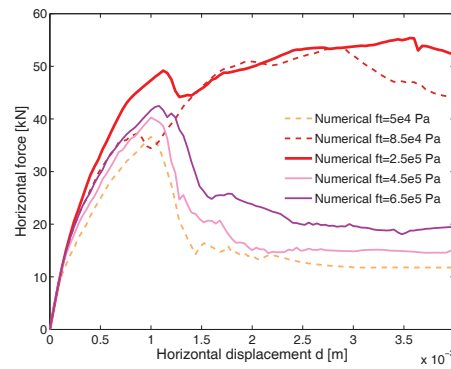
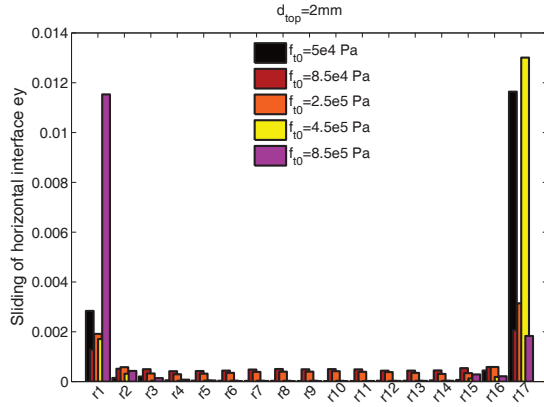
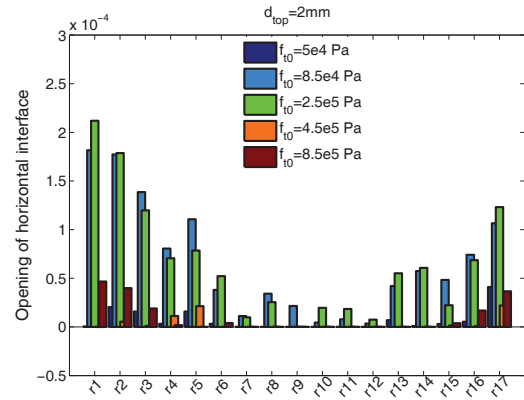


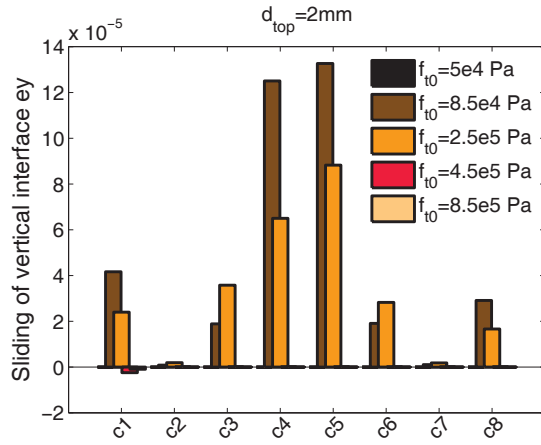
Figure 4.75: Pushover curves for the walls with different tensile strengths



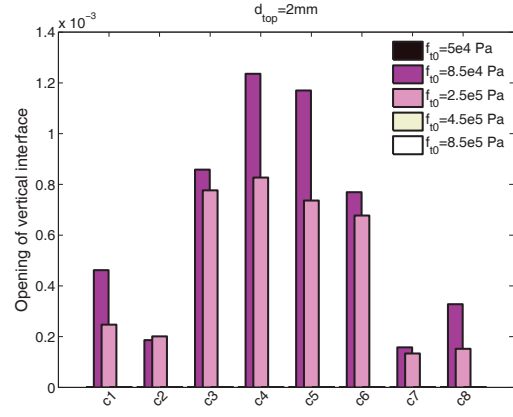
(a) Sliding of horizontal mortars



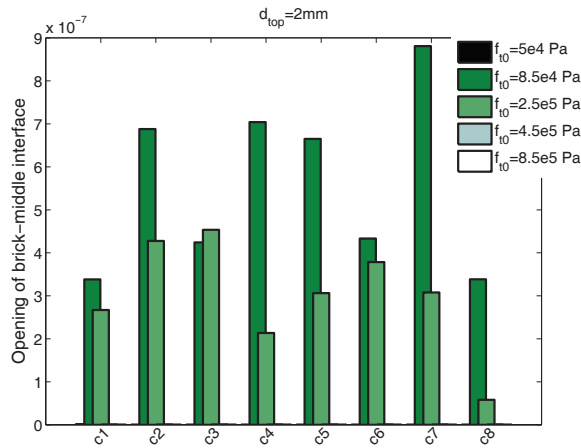
(b) Opening of horizontal mortars



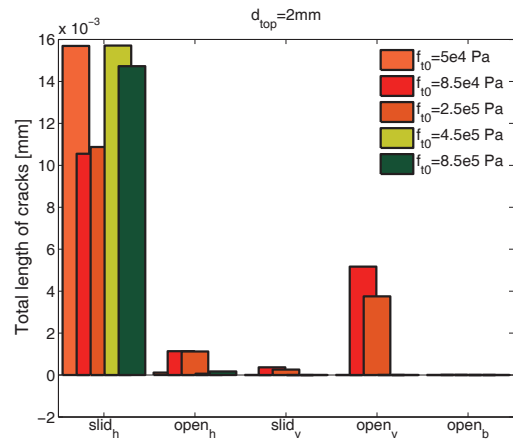
(c) Sliding of vertical mortars



(d) Opening of vertical mortars



(e) Opening of brick interfaces



(f) Total length of cracks

Figure 4.76: Length of cracks in different types of elements for walls with different tensile strengths at $d = 2mm$

4.7.3 Compression strength of masonry

The low value for f_{c0} causes the corner joints to fail in compression sooner and consequently wall loses its shear strength and undergoes sliding shear failure at its top rows. In cases 1 and 2 with lower compression strength, horizontal mortars open at the corners first. Then, diagonal cracks appear in the walls whereas after a while sliding shear failure of top row becomes predominant and walls lose their lateral strength a lot. As there is a relation between lateral strength of the wall and compression strength of masonry, increasing compressive strength of masonry causes the wall to undergo more lateral loads. Masonry wall with high compressive strength carries out higher lateral strength and crushes due to higher deformations. The crack profile is diagonal and wall experiences the compression failure. As shown in Figure 4.77(h) and (j) the diagonal cracks are formed in the wall. Moreover, the compression toes of the wall experience crushing.

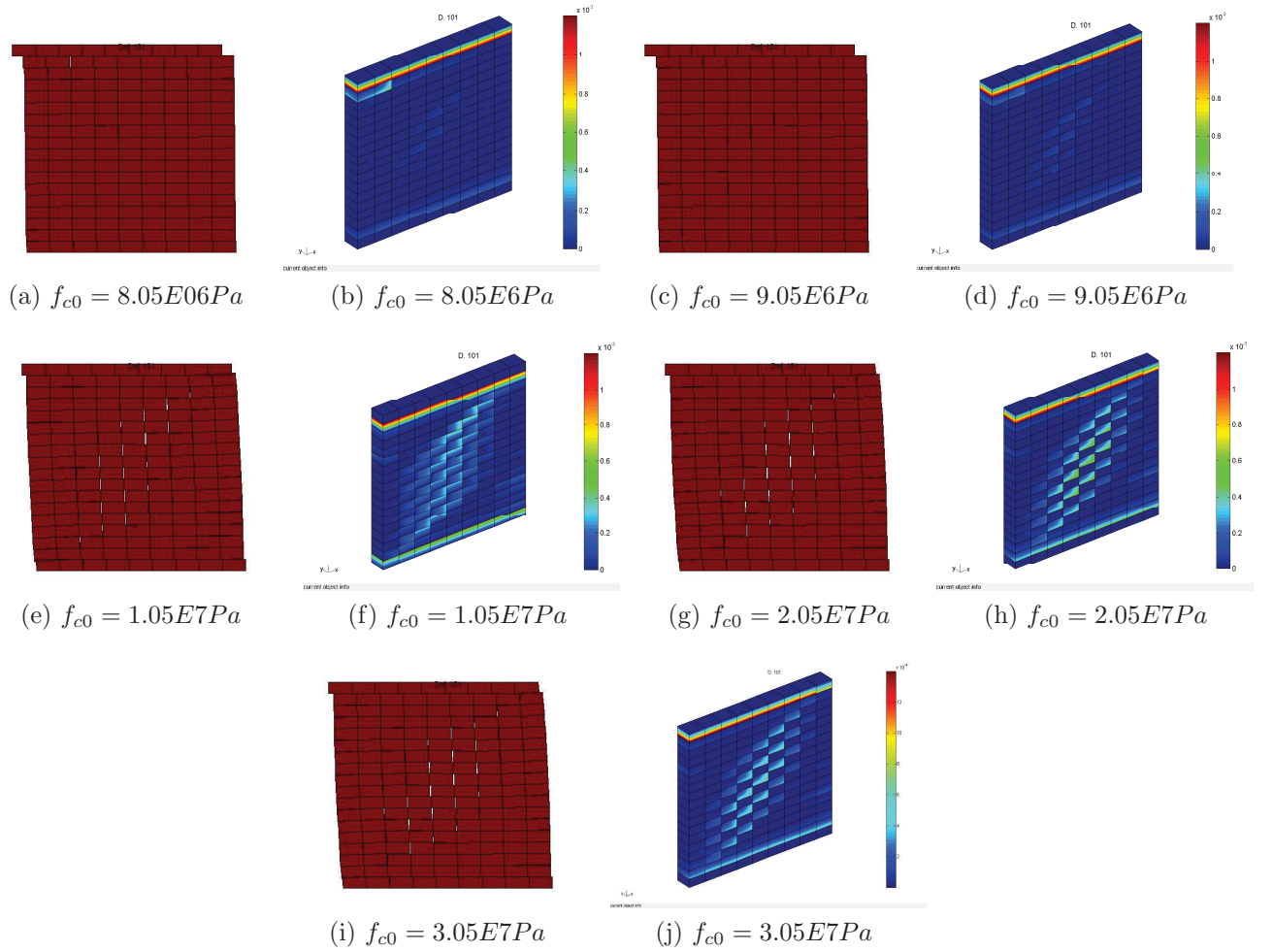


Figure 4.77: Deformed shapes and crack patterns in the walls with different compressive strengths at $d = 4mm$

Lateral load-displacement curves for different walls are shown in Figure 4.78. According to this

figure, increasing the compression strength of masonry improves wall's performance and causes the wall to endure more shear stresses. As shear strength of masonry depends on its compression strength, the masonry walls with low compressive strength loose their lateral strength sooner and fail due to sliding shear failure. Hence, the failure mechanism of masonry wall depends on its compressive strength. The responses of the last two cases are the same and both fail in compression at $d = 3.4mm$.

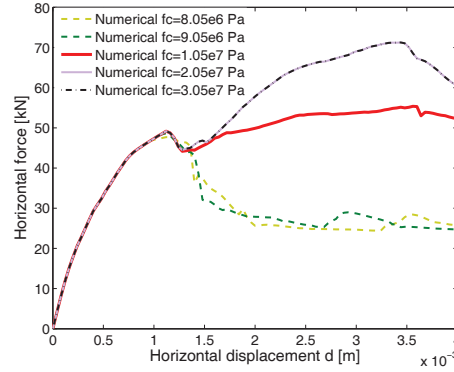
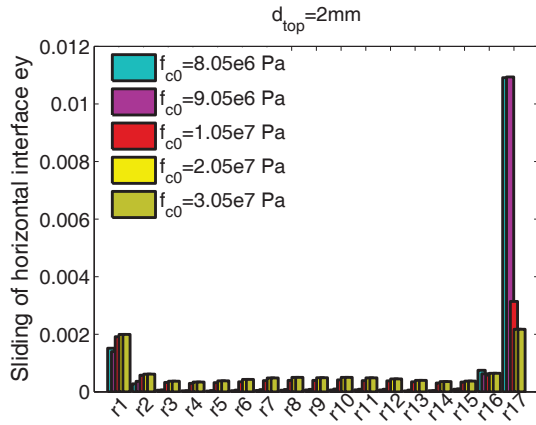


Figure 4.78: Pushover curves for the walls with different compressive strengths

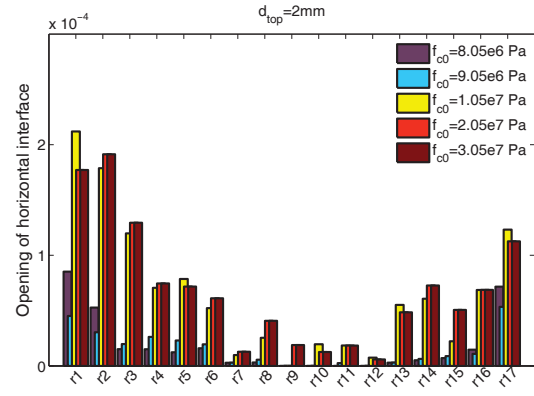
The length of cracks in different walls with different compressive strength shows that the sliding of horizontal elements decreases by compression strength increment in upper row of mortar. Opening of vertical elements increases also by using mortar elements with high compressive strength. Moreover, vertical elements also slide and open more in these cases. The length of cracks in the walls with higher compressive strength is approximately uniformly distributed. The walls with higher compressive strength have better performance because the difference between total length of opening in vertical elements and sliding in horizontal interfaces is less than other cases. Therefore, better performance belongs to a wall which uses its maximum capacity and the total length of cracks in horizontal and vertical elements are closer.

4.7.4 Initial normal load

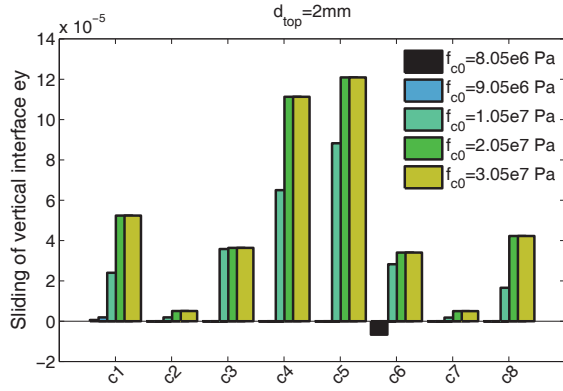
In this section, effect of initial normal load on behavior of masonry wall will be investigated. Hence, different vertical stresses such as $\sigma_{n0} = 0.05MPa$, $\sigma_{n0} = 0.2MPa$, $\sigma_{n0} = 0.3MPa$, $\sigma_{n0} = 1.21MPa$ and $\sigma_{n0} = 2.12MPa$ are applied to the same wall. The pushover curves for $\sigma_{n0} = 0.3MPa$, $\sigma_{n0} = 1.21MPa$ and $\sigma_{n0} = 2.12MPa$ are compared with the experimental data in the literature [60]. The results of first case with $\sigma_n = 0.05MPa$ show that when there is no sufficient normal load on the wall, diagonal cracks are not formed and the wall sustains sliding shear failure at top horizontal mortars and exhibits it in a brittle manner. Softening behavior of mortars in cohesion also causes the wall to loose more shear strength under displacements and



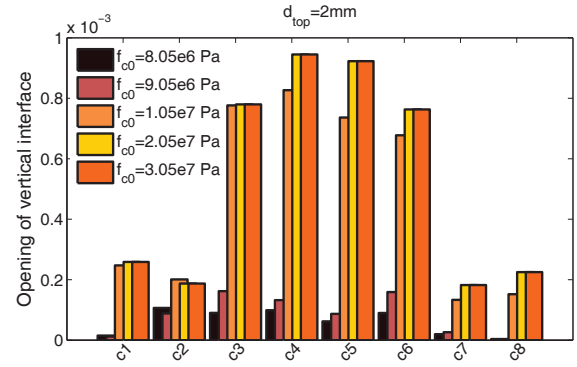
(a) Sliding of horizontal mortars



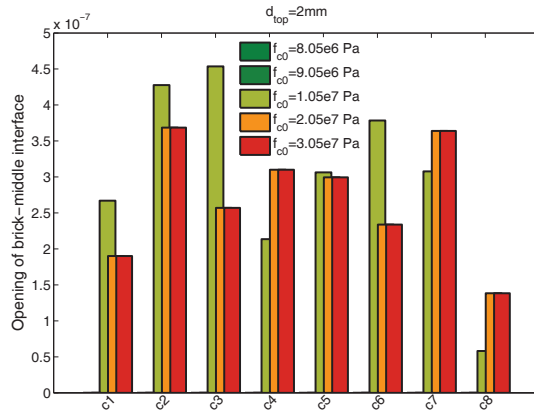
(b) Opening of horizontal mortars



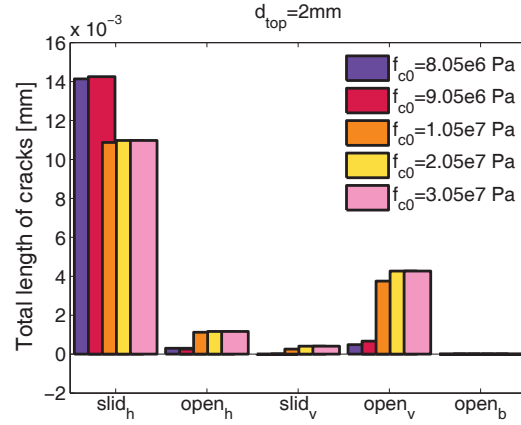
(c) Sliding of vertical mortars



(d) Opening of vertical mortars



(e) Opening of brick interfaces



(f) Total length of cracks

Figure 4.79: Length of cracks in different types of elements for walls with different compressive strengths at $d = 2mm$

experiences sliding shear failure sooner. In the second wall with $\sigma_n = 0.2MPa$ the maximum shear strength of wall is greater than the previous case. In this case, diagonal cracks form in the wall but sliding shear failure of top and bottom rows of mortars causes the wall to undergo low shear strength after $d = 2.1mm$.

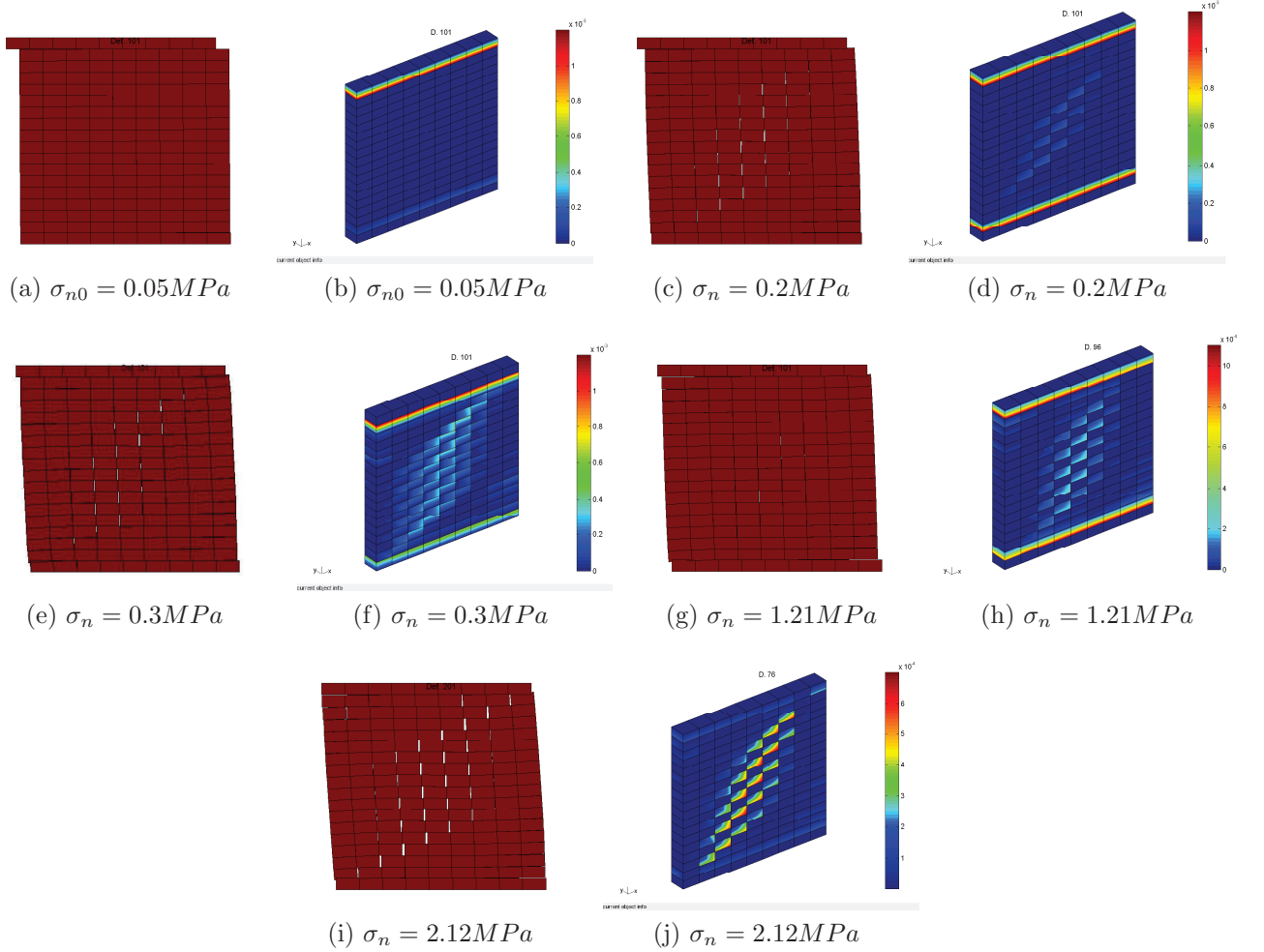


Figure 4.80: Deformed shapes and crack patterns in the walls with different initial normal stresses at $d = 4mm$

Comparing the numerical results and experimental evidences in case 3 with $\sigma_{n0} = 1.21MPa$ reveals that the model can reproduce the load-displacement curve and the pre- and post-peak behavior of the wall well. The crack pattern in the model is shown in Figure 4.80(h) but no horizontal cracks at the top and bottom mortars are observed in test's results whereas in numerical model top and bottom mortars slide and horizontal cracks appear at these locations. This discrepancy may happen due to difference between applying load in real case and numerical one. In the last wall with $\sigma_{n0} = 2.12MPa$ there is a good agreement between results and experimental

data as shown in Figure 4.80(j). As shown in this figure, diagonal cracks are reproduced well and are predominant. In pushover curve the initial stiffness of the wall was not obtained well. That is because of this fact that after the crushing of element due to high compression it still carries out the loads and stresses in the element do not set to zero. The softening behavior assessed well in the model but maximum load is underestimated 8% in numerical model. It should note that in this case although the wall undergoes larger lateral loads but behavior of wall is brittle after formation of diagonal cracks in the wall and it loses more lateral strength than previous cases.

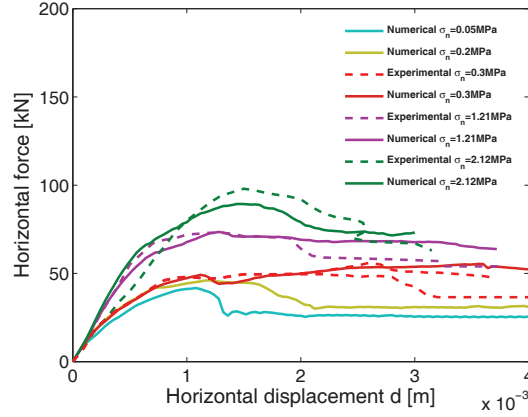


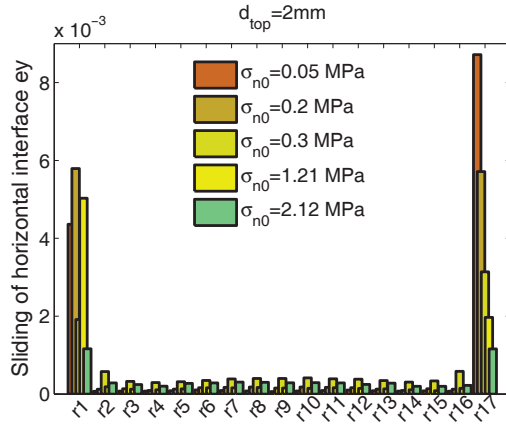
Figure 4.81: Pushover curve for the wall with different σ_n

As represented in Figure 4.81, by increasing the normal pressure on the wall, the stiffness of wall increases (except the last case) and wall carries out greater lateral loads. Diagonal cracks appear in the wall with higher normal stress and sliding of horizontal mortars decreases. On the other side, walls with low level of confinement for example the wall with $\sigma_n = 0.05MPa$ fail due to sliding shear failure of top horizontal mortars and they exhibit brittle behavior. Thus as shown in Figure 4.80, the wall with low level of confinement, the sliding failure is predominant while in the wall with higher applied normal stress the sliding of top and bottom rows are almost vanished and diagonal crack pattern becomes predominant. Increasing the normal stress prevents opening of horizontal elements and increases the shear strength of the wall. Hence, this parameter has a key role in performance of masonry wall under in-plane loading. The length of cracks in different cases are shown in Figure 4.82. Sliding of horizontal cracks decreases by increasing normal stress. Moreover according to Figure 4.82(b) opening of horizontal elements also decreases by normal stress increment and even for the wall with $\sigma_{n0} = 2.12MPa$ negative displacements create in the elements. Sliding of vertical elements is decreased by initial load increment in the walls related with diagonal crack pattern. Figure 4.82(e) shows that the bricks in the walls with lower initial normal stresses do not experience tension failure. As explained before, the length of opening in vertical elements in addition to sliding of horizontal elements can demonstrate the type of failure and maximum lateral strength of the wall. Best performance belongs to the wall with $\sigma_{n0} = 2.12MPa$ in which the total length of cracks in horizontal elements (sliding) and vertical

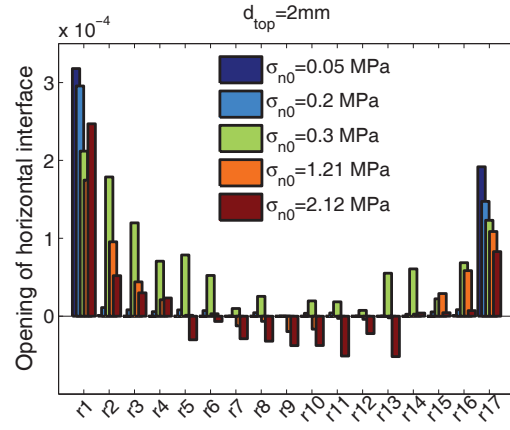
elements (opening) are close but in the first case the difference between these values are high and wall exhibits brittle performance.

4.7.5 Captured crack patterns

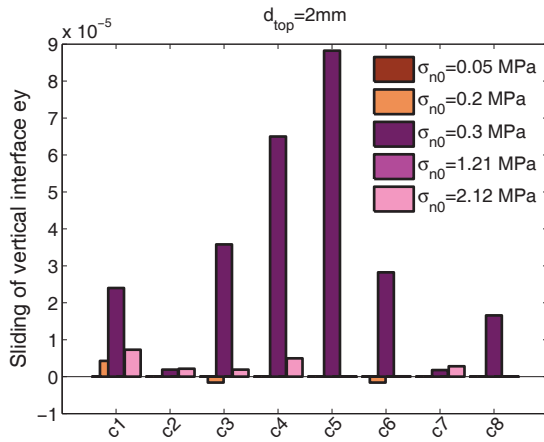
In this section different failure mechanisms which were captured by numerical modeling and their characteristics are demonstrated in the following. These results are valid for the mentioned boundary condition. A collection of properties needs to enhance the behavior of wall. For example as shown before using mortars with very high cohesion value may cause the brittle behavior. As explained in this case, the displacements applied at the top row of bricks forces the top row into nonlinear region sooner and consequently softening behavior in shear strength which is accompanied by opening of vertical elements causes sliding shear failure at top row. As a results wall exhibits brittle behavior at the top row and endures sliding failure as opposed to distributed cracks along the diameter of the wall.



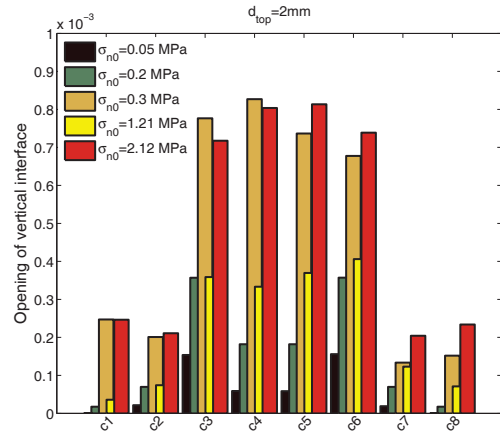
(a) Sliding of horizontal mortars



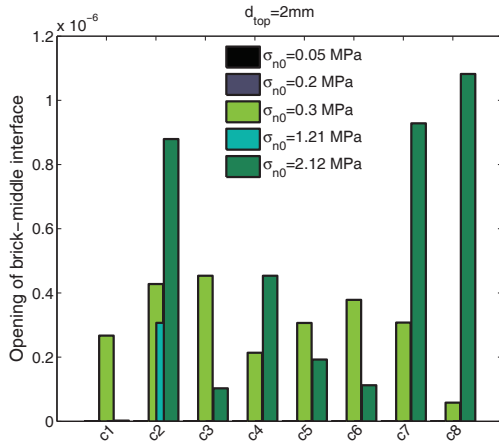
(b) Opening of horizontal mortars



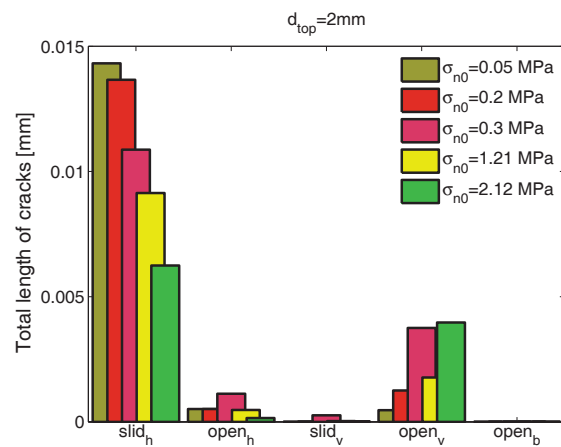
(c) Sliding of vertical mortars



(d) Opening of vertical mortars

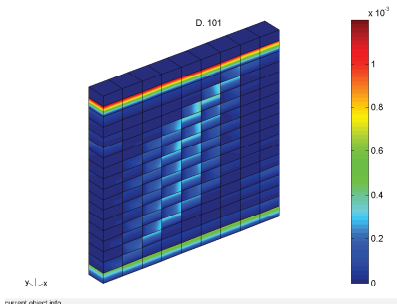
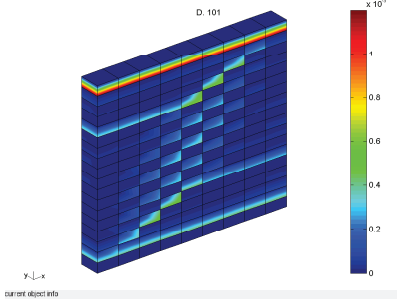


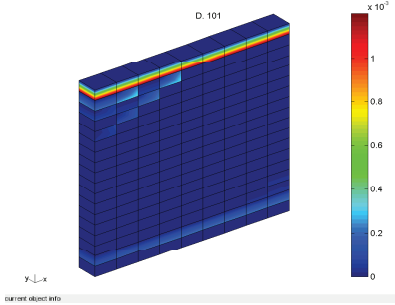
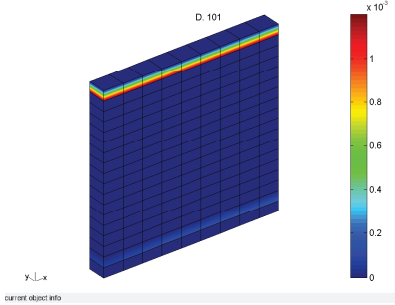
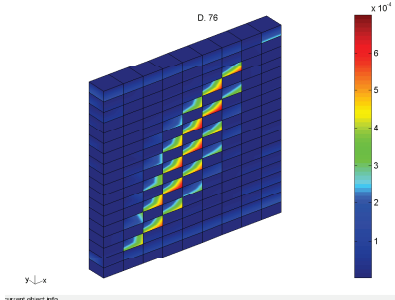
(e) Opening of brick interfaces



(f) Total length of cracks

Figure 4.82: Length of cracks in different types of elements for walls with different initial vertical stresses at $d = 2mm$

Cracking profile	Specifications	Observed in:
	<ul style="list-style-type: none"> • Sliding of horizontal mortars at top and bottom rows • Formation of Diagonal cracks • Crushing of horizontal mortars at the corners of wall • Ductile behavior 	<ul style="list-style-type: none"> • The tested wall • The walls with high compression strength
	<ul style="list-style-type: none"> • Sliding of horizontal mortars in different rows • Formation of Diagonal cracks which are more severe at top and bottom parts of the wall • Approximately tri-linear pushover curve 	<ul style="list-style-type: none"> • Walls with low cohesion values

Cracking profile	Specifications	Observed in:
	<ul style="list-style-type: none"> • Sliding of a row of horizontal mortars • No diagonal cracks • Opening of some vertical elements at the top rows • Brittle behavior, sudden drop in pushover curve 	<ul style="list-style-type: none"> • Walls with high cohesion values
	<ul style="list-style-type: none"> • Sliding of horizontal mortars in a row • No diagonal crack • Brittle behavior 	<ul style="list-style-type: none"> • The wall with very low tensile strength • The walls with very high tensile strength • The walls with Low initial vertical stress • The walls with low compressive strength
	<ul style="list-style-type: none"> • Predominant diagonal crack • High lateral strength 	<ul style="list-style-type: none"> • Wall with high initial vertical stress

4.8 Conclusion

A micro-modeling strategy is presented to model the mechanical behavior of masonry walls in this chapter. In this modeling, bricks are discretized with continuum elements which are connected by interface elements representing mortars. The mortars are supposed to be the plane of weakness and the nonlinearity takes place in these elements. A bilinear yield function considering shear and tension failure of mortars was implemented. Then, the model was enhanced and a compression cap was added to the model in order to take into account compression failure of mortars. Softening was integrated in the three tensile, compression and shear mechanisms using the failure energy as the controlling parameter for each failure. The model was introduced in software GEFDyn and a large number of computations were done. The numerical results were validated by comparison with experimental evidence. The behavior of wall at different levels of loading was studied accurately. The model was able to reproduce the behavior of masonry before and after peak very well. The crucial role of compression cap in capturing the correct failure mechanism and load-displacement curve was demonstrated by comparing the computational results of wall with opening and walls with different aspect ratios using yield function with and without compression cap.

A parametric study has been done with respect to aspect ratio of the wall to investigate its influence on failure mechanism of the wall. Studies show that the aspect ratio has a great influence on failure mechanism and ultimate lateral strength of the wall. Results illustrate that walls with lower aspect ratio have greater stiffness and withstand larger lateral strength than walls with aspect ratio greater or equal to 1 but they fail sooner because of sliding of their top or bottom row. In the analyzed walls with aspect ratio less than 1, normal stress on the walls was not sufficient to prevent sliding shear failure of the wall. On the other side, the cohesion of mortars decreases by increasing displacements and for the walls with the same aspect ratio, the one with larger dimensions withstands larger stresses and its maximum strength is highly greater. Moreover, walls with larger aspect ratio than 1 have lower stiffness than walls with aspect ratio equal to 1 and the stiffness is decreased when aspect ratio increases. The failure mechanism for the wall with aspect ratio greater than 1 is crushing failure at the compressed corners which was captured for wall with AS=1.5.

Finally a parametric study has been done in order to find the importance of each parameter on wall's behavior. Cracking profiles, pushover curves and the summation of cracks' lengths in different types of elements located at different rows and columns are compared in order to find the role of each parameter in the performance of the wall and to find the most suitable condition. Studies illustrate that combination of factors contribute and shape the structural behavior of a wall including cohesion, tension strength, compression strength of mortars and initial vertical loads which are applied to the wall. Each of the parameters should stay in a certain range in order for the wall to exhibit predictable behavior under specific loading condition. Between these parameters increasing the initial normal load will certainly improve the behavior of wall

because the normal stress increases both shear strength of the wall and postpones the opening of horizontal mortars due to tension. However, in practice, this parameter depends on the location of the wall in the structure and is almost an input of design process. It is also shown that the larger total length of opening in vertical elements and lower total sliding in horizontal elements and formation of diagonal cracks in the wall cause the wall to undergo greater loads and to exhibit more ductile behavior. Hence, the removal of mortar between vertical interfaces along the diagonal of the wall may force a desirable failure mechanism with stepped diagonal cracks. Results also show that tension failure in the bricks does not affect the results considerably. Thus, its modeling using interface element in the middle of bricks can be neglected for the simplicity.

As noted before, the boundary conditions play an important role on the behavior of the wall. The results presented in this chapter were limited to a unique type of boundary conditions. Therefore, in the next chapter this effect is studied, analyzing the behavior of connected walls.

Chapter 5

Micro modeling: out of plane loading

5.1 Introduction

As mentioned in the literature review, failure of masonry wall under out-of-plane loads is one of the most critical issues in masonry construction. Other type of loadings such as explosion, flood, avalanche or soil horizontal movement are also possible configurations. The masonry walls perpendicular to a seismic motion are subjected to out-of-plane loads and fail in out of plane direction. Out-of-plane failure of masonry constructions is the main cause of injury and loss of life when they are subjected to earthquake loads. Figures 5.1 and Figures 5.1 show different types of cracks in perpendicular masonry walls under different earthquakes. In-plane loading in a wall resulting out of plane failure to the other one.



Figure 5.1: (a) Failure of masonry wall, Haiti earthquake (b) Out-of-plane collapse of masonry wall, Champerico, Guatemala

Figure 5.1(a) shows the failure of a masonry wall in Haiti. A diagonal crack is initiated from top right to the middle of the wall which is accompanied by a horizontal sliding crack from middle to the edge of the wall. In Figure 5.1(b) damage of two perpendicular masonry walls under earthquake movement is shown. The walls are separated from their intersection and damage is mostly concentrated at the top part of the walls joint. Moreover, a diagonal cracks is also formed in the lower part of the wall I. Some horizontal crack in connection of wall I and roof can be seen whereas wall II also moved and some cracks in its common corner with wall I are appeared. Figure 5.2(a) shows the shear sliding failure of a masonry wall in a rural building in Turkey [16]. A continuous horizontal crack is obvious in the wall as its length is much greater than its height. Earthquake movement in Turkey also caused a slight damage in a one-story masonry building in Palu, as shown in Figure 5.2(b) [16]. Walls experienced horizontal sliding failure at their top. In addition, a diagonal crack which is initiated from the corner of opening to the bottom of the wall is also obvious. The aim of this study is to reproduce such crack patterns in a wall due to

out of plane loads and in a set of two perpendicularly jointed walls due to roof's movement.

The performance of masonry wall under out-of-plane loads has not been studied considerably.



Figure 5.2: (a) Damage of a rural masonry building at Yukar Demirci Village, Turkey [16](b) Failure of a rural masonry building in Palu, Turkey [16]

In most of experimental studies, masonry wall was subjected to the uniform pressure perpendicular to its surface in order to simulate the out-of-plane load condition [1], [29], [44],[103] and the effect of different parameters such as axial compression load, mortar type, unit type, aspect ratio, boundary condition etc. on the behavior of masonry wall under different conditions were studied. But in this study the effect of out-of-plane loads on the behavior of unreinforced masonry wall will be studied. Therefore displacements are applied to the panel in different locations and effect of gradual monotonic out-of-plane loads on performance of unreinforced masonry wall will be investigated.

In this chapter, behavior of one wall and two perpendicular walls under out-of-plane loading will be studied. In the first section behavior of a wall under different boundary conditions and different out-of-plane displacements is studied and the crack pattern analyzed. A parametric study will be done in order to assess the effect of different parameters on the behavior of a masonry wall under out-of-plane displacements. Then, two walls with same lengths will be attached and subjected to loads in different directions. A parametric study on vertical stress applied on the wall and cohesion of mortar will be done to assess the effect of each parameter on the performance of the set.

Afterward, a rigid roof is supposed to connect the walls and the influence of its movement on the behavior of each wall will be studied. For simulating the movement of the roof, all nodes at the top of walls are subjected to the same displacement in different directions. Roof rotation will be modeled by applying different displacements in x and y directions to the top nodes proportional to their distance to the roof's center of gravity. Finally, the length of the wall in y direction is multiplied by 2 to obtain the influence of wall's geometry on ultimate strength carried out by the walls, cracks profile and deformed shape.

5.2 Behavior of a wall under out-of-plane displacements

In this section, in order to study the out-of-plane behavior of unreinforced masonry walls, two simple walls are modeled and subjected to out-of plane displacements. These walls and the applied displacements on them, are schematically shown in Figure 5.3. The dimension of walls is the same as those used in chapter 3 namely: 990×1000 [mm²] and it consists of 18 courses of bricks with dimension: $210 \times 52 \times 100$ [mm³]. As shown in this figure, in Case A, the wall's right edge is subjected to out of plane displacement while the movement in x, y and z directions of its base and left edge is precluded. A vertical pre-compression equal to $\sigma_{n0} = 0.3MPa$ is applied to the wall and the vertical degree of freedom of the top nodes is fixed. The displacement applied to the wall's top corner is twice the displacement applied to the middle of its height.

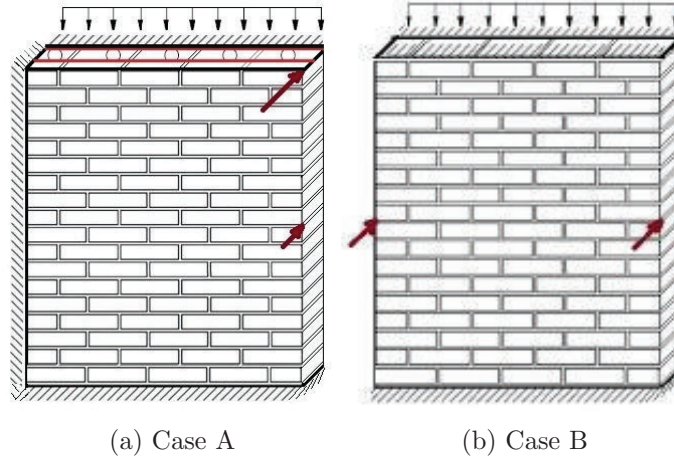


Figure 5.3: Studied walls subjected to out of plane displacement

In order to study another type of out of plane loading, the Case B is modeled. In this case, the horizontal and vertical movements at top and bottom nodes are precluded and equal displacements are applied to the wall's middle height at right and left edges. Similar to Case A, the wall is subjected to a vertical pre-compression equal to $\sigma_{n0} = 0.3MPa$. The modeling strategy is the same as that of previous chapter so that the bricks are divided to two parts, each part is modeled using 3D solid elements and at their connection, horizontal and vertical mortars are modeled by interface elements. The material properties which are the same as those of the previous chapter are shown in Table 5.1.

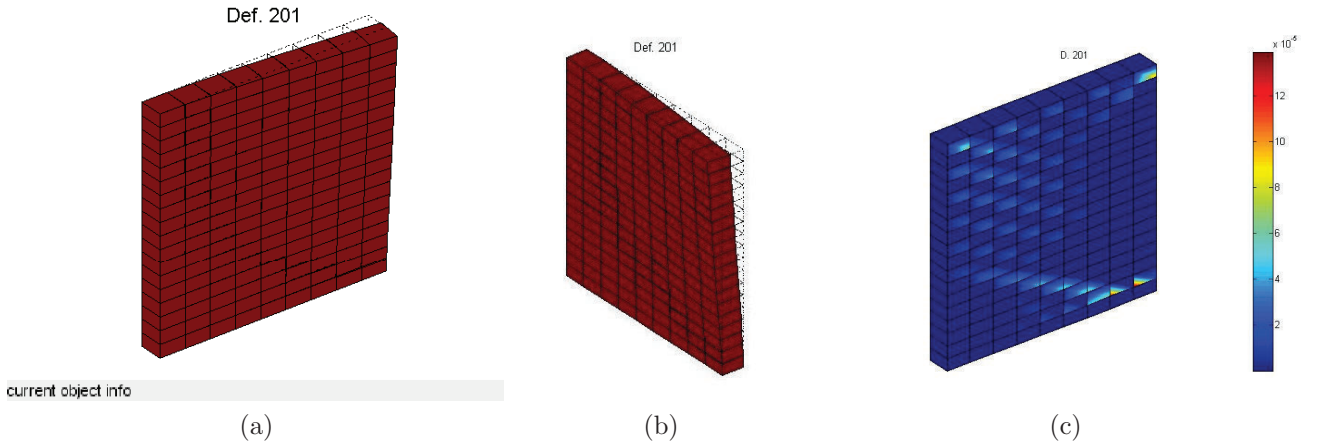
After modeling and capturing the results, a parametric study by changing the mortar's cohesion C_0 , the compression strength f_{c0} and the initial compression σ_{n0} will be conducted. The numerical results for each wall are presented separately.

Table 5.1: Inelastic properties for the horizontal and vertical interface elements

Tension		Shear				Compression				Thickness
f_{t0}	GI	C_0	$\tan\phi$	$\tan\psi$	GII	f_{c0}	$GIII$	θ	β	e
0.25 MPa	18 [Nm/m ²]	0.35 MPa	36.9°	0	125 [Nm/m ²]	10.5 MPa	5e3 [Nm/m ²]	32.8°	45°	3e-6 [m]

5.2.1 Case A

The initial modeling involves applying 2mm and 1mm displacements to the top and middle heights of the wall as demonstrated in Figure 5.3(a). The deformed shape in different views are shown in Figure 5.4(a) and (b). The stepped cracks at the lower part of the wall as well as horizontal sliding of the lower row of mortar are obvious in these figures. As shown in Figure 5.4(c), the applied out of plane displacements cause stepping cracks at lower part of the wall. In earlier steps of loading, the out of plane displacement causes some cracks due to opening of lowest row of the horizontal mortars. Moreover, the horizontal and vertical mortars at left and right top corners of the wall slid and open because of the concentration of loads. Afterward, cracks are forming a distributed pattern from left top corner to the middle of the wall. Suddenly the stepped cracks are formed in displacement equal to 1.5mm in the bottom part of the wall.

Figure 5.4: (a), (b) Deformed shape (c) total crack pattern in the wall, Case A, at $d_{top} = 2mm$

The base shear in y direction versus displacement applied at the top right corner, pushover curve, is shown in Figure 5.5. The wall maximum lateral strength in y direction (out-of-plane) is 4.1kN. It shows that the out-of-plane lateral strength of the wall for this case is very low. The initial stiffness of the wall changes at $d = 0.0004$ mm due to opening of some of bottom right horizontal mortars. Stepped cracks appear at 0.91mm at the lower part of the wall. Wall's condition before and after of this point is shown in Figure 5.6. The wall's crack profile as well as cracks created

in vertical, horizontal and brick-middle interfaces at final step, are shown in Figure 5.8.

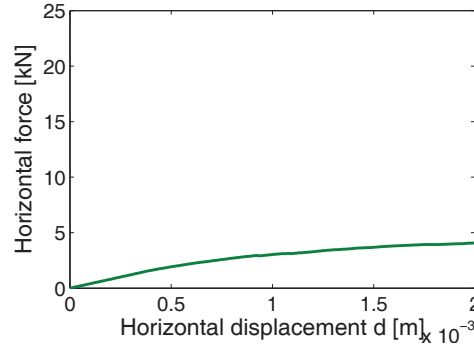


Figure 5.5: Lateral displacement vs. horizontal loads in y direction, Case A

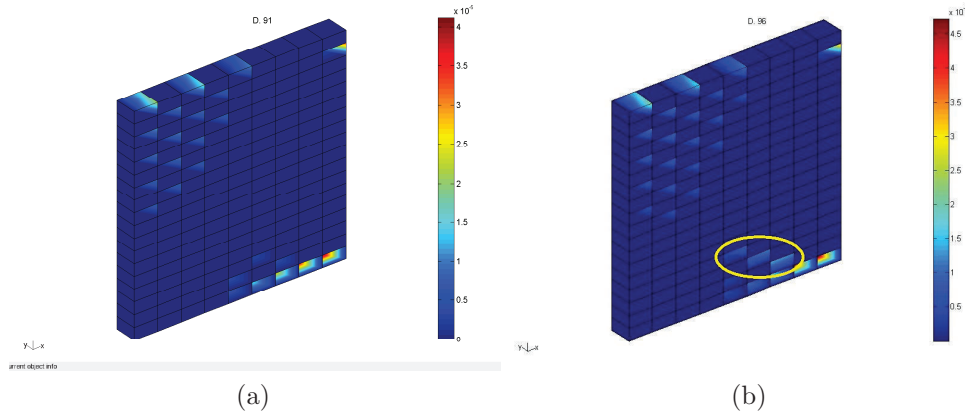


Figure 5.6: Cracks on the wall (a) at $d = 0.91mm$ (b) at $d = 1.03mm$, Case A

Shear stress in yz plane as well as the major and minor principle stresses in the bricks are illustrated in Figure 5.7. High shear stresses in the bricks correspond to the pattern of cracks in the wall. The major and minor principle stresses represent the location of tension and compression failure if their value violates the tensile and compressive strength of the bricks. The compressive strength horizontal mortars is $F_c = 10.5MPa$ whereas maximum minor principle stresses in the wall are about $-2.2MPa$. Hence, horizontal and vertical elements were not crushed in this case. On the other side, wherever the major principal stresses exceeds $f_t = 2MPa$, the element fails in tension and open.

The sliding of interface elements in two directions as well as their opening which represents shear and tension failure of the interface respectively, are shown for different interface elements in the wall in Figure 5.8. As illustrated in this figure, sliding of horizontal mortars in \vec{y} direction, parallel

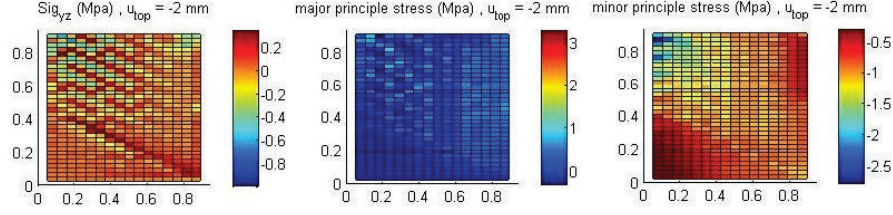


Figure 5.7: Stress distribution in bricks at $d = 2mm$ for Case A

to direction of applied displacement, has diagonal tendency with highest value of $0.035mm$ while sliding of horizontal interfaces in \vec{x} direction just can be seen in the top (near the applied displacement) and bottom left horizontal mortars with maximum length of $0.052mm$. The opening of horizontal interfaces is clearer in the top left corner because of concentration of tensions and bottom left corner of the wall in addition to stepped cracks in lower part of the wall. The maximum opening in horizontal interfaces is $0.135mm$. No sliding in \vec{z} direction is observed for vertical mortars whereas the stepped diagonal pattern cracks due to sliding of vertical mortars in \vec{y} direction are observed with maximum value equal to $0.052mm$. The opening of vertical mortars namely their tension failure is also shown in this figure and it seems that this kind of failure causes the stepped sliding cracks in horizontal and vertical mortars which formed total crack pattern. The maximum length of opening in the vertical mortars is $0.069mm$ at the top right corner. The bricks which are failed due to tension are the top left ones as shown in Figure 5.8(g). According to the results, main cause of failure in the wall due to out of plane loads is formation of stepped cracks in lower part of the wall.

5.2.2 Parametric study on Case A

In this section, the results of parametric study will be presented in order to find the influence of some material properties on the behavior of the wall and to distinguish which parameter has more influence on the performance of the wall against out-of-plane loading. These parameters are initial cohesion of mortars, compression failure of mortars and initial normal compression applied to the wall. Two different values, one less and another greater than actual value are chosen to investigate the wall's behavior. These values are $C_0 = 0.035MPa$ and $C_0 = 3.5MPa$ for mortar's cohesion, $\sigma_{n0} = 0.05MPa$ and $\sigma_{n0} = 2.12MPa$ for initial vertical stress and $F_{c0} = 10.5e5Pa$ and $F_{c0} = 10.5e7Pa$ for compressive strength of masonry. The results of main case with $C_0 = 0.35MPa$, $\sigma_{n0} = 0.3MPa$, $F_{c0} = 10.5e6Pa$ is also compared with other cases. For having a better comparison, maximum length of cracks fits to $0.1mm$ in total crack pattern's figures in all cases.

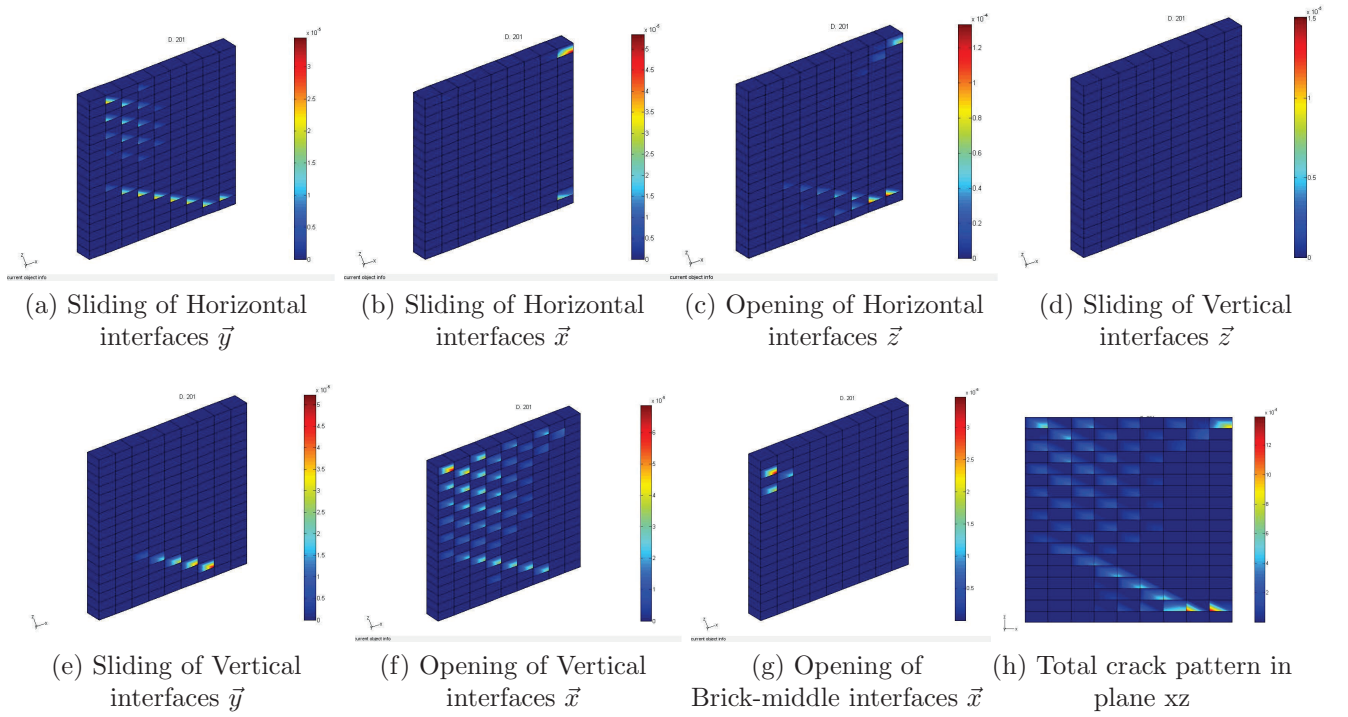


Figure 5.8: Crack pattern in the masonry wall $d = 2mm$, Case A

(a) Cohesion of mortars

The deformed shape and crack profile for the walls with different cohesions are shown in Figure 5.9. From the Figure 5.9 it can be found that increasing mortar's cohesion causes decrement in the size of cracks and their distribution in the wall. According to Mohr-Coulomb failure criterion, the cohesion of mortar has a key role to shear strength of the wall and as its value rises, the sliding of horizontal and vertical mortars is postponed. For example in case with $C_0 = 3.5e6Pa$, no sliding is observed in \vec{x} and \vec{y} directions in horizontal mortars as well as in \vec{y} and \vec{z} directions in vertical mortars but mainly opening of vertical mortars and formation of stepped cracks in the wall may cause the failure of the wall under out-of-plane loads.

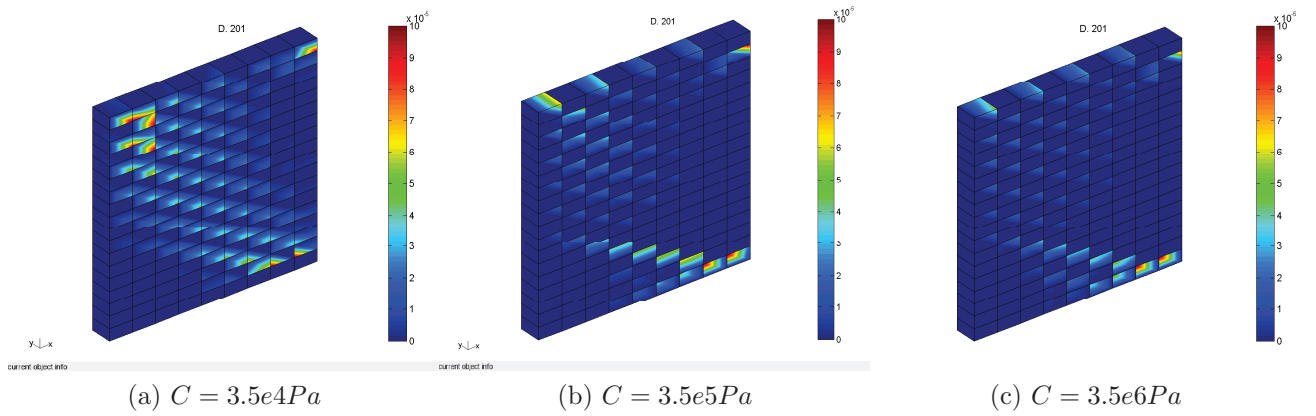


Figure 5.9: Cracking profile for the walls with different mortar's cohesion

As shown in Figure 5.9, for the wall with $C = 3.5e4Pa$, the stepped cracks are more distributed in the wall and mortars in top left corners experience greater opening and sliding. Maximum lateral load supported by this wall is $2.8kN$ and in comparison with previous case with $C = 3.5e5Pa$, the lateral maximum strength is decreased. It should be noted that the lateral strength of the wall under out-of plane displacements is very low in this case. Maximum crack length which is formed in the wall is $0.142mm$ which is greater than previous case $C = 3.5e5Pa$ with $0.138mm$. For the wall with $C = 3.5e6Pa$ the mortars' cracks decreased in term of size and spreading through the wall and the maximum length of the crack was $0.125mm$. Hence, by increasing the cohesion lateral strength of the wall under out-of plane displacement increases whereas the number and length of sliding elements decrease a lot. As shown in Figure 4.72 in previous chapter, r1 is the bottom row and r17 is the top row of horizontal mortars. In addition, c1 and c8 correspond to the left and right columns in the wall.

In Figure 5.10 horizontal displacement of the base nodes in y direction versus out-of-plane displacement of top right corner is shown. As shown in this figure, the lateral load which is carried out by the wall for wall with $C = 3.5e4Pa$ after $d = 8.2mm$ remains unchanged. Studying the

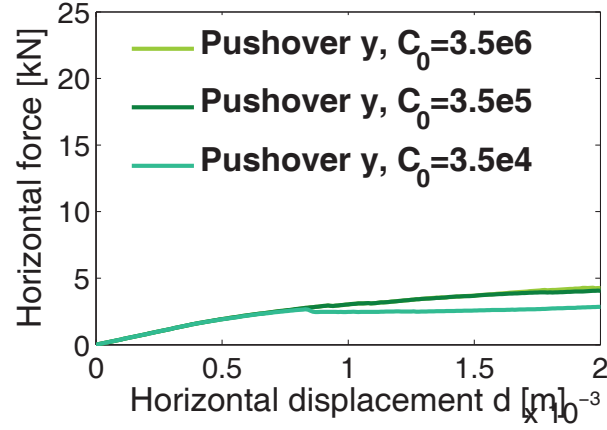


Figure 5.10: Effect of mortar's cohesion on pushover curve

stresses and strains in the wall showed that formation of throughout stepped cracks from top left to bottom right of the wall at his displacement, was its main reason. These cracks were formed in the wall mainly due to opening of vertical elements and as after opening of these elements, the cohesion of mortars sets to zero, some elements loses their lateral strength and their summation remains unchanged. The cracking profiles in the wall with $C = 3.5e4Pa$ before and after peak is shown in Figure 5.11.

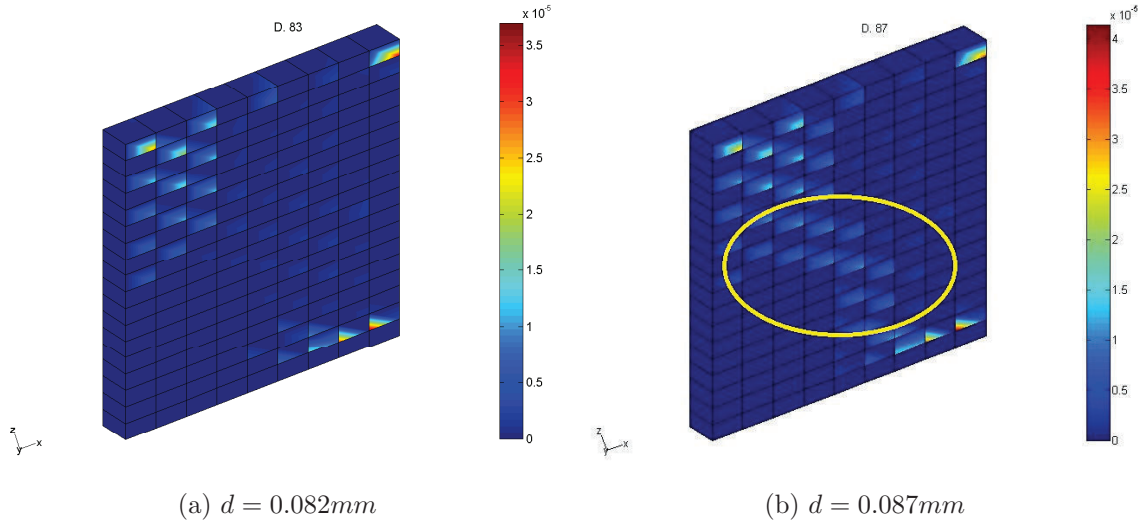
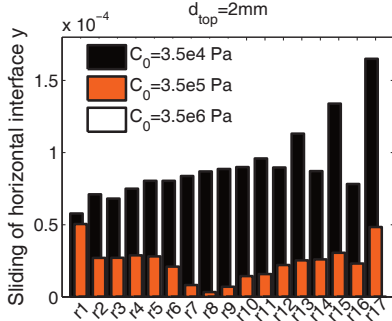


Figure 5.11: Crack pattern (a) before and (b) after stepped cracks for wall with $C = 3.5e4Pa$

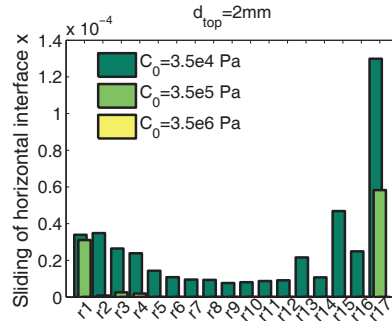
The length of sliding in in-plane and out-of-plane directions as well as opening of horizontal interfaces for wall with different C in different rows are drawn in Figure 5.12. Length of cracks in different rows shows how they are distributed in the wall. According to Figure 5.12(a) and

(b) the sliding of mortars in both directions (parallel and perpendicular to the loading) increases considerably by decrement of cohesion of mortars and the critical locations are the top and bottom rows of the wall. Figure 5.12(c) shows that opening of horizontal mortars is approximately the same for walls with different cohesions and greatest opening cracks belong to first row of mortars.

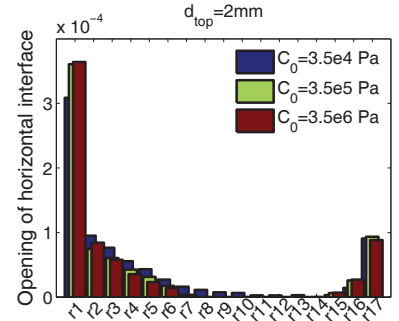
Sliding of vertical elements in both directions also is higher for walls with lower cohesion, see Figure 5.12(d) and Figure 5.12(e). As shown in Figure 5.12(f), vertical mortars at the left part of the wall open more and the length of opening decreases by cohesion increment. Tension failure of bricks also is illustrated in Figure 5.12(g). According to this figure, more bricks fail in tension in walls with higher cohesion. These bricks are located at left corner of the wall because as illustrated before, the movement of wall at its left edge is prevented. The summation of cracks' length (sliding and opening) for all types of interfaces were shown in Figure 5.12(h) in order to find which parameter causes failure in the wall due to out-of-plane displacements. As shown in this figure, as the length of opening in horizontal mortars is the same for all cases and the length of sliding of horizontal elements in out-of-plane direction and opening of vertical elements is higher for the wall with lowest cohesion, it can be concluded that these parameters play a key role to performance of the wall. The high value for sliding of mortars in out-of-plane direction and opening of vertical elements cause brittle failure in the wall. These parameters change a lot by increasing the mortar's cohesion.



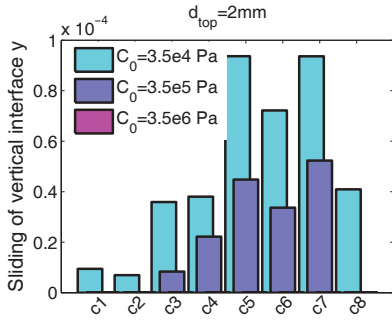
(a) Sliding of horizontal mortars \vec{y}



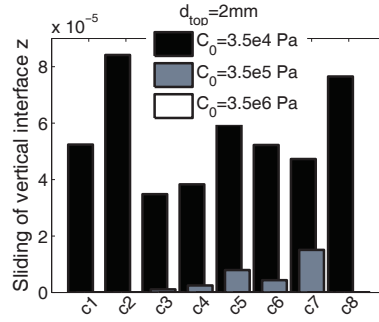
(b) Sliding of horizontal mortars \vec{x}



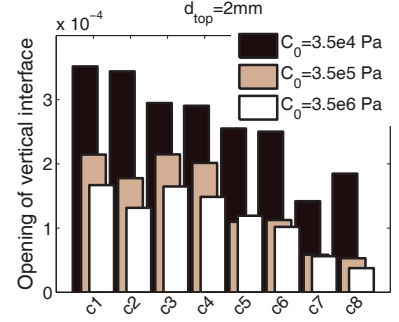
(c) Opening of horizontal mortars



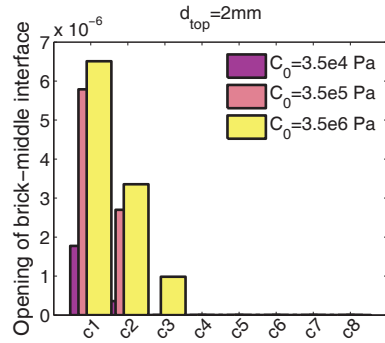
(d) Sliding of vertical mortars \vec{y}



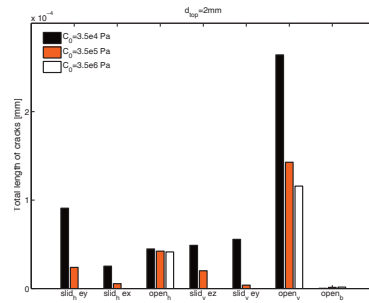
(e) Sliding of vertical mortars \vec{z}



(f) Opening of vertical mortars



(g) Opening of brick interfaces



(h) Total length of crack

Figure 5.12: Length of different types of cracks in different interface elements at rows and columns of walls with different C , Case A

(b) Initial normal compression

In this part the vertical compression which is initially applied to the wall is changed to investigate its influence on the overall behavior of the wall under out-of plane displacements. Profile of cracks for $\sigma_{n0} = 0.05MPa$, $\sigma_{n0} = 0.3MPa$ and $\sigma_{n0} = 2.12MPa$ at $d_{top} = 2mm$ are illustrated in Figure 5.13.

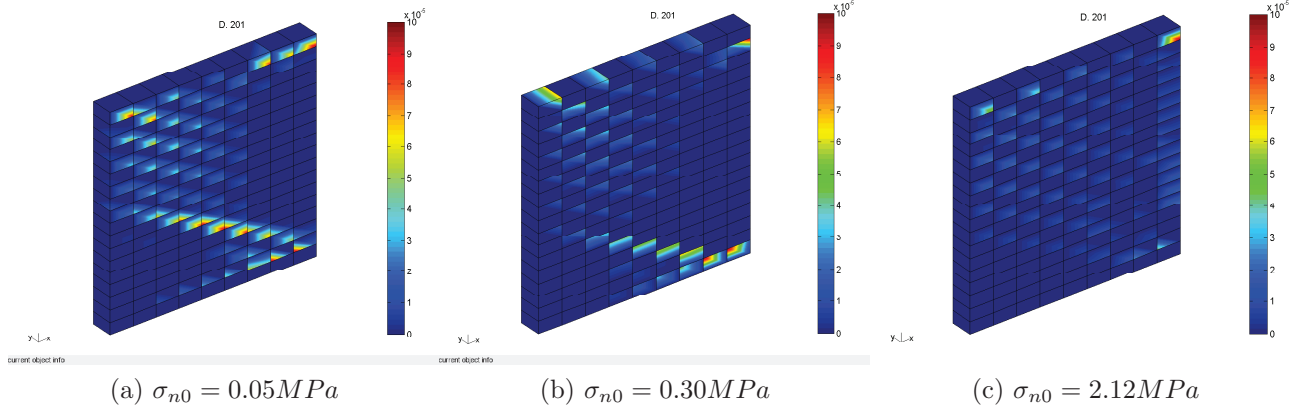


Figure 5.13: Total crack pattern for walls with different σ_{n0}

As shown in Figure 5.13, the initial normal confinement has a considerable role to the behavior of wall under out-of-plane displacement. By increasing normal stress on wall, the size of cracks in the wall decreases significantly. For the wall with $\sigma_n = 0.05MPa$, maximum crack's length is $0.162mm$ which is the greatest value among the walls with different cohesion and initial normal stresses. Studying the behavior of wall with $\sigma_n = 0.05MPa$ shows that at $d = 0.3mm$ more than half of horizontal mortars located at right part of lower row open and simultaneously the vertical mortars at the top left of the wall begins to open. This situation causes the wall to undergo shear stresses in x direction and as can be seen in the following figures, the sliding of horizontal elements in x direction in this case is very larger than the wall with $\sigma_n = 0.3MPa$. As a result a drop in pushover curve appears. The wall loses its lateral strength more than the other cases because the number of horizontal interface which are opened is greater than other ones due to lack of enough vertical compression to prevent their opening. Afterward, cracks form and spread through the top left corner and bottom row of horizontal mortars. Then, at $d = 1.4mm$ stepped diagonal cracks which connect the top left cracks to the bottom row of horizontal mortars form in the wall and causes another draft in the pushover curve. The larger cracks form in the lower row of horizontal mortars due to tension failure of those elements. Maximum lateral load which is carried out by the wall is $2.52kN$ which is much lower than the other cases. Comparing to the case with $\sigma_n = 0.3MPa$, the sliding of mortars increases and more mortars slide in both directions. Moreover, the length of mortar's opening increases by reducing the initial normal stress on the wall. In this case, just one brick fails in tension. Maximum principle stress also

concentrates at the top left corner of the wall similar to the other cases.

For wall with $\sigma_n = 2.12MPa$, horizontal mortars except the one at the top right corner do not slide because of high level of normal compression. At $d = 0.37mm$ some of horizontal mortars located at the right part of the wall are compressed under out-of-plane displacements and on the other side some of vertical elements at top left corner of the wall begin to open. The combined effect of overturning moments and opening of vertical mortars causes the wall to carry out more lateral strength at this step. In this case, the sliding of horizontal elements in x direction is 0 in all rows except the top one. Maximum lateral load which is carried out by this wall is $8kN$ which is much more greater than the other cases. The number of horizontal elements which experience tension failure and open is much less than the other cases. Vertical elements slide and open mainly at top left corner of wall toward its middle. On the other hand by increasing the strength of horizontal and vertical mortars, more bricks fail in tension. The maximum major principle stress takes place in bottom right corner of the wall. It should be noted that in this case, no stepped cracks appear in the wall.

As shown in pushover curve, the lateral shear strength which is carried out by the wall in-

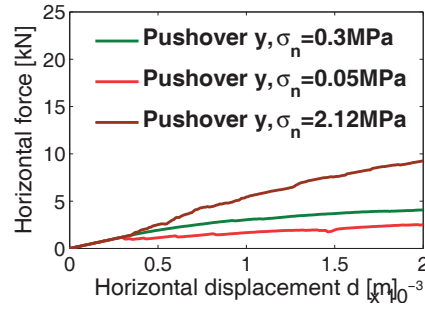


Figure 5.14: Influence of initial normal stress on the behavior of the wall

creases by increment of initial vertical load applied to the wall. On the other hand, the wall with lower initial normal stress yields sooner and withstands lower lateral strength than other cases. It should be noted that the variation of stiffness in the walls with $\sigma_n = 0.05MPa$ and $\sigma_n = 2.12MPa$ depends on the movement of horizontal elements in x direction. Horizontal mortars in the wall with $\sigma_n = 0.05MPa$ slide considerably in x direction whereas no sliding in x direction was observed for the wall with $\sigma_n = 2.12MPa$ (except the movement of top left horizontal mortar in the location of applied displacement).

Figure 5.15 displays the length of sliding and opening cracks in different types of elements. As shown in Figure 5.15(a) and Figure 5.15(b), the length of sliding cracks in horizontal elements decreases by increasing the initial normal stresses. The opening of horizontal mortars also decreases considerably in the upper rows by increasing the normal compression on the wall. As shown in Figure 5.15(c) for the wall with $\sigma_{n0} = 2.12MPa$ in some rows, horizontal interfaces close. The opening of horizontal mortars at first and top rows are higher than the other rows.

Sliding of vertical interface parallel to applied displacement also considerably decreases by normal compression increment. Vertical elements at the middle of the wall slid more than ones located at the wall's edges. Sliding of vertical interfaces at z direction for the wall subjected to $\sigma_{n0} = 0.05MPa$ is also noticeable so under low level of normal stresses, vertical mortars slide more in z direction. Opening of vertical elements in left side of the wall is greater for lower values of σ_{n0} whereas for wall with $\sigma_{n0} = 2.12MPa$ opening of vertical elements in different columns does not vary a lot. Increasing the normal stress, decrease the length of opening in vertical elements too. Brick fail in tension mostly at the left part of the wall and the length of opening increase by increment of initial normal stress on the wall as shown in Figure 5.15(g). The summation of crack's length for different categories of cracks are shown in Figure 5.15(h). Opening of horizontal interfaces, opening of vertical interfaces and sliding of horizontal interface parallel to the thickness of the wall are the parameters which have greater values for the wall with lower lateral strength. As shown in Figure 5.15(a) by increasing initial normal stress, total length of opening and sliding cracks in mortars decrease considerably. It should be noted that the displacement in x direction also may change the stiffness of the wall as described before.

(c) Compressive strength of masonry

In this section, the pushover curves and total crack pattern for wall with different masonry compressive strength namely $F_{c0} = 10.5e5Pa$, $F_{c0} = 10.5e6Pa$ and $F_{c0} = 10.5e7Pa$ are compared in order to assess the effect of this parameter on behavior of wall under out of plane loading. In the wall with $F_{c0} = 10.5e5Pa$, the top and bottom left horizontal mortars slide a lot as shown in Figure 5.16(a). By increasing the displacement in this case, shear strength of the wall decreases by normal stress increment and mortars slide more. As a result, the size of cracks will increase by reducing of masonry compressive strength and thus the wall carries out lower lateral strength than the other cases. The stiffness of wall in this case changes firstly at $d = 0.4mm$ due to opening of horizontal interfaces at the first row. Then, at $d = 0.8mm$ stepped cracks appear on the wall and wall loses its stiffness again. On the other hand, there is no difference between the cracking profiles and pushover curves in the walls with $F_{c0} = 10.5e6Pa$ and $F_{c0} = 10.5e7Pa$ for displacement up to $2mm$ because the displacement is not sufficient to cause the crushing in their mortars or decrease their shear strength.

The sliding of horizontal elements in both perpendicular and parallel to the loading at first and last rows for the wall with lower compressive strength is much greater than other walls as shown in Figure 5.18. In the wall with low compressive strength, the shear strength of the wall decreases sooner with normal stress increment. Hence, elements in right top and bottom rows lose their shear strength and slide. Generally by increasing compressive strength of masonry, the sliding of horizontal cracks decreases a lot especially at top and bottom rows whereas the length of the other types of cracks increases a little and wall carries out more lateral strength.

The summation of length of cracks in different cases are displayed in Figure 5.18. Maximum length of cracks belongs to opening of vertical interface. The total length of opening of horizontal interface is also considerable. By comparing the length of cracks in different cases, it can be found that the high level of sliding cracks of horizontal mortars in x direction also can represent

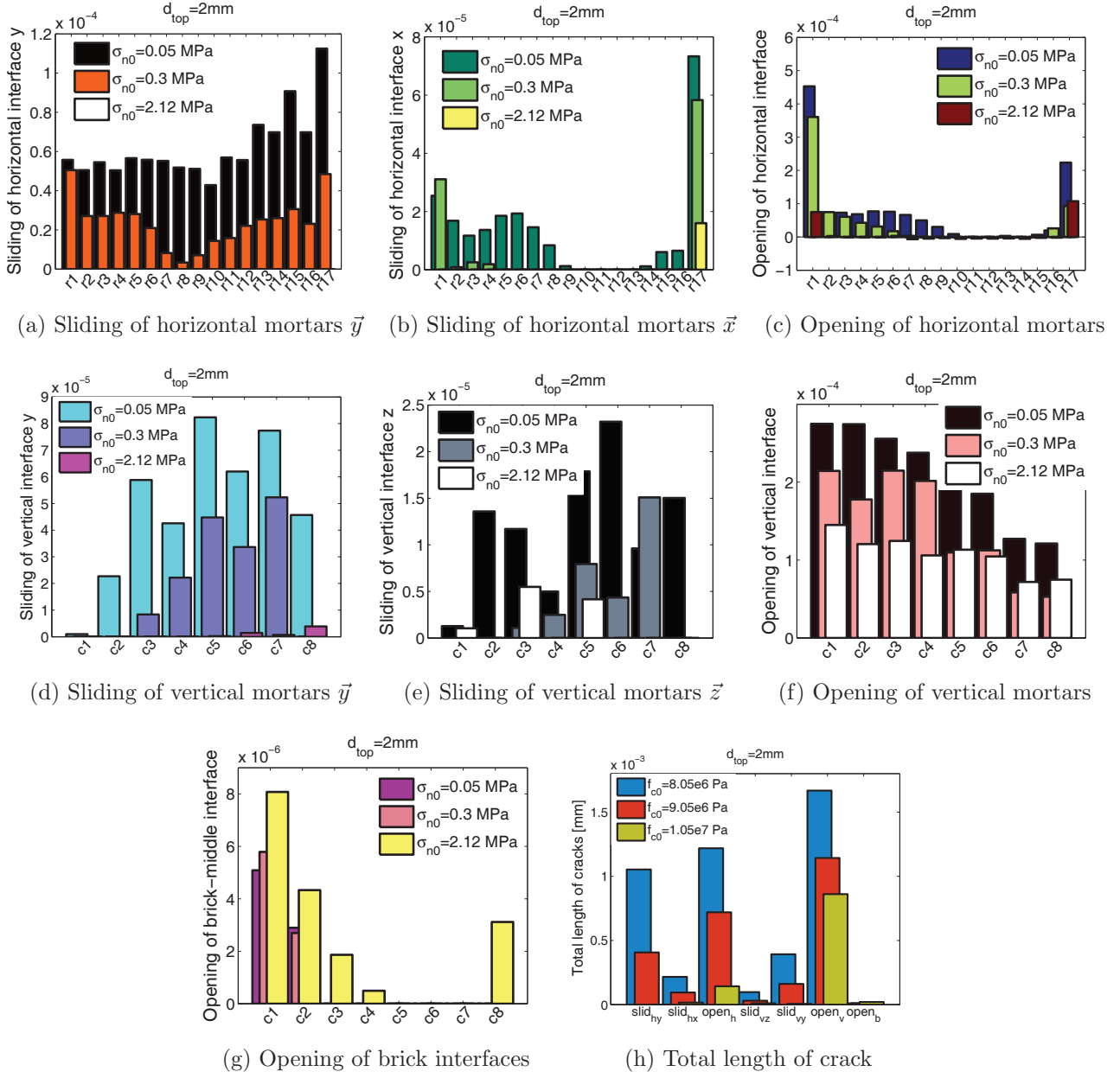


Figure 5.15: Length of different types of cracks in different interface elements at rows and columns of walls with different σ_{n0} , Case A

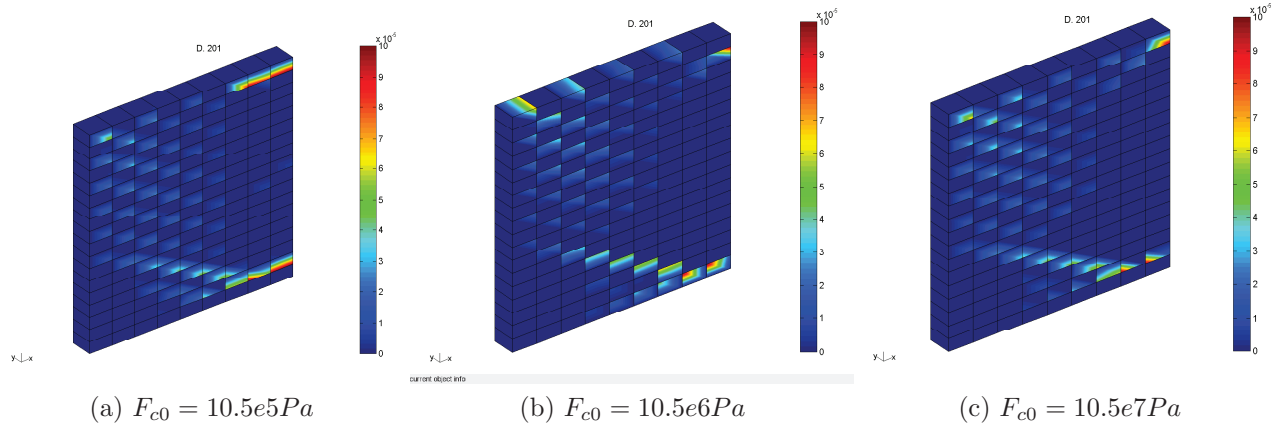


Figure 5.16: Profile of cracking for walls with different compressive strength for masonry

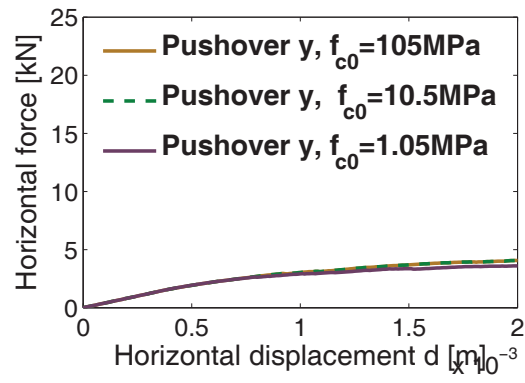


Figure 5.17: Influence of masonry compressive strength on the behavior of wall

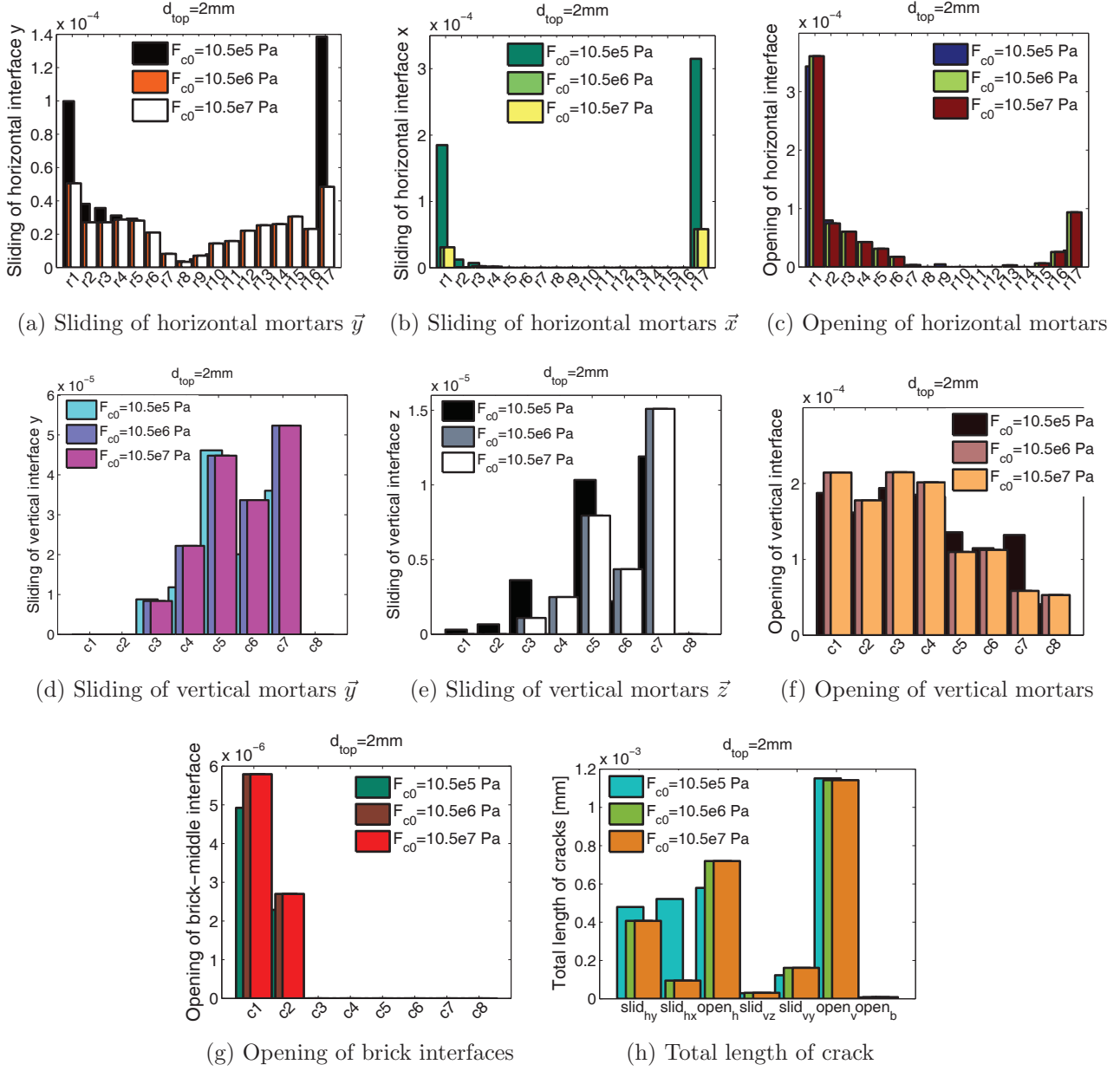
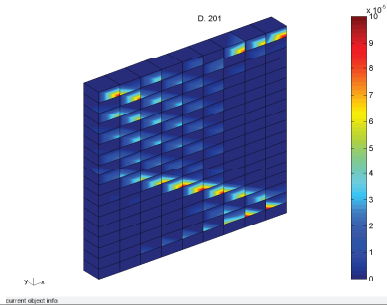


Figure 5.18: Length of different types of cracks in different interface elements at rows and columns of walls with different F_{c0} , Case A

a type of damage in the wall.

In this part, a masonry wall with specific boundary condition (Case A) was loaded under out-of-plane displacement at two points in its right edge. The behavior of wall was studied and parametric study has been done in order to find the most important parameters in the behavior of masonry wall under out of plane loading. The results proves that the shear strength of the wall under out of plane displacements is very lower than that of in-plane and its value greatly depends on the boundary condition and position of applied loads. The cohesion of mortars and compressive strength of masonry were divided and multiplied by 10. Moreover, the wall was analyzed for 3 different values of initial normal stress. Results show that the initial normal compression has the greatest influence on behavior of the wall and after that cohesion of mortars also is an important parameter. Opening of vertical cracks is the main reason of failure in the wall. Moreover, opening and sliding of horizontal mortars in x direction (perpendicular to the loading's direction) also have considerable influence on failure of the wall. The cracking profile for most vulnerable cases is drawn in below Table 5.2.

Table 5.2: The crack profile for the damaged walls, Case A

Cracking profile	Specifications	Observed in:
	<ul style="list-style-type: none"> • A continous diagonal zigzag cracks from top left to the right bot-tom 	<ul style="list-style-type: none"> • The wall with low value of initial normal stress • The walls with low co-hesion value for mor-tars

5.2.3 Case B

Case B (see Figure 5.3(b)) is studied here to investigate the effect of boundary condition on behavior of masonry wall under out-of-plane loading. The material properties of Case B is the same as Case A. In this case, two punctual displacements equal to $d = 1.5mm$ are gradually applied to middle edges of the wall as shown in Figure 5.3(b) and the behavior of wall will be analyzed. Then, cohesion, normal stress and compressive strength of mortars are changed in order to study their effect on the wall's performance.

The deformed shape and total crack pattern of Case B are shown in Figure 5.19. As illustrated in this figure, the cracks are formed in the middle of the wall just right to the applied displacement

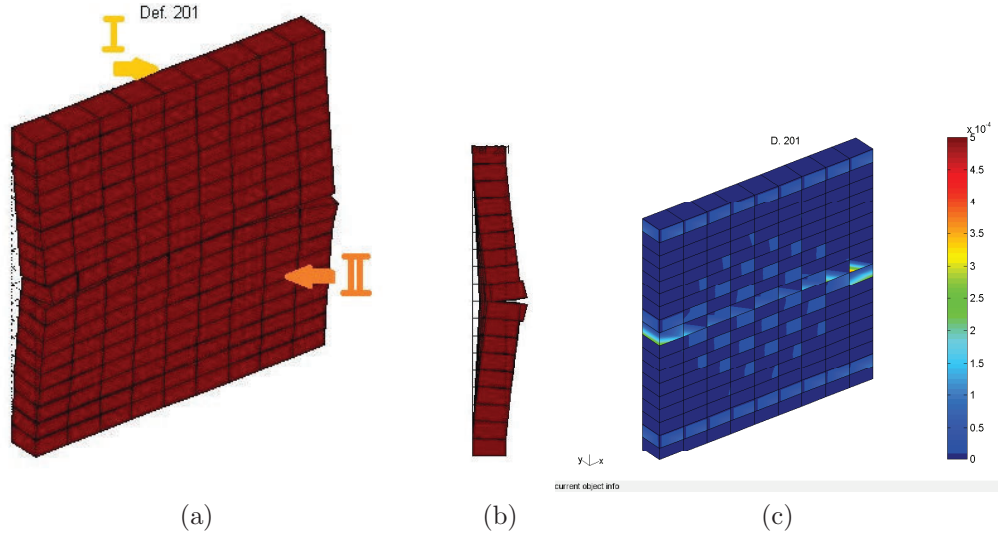


Figure 5.19: (a), (b) Deformation of wall (c) cracking profile of the wall, Case B

and then cracks develop to the middle of the wall in rhomboid shape. Opening cracks at the top and bottom rows of horizontal mortars also can be seen. The length of cracks at the edges of wall which are the location of applied displacements is greater than the other part of the wall.

The horizontal load in y direction as a function of applied out-of-plane displacements to the wall is drawn in Figure 5.20(a). Maximum load which is carried out by the wall is $21kN$. As shown in this figure, the stiffness of wall changed gradually in 3 points. First stiffness reduction belongs to sliding of the left end mortar in the middle of wall in x direction at $d = 0.22mm$. Although displacements are applied to the wall in a same coordinate but they are imposed to two different bricks at top (left edge) and bottom (right edge) of middle line. Hence, the left one slid sooner. The stiffness of wall reduces again at $d = 0.66mm$ due to sliding of the right end mortar in the middle in x direction. The third reduction corresponds to initiation of tension failure in the bricks located in the middle of the wall. In Figure 5.20(b), the pushover curve obtained from out-of-plane loading is compared to the one for in-plane loading. The lateral strength of the wall under top in-plane displacement is much higher than that of out-of-plane displacement. The distribution cracks in different types of elements are shown in Figure 5.21 for more information.

Figure 5.21 shows that the horizontal mortars just right to the applied loads, slide in \vec{y} and \vec{x} directions. The horizontal mortars fail in tension and open at the top, middle and bottom rows. The sliding of vertical elements is not considerable compared to the horizontal mortars. The shape of opening of vertical mortars is like a rhomboid with highest value at the middle corners. As shown in the Figure 5.21(g), almost all the bricks in the middle of the wall are failed in tension.

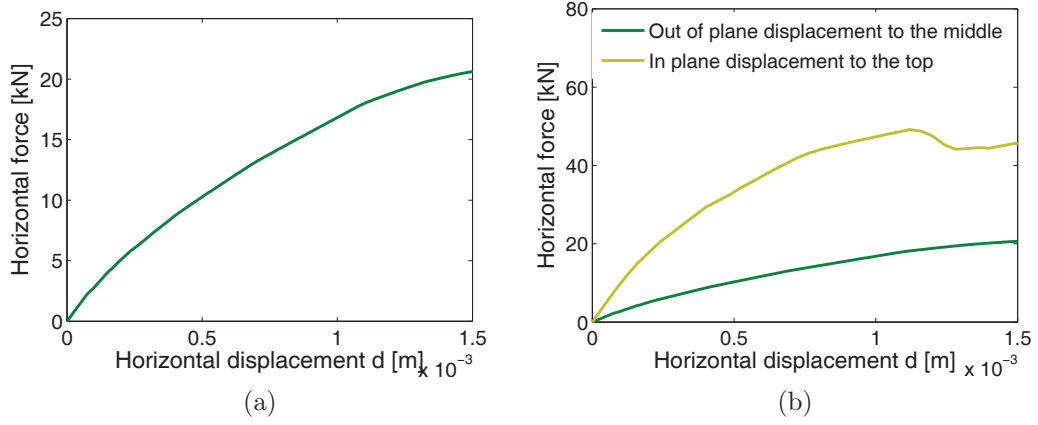


Figure 5.20: (a) Pushover curve for out-of-plane displacement (b) Pushover for in-plane and out-of-plane displacement

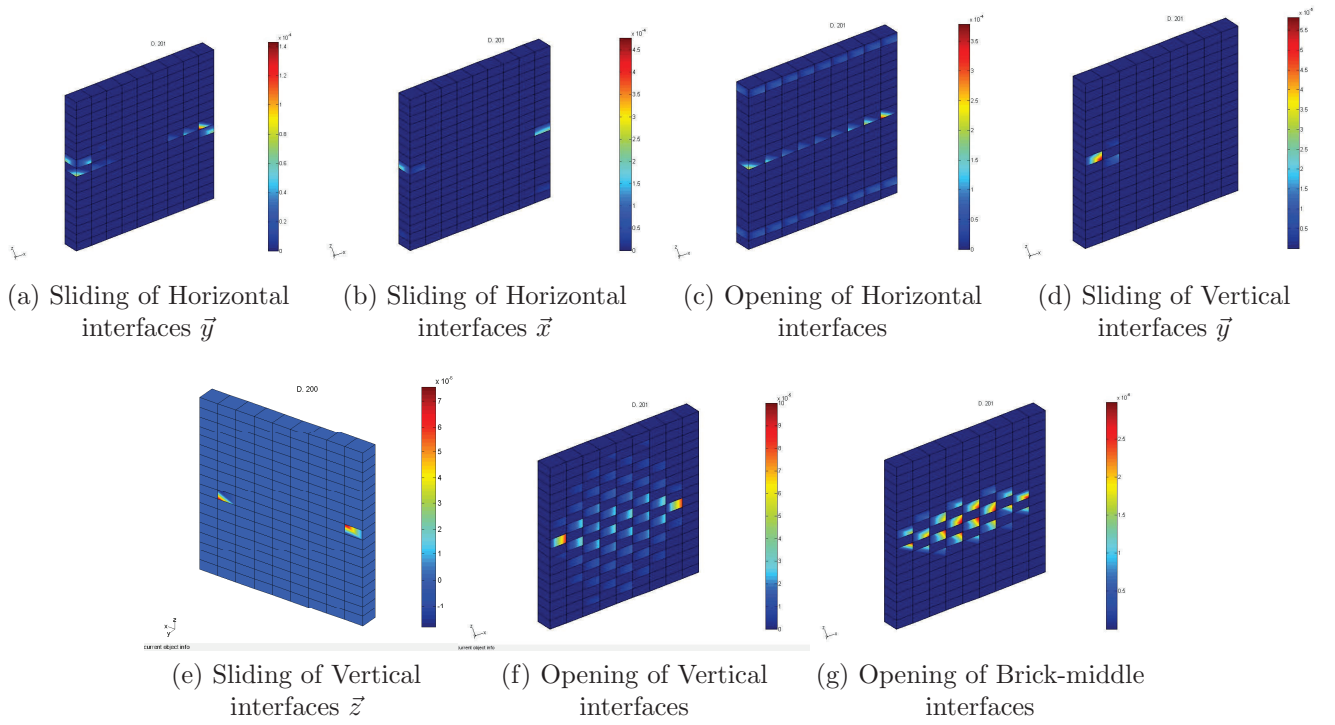


Figure 5.21: Crack pattern in the masonry wall $d = 1.5mm$, Case B

5.2.4 Parametric study on Case B

Similar to Case A, a parametric study also has been done on the Case B to recognize the effect of some parameters on the wall's performance under this boundary conditions. Mortar's cohesion, initial normal stress and compressive strength of masonry have been changed to see what their influence on the performance of wall is.

(a) Cohesion of mortars

Figure 5.22 represents the response of masonry wall with different cohesions for mortars. The values of cohesion are $C_0 = 3.5e4Pa$, $C_0 = 3.5e5Pa$ and $C_0 = 3.5e6Pa$ from left to right. In the wall with $C_0 = 3.5e4Pa$, first cracks appear in the middle edges of the wall where the displacements applied to the wall due to sliding of horizontal mortars. By increasing the displacements, vertical mortars begin to fail in tension and open at the middle edges of the wall first. Then, the tension failure distributes in vertical elements in a rhombic shape. Horizontal mortars in the middle of wall crack first and then the horizontal mortars at top and bottom rows open. Stiffness of the wall decreases at $d = 0.18mm$ because of slipping of two side bricks. The other decrease in pushover curve is also because of slipping of horizontal mortars next to previous ones. Maximum length's crack in this case is $1.22mm$ but for have a more accurate comparison, maximum length of cracks are fixed to $d = 0.5mm$. In this case bricks do not fail in tension.

Horizontal mortars in \vec{y} direction and vertical mortars in \vec{y} and \vec{z} directions do not slide in the wall with $C_0 = 3.5e6Pa$. Horizontal mortars in top, bottom fail in tension and open. The lengths of opening cracks are greater in the middle of wall. In this case, the number of vertical elements which fail in tension is much greater than the other cases. Stiffness of structure changes first when the end left horizontal mortar slid in x direction at $d = 0.37mm$ and then when bricks in the middle fail in tension at $d = 1mm$. So, the wall with highest cohesion $C_0 = 3.5e6Pa$ is stronger in shear and formed cracks in the wall are due to tension failure of mortars and bricks whereas wall with lowest cohesion $C_0 = 3.5e4Pa$ loses its strength mainly due to considerable sliding of horizontal mortars.

Pushover curves for different value of cohesion of mortar are shown in Figure 5.23. Results show the wall with cohesion of $C_0 = 3.5e6Pa$ is a little stronger than wall with $C_0 = 3.5e5Pa$ because in the first case, high cohesion decreases the sliding of horizontal mortars in x direction. The stiffness reduction of wall with $C_0 = 3.5e4Pa$ is also explained before.

Similar to case A, length of cracks for horizontal, vertical and brick-middle interfaces for different cases are shown in Figure 5.24. Figure 5.24(a) and Figure 5.24(b) indicate that the sliding of horizontal elements in x and y direction considerably decreases by cohesion increment. It should be noted that in the wall with lower cohesion, horizontal mortars at the upper and lower middle row slide significantly. Increasing the cohesion causes increment of opening cracks' length in

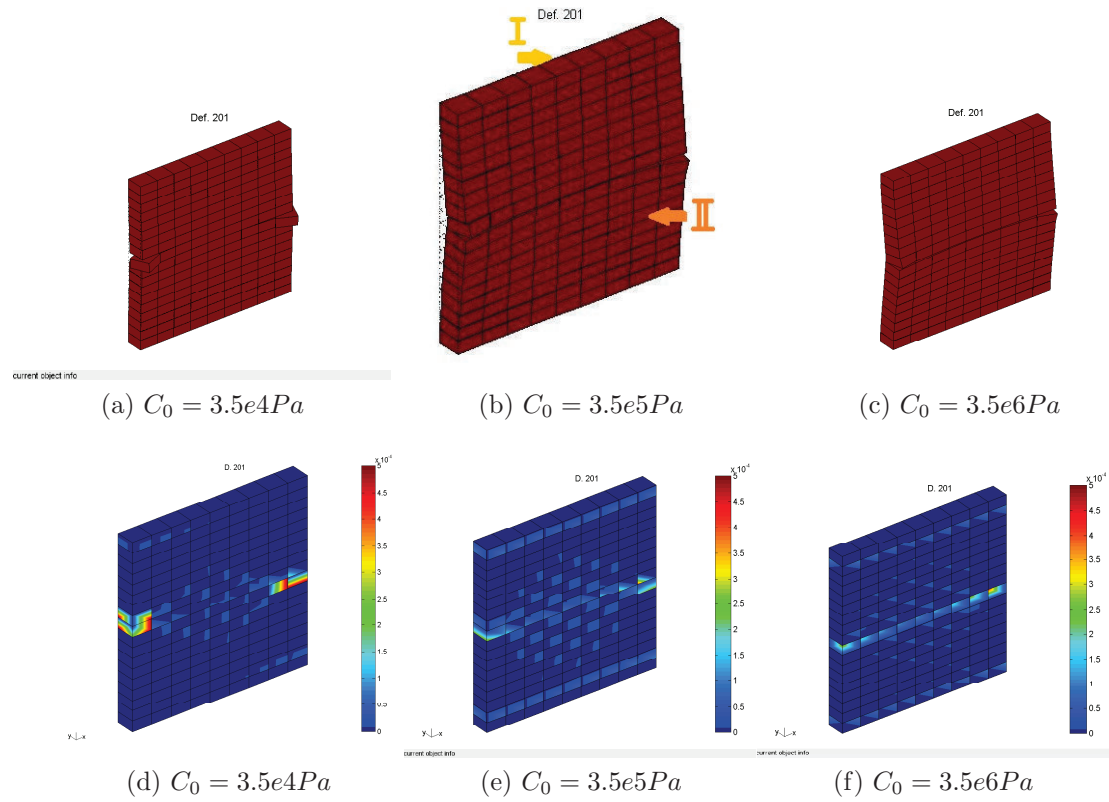


Figure 5.22: Deformation and cracking profile for different C_0 , Case B

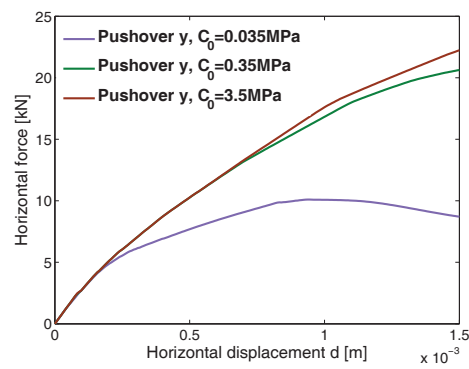
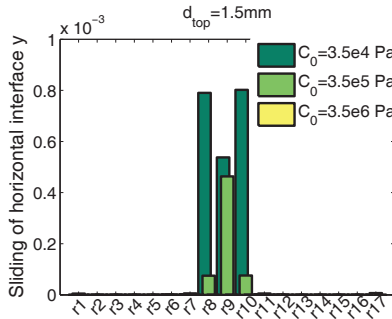
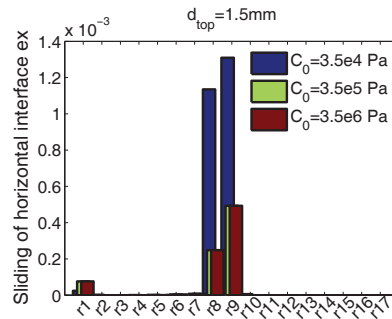


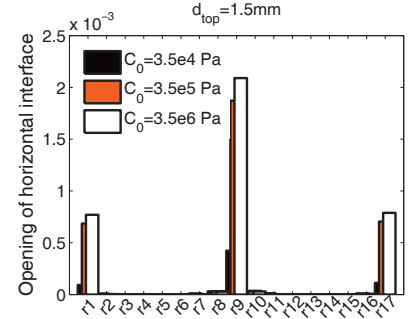
Figure 5.23: Load displacement curve for different C_0 , Case B



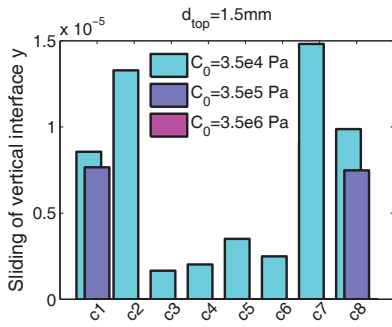
(a) Sliding of horizontal mortars \vec{y}



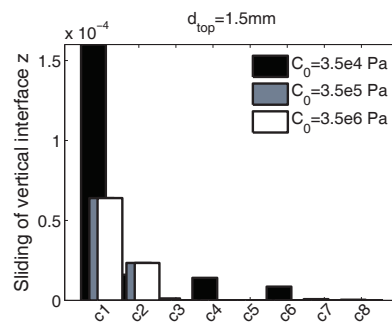
(b) Sliding of horizontal mortars \vec{x}



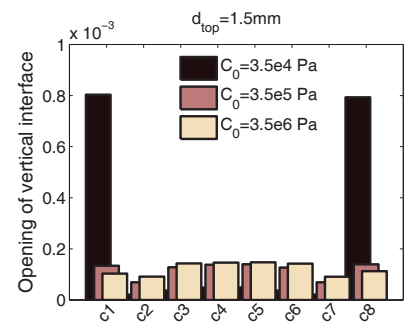
(c) Opening of horizontal mortars



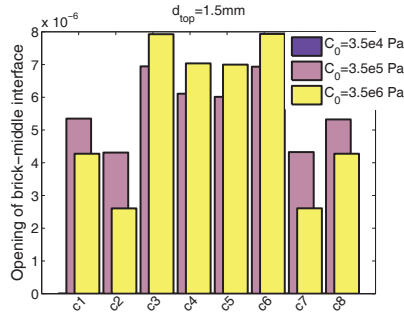
(d) Sliding of vertical mortars \vec{y}



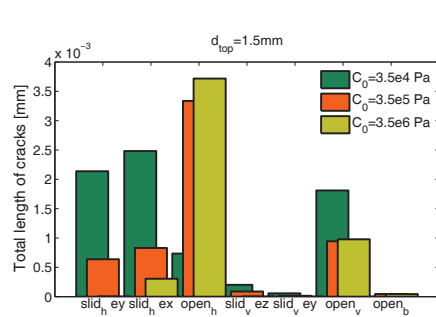
(e) Sliding of vertical mortars \vec{z}



(f) Opening of vertical mortars



(g) Opening of brick interfaces



(h) Total length of crack

Figure 5.24: Length of different types of cracks in different interface elements at rows and columns of walls with different C , Case B

the wall and generally better performance of these walls. The length of sliding cracks in both y and z direction decreases by cohesion increment. Moreover, the distribution of cracks in different columns reduces and lower number of vertical elements slide and in vertical element Figure 5.24(d) and Figure 5.24(e). Opening of two vertical elements at the middle edges of the wall also decreases greatly by cohesion increment. There is a smooth distribution of opening cracks in different columns for the wall with $C_0 = 3.5e5Pa$ and $C_0 = 3.5e6Pa$. Opening of brick-middle interface elements also increases by cohesion's increment. According to Figure 5.24(h), the sliding of horizontal mortars at x and y direction and opening of vertical mortars for the wall with lowest lateral strength $C_0 = 3.5e4Pa$ is greater than the other walls. Hence, it can be concluded that these parameter are very important by increasing the cohesion of mortars their values decrease and wall reacts better under loading.

(b) Initial normal compression

In Figure 5.25, the response of wall for $\sigma_{n0} = 0.05MPa$, $\sigma_{n0} = 0.3MPa$ and $\sigma_{n0} = 2.12MPa$ are illustrated. The horizontal mortar in the end left middle of wall with $\sigma_{n0} = 0.05MPa$ slides in x direction at earlier steps of loading and causes stiffness reduction in the wall. In this case, the opening of mortars at the top, bottom and middle rows of horizontal mortars is significant and the cracks due to sliding and opening of vertical mortar are distributed in rhomboid shape. At $d = 1.27mm$ bricks in the middle of wall fail in tension and the stiffness of wall decreases again. As shown in Figure 5.25 the length of cracks decreases from $\sigma_{n0} = 0.05MPa$ to $\sigma_{n0} = 0.3MPa$ but their distribution changes for $\sigma_{n0} = 2.12MPa$. In this case high opening of vertical mortars in the middle of edge columns in x direction and sliding of horizontal mortars in the middle edges cause damage in the wall.

By increasing the normal stress to $\sigma_{n0} = 2.12MPa$ the opening of horizontal mortars is decreased a lot in all rows. In this case the loaded bricks in corners rotate and separate from the wall and the rest of horizontal mortars do not displace considerable. The amount of this movement can be represented by the length of opening and sliding cracks in adjacent horizontal and vertical mortars. According to pushover curve, the stiffness of wall changes at $d = 0.22mm$ due to sliding of the end right middle brick in x direction. At $d = 0.34mm$, separation of end middle bricks causes reduction of compressive forces in the end columns of bricks. It should be noted that after $d = 1mm$, the lateral strength of wall decreases because of large plastic deformation of some horizontal elements located in the middle of the wall. Thus, as shown in Figures 5.25(a), (b) and (c) as normal stress increment, the wall deforms less and less number of horizontal mortars slide.

Lateral load resistance of wall increases with normal compression enhancement. As shown in Figure 5.26, for low displacements wall with higher pre-compression withstands more lateral shear and is stiffer. The strength of wall is approximately the same at $d = 1.5mm$ for the wall with different initial normal stress, because of different failure mechanisms in each case. As a result, the initial normal stress has a positive influence on performance of wall under out-of-plane loading. By increasing initial normal stress on the wall, the tension failure of horizontal elements

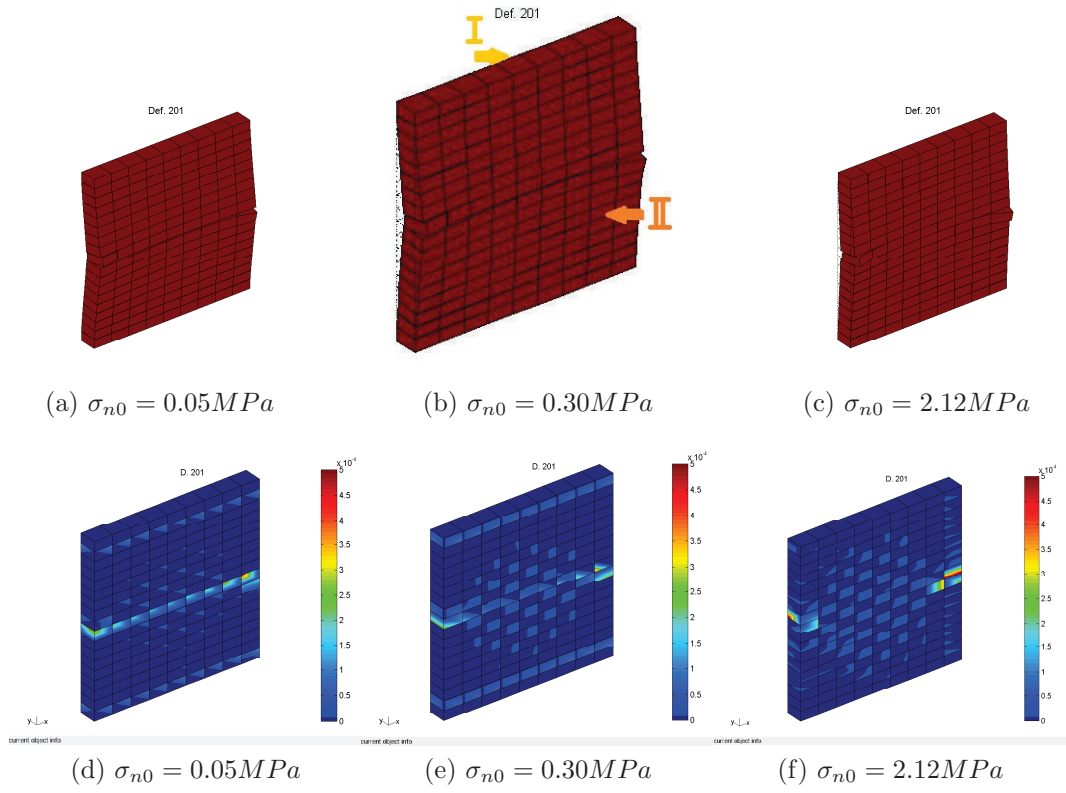


Figure 5.25: Deformation and cracks profile in Case B with different σ_{n0}

postpone.

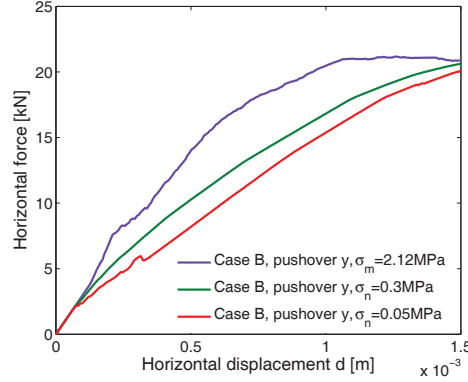


Figure 5.26: Load displacement curve for different σ_{n0} , Case B

The length of cracks in different elements as well as their variation by normal stress are shown in Figure 5.27. According to these figures, opening of horizontal elements decreases by normal stress increment whereas the length of opening cracks in vertical and brick-middle interfaces decrease. It is important to know that boundary conditions and the way that displacements are applied to the wall are very important factors in the response of the wall. For example for the wall with $\sigma_{n0} = 2.12MPa$ high level of normal loads can not prevent the movement of loaded bricks and large plastic deformations in the wall causes reduction of lateral strength in the loaded elements. Figure 5.27(h) the summation of cracks' length at different rows and columns for horizontal and vertical mortars shows that the length of sliding in horizontal mortars and opening in vertical mortars increase by initial normal stress increment because of slipping of two middle corner bricks. High normal stress on the wall can not prevent the opening of beside vertical mortars because of punctual nature of applied displacements. The tension failure of horizontal interfaces has not great influence on behavior of the wall because although its value is very high for $\sigma_{n0} = 0.05MPa$, its maximum lateral strength at $d = 1.5mm$ is approximately the same with other cases.

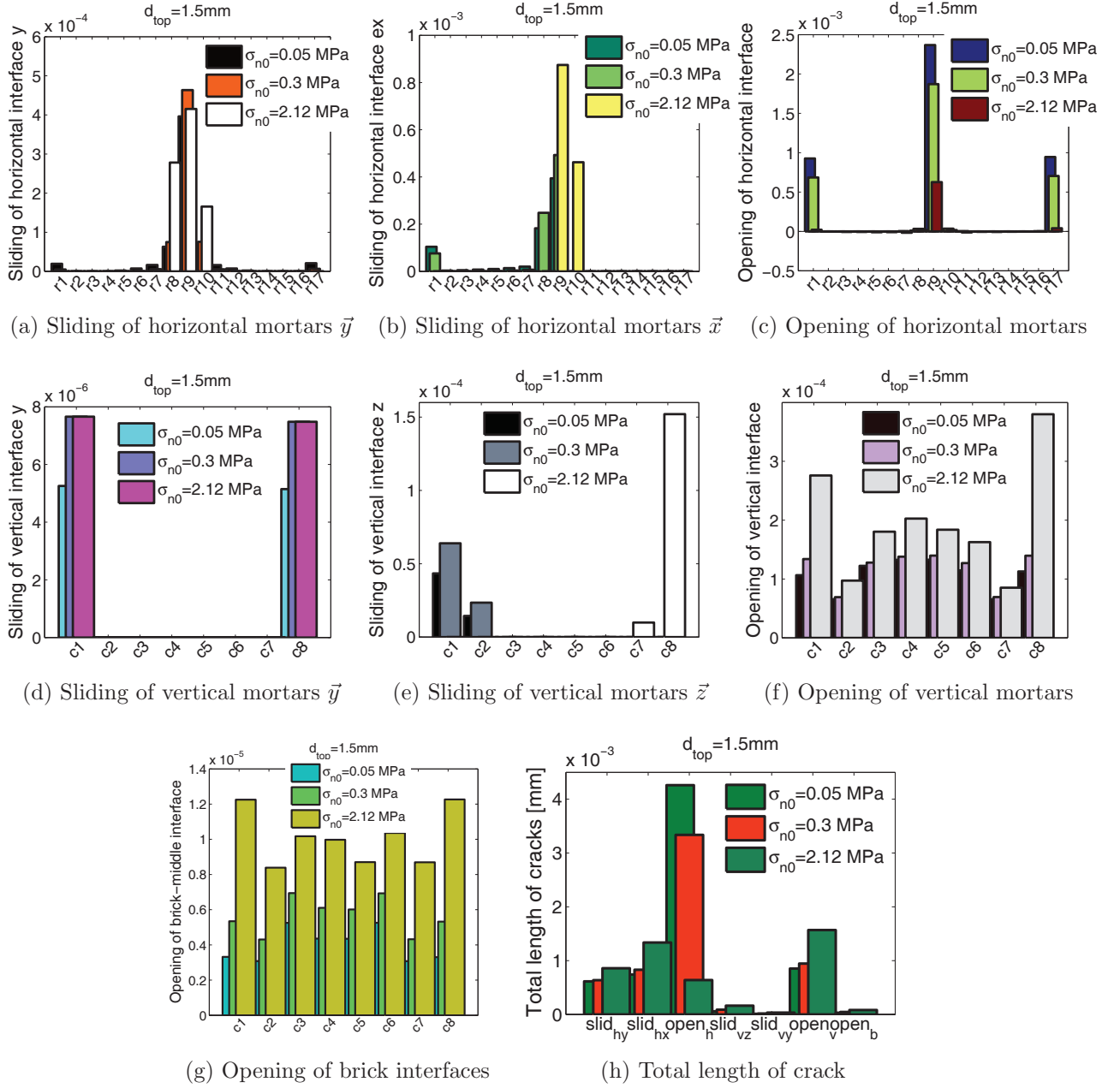


Figure 5.27: Length of different types of cracks in different interface elements at rows and columns of walls with different σ_{n0} , Case B

(c) Compressive strength of masonry

Influence of compressive strength of masonry is the subject of this part. The initial compressive strength of mortars has been changed to $F_{c0} = 5.05e6Pa$ and $F_{c0} = 10.5e7Pa$. Figure 5.28 shows the cracking profile and deformed shape of the walls. The length of cracks in the wall with lower compressive strength $F_{c0} = 5.05e6Pa$ is greater than the other cases. The obtained load-displacement curves for different cases are shown in Figure 5.29.

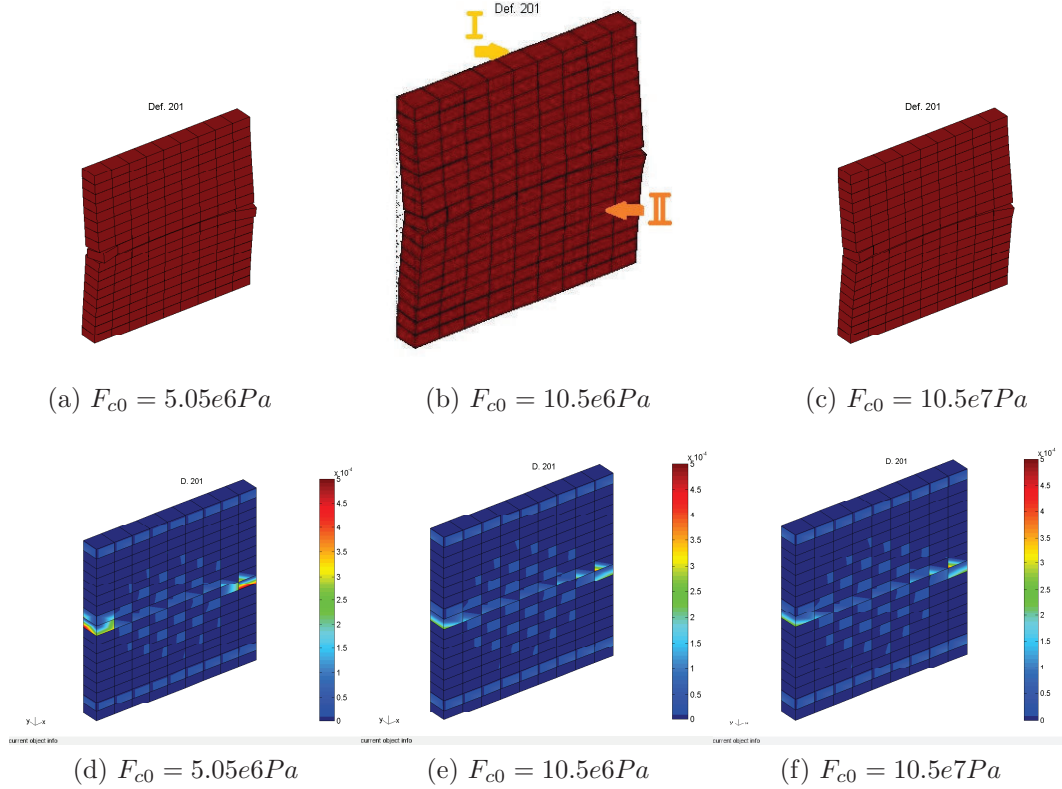


Figure 5.28: Deformation and crack pattern for wall with different F_{c0}

Figure 5.29 proves that multiplying compressive strength 10 times does not change the shear strength of masonry under applied displacement. It does not change the cracking pattern too. Results show that for the wall with low compressive strength $F_{c0} = 5.05e6Pa$ the compressed mortars at the middle edges of the wall crush sooner and the shear strength of the wall reduces. Therefore as shown in Figure 5.29 the shear strength decrease after $d = 1mm$ and mortars slid more. Results show that compression strength of masonry has not important influence on the behavior of the wall under out of plane displacements. This parameter may be important when higher displacements apply to the wall and mortars subject to high normal stresses.

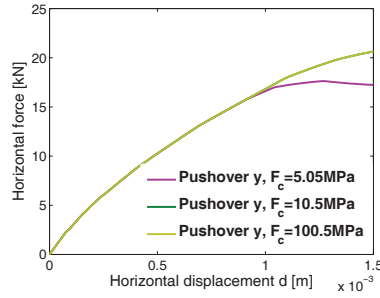
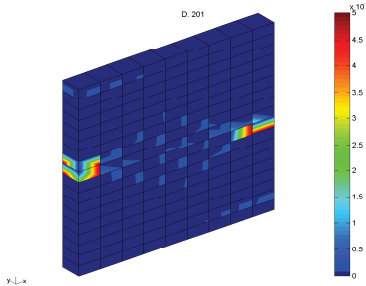


Figure 5.29: Pushover curve for wall with different F_{c0} , Case B

The length of sliding cracks in horizontal and vertical cracks as well as opening cracks in vertical elements and brick-middle interfaces decrease by compression strength increment as shown in Figure 5.30. In the wall with low compressive strength two horizontal interfaces at the left and right middle edges of the wall begin to crush and their lateral strength decreases and slide more. As shown in Figure 5.30(h) for the most vulnerable case, the length of sliding cracks in horizontal and opening cracks in vertical elements are more than the other cases.

The results of this section shows that the cohesion of mortars has the most important role on behavior of masonry wall under such boundary conditions and loading. The opening cracks in vertical interfaces and sliding cracks in two directions in horizontal interfaces are the greatest among all studied cases in this section. The corresponding crack pattern is shown in Table 5.3.

Table 5.3: The crack profile for the damaged walls, Case B

Cracking profile	Specifications	Observed in:
	<ul style="list-style-type: none"> • The cracks concentrated in the middle of the wall • The loaded bricks rotate a lot 	<ul style="list-style-type: none"> • Masonry wall with low cohesion

In this section, two walls with different boundary conditions and loading patterns are subjected to out of plane displacements. A parametric study for each case also has been done to investigate the influence of mortar's cohesion, initial normal stress on the wall and compressive strength of masonry on the wall's response. Results show that increasing all of these parameters enhances the performance of the wall. The level of pre-compression is the most important parameter is most important parameter for Case A because high value of normal stress prevents sliding of

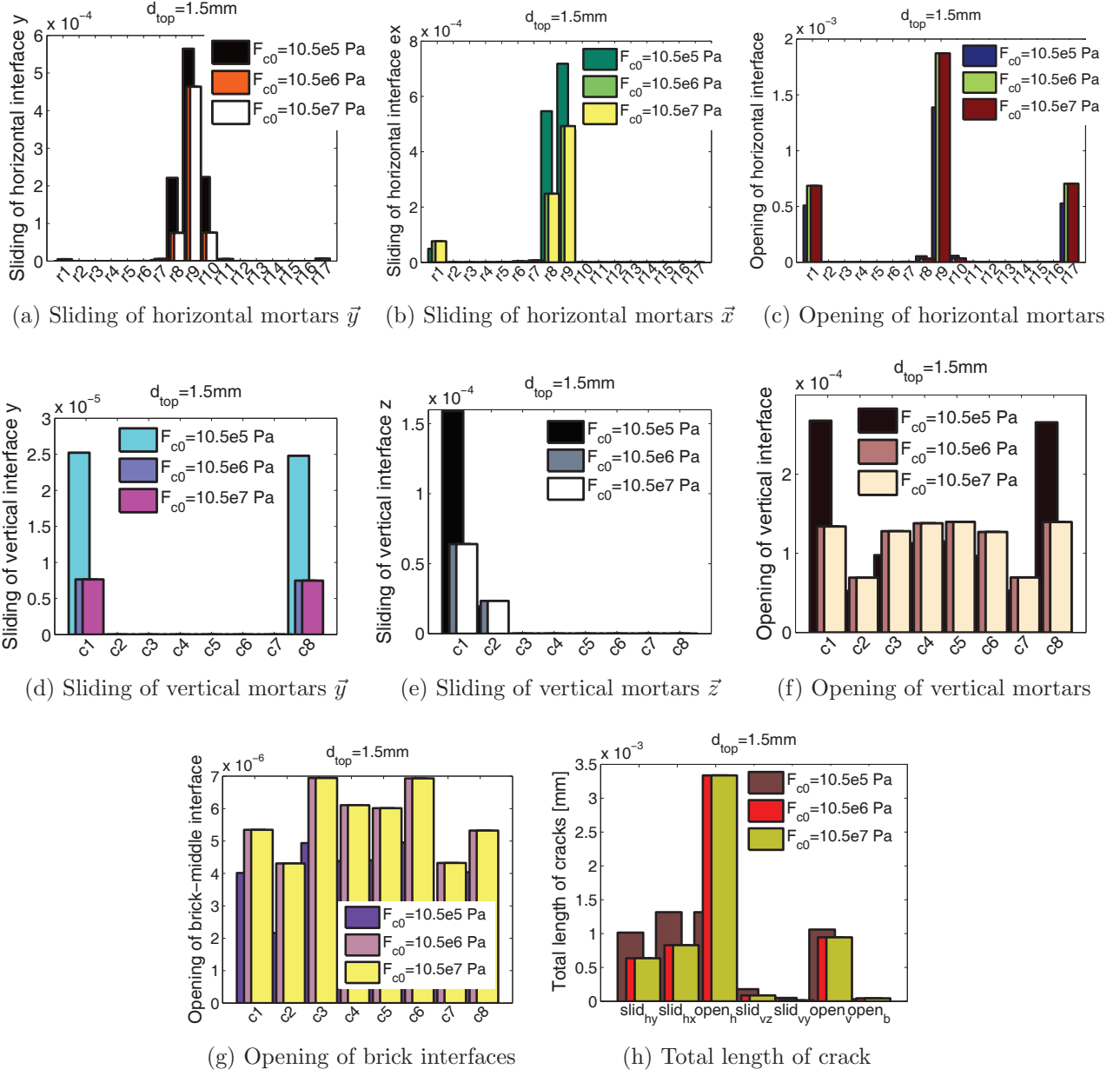


Figure 5.30: Length of different types of cracks in different interface elements at rows and columns of walls with different F_{c0} , Case B

horizontal mortars and opening of vertical mortars whereas mortar's cohesion plays the most important role to the behavior of Case B. It should be noted that applying too high initial normal stress on the wall may cause the concentration of stress on the loaded elements and imposing considerable shear plastic deformations and the lateral strength reduction of the wall. Results show that compressive strength of masonry has the lowest influence on the behavior of wall under out-of-plane displacements for both cases. For having a masonry wall with a good performance under out-of-plane displacements, the sliding cracks of horizontal mortars in parallel and perpendicular directions to the loading and opening of vertical elements should be decreased.

5.3 Behavior of two walls under out-of-plane Loads

In this section the behavior of two perpendicular walls is investigated. In this configuration, applying in-plane loading to a wall imposes out-of-plane loading to the other wall. The two walls has the same geometry $1 \times 1 \times 0.1$ [m^3] as shown in Figure 5.31. The properties of mortars at the walls' connection are the same as those of horizontal and vertical. The properties of mortars and blocks are the same as the validated wall in chapter 3. All top nodes are precluded from vertical movement and $\sigma_{n0} = 0.3MPa$ is applied to the set. The behavior of the set is analyzed first and then the obtained results of a parametric study by changing mortar's cohesion and initial normal stress will be studied.

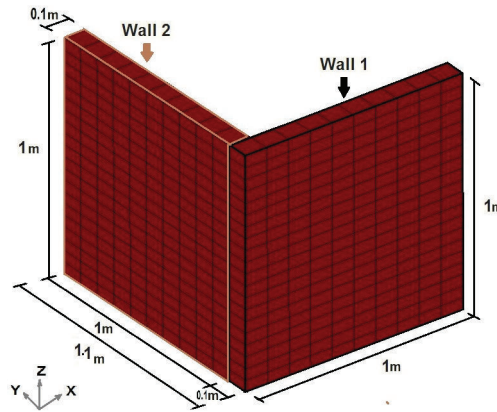


Figure 5.31: Series 1: two perpendicular walls ($1 \times 1 \times 0.1$) subjected to out-of-plane loads

In this study, first the top nodes of Wall 1 are subjected to the incremental in-plane displacements (x direction) up to $2mm$. This loading imposes out-of-plane loads to the Wall 2. Then, the effect of cohesion and initial normal loads on the behavior of the series are investigated. Afterward, a supposed roof is considered for two walls and its movement namely the movement of all top nodes (Wall 1 + Wall 2) in x and y directions as well as its rotation will be studied. In the later one, all top nodes rotates 0.05 degree to simulate roof's movement under earthquake. Next,

effect of walls' length on performance of the set under roof's movement will be studied. Hence, the length of Wall 2 is multiplied times 1.5, see Figure 5.32.

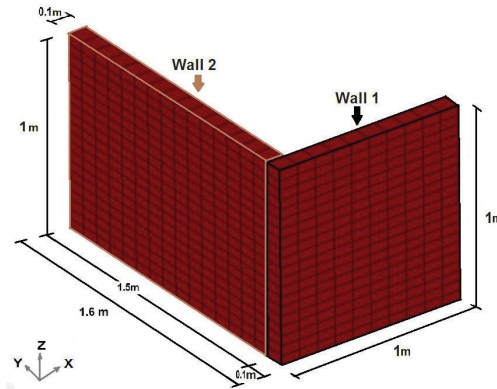


Figure 5.32: Series 2: two perpendicular walls ($1 \times 1 \times 0.1$ and $1.5 \times 1 \times 0.1$) subjected to out-of-plane loads

5.3.1 Series 1: Top nodes of Wall 1 move in x direction

In this section, top nodes of Wall 1 are subjected to in-plane displacement gradually up to $2mm$, so Wall 2 is subjected to out-of-plane displacement equal to $2mm$ at its connection with Wall 1. In order to have a good understanding of what happens in the different walls, those deformations and final crack pattern are shown in Figure 5.33 in different views .

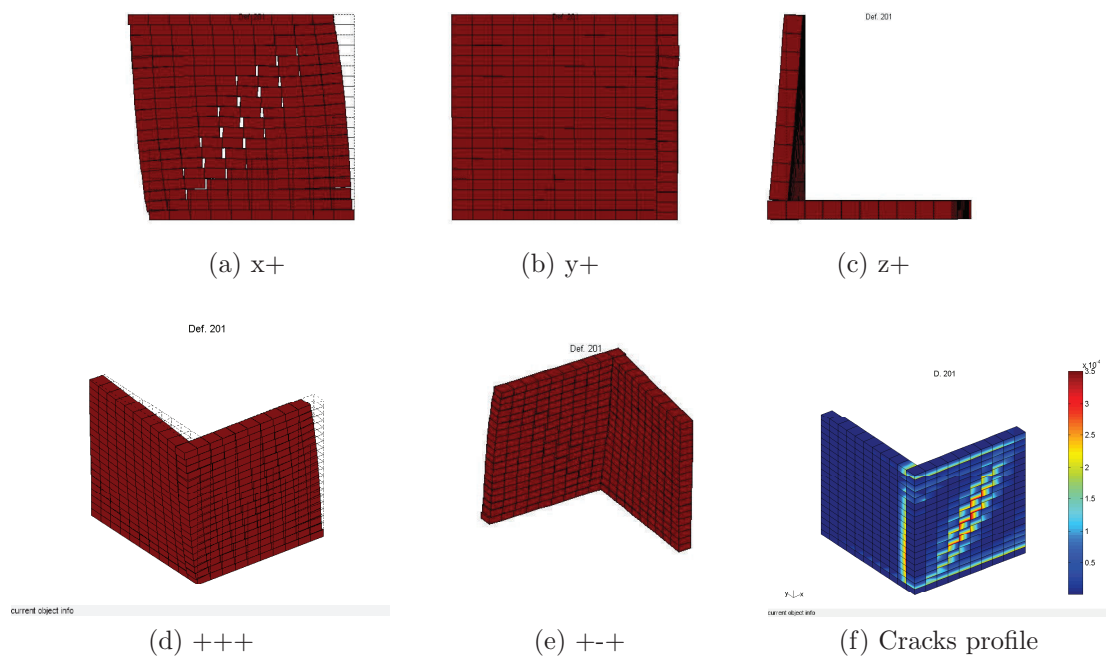


Figure 5.33: Deformation of the set, top nodes of Wall 1 move in x direction, Series 1

As shown in Figure 5.33, applied in-plane displacements to the Wall 1 cause diagonal stepped crack in the wall as predicted. This type of loading forces out of plane movement in Wall 2, see Figure 5.33(c). Due to this loading, the vertical mortars of walls' intersection open and slide as shown in Figure 5.33 and some of the bricks at the connection of walls (rows 2, 16 and 17) also move forward. Out-of-plane displacements on Wall 2 cause tension failure at its lower row of horizontal mortars and opening cracks appear on that. Total crack pattern is illustrated in Figure 5.37(f). As shown in this figure, the length of diagonal crack pattern in Wall 1 is greater than other cracks. Moreover, the loading creates cracks in the joint mortars and the length of cracks in the bottom part of the connection is greater. Base shear versus applied displacement for Wall 1, Wall 2 and the set in x direction, parallel to applied displacements, are illustrated in Figure 5.34. As shown in this figure, Wall 2 has a little strength under out of plane displacements but its existence makes the set stronger against lateral loads. The main resistance of the set comes from Wall 1 to which in-plane displacements are applied.

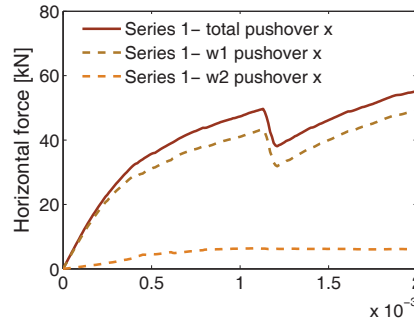


Figure 5.34: Load-displacement curve for the Series 1, Wall 1 moves in x direction

The results show that after applying displacements, firstly the right bottom and left top corners of Wall 1 open and fail in tension. By increasing the displacements the top and bottom rows of horizontal mortars in Wall 1 slide and fail in shear. Then, at $d = 0.48mm$ the vertical mortars in the connection of two walls slide in both y and x directions and mortars open and consequently as shown in Figure 5.34, the stiffness of the Wall 2 under lateral loads decreases considerably. The position of cracks in the set before and after the $d = 0.48mm$ are shown in Figure ???. By increasing the loading at $d = 1.13mm$ diagonal stepped cracks are formed in the Wall 1 and cause a drop in pushover curve of Wall 1. The cracking profile at local peak and drop are shown in Figure 5.36. By increasing the loads the length of cracks increases and at $d = 1.37mm$ walls separates from the lower part of their connection and the lateral strength of Wall 2 decreases again after this point. Thus, as a result, presence of Wall 2 increases the strength of the set under lateral loading but not too much. On the other hand, the resistance of Wall 2 under out-of-plane displacement is insignificant.

Figure 5.37 represents the sliding and opening cracks in different elements. Figure 5.37(h) and (i) also show total cracking pattern in different views. The sliding of horizontal elements mainly

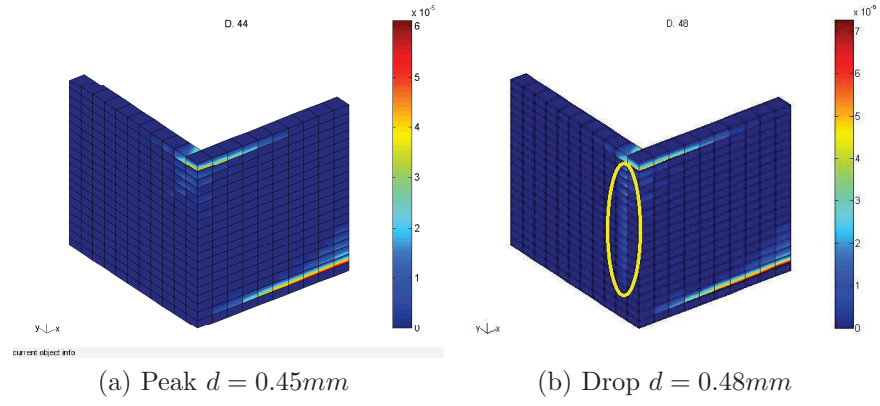


Figure 5.35: Crack pattern of the set before and after stiffness reduction in Wall 2, Series 1

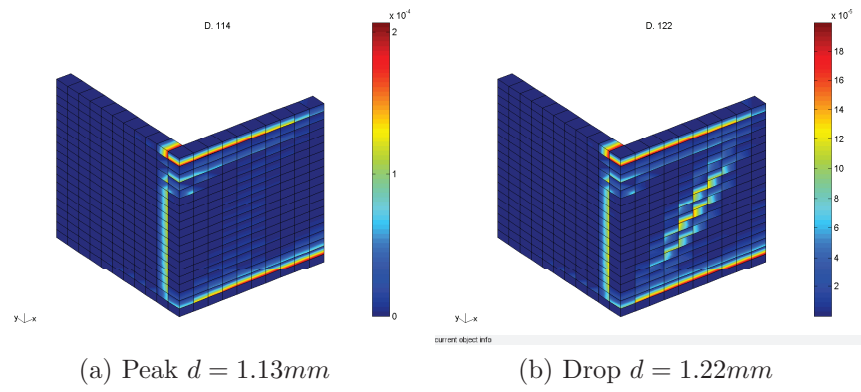


Figure 5.36: Crack pattern of Wall 1 at local peak and drop, Series 1

takes place in Wall 1. As shown in this figure, top and bottom rows of horizontal mortars as well as the mortars placed in diagonal of Wall 1 experienced more shear failure. The horizontal mortars located in the corners and diagonal of Wall 1 as well as top and bottom rows of Wall 2 fail in tension and open as shown in Figure 5.37(c). The vertical mortars in walls' connection open represented in Figure 5.37(c). Sliding and opening of vertical mortars are presented in Figures 5.37(d), (e) and (f). Figure 5.37(g) shows that just the bricks in diagonal of Wall 1 fail in tension.

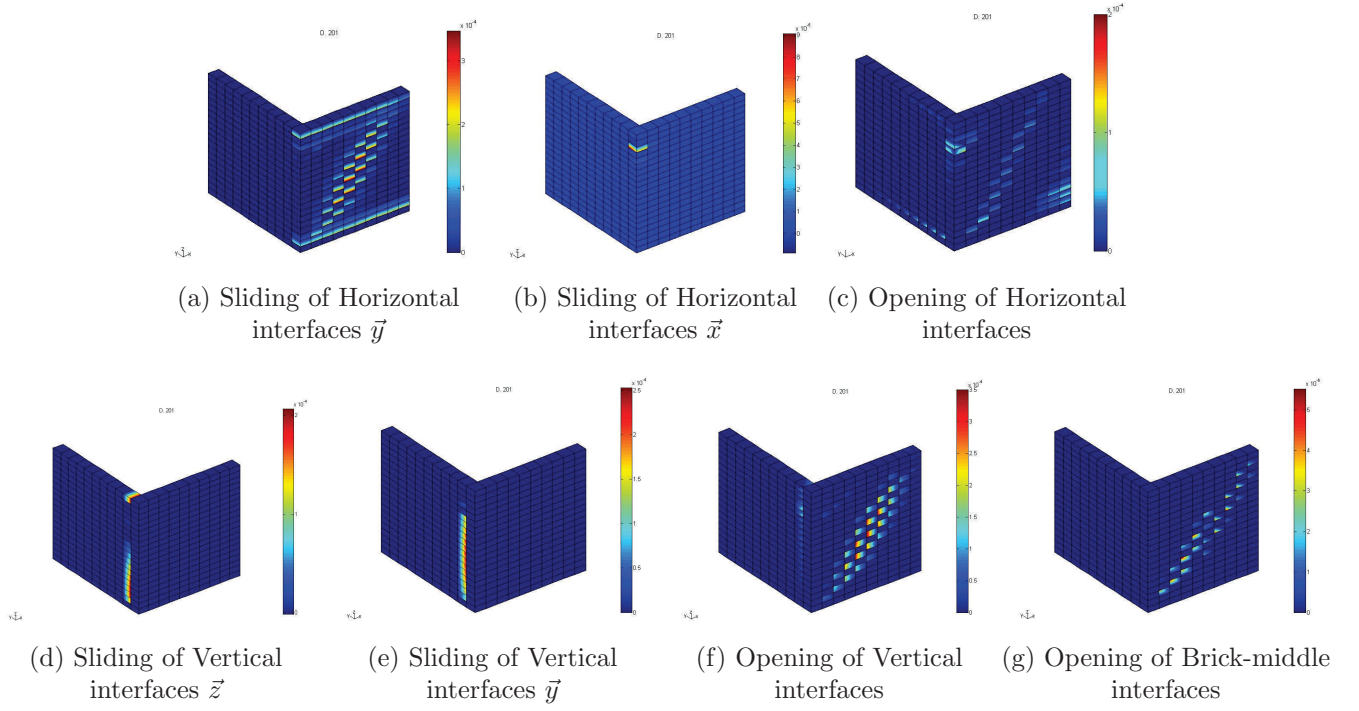


Figure 5.37: Crack pattern in the masonry walls $d = 2mm$, Series 1

5.3.2 Parametric study on Series 1: displacement applied to Wall 1

In this part a parametric study by variation of mortar's cohesion and initial normal loads on the wall has been done. It should be noted that displacements are just applied to Wall 1 in x direction. The cohesion of all mortars are changed to $C_0 = 1e5Pa$ and $C_0 = 7e5Pa$ respectively while the effect of pre-compression on behavior of complex is investigated by setting normal stress to $\sigma_n = 0.05MPa$ and $\sigma_n = 2.12MPa$. The pushover curves, total crack pattern and final deformed shape are represented here for different cases are represented in the following.

(a) Cohesion of Mortars

Deformed shape and total crack pattern for the Series 1 with different cohesion values are displayed in Figure 5.38. The first case corresponds to walls with $C_0 = 1.0e5 Pa$. In this case, the diagonal cracks appear in the wall at $d = 0.42mm$ whereas they formed at $d = 1.13mm$ in the wall with $C_0 = 3.5e5 Pa$. Hence, formation of diagonal cracks decreases the lateral strength of the Wall 1. Thus, decrease of cohesion causes diagonal cracks to happen sooner. By increment of displacements, the size of diagonal cracks as well as cracks in the intersection of walls increases. In this case maximum cracks correspond to the sliding of top vertical mortar of the walls' joint whereas the maximum value of cracks for walls with $C_0 = 3.5e5 Pa$, happens in diagonal region. In pushover curve, y label represents the summation of horizontal force of all nodes at the base of the set in x direction. Walls slide from the top vertical mortar in intersection at $d = 0.22mm$ and the stiffness of the set decreased. Moreover, at this point walls begin to slid at their intersection and the lateral strength of Wall 2 also reduces.

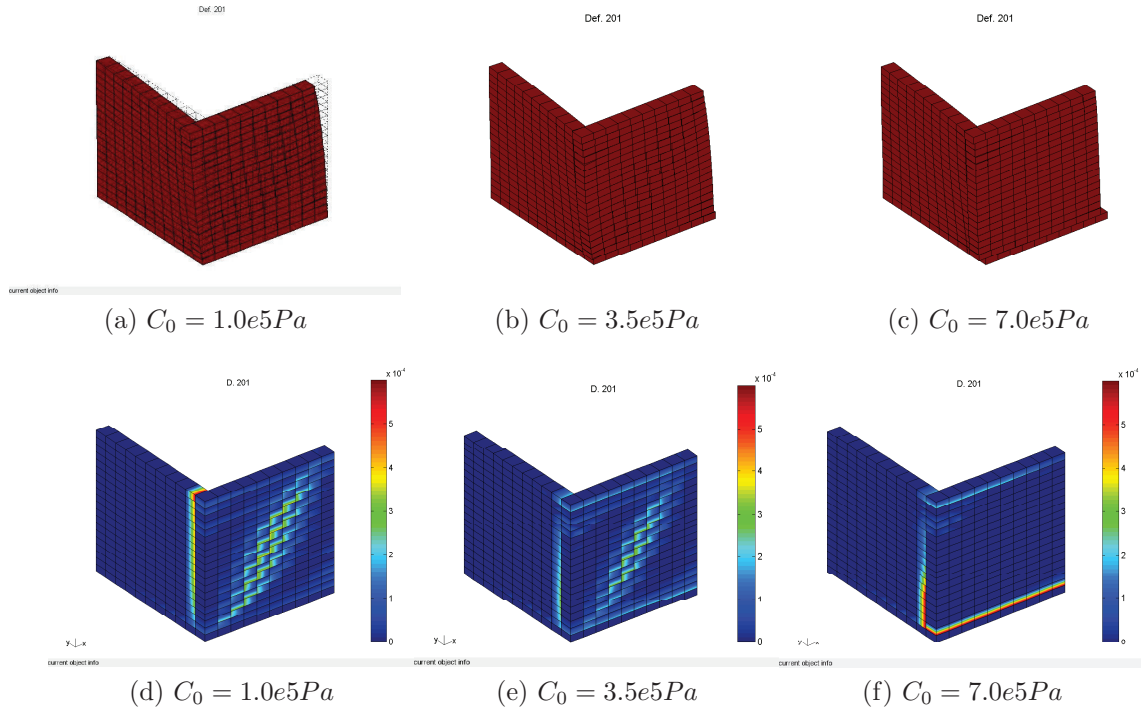


Figure 5.38: Deformation and crack pattern for Series 1 with different C_0 , displacements are applied to Wall 1

By modeling the masonry complex with $C_0 = 7.0e5$, diagonal cracks are not formed in the wall and the Wall 1 slips on its lowest row of horizontal mortars. The failure mechanism in this case is sliding shear failure and the set exhibits the brittle behavior. The pushover curve of Walls 1, 2 and the set are shown in Figure 5.40 separately. In this case by applying the displacements to the Wall 1, the horizontal mortars at bottom right of the Wall 1 and top left intersection fail in tension and shear at earlier steps. Afterward, by increasing the loads, at $d = 0.82mm$ the vertical mortars at the connection of two walls slide and open and the lateral strength of the

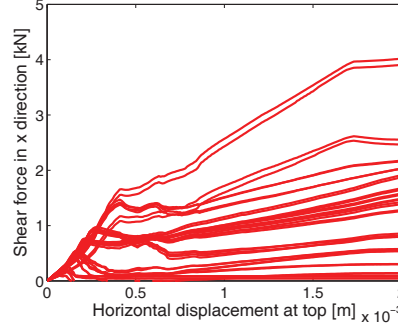


Figure 5.39: Pushover curve for the wall 1 in the set with $C_0 = 1e5Pa$

Wall 2 reduces considerably. Next, at $d = 1.54mm$, the horizontal mortar at the bottom left of the wall crush due to high level of compression strength. Hence, the horizontal mortars at the first row of Wall 1 slide considerably and walls separate. The jump in pushover curve of Wall 1 is because of this phenomenon. The minor principal stress before and after the jump are shown in Figure 5.41. As can be seen in this figure, the minor principal stress after crushing of horizontal element decreases.

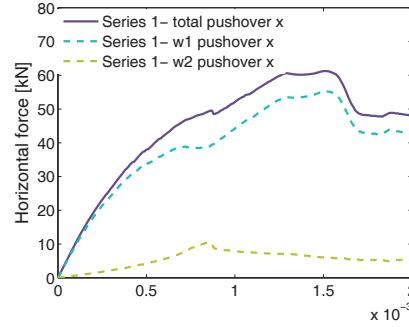


Figure 5.40: Pushover curve for the case $C_0 = 7.0e5Pa$, Series 1, Wall 1 loaded in x direction

The maximum length of cracks is set to a fixed number for all cases to have a easier comparison. For the wall with $C_0 = 1e5Pa$, the length of diagonal cracks increases and the mortars in intersection of walls slip and open considerably. Thus, cohesion increment causes reduction in the length of cracks in the walls as well as in the vertical mortars at the walls' connection. Pushover curves, for walls with different cohesion values are drawn in Figure 5.42. The series with $C_0 = 7e5Pa$ undergoes greater lateral strength but slipping of Wall 1 in the last case causes a brittle sliding shear failure in the system. The relative displacement between two walls also is reduced by cohesion increase. In order to have a good understanding about the pushover curve of the set with $C_0 = 1e5Pa$, the shear forces of each node at the base of wall 1 are drawn in Figure 5.39. The summation of shear forces of these nodes makes the base shear of Wall 1. As

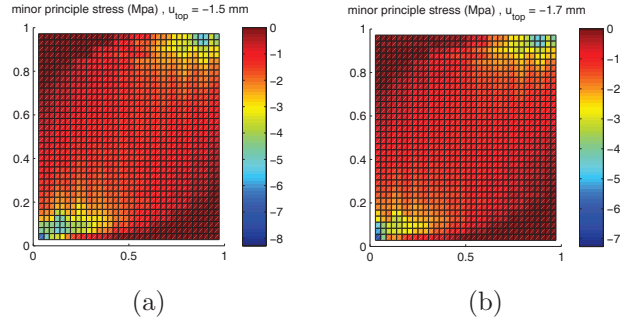


Figure 5.41: Minor principal stress (a) $d = 1.54$ (b) $d = 1.72$

can be seen in this figure, formation of diagonal cracks in the Wall 1 and setting all stresses to zero in the vertical elements cause a drop in lateral force-displacement curve of all nodes except in nodes which are located at the bottom left of the Wall 1 and are attached to the Wall 2. The formation of diagonal cracks causes stiffness reduction in these nodes and at $d = 1.74mm$ initiation of negative plastic displacements in corresponding horizontal element causes another stiffness reduction in these nodes.

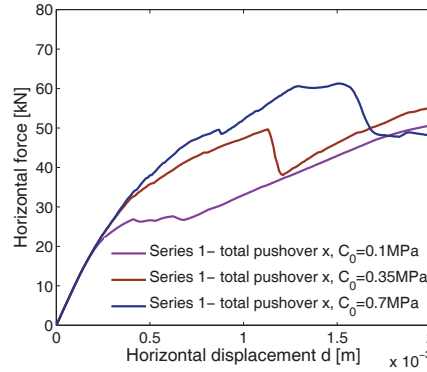


Figure 5.42: Pushover curve for different C_0 , Series 1, Wall 1 loaded in x direction

(b) Initial normal stress

The effect of normal stress on the behavior of complex is studied in this part. In the set with $\sigma_{n0} = 0.05MPa$ after applying the displacements, the top and bottom rows of Wall 1 open and slide and by increasing the displacements at earlier steps. In the obtained pushover curve Figure 5.44 the first reduction in the stiffness of the set is due to these opening and sliding cracks. Thereupon, at $d = 0.6mm$, the Wall 1 slips on its first row of horizontal mortars and the lateral strength of the wall decreases considerably. As can be seen in pushover curve, the set exhibit brittle behavior under low normal stresses. Consequently, two walls separate and their

intersection slides in the bottom part. The vertical mortars at the intersection of two walls slide in both directions at its bottom part and open at its upper part. In this case, bricks do not fail in tension.

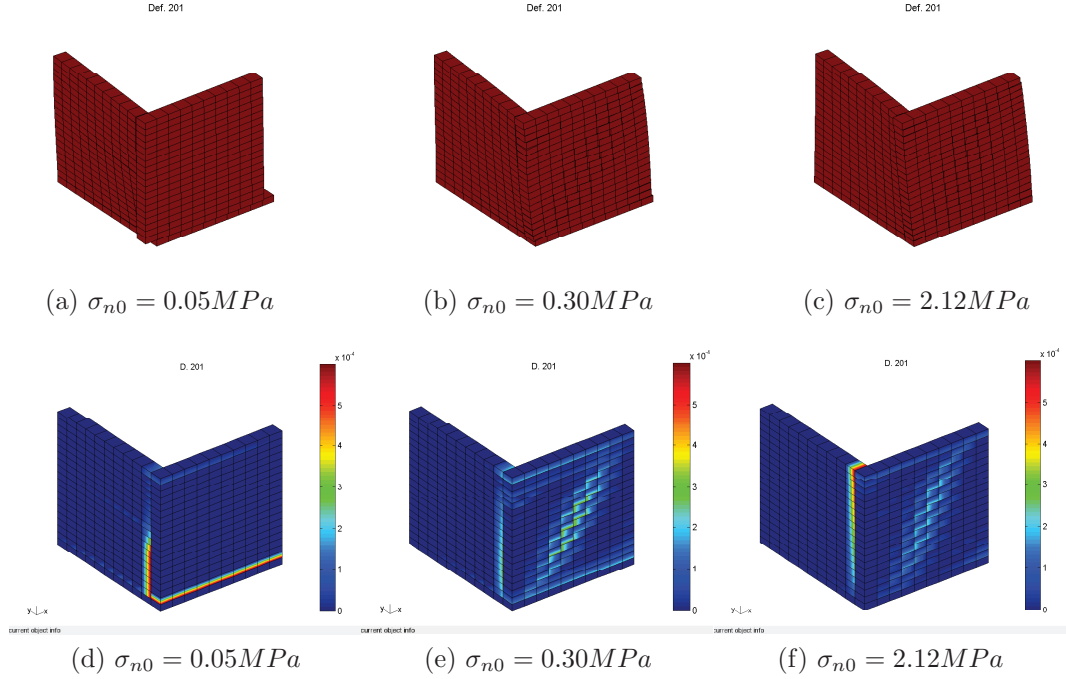


Figure 5.43: Deformation and crack pattern for Series 1 with different σ_{n0} , displacements are applied to Wall 1

As demonstrated in Figure 5.43 in the set with $\sigma_{n0} = 2.12 MPa$, the relative displacement and length of cracks in the set decrease by normal stress increment. In this case, cracks develop first in the walls intersection at $d = 0.7mm$ and thus the stiffness of the set reduces at this point as shown in Figure 5.44. By increasing the displacement, first horizontal mortars in the top left and bottom right corners of Wall 1 open and slide. Then, at $d = 1.46mm$ the diagonal cracks are formed in the Wall 1 and lateral strength of the assembly decreases, see Figure 5.44. Finally at $d = 1.7mm$ walls separate and moves individually. In this case, the horizontal cracks at top and bottom rows of Wall 1 decrease a lot and just the diagonal cracks are created in the wall. The normal stress increment also increases the resistance of Wall 2 under out-of-plane displacements. By comparing the obtained load-displacements of different sets it can be concluded that the shear strength of horizontal mortars increases by normal stress increment. But, initial normal stress increment has not significant effect on the movement of vertical mortars in the joint and in this case, they move considerable.

As a result, the failure mechanism also may change by variation of initial pre-compression value. The set with low normal stress show brittle performance while the wall with high normal stress

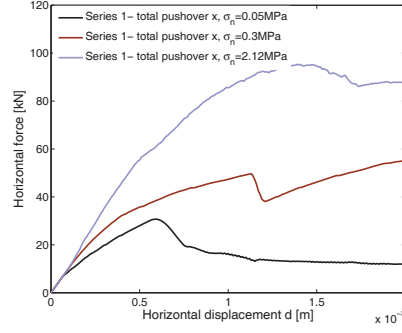


Figure 5.44: Pushover curve for different σ_{n0} , Series 1, Wall 1 loaded in x direction

exhibits ductile performance. As shown in the figures, walls with lower value of initial normal stresses undergoes considerably lower shear strength than the wall with higher initial normal stresses and initiation of cracks in the mortars happens sooner than that of the set with higher initial normal stress. Hence, the normal stress has a great influence on the behavior of masonry walls both under in-plane and out-of-plane loading.

In this section the effect of mortar's cohesion and initial normal loads on the behavior of two perpendicular walls under specific loading condition was investigated. Obtained results showed that both cohesion of mortars and initial normal stress have very important role to the behavior of walls under in-plane and out-of-plane loadings. These parameters enhance the performance of wall under both types of loading. It was shown that the influence of normal stress on behavior of two perpendicular walls is greater than wall's cohesion. The studies show that the properties of mortars in walls' joint may have a significant influence on the performance of the system. By using the mortars with higher cohesion in the intersection of the walls the integrity of the system will be preserved under larger loads and thus the system carries out larger displacements.

5.3.3 Series 1: roof's movement simulation

Presence of a rigid roof with appropriate connections to the walls in masonry constructions causes the surrounding walls to be subjected to the same displacement as that of the roof in different directions. Hence, for simulating the behavior of a system with a rigid roof, all top nodes are submitted to the same displacements as the roof's center of gravity. This section is composed of three different types of movement. First, all top nodes belong to Wall 1 and Wall 2 are subjected to the same displacements in x direction. The displacements (in-plane for Wall 1 and out-of-plane for Wall 2) are gradually applied to the set from 0 to 2mm. As the length of the series 1 in x and y direction is not the same, to study the difference arises from this variation, the same displacements are imposed to the top nodes in y direction. Finally the rotation of roof is simulated by applying different displacements in x and y directions to the top nodes. The roof's center of gravity supposed to rotate 0.05 degree anticlockwise. Maximum displacement in x and

y directions are $4.8mm$ and $4.38mm$ respectively which are applied to different nodes according to their position with respect to roof's center of gravity. The results are represented in following sections. It should be noted that for all cases, the initial normal stress equal to $\sigma_n = 0.3MPa$ are applied to the walls.

Series 1: displacements are applied to all top nodes in x direction

The results of numerical study on the behavior of the set when all top nodes move $d = 2mm$ in x direction are represented here. The deformed shape in different planes as well as total crack pattern is shown in Figure 5.45. As illustrated in this figure, Wall 1 slips on its first row of horizontal mortars. As can be seen in the figure, walls separate from the bottom part of intersection and some stepped cracks with small length also are observed at top left corner of Wall 1. Some cracks at bottom and top rows of Wall 2 also appears but their value is negligible compared to the sliding of Wall 1. By applying the loads, the cracks are created firstly in the bottom right of Wall 1 and the top common corner of walls. Cracks grow as applied displacements increase. Then at $0.5mm$ stepped cracks at the Wall 1 top left corner initiate and develop to the top horizontal mortars of Wall 1. Afterward, lower joints mortars slide and grow upward. Finally Wall 1 slips completely on its lower horizontal mortars at $d = 1.12mm$ and as a result the lateral load carried out by the system decreases as shown in load-displacement curve Fig 5.47.

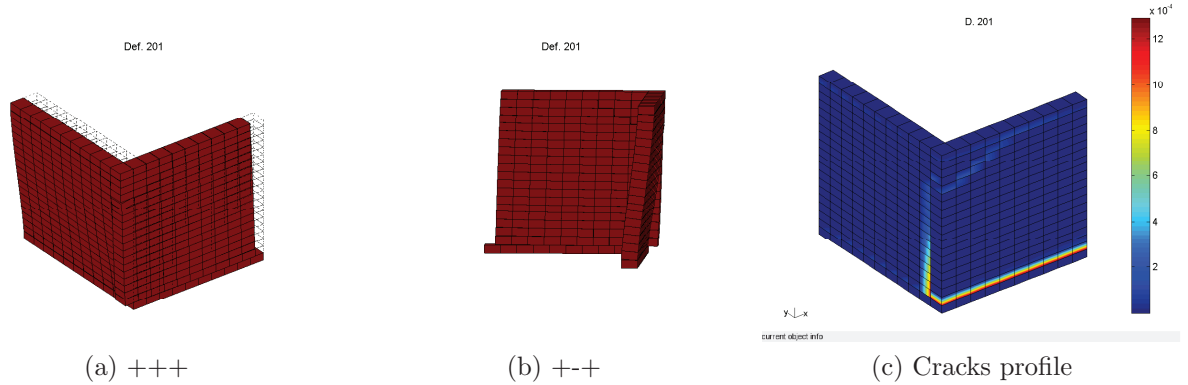


Figure 5.45: Deformation in different planes, Series 1, $d = 2mm$, all top nodes move in x direction

The deformed shape of this set is compared to that of in previous section in which just top nodes of Wall 1 were subjected to displacement in x direction, see Figure 5.46. According to this figure, in the later one, diagonal cracks are not formed in the Wall 1, the behavior of the set is brittle and the failure mechanism is sliding shear failure while in the former one, diagonal cracks appear in the wall and the failure mechanism is tension-shear and the system undergoes greater lateral strength.

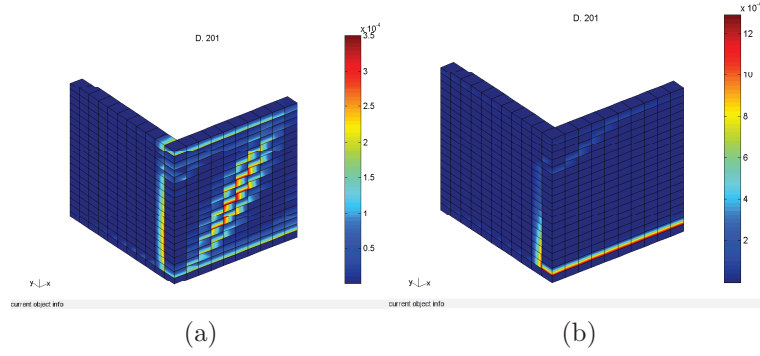


Figure 5.46: Crack's pattern for Series 1 (a) Wall 1 subjected to u_x (b) Walls 1 and 2 subjected to u_x

Detailed pushover curves for Wall 1, Wall 2 and total set for this case as well as a comparison between the load-displacement curves for both cases are displayed in Figure 5.47. According to Figure 5.47(a), a large part of shear loads are sustained by Wall 1 and it proves that the resistance of wall under in-plane loads is much higher than that of under out-of-plane loads. The first stiffness reduction in pushover curve of Wall 1 at $d = 0.42$ corresponds the sliding shear failure of some of horizontal mortars at the first row. The sliding failure of mortars in the bottom part of walls' connection reduces the lateral strength of Wall 2 at $d = 0.91mm$. Finally, at $d = 1.12mm$ all horizontal mortars in the first row slide and the lateral strength of the wall decreases after that point. Comparison between results of the set with different loading condition at Figure 5.47(b) shows that the set in which just one wall was subjected to the loads undergoes greater lateral strength under loads.

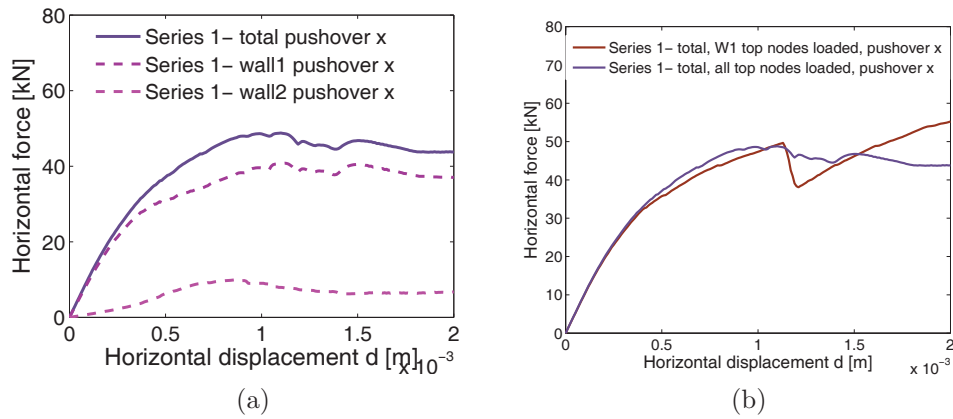


Figure 5.47: Load displacement curves for Series 1 (a) all top nodes are loaded in x direction (b) comparison between two cases: Series 1, all nodes loaded and Wall 1 top nodes are loaded in x direction

Series 1: displacement are applied to all top nodes in y direction

In this section, top nodes of Wall 1 and Wall 2 are subjected to the same displacements in y direction. Although the length of Wall 1 and Wall 2 is the same and is $1mm$, as shown in Figure 5.31, the total length in y direction is 1.1 which is summation of Wall 2 length and Wall 1 thickness. Deformed shape results from such loading as well as total crack patterns formed in the walls at $d = 2mm$ are shown in Figure 5.48. As shown in this figure, top row of horizontal mortars in Wall 2 slides and causes separation of two walls.

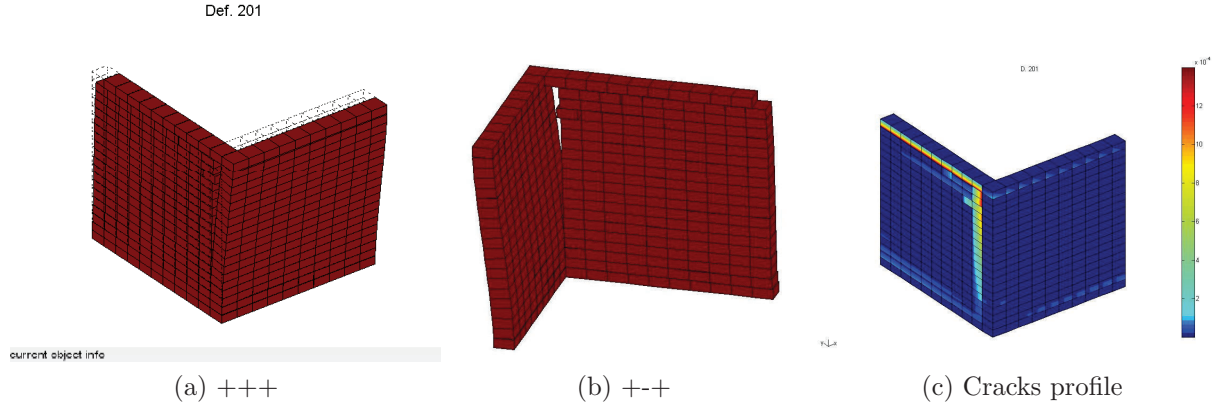


Figure 5.48: Deformation in different planes, Series 1, $d = 2mm$, all top nodes move in y direction

By applying displacements in y direction to the top nodes, first some cracks in bottom right of Wall 1 and top corner of the intersection are formed. By increasing the displacement, the cracks grow and their length increase and then at $d = 0.7mm$ vertical mortars at the intersection of walls slide and open and Wall 1 loses its lateral strength after this point as shown in the pushover curve Figure 5.49(a). Finally, the top row of horizontal mortars in Wall 2 slip $d = 1.25mm$ and causes a drop in load-displacement curve of Wall 2, see Figure 5.49(a). Total cracks pattern of walls is shown in Figure 5.48(c). Since the size of the set in y direction is greater than x direction, its lateral strength is different in x and y directions.

Figure 5.49(b) represents a comparison between load-displacement curves of Series 1 under displacement in y and x directions. As illustrated in this figure, the set has greater lateral strength when subjected to displacements in x direction. Results show that all with higher aspect ratio subjected to in-plane displacements sliding shear failure of the loaded wall causes its brittle behavior. The strength of walls when subjected to out-of-plane loads and in-plane loads, are compared in Figure 5.50.

In Figure 5.50(a), pushover curves of Wall 2 in y direction (in-plane) is represented by solid blue one whereas the solid violet curve deposes pushover curve of Wall 1 subjected to displacements

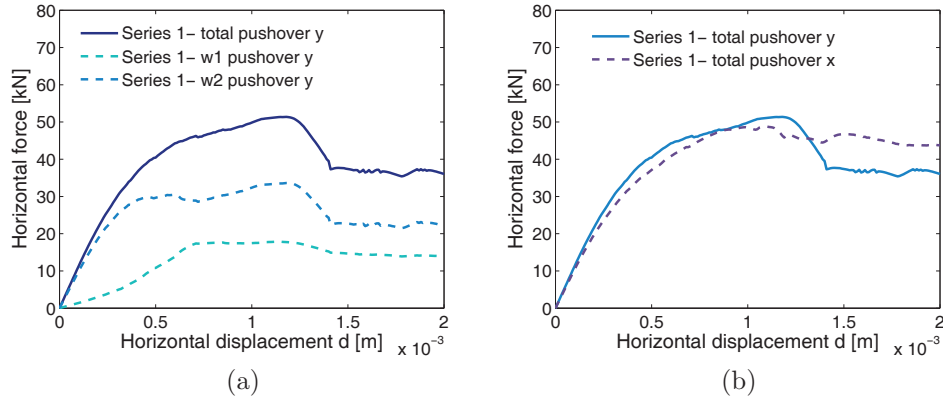


Figure 5.49: Load displacement curve for Series 1 (a) all top nodes are loaded in y direction (b) comparison between two cases: Series 1, all nodes move in x direction and all nodes move in y direction

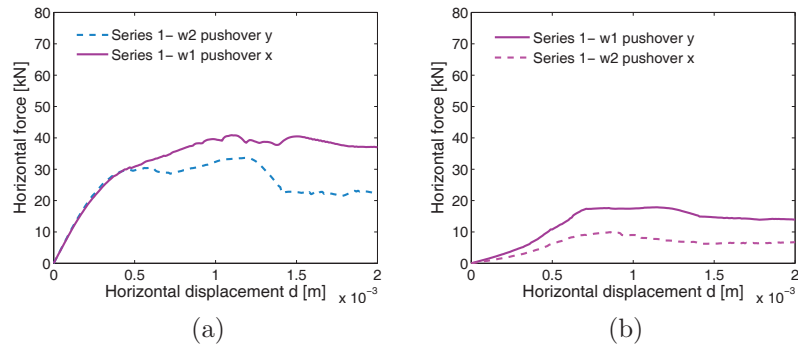


Figure 5.50: Load displacement curve comparison: (a) walls subjected to in-plane displacements (b) walls are subjected to out-of-plane displacements

in x direction (in-plane). This figure shows that the wall with higher length has lower strength against in-plane loads because of sliding shear failure of the top row of horizontal mortars. In this case, vertical mortars at the connection of walls also move significantly greater than the other case. In Figure 5.50(a) the greater length of the set carries out lower lateral loads. Hence, it can be concluded that the geometry of the walls in a set has an important influence on its performance.

Series 1: roof's center of gravity rotates 0.05 degree

In this part, the center of gravity of supposed roof rotates 0.05 degree. The movement of top nodes in y and x directions is determined according to the distance of each node to the center of gravity. The final deformed shape in x, y, z and two other planes are represented in Figure 5.51. According to this figure, top horizontal mortar row of Wall 2 slide, the walls separate and different series of stepped cracks also propagate in the Wall 1.

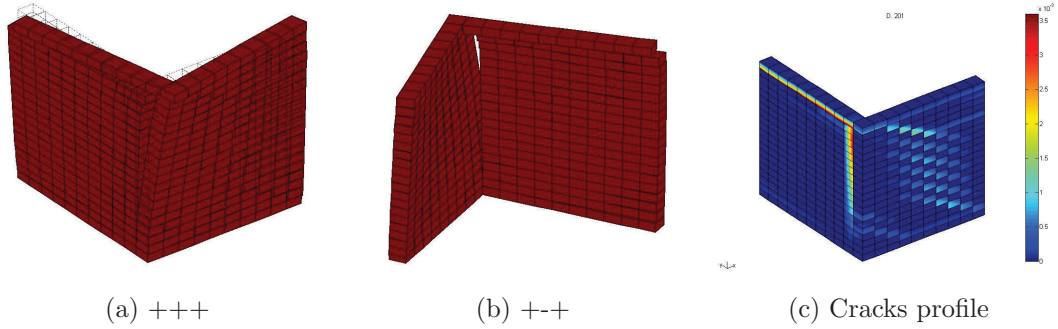


Figure 5.51: Deformation and total crack pattern for walls subjected to 0.05 degree rotation, Series 1

The resistance of the set under shear deformations in x and y directions are displayed separately in Figure 5.52(a) and Figure 5.52(b). Vertical axis represents the summation of shear forces in the base nodes in x and y directions for figures (a) and (b) whereas the deformation of node 8 (1, 0, 1) top corner of Wall 1 in x and y direction respectively, is shown in x axis. As shown in Figure 5.51(a) the rotation of roof imposes positive and negative displacements in x direction to different nodes of Wall 2 and the corresponding load-displacement curve in x direction is negligible comparing to that of Wall 1. By applying the rotation, the vertical mortars in the intersection of the wall slide very soon and right after a stepped diagonal cracks appear in the Wall 1. Hence, the reduction of the stiffness of the Wall 1 at $d = 0.31mm$ (node 8 deformation in x direction) corresponds to formation of first stepped cracks at the top left corner of Wall 1. Sudden drop in pushover curve in x direction of the set at $d = 1mm$ is associated with the creation of diagonal cracks in the middle of Wall 1. Then, the shear strength of the set increases by increasing the rotation until $d = 4.5mm$ which compression failure happens in the bottom right horizontal mortar of Wall 1.

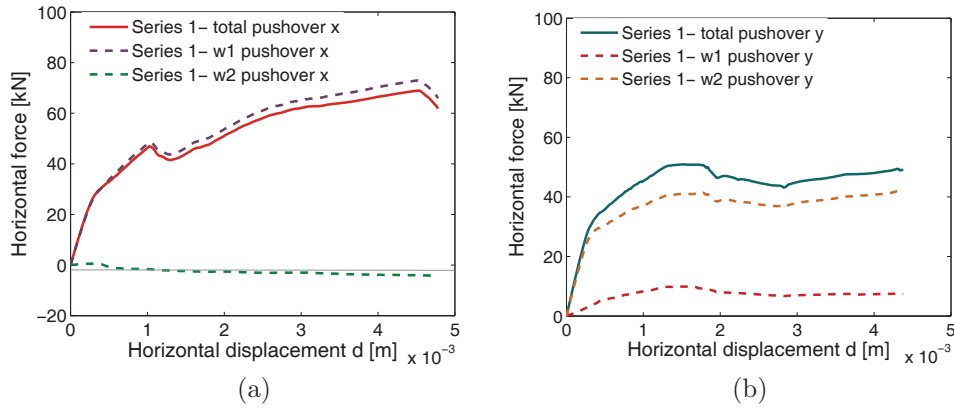


Figure 5.52: Lateral load-displacement curves of walls in (a) x direction (b) y direction, Series 1, 0.05 degree rotation

As displayed in Figure 5.52(b) the walls stiffness in y direction decreases at $0.44mm$ (displacement of node 8 in y direction) when the intersection of walls begins to slide. At $d = 1.3mm$ the shear strength remains constant because the Wall 2 separates from Wall 1 in 5 rows of bricks in upper top of walls connection. After $d = 1.8mm$ top row of horizontal mortars in Wall 2 slip and almost rotates separately from the other parts of Wall 2. The resistance of system in x direction is more than y direction because of the geometry of walls.

Cracking profile for vertical, horizontal and brick-middle interfaces are shown in Figure 5.53. The horizontal mortars in top row of Wall 2 slid whereas some stepped cracks propagate in the middle part of Wall 1 as shown in Figure 5.53(a). Sliding of horizontal mortars mainly happens in top mortars of Wall 2. Some of horizontal mortars at the lower part of connection also experience such shear failure. Horizontal mortars located in the corners open and fail in tension. In addition, some horizontal mortars in the middle part of Wall 1 also open, see Figure 5.53(c). Vertical mortars located at the walls connection, slid in both shear direction as illustrated in Figure 5.53(d) and (e). The walls separated from the upper side of connection as demonstrated in Figure 5.53(f). The opened vertical mortars are also shown in this figure. A lot of bricks in the Wall 1 with lower dimension also fail in tension due to roof's rotation. The obtained results show that the wall with lower dimension undergoes more lateral strength in rotation because of the different failure mechanism with the other wall.

5.3.4 Series 2: roof movement simulation

In this part, the effect of length of walls on behavior of the set is studied. Hence, as shown in the Figure 5.32, the length of Wall 2 is multiplied by 1.5. The dimension of set is: $1.6m$ length in y direction, $1m$ length in x direction and $0.1m$ thickness. In this section similar to

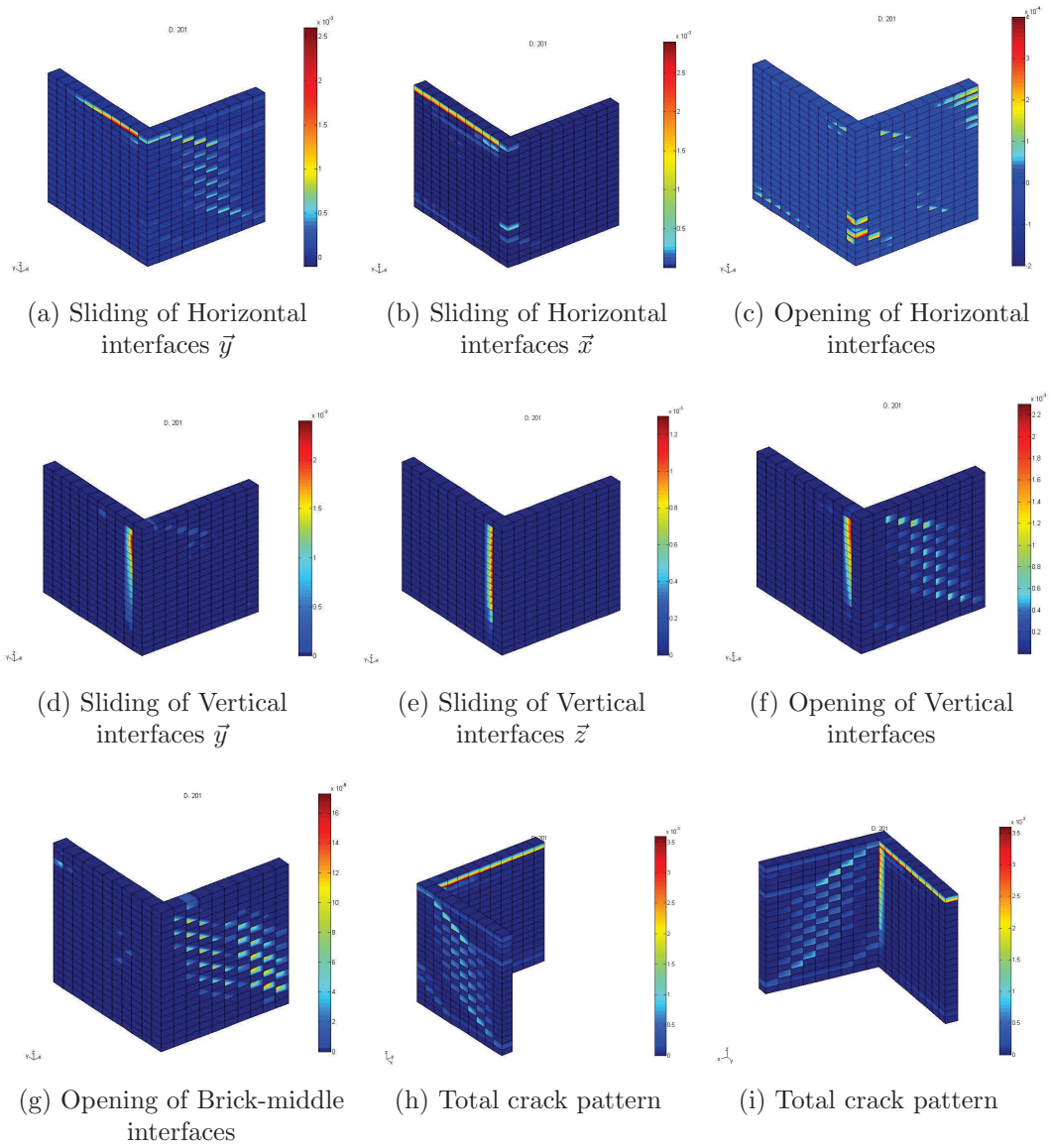


Figure 5.53: Crack pattern in the masonry walls ,Series 1, roof rotates 0.05 degree

the Series 1, displacements from 0 to $2mm$ are gradually applied to the top nodes in x direction and y directions. Afterward, supposed roof rotates 0.05 degree anticlockwise. The results of each section will be discussed and compared to the previous case. It should be noted that the properties of the different series is the same.

Series 2: displacement are applied to all top nodes in x direction

In this case, all top nodes are subjected to the displacements in x direction. The obtained deformed shape and total crack pattern are shown in Figure 5.54. In this case, diagonal cracks are formed in the Wall 1 due to applied in-plane displacements on it. As shown in the figures, the walls just slide in shear directions but do not separate. Therefore, the dimension of perpendicular walls has an important role to the behavior of the set. By increasing the length of perpendicular walls, the wall subjected to in-plane displacements undergoes more lateral strength and behave very better. In addition, in this case the walls do no disconnect. Cracks first are formed in Wall 1 bottom right and top corners. By increasing the loads, cracks propagate at top and greatly in bottom horizontal mortars of Wall 1 at $d = 0.6mm$ that reduces the stiffness of Wall 1 under lateral loads, Figure 5.56(a). Then stepped cracks at top left corner of Wall 1. Simultaneously, top and bottom rows of Wall 2 also crack and the vertical mortars in the walls' intersection slid on each other at $d = 0.8mm$, see stiffness reduction of Wall 2 at this point in Figure 5.56(a). Then, diagonal cracks propagate in the Wall 1 at $d = 1mm$. The drop in pushover curve of the set corresponds to formation of these cracks, see Figure 5.56. By increasing the displacements, the length of diagonal cracks, sliding cracks in the bottom rows of horizontal mortars in Wall 1 and sliding of vertical mortars at walls' intersection increase.

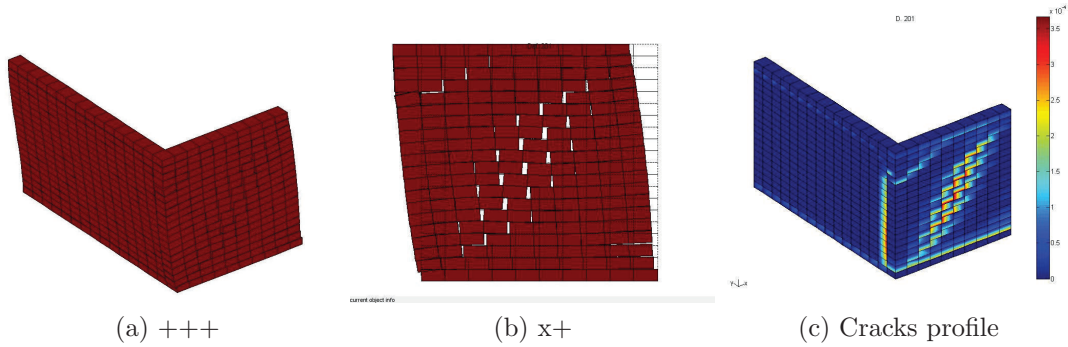


Figure 5.54: Deformation in different planes, Series 2, all top nodes move $d = 2mm$ in x direction

To make a better comparison of the behavior of the set with two different dimensions in x and y, total crack patterns of each assembly as well as their pushover curves are demonstrated in Figure 5.55 and Figure 5.56. The diagonal cracks are not formed in the set with the lower Wall 2. In the later case with lower dimension, Wall 1 slip on its lower horizontal mortars and the walls separates whereas for the case with larger length, Wall 2 has enough strength to prevent

slipping of Wall 1 and separation of walls, so diagonal cracks propagate in the Wall 1 and totally the series carries out greater lateral loads. Figure 5.56(b) represents Series 1 and Series 2 total pushover curves. As illustrated in the figure, the lateral strength of Series 2 is considerably higher than the Series 1.

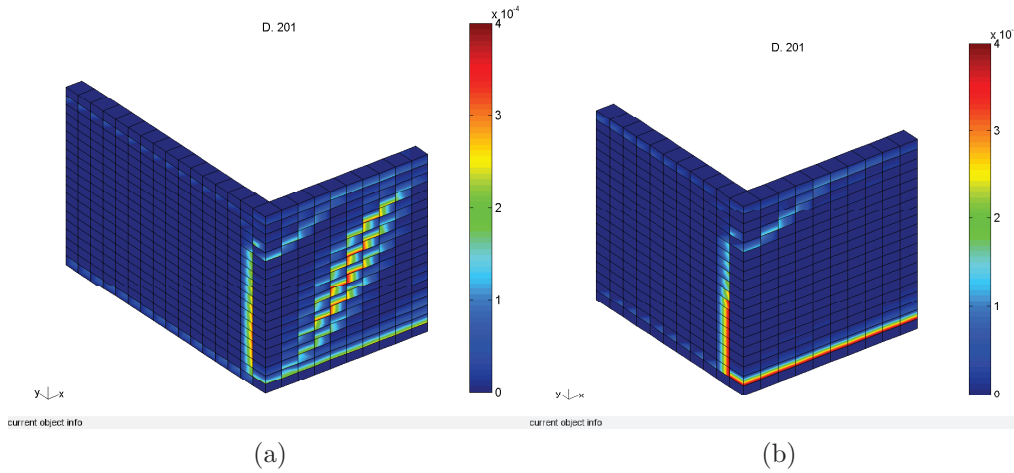


Figure 5.55: Total cracks pattern, all top nodes move 2mm in x direction (a) Series 2 (b) Series 1

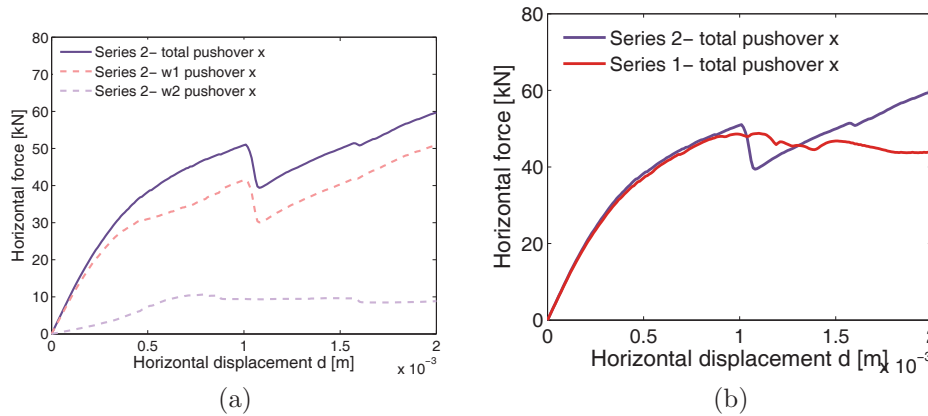


Figure 5.56: Load displacement curve, all top nodes move 2mm in x direction (a) Series 2 (b) comparison between Series 2 and Series 1

Series 2: displacement are applied to all top nodes in y direction

All top nodes of Series 2 in this section are subjected to the incremental displacement from 0 to 2mm in y direction. Response of Wall 1 under out-of-plane displacement, Wall 2 under in-plane displacement and the set in different views are shown in Figure 5.57. As can be seen in this

figure, walls separate and walls considerably separate at their intersection. As studied before, since the aspect ratio of Wall 2 is 1.5 (higher than 1) at it is subjected to in plane loads, the wall exhibits brittle behavior and horizontal mortars at the top rows of Wall 2 slip and forces such separation in the walls connection. The sliding of top horizontal mortars together with walls' separation happens at $d = 0.8mm$ as can be distinguished from its pushover curve, see Figure 5.59.

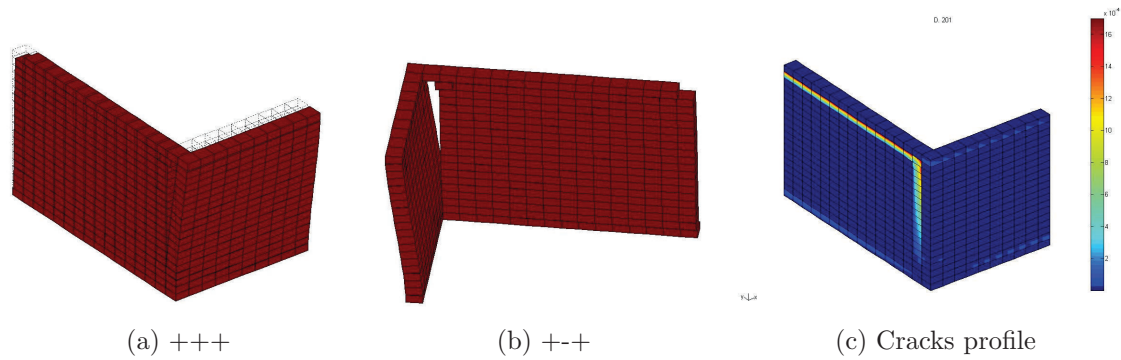


Figure 5.57: Deformation in different planes, Series 2, all top nodes move $d = 2mm$ in y direction

The lateral strength of the set under loading in y direction for each individual walls and the set are shown in Figure 5.59(a). Wall 1 is loaded under out-of-plane displacements so it undergoes lower lateral resistance whereas Wall 2 is subjected to in-plane displacements and it carries out much bigger lateral displacements. The significant drop in pushover curves is due to slipping the top row of horizontal mortars of Wall 2. Figure 5.59(b) indicates that the combination of walls with larger dimensions is much more stiffer and its ultimate lateral strength is noticeably higher than that of with lower length but it exhibits the brittle behavior and the drop in the pushover curve for the walls with larger length is much greater than the one with smaller length.

Series 2: supposed roof's center of gravity of walls rotates 0.05 degree

In this section, the supposed roof at the top of the walls rotates 0.05 degree. As the dimension of Wall 2 in Series 2 is 1.5 greater than Series 1, the total movement of walls in x and y direction is much more greater than Series 1. For example, maximum displacement in x and y directions are $7mm$ and $4.39mm$. By applying this rotation to the supposed roof, some stepped cracks are formed in Wall 1 (as shown in Figure 5.60(a), walls separates according to Figure 5.60(b) and top rows of horizontal mortars slip and separate from the whole structure.

Pushover curves of the set in x and y directions are shown in Figure 5.61(a) and Figure 5.61(b). The stiffness of system in x direction decreases first at $d = 0.38mm$ by formation of stepped cracks

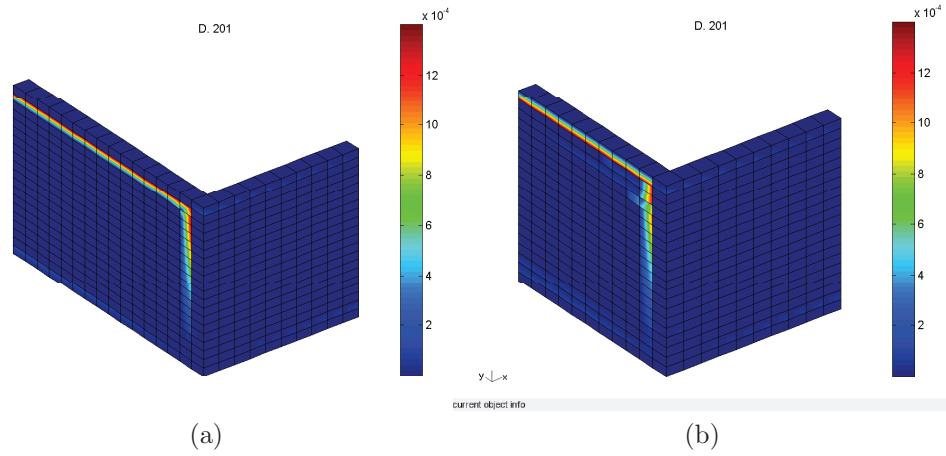


Figure 5.58: Total cracks pattern, all top nodes move $2mm$ in y direction (a) Series 2 (b) Series 1

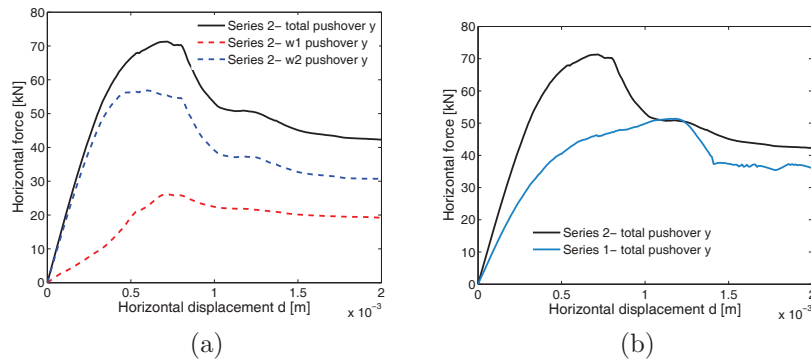


Figure 5.59: Load displacement curve, all top nodes move $2mm$ in y direction (a) Series 2 (b) comparison between Series 2 and Series 1

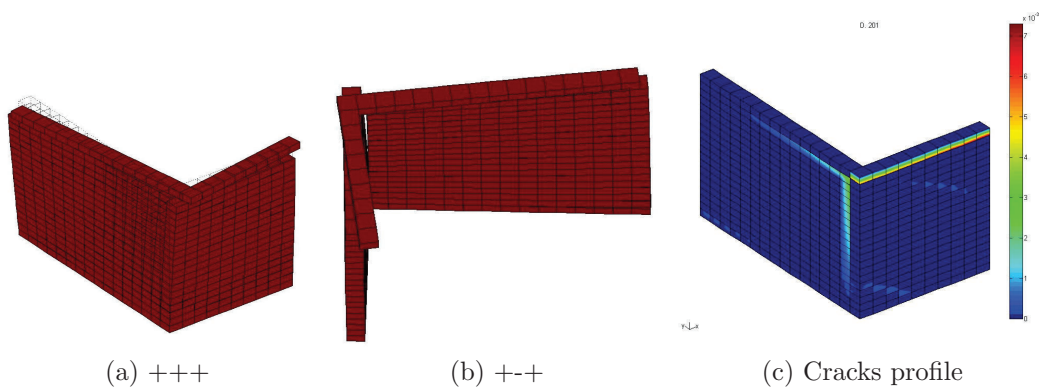


Figure 5.60: Deformation and total crack pattern for walls whose supposed roof is subjected to 0.05 degree of rotation, Series 2

at bottom left and top right of the Wall 1. The vertical mortars in the walls' intersection also slide and reduces the lateral strength of Wall 2 in y direction. Then, at $d = 0.87mm$ all top horizontal mortars of the Wall 1 slip considerably in x and y directions, rotate and move separately from the other part of the wall the set loses its lateral strength in x direction considerably. Moreover, the vertical interfaces at the walls' intersection open considerably at $d = 0.92mm$. The drop in the lateral strength in y direction represents the walls separation.

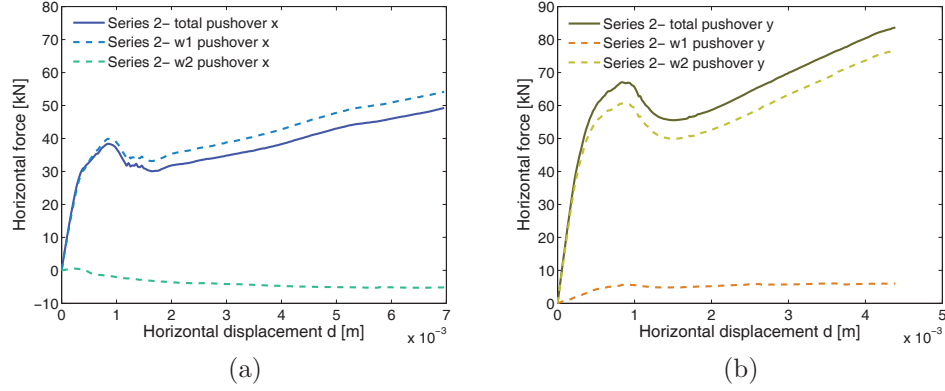


Figure 5.61: Lateral load-displacement curves of walls in (a) x direction (b) y direction, Series 2, 0.05 degree rotation

In this case the profile of sliding and cracking in Wall 1 and Wall 2 are represented in Figure 5.62. As deformation due to the rotation in x direction is almost 2 times greater than y direction because of the geometry of the walls, the sliding of horizontal mortars in Wall 1 which is parallel to x direction, is larger than Wall 2. Horizontal mortars open in different parts of Wall 1 and Wall 2 due to the rotation. In addition to opening of horizontal mortars in the corners of walls, some stepped cracks in Wall 1 and the diagonal of Wall 2 also develop. Vertical mortars in the intersection of walls slide and open. Moreover, some series of vertical elements located in diagonal of Wall 2 also fail in tension and crack. It should be noted that the bricks located at top left corner of Wall 2 also fail in tension.

Comparing the results of different series with different dimensions under the same rotation reveals that the structure with larger dimension is subjected to larger displacements with the same rotation. The larger wall carries out larger displacements while the smaller one undergoes the lower loads.

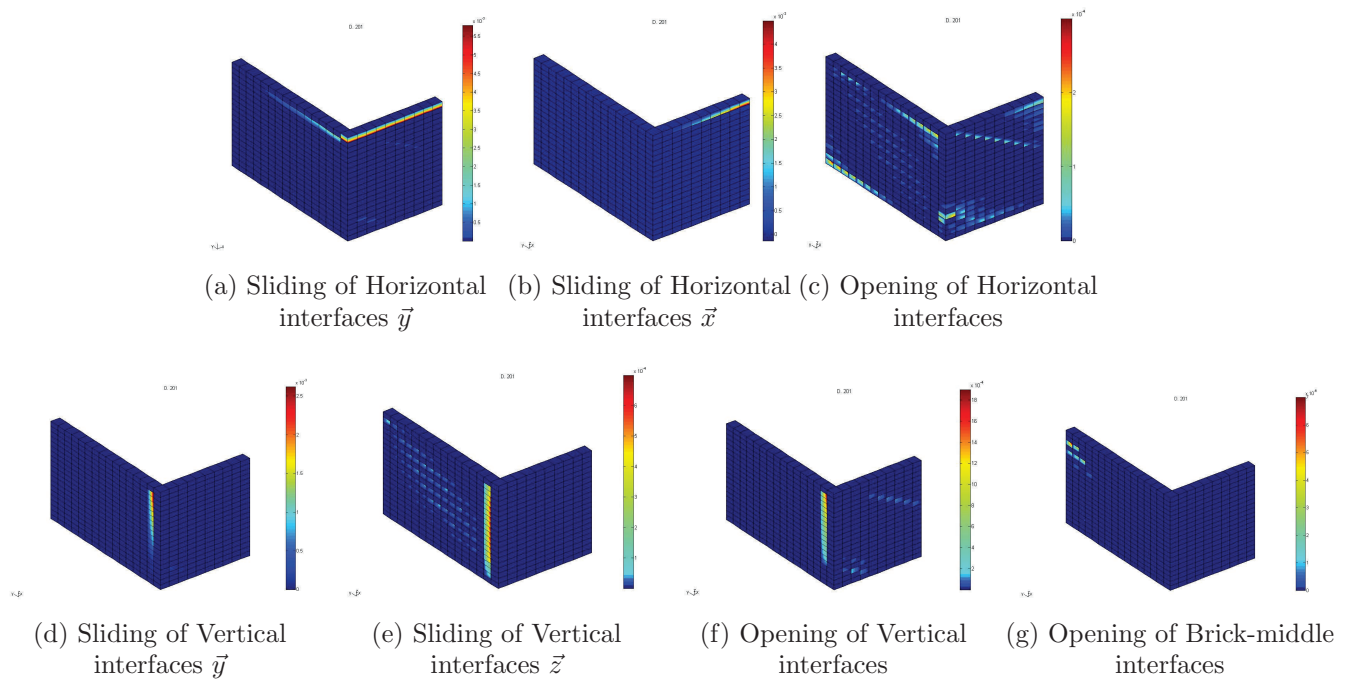


Figure 5.62: Crack pattern in the masonry walls, Series 2, 0.05 rotation

5.4 Conclusion

Studying the behavior of masonry walls under out-of-plane loading was the main purpose of this chapter. In the first part, two simple walls with different boundary conditions were subjected to out-of-plane displacement at various locations. The effects of cohesion of mortars, normal stress and compression strength of masonry on out-of-plane behavior of wall were investigated. The results can be concluded as:

- Resistance of a masonry wall under out-of-plane displacements is much lower than that of under in-plane ones. The wall's resistance depends on boundary condition and the way out-of-plane loads are applied to the wall.
- Cohesion of mortars has a significant effect on behavior of masonry wall under out-of-plane loads. By raise of cohesion, the resistance of wall under shear loads, consequently under out-of-plane displacement increases and masonry wall carries out larger out-of-plane displacements.
- Initial normal stress has a great influence on masonry wall performance under out-of-plane displacements. High level of initial stress on the wall causes horizontal mortars open later under out-of-plane displacements and on the other side, according to Mohr-Coulomb criterion, the shear strength of masonry wall directly depends on normal stress and enhances by normal stress increase.
- Compression strength of masonry affects the resistance of masonry under out-of-plane loads. In some cases, multiplying the compression strength of masonry by 10 did not change the lateral resistance of the wall because the loads were not sufficient to cause crushing failure in the mortars.
- Opening of vertical and horizontal interfaces are the main reason of failure of masonry walls under out-of-plane loads. Thus, the tensile strength of the mortars has an important role on its behavior under these loads.

Second part of this section was attributed to the behavior of a set composed of two walls which were connected together by vertical mortars. The size of walls was the same. First, one of the walls was subjected to in-plane displacements which were acted as out-of-plane for the other wall. The properties of the walls were changed to investigate the effect of materials strength on performance of the set. The following results were obtained:

- Masonry wall shows higher structural strength when perpendicularly connected to a similar wall compared with a single wall standing by itself.
- Property of mortars in the intersection of two perpendicular walls has a great role on performance of the set. A strong intersection can transfer the loads well and decrease the damage of the set.

- Cohesion of mortars affects the behavior of walls both under in-plane and out-of-plane loads. As cohesion increases, the performance of the set and each individual wall improves and their strength under in-plane and out-of-plane displacements increases.
- Initial normal pressure imposed on the wall has a considerable effect on the behavior of masonry walls. When higher normal stress is imposed initially on the wall, its performance under in-plane and out-of-plane loads increases. Larger lateral loads are carried out by the wall depending on the geometry and boundary condition of walls. On the other side, in the wall with higher level of pre-compression, the shear failure of bottom horizontal rows can be prevented.

Afterward, a rigid roof was supposed to connect both walls and the roof's movement was simulated by moving all top nodes simultaneously. So, first, all top nodes move in x direction $2mm$, then move in y direction $2mm$ (the length of the set in x direction was $1m$ whereas it is $1.1m$ in y direction), thereafter the same displacements at x and y direction were imposed to the top nodes and finally walls rotate 0.05 degree around the center of gravity of supposed roof. The numerical modeling shows that:

- Aspect ratio of wall subjected to the displacement has an important role on the behavior of the wall. The ultimate strength of a masonry wall under out-of-plane displacements is higher for the wall with lower aspect ratio. The same results are also obtained for the strength of the walls under in-plane displacements where a set composed of two perpendicular walls is subjected to displacements.
- Response of the wall highly depends on relative displacement applied on it. The stiffness as well as ultimate lateral strength of the set is influenced by such relative displacements.
- Roof's rotation causes diagonal cracks in the wall with lower length, sliding shear failure in the wall with larger length and separation of walls from their intersection. The results show that properties of mortars in the connection of two walls have an important role on the performance of the assembly.

Finally, the length of the perpendicular wall was changed in order to see how the geometry of different walls can influence the behavior of the set. Results show the behavior of the set as well as each individual wall, improve by using a larger wall in the system. The lateral strength of the wall in the direction parallel to larger one is greater. It was shown that the main issue in these cases is separation of walls due to sliding and opening of vertical mortars in the intersection of walls.

Chapter 6

Conclusion

6.1 Summary and conclusion

Masonry construction involves intricate structures with complex behavior under different loads. These structures are wide-spread around the world constituting a great number of existing facilities as well as historical landmarks in different countries. Therefore, design, maintenance, and reinforcement of such structures against different load conditions are at the center of attention of many researchers. Safety assessment of such complex structures necessitates development of robust modeling tools and techniques that can analyze the behavior of such constructions in order to enhance their structural performance. The comprehensive literature review shows variation of experimental test results due to the effect of different parameters that contribute to the behavior of such structures. High cost of conducting experiments and dependence of the obtained data on the experimental conditions make numerical methods competitive. Macro and micro modeling, two well established numerical methods, are comprehensively investigated. A robust computational tool, developed to conduct this research, is used to analyze the masonry structure in a three dimensional environment. Unlike the past studies, the 3D analysis of masonry wall allowed studying its out-of-plane behavior as well. The performance of unreinforced masonry wall under both in-plane and out-of-plane loading were studied in detail in chapters 4 and 5.

Macro modeling:

This strategy is selected in order to assess the ultimate strength of infill masonry panels. The author tested the numerical models developed in past research works to reproduce the experimental data. However, some drawbacks of those methods were revealed and the new tri-linear stress-strain curve is proposed to address those limitations. Determination of modulus of elasticity value plays a great role in obtaining meaningful results in this approach. The proposed model is justified again by comparing the obtained numerical results with experimental data available in the literature. This model is mainly used to model infill masonry panels. In the proposed macro model, flexural behavior of masonry wall can not be captured because the connection of macro-element and frame are supposed to be rigid and the relative rotation between wall and frame can not be simulated. Moreover, the failure mechanism of masonry wall and the local damages which are very important factors for the rehabilitation of masonry walls, can not be predicted by this model either. Therefore, the study on behavior of masonry walls has been further developed using micro-modeling.

Micro modeling strategy: in-plane loading

A masonry wall has been modeled in three dimension configuration using micro-modeling strategy where bricks are modeled with 3D solid elements whereas interface elements are used for representing mortars. The bricks are supposed to remain unchanged whereas the nonlinear behavior of this complex composite is supposed to happen in weakness planes namely interface elements. Two different multisurface models, model I and model II were developed in the program, capable to predict tension, shear failures and tension, shear and compression failures as well as softening behavior for strength of the wall respectively. The elastic properties and crack-

ing profile of masonry shear wall under in-plane loads were reproduced well with model I but the model was not capable to assess the maximum lateral strength of the wall. In addition, a considerable difference between the obtained ultimate lateral strengths from numerical and experimental data was found for the wall with an opening. Studies showed that considering compression failure of the mortar and limitation of shear stress in the interface element with its compressive strength has an essential role to predict the real ultimate strength of masonry wall under in-plane loads. The validity of the later model was verified by comparing its response to experimental data for both the wall without and with opening under in-plane loads. The effect of aspect ratio (ratio between wall's height and length) on performance and damage profile of the masonry wall was investigated for two different categories: $AS > 1$ and $AS < 1$. Results demonstrate that the wall with lower aspect ratio is stiffer and undergoes greater lateral strength but it exhibits brittle behavior. Failure mode in this wall was sliding shear failure of a row of horizontal mortars. Moreover, analyzing the behavior of the walls with the same aspect ratio and different dimensions shows that the lower wall carries out lower lateral load. On the other side, the failure mechanism of walls with the aspect ratio greater than 1 was compression failure of corner mortars. The pushover curves of different walls showed that the walls with greater aspect ratio have lower strength under lateral loads.

Different properties of mortars such as: its tensile strength, cohesion, compressive strength, the slope of compression cap and initial normal stress on the wall were changed and the lateral behavior of the wall and profile of cracks were drawn for each case. Then, the length of the cracks in different types of elements were measured and used as a damage index. It was shown that sliding of horizontal mortars and opening of vertical mortars are the most important issues in failure of masonry walls. Increasing the initial normal stress on the wall decreases considerably both of these parameters and improves the performance of the wall. However, the cracks being distributed smoothly in different elements, the wall exhibits more stable behavior. The tension failure of bricks and horizontal mortars do not influence considerably the response of masonry walls. Finally, the obtained cracking profiles were associated to the walls with different material characteristics.

Micro modeling strategy: out-of-plane loading

The validated 3D micro-modeling is implemented for analysis of unreinforced masonry walls' behavior under out-of-plane movement. First, a masonry wall with two different boundary conditions was subjected to out-of-plane displacements. Results show that initial normal stress on the wall and cohesion of mortars have positive influence on the behavior of masonry wall under this type of loading while its compressive strength is not very important. Opening of vertical elements and sliding of horizontal ones in parallel and perpendicular directions to that of loading, are the most important damage indexes. According to the numerical modeling, the strength of masonry walls under out-of-plane actions is much lower than that of under in-plane loads. It should be noted that sometimes the concentration of loads causes the failure in the wall. The effect of surrounding walls on behavior of the masonry wall under different types of loading was investigated using two sets of two perpendicular walls with different geometries. The sets were

subjected to uniform loading in x and y directions and also a slight rotation. The presence of surrounding wall increases the lateral strength of the wall in in-plane direction and whatever the length of surrounding wall is greater, the system undergoes greater loads. The mortars in the joint have an essential role on the behavior of two attached walls. Increasing initial confinement enhances the performance of the set considerably. It should be noted that the same applied rotation to the supposed walls' roof causes a greater damage in the set with greater geometries.

6.2 Perspective and future work

In term of macro models, only the behavior of the walls under monotonic loads was studied, so development of constitutive law for simulating the behavior of infill under cyclic loads is necessary specially for the analysis of seismic behavior.

A comprehensive probabilistic study of different variables that affect the strength and failure mechanism of masonry walls, including but not limited to aspect ratio, opening location and size, and material properties is recommended for the future work. Investigating the effect of variation of different parameters on the behavior of such structures will lead to highly useful information that is instrumental in identifying and setting rehabilitation priorities for vulnerable structures that are often located in highly populated areas of the world.

The micro modeling strategy is very time consuming and costly and it is not applicable to model all of masonry walls in a building. Hence, predicting the failure mechanism of the wall to assign the appropriate macro-elements can be a very useful tool for analyzing masonry buildings under different loading.

Chapter 7

Appendixes

Appendix A

Macro models formulations

FEMA 356 model

$$a = 0.175(\lambda.h_{col})^{-0.4}.r_{inf} \quad (A.1)$$

Where :

$$\lambda = \left[\frac{E_{me}.t_{inf}.\sin(2\theta)}{4.E_{fe}.I_{col}.h_{inf}} \right]^{0.25} \quad (A.2)$$

h_{col} : Column height between centerlines of the beams,

r_{inf} : Diagonal length of infill panel,

E_{me} : Expected modulus of elasticity of infill wall material,

t_{inf} : Thickness of infill panel and equivalent strut,

θ : Angle whose tangent is the infill height-to-length aspect ratio,

E_{fe} : Expected modulus of elasticity of frame material,

I_{col} : Moment of inertia of columns about the axis perpendicular to the loading direction,

h_{inf} : Height of infill wall.

For the infilled RC frame of the CSTB test structure, the equation's parameters are: $h_{col} = 2.8m$, $r_{inf} = 4.53m$, $t_{inf} = 20cm$, assumed: $E_{fe} = 24.82 \times 10^9 Pa$, $h_{inf} = 2.6m$ and:

$$\theta = \arctan(h_{inf}/l_{inf}) \quad (A.3)$$

$$l_{inf} = 3.71m \text{ so } \Rightarrow \theta = 35.2^\circ, \Rightarrow \sin(2\theta) = 0.94$$

$$I_{col} = \frac{b \times h^3}{12} \quad (A.4)$$

$$I_{col} = \frac{0.2 \times 0.15^3}{12} = 5.625 \times 10^{-5} m^4$$

$$f'_m = \frac{f'_{cb} (f'_{tb} + \alpha \cdot f'_j)}{U_u (f'_{tb} + \alpha \cdot f'_{cb})} \quad (\text{A.5})$$

$$\begin{aligned} \alpha &= \frac{15}{4.1 \times 200} = 0.0183 \\ f'_m &= \frac{9.3 (0.93 + 0.0183 \times 17.9)}{1.5 (0.93 + 0.0183 \times 9.3)} = 7.09 \text{ MPa} \\ E_m &= 750 \times 7.1 = 5325 \text{ MPa} \\ \lambda &= \left[\frac{5.325 \times 10^9 \times 0.2 \times 0.94}{4 \times 24.82 \times 10^9 \times 5.625 \times 10^{-5} \times 2.6} \right]^{0.25} = 2.881 \\ \Rightarrow a &= 0.175 (2.881 \times 2.8)^{-0.4} \times 4.53 = 0.344 \text{ m} \end{aligned}$$

$$V_{ine} = A_n \cdot f_{vie} \quad (\text{A.6})$$

$$A_n = t_{inf} \cdot l_{inf} \quad (\text{A.7})$$

$$f_{vie} = \nu_{me} = 0.75 \left[\nu_{ts} + \frac{P_{CE}}{A_n} \right] \quad (\text{A.8})$$

$$\begin{aligned} A_n &= 0.2 \times 3.71 = 0.743 \text{ m}^2 \\ \nu_{ts} + \frac{P_{CE}}{A_n} \text{ assumed : } 620 \text{ kPa} &\Rightarrow \nu_{me} = 0.75 \times 620 = 496 \text{ kPa} \\ V_{ine} &= 0.743 \times 0.496 = 368.03 \text{ kN} \\ A_{strut} &= 0.2 \times 0.344 = 0.0688 \text{ m}^2 \\ f_{my} &= \frac{0.368 \cdot 4.53}{0.688 \cdot 3.71} = 6.51 \text{ MPa} \\ \epsilon_{my} &= \frac{6.51 \times 10^6}{5.32 \times 10^9} = 0.0012 \\ \epsilon_{mu} &= 0.35\% \times \frac{2.6 \times 3.71}{4.53^2} = 0.001645 \end{aligned}$$

Calibrated model

$$A_{strut} = \frac{V_{inf}}{f'_m} \quad (\text{A.9})$$

$$\epsilon_{mo} = \frac{l_{inf}}{r_{inf}^2} \cdot \Delta_y \quad (\text{A.10})$$

$$f_{mu} = \frac{V_{res}}{A_{strut}} \quad (\text{A.11})$$

$$\epsilon_{mu} = \frac{l_{inf}}{r_{inf}^2} \cdot \Delta_{res} \quad (\text{A.12})$$

By substituting the value of each parameter, the area of strut model as well as material model are calculated:

$$\begin{aligned} A_{strut} &= \frac{361 \times 10^3}{7.09 \times 10^6} = 0.0508 \text{ m}^2, \quad \epsilon_{mo} = \frac{3.71}{4.53^2} \times 3.46 \times 10^{-3} = 6.25 \times 10^{-4}, \quad f_{mu} = 2.87 \text{ MPa}, \\ \epsilon_{mu} &= \frac{3.71}{4.53^2} \times 7.56 \times 10^{-3} = 0.0014. \end{aligned}$$

Mostafaei and Kawashima

$$\begin{aligned}
 \frac{V_c}{t.l_m} &= 0.28 \times 0.2 \times 7.09 \times \frac{\cos(0.6113)}{0.2 \times 3.71} = 0.44 MPa \\
 \frac{V_f}{t.l_m} &= \frac{0.284}{(1-0.6632 \times 0.7009)} = 0.5306 MPa \quad \epsilon_m = \frac{f'_m}{E_m} = \frac{7.09 \times 10^{-6}}{5.325 \times 10^9} = 1.33 \times 10^{-3} \\
 U_m &= \frac{0.00133 \times 4.53}{\cos(0.6113)} = 0.0074 m \\
 K_0 &= 2 \times \left(\frac{0.33}{0.0074} \right) = 89.19 MN/m \\
 V_y &= \frac{0.33 - 0.2 \times 89.19 \times 0.0074}{1 - 0.2} = 0.2475 MN \\
 U_y &= \frac{0.2475}{89.19} = 0.0028 m
 \end{aligned}$$

Proposed model

$$\begin{aligned}
 E_m &= 900 \times f'_m = 6381 MPa \\
 \lambda &= 3.226 \Rightarrow a = 0.3287 m \Rightarrow A_{strut} = 0.0657 m^2 \\
 V_m &= V_{ini} = 0.33 MN \\
 \epsilon'_m &= \frac{f'_m}{E_m} = \frac{7.09 \times 10^6}{6.39 \times 10^9} \Rightarrow U_m = \frac{\epsilon'_m \cdot d_m}{\cos(\theta)} = \frac{0.001 \times 4.53}{\cos(0.6113)} = 0.0047 m \\
 K_0 &= 2 \left(\frac{V_m}{U_m} \right) = 2 \left(\frac{0.33}{0.0047} \right) = 143.6 MN/m \\
 V_y &= \frac{V_m - \alpha \cdot K_0 \cdot U_m}{1 - \alpha} = \frac{0.33 - 0.2 \times 143.6 \times 0.0047}{1 - 0.2} = 0.244 MN \\
 U_y &= \frac{V_y}{K_0} = \frac{0.2475}{143.6} = 0.0018 m \\
 V_p &= 0.5 V_m = 0.5 \times 0.33 = 0.165 \\
 U_p &= \frac{0.5 \times 0.33}{0.2 \times 143.6} + 0.0047 = 0.0106 m \\
 \sigma_m &= \frac{0.33 \times 10^6}{0.0657 \times 0.8417} = 6.65 MPa \\
 \sigma_y &= \frac{0.276 \times 10^6}{0.0657 \times 0.8417} = 4.99 MPa \\
 \sigma_p &= \frac{0.184 \times 10^6}{0.0657 \times 0.8417} = 3.33 MPa \\
 \epsilon_m &= \frac{0.0047 \times 0.8417}{5.256} = 7.5e - 4 \\
 \epsilon_m &= \frac{0.0018 \times 0.8417}{5.256} = 2.88e - 4 \\
 \epsilon_p &= \frac{0.0106 \times 0.8417}{5.256} = 0.0017
 \end{aligned}$$

Appendix B

Parametric study using micro model

Effect of plastic flow angle in compression plasticity β

In this section, the value of β is changed in order to find its influence on behavior of the wall. Masonry wall with 3 different β are studied here.

- $\beta = 15^\circ$

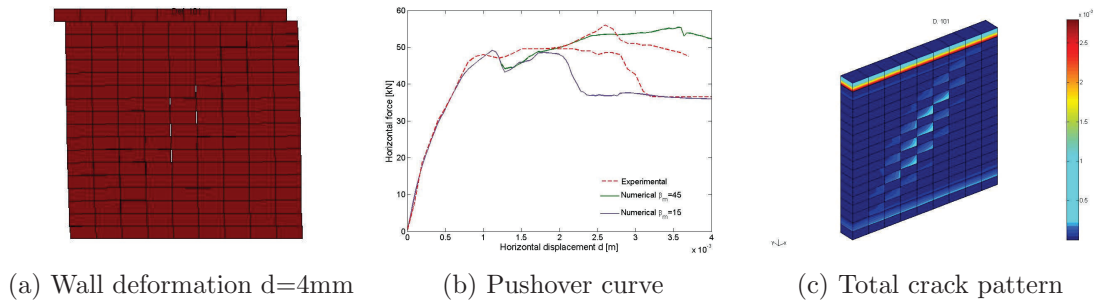


Figure B.1: Shear wall results for $\beta = 15^\circ$

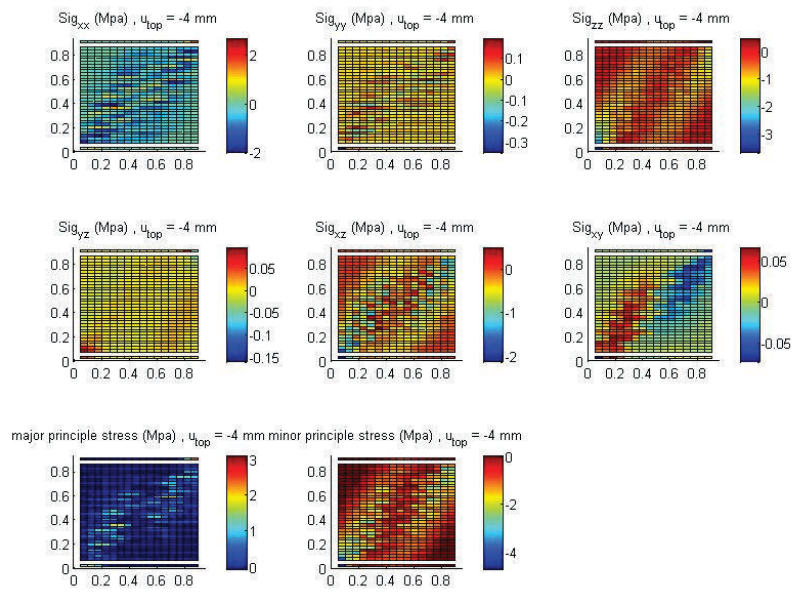


Figure B.2: Stress distribution in bricks d=4mm for $\beta = 15^\circ$

- $\beta = 32.8^\circ$

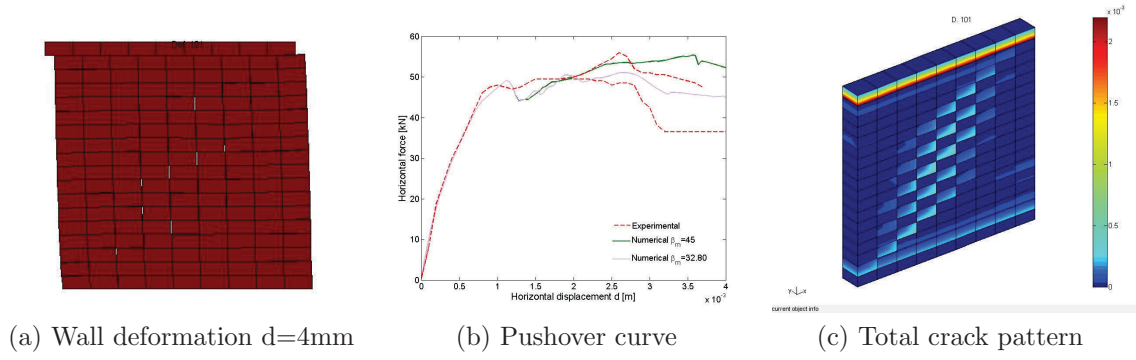


Figure B.3: Shear wall results for $\beta = 32.80^\circ$

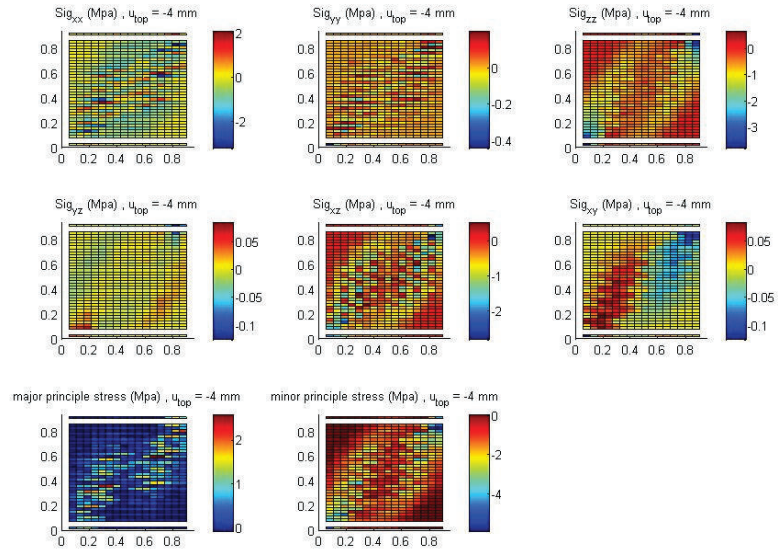


Figure B.4: Stress distribution in bricks $d=4\text{mm}$ for $\beta = 30^\circ$

- $\beta = 67^\circ$

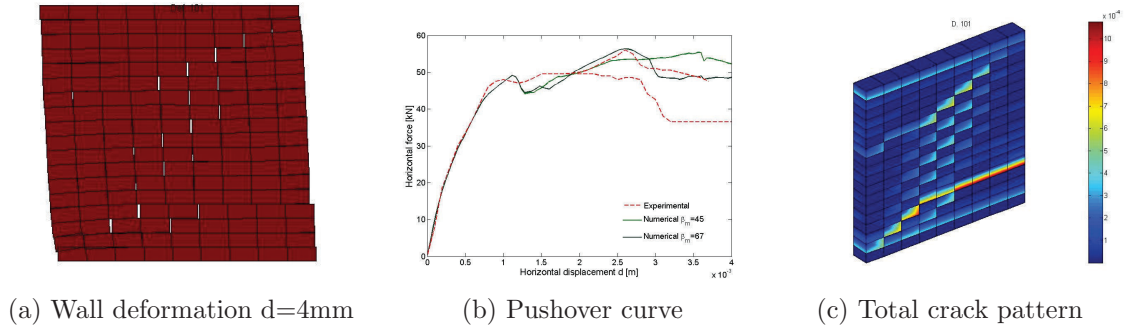


Figure B.5: Shear wall results for $\beta = 67^\circ$

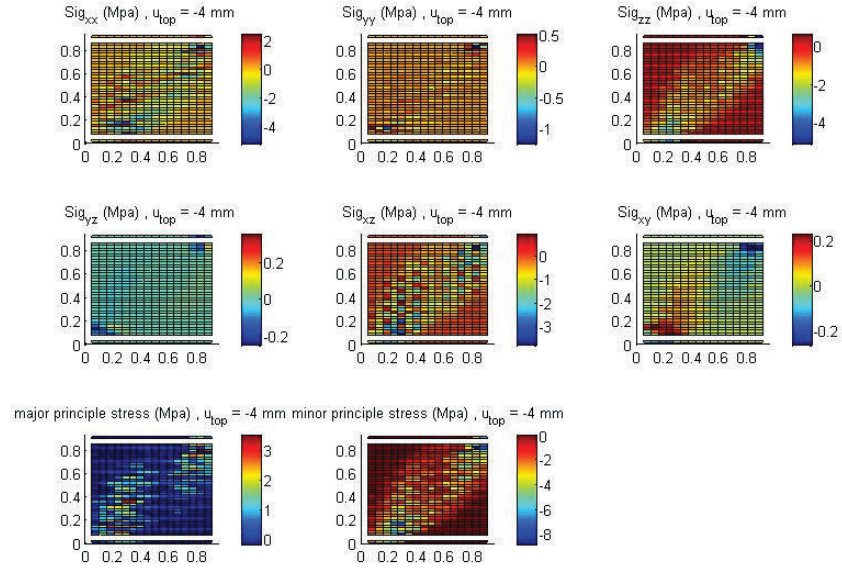


Figure B.6: Stress distribution in bricks $d=4\text{mm}$ for $\beta = 67^\circ$

- $\beta = 75^\circ$

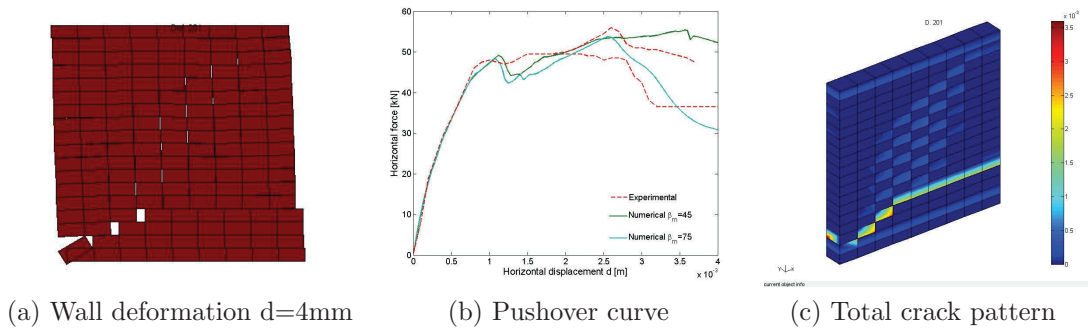


Figure B.7: Shear wall results for $\beta = 75^\circ$

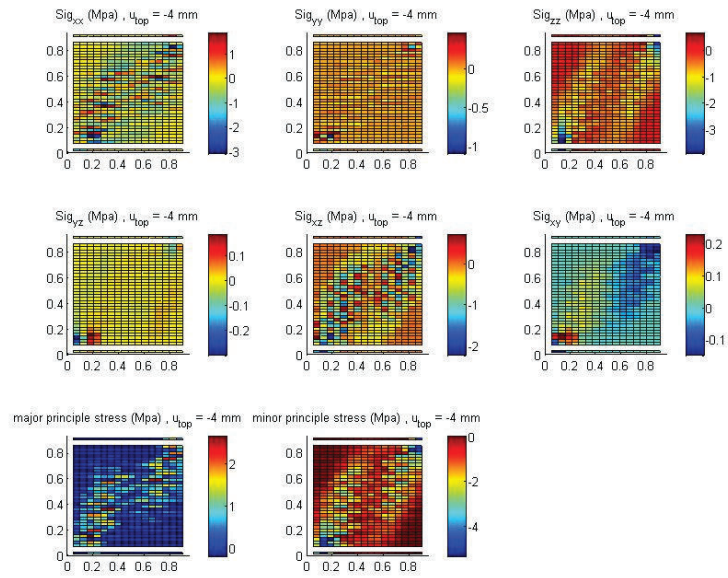


Figure B.8: Stress distribution in bricks $d=4\text{mm}$ for $\beta = 75^\circ$

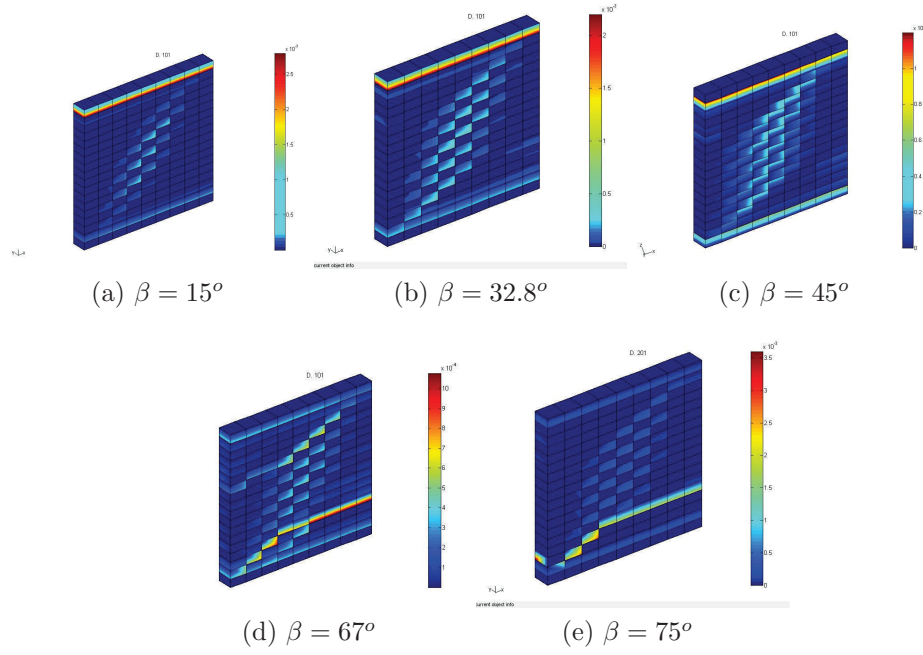


Figure B.9: Profile of cracking in the wall with different β

Deformed shape and total crack pattern for each case are shown in Figure B.10. Results shows there is a good agreement between experimental and computational results for walls with $\beta = 45^\circ$ and $\beta = 32.8^\circ$. Therefore, considering associated flow rule for compression leads to reliable results.

Effect of mode I fracture energy GI

In this section, the mode I fracture energy is changed and its behavior will be studied.

- $GI = 8N/m^2$
- $GI = 13N/m^2$

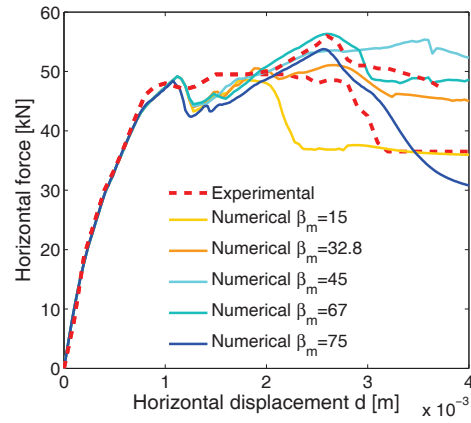
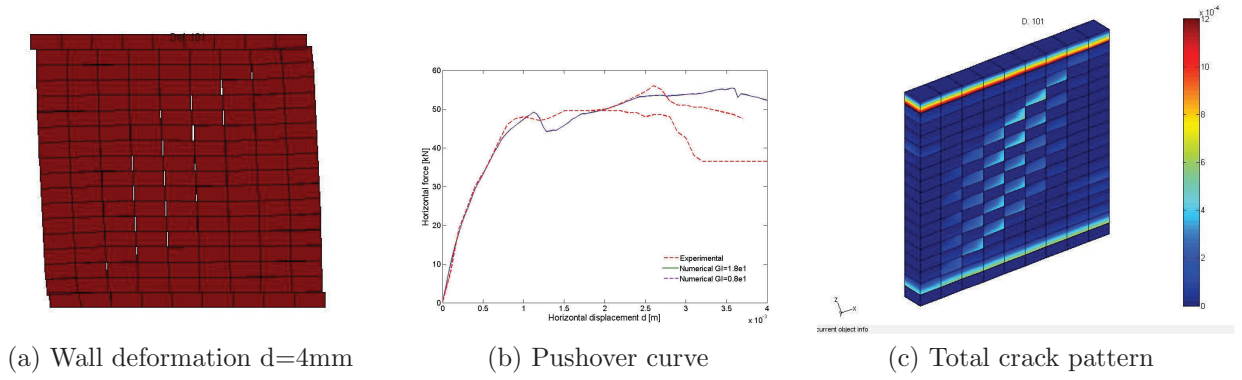


Figure B.10: Pushover curve for the wall with different β

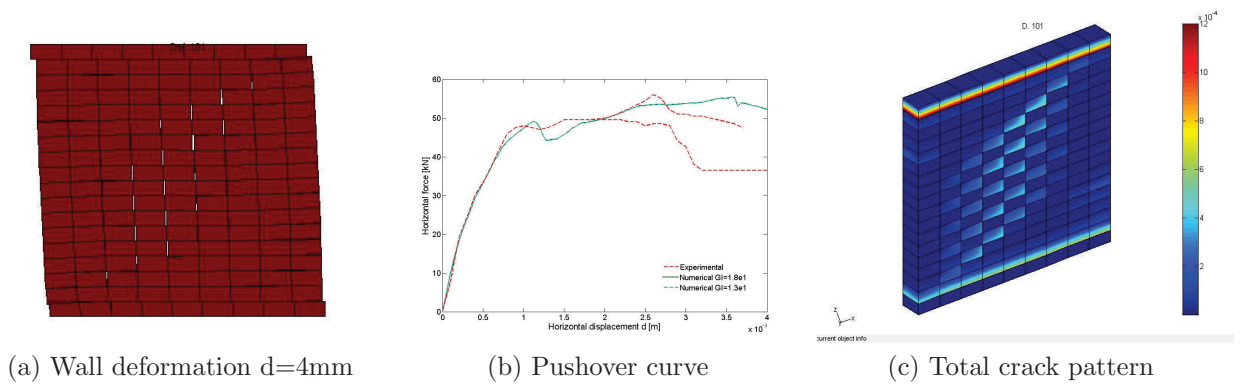


(a) Wall deformation $d=4\text{mm}$

(b) Pushover curve

(c) Total crack pattern

Figure B.11: Shear wall results for $GI = 8\text{N/m}^2$



(a) Wall deformation $d=4\text{mm}$

(b) Pushover curve

(c) Total crack pattern

Figure B.12: Shear wall results for $GI = 13\text{N/m}^2$

- $GI = 23N/m^2$

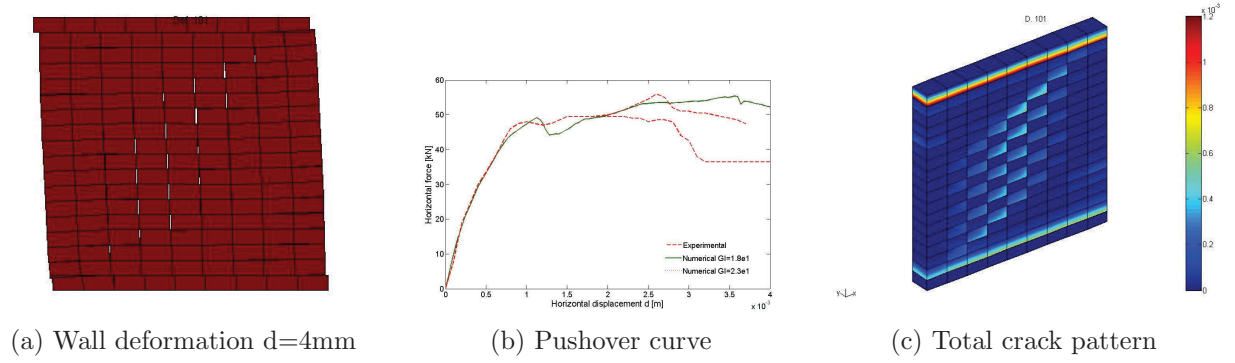


Figure B.13: Shear wall results for $GI = 23N/m^2$

- $GI = 33N/m^2$

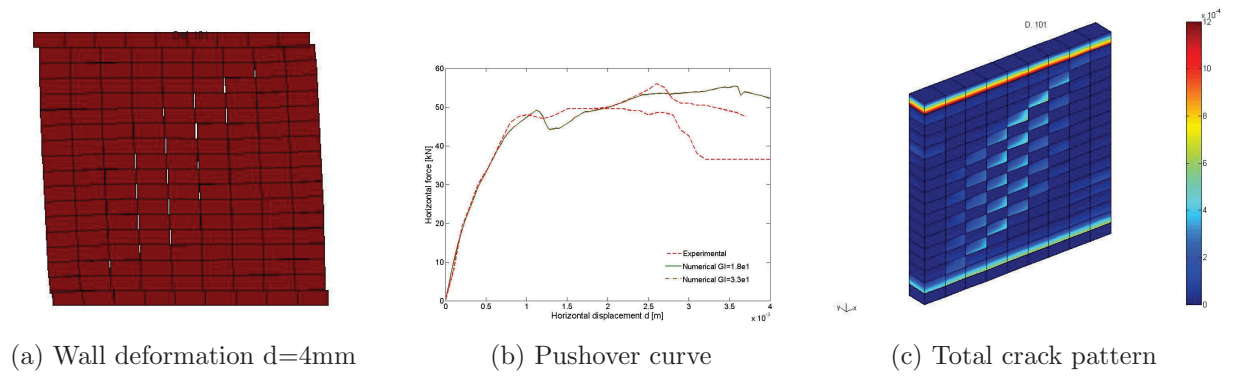


Figure B.14: Shear wall results for $GI = 33N/m^2$

Changing mode I failure energy do not change the behavior of wall significantly because after opening of mortars, all stresses set to zero. The same crack pattern and same load-displacement are obtained for four different values of GI .

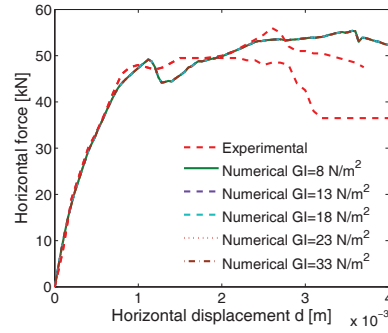


Figure B.15: Pushover curve for the wall with different GI

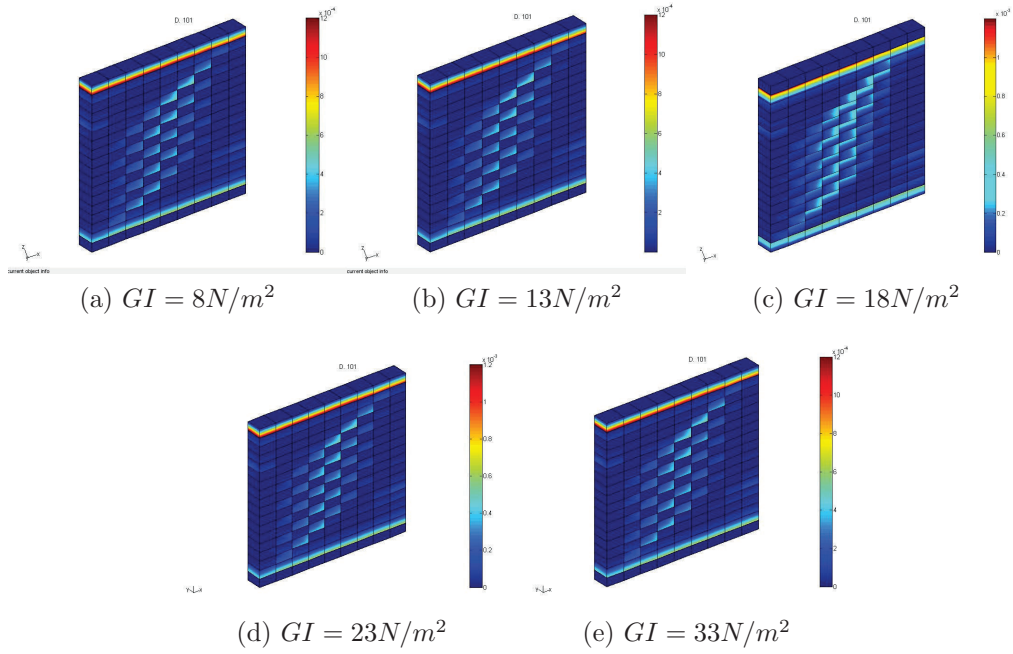


Figure B.16: Profile of cracking in the wall with different GI

Effect of mode II fracture energy G_{II}

- $G_{II} = 9.25 N/m^2$

The effect of mode II of fracture energy on behavior of the shear wall is studied here.

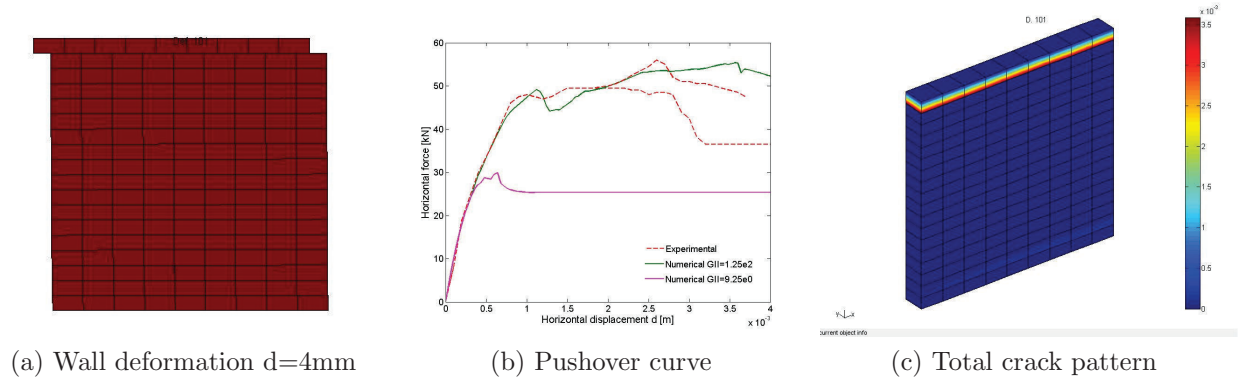


Figure B.17: Shear wall results for $G_{II} = 9.25 N/m^2$

- $G_{II} = 1.25 E1 N/m^2$

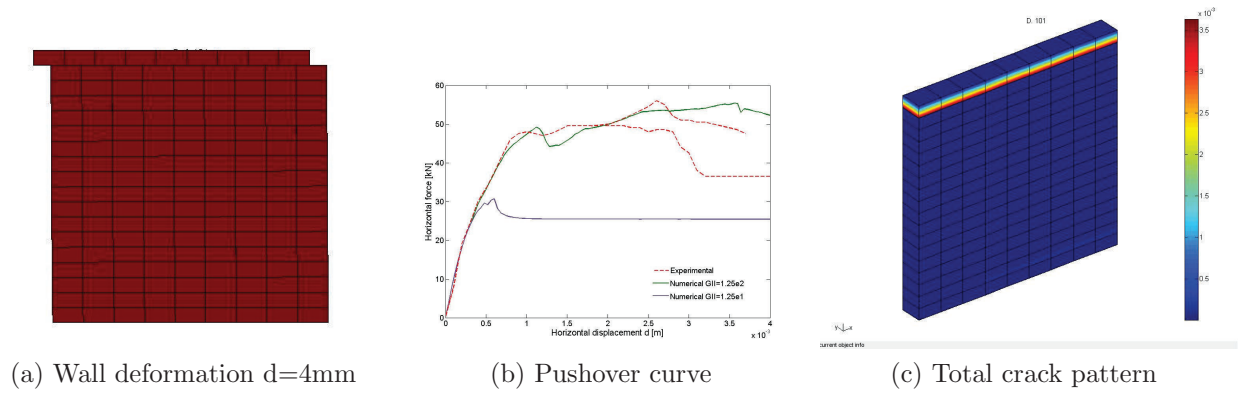


Figure B.18: Shear wall results for $G_{II} = 1.25 E1 N/m^2$

- $GII = 1.25E3N/m^2$

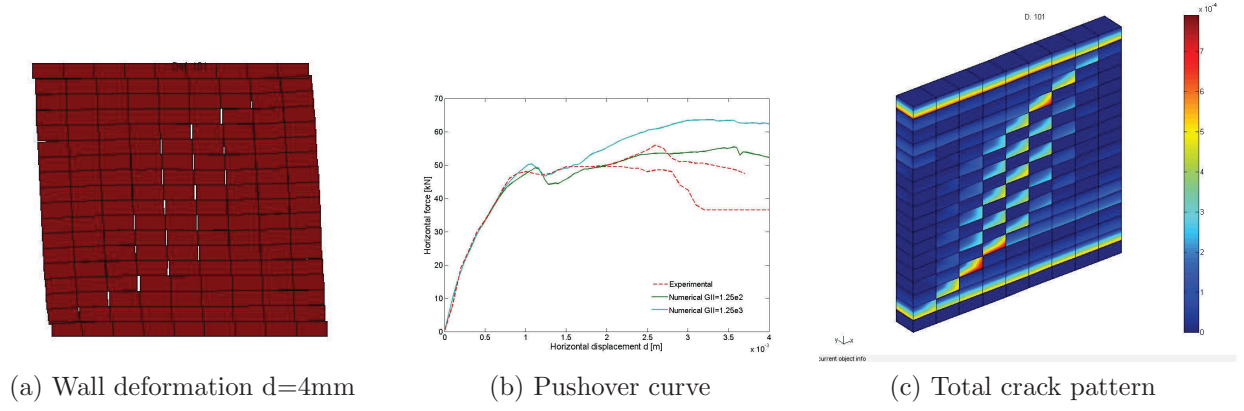


Figure B.19: Shear wall results for $GII = 1.25E3N/m^2$

- $GII = 1.25E4N/m^2$

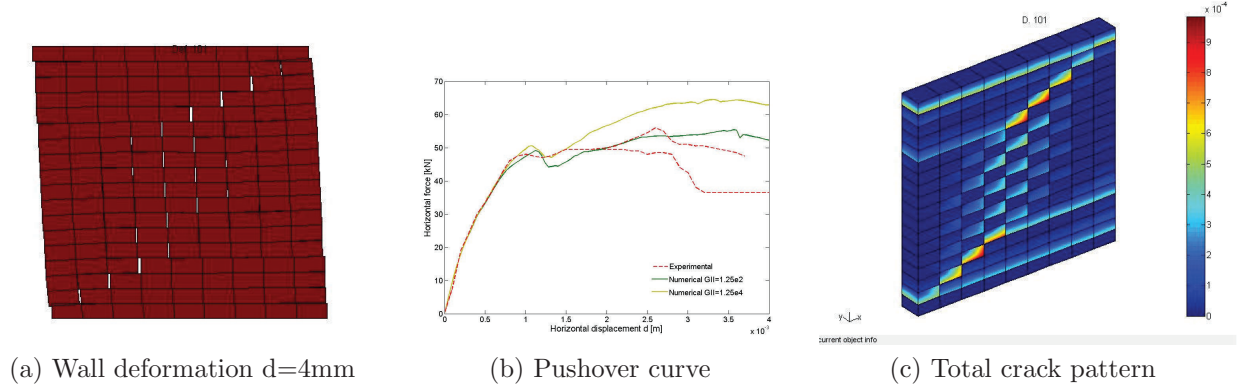


Figure B.20: Shear wall results for $GII = 1.25E4N/m^2$

Variation of mode II fracture energy affects the behavior of shear wall. As in yield surface formulation cohesion depends on mode II fracture energy, so its variation affect the wall's behavior. By increasing the GII , the mortars lose lower cohesion and consequently wall undergoes more shear strength. on the other side, reducing the fracture energy of mode II causes the mortars to loose their cohesion sooner and wall's failure happens sooner.

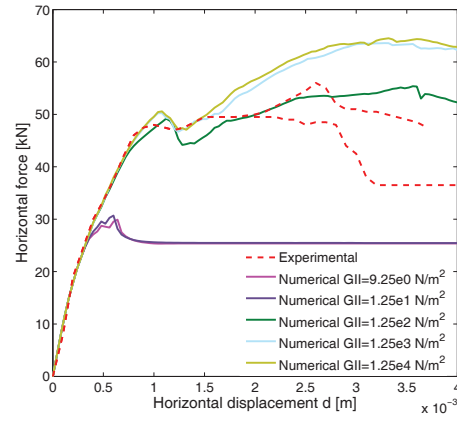


Figure B.21: Pushover curve for the wall with different GII

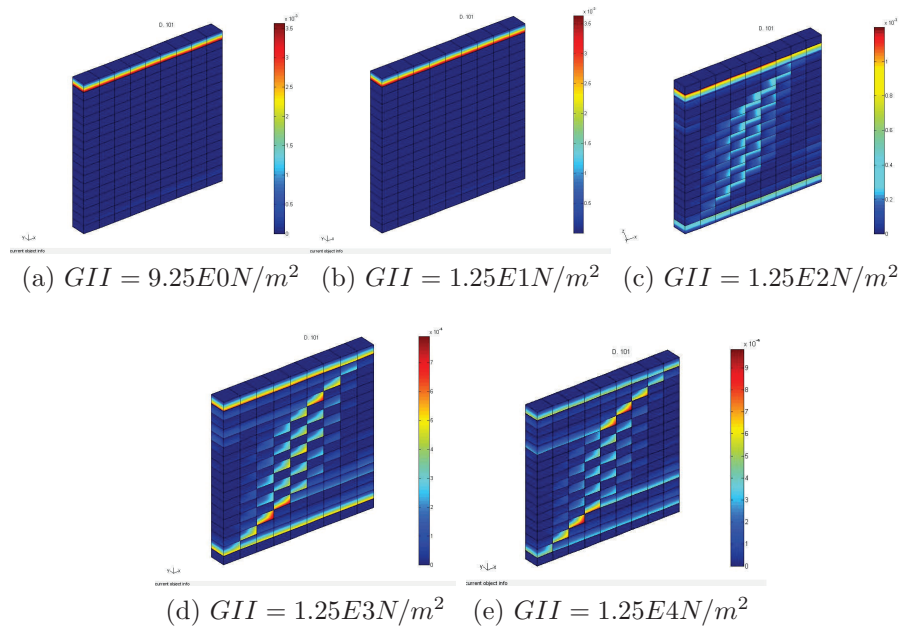


Figure B.22: Profile of cracking in the wall with different GII

Effect of mode III fracture energy G_{III}

- $G_{III} = 1E2N/m^2$

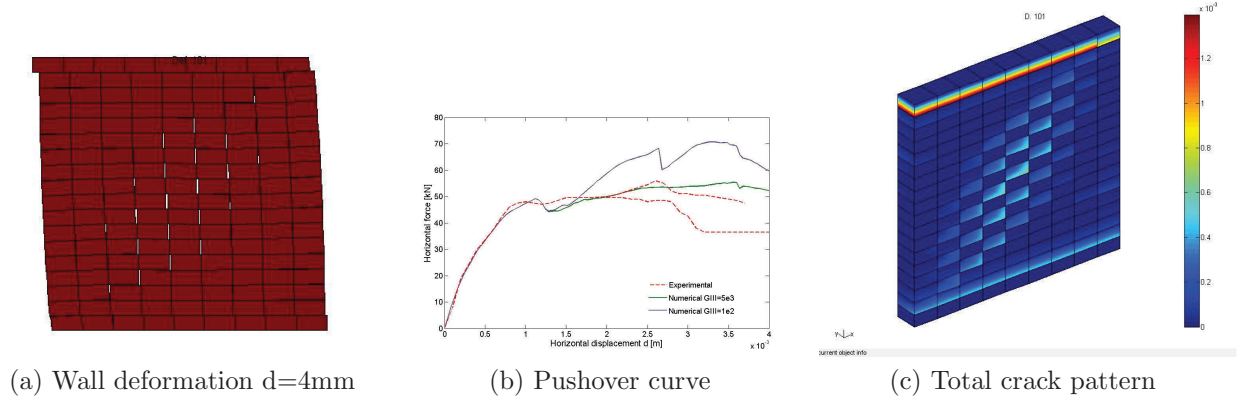


Figure B.23: Shear wall results for $G_{III} = 1E2N/m^2$

- $G_{III} = 4E3N/m^2$

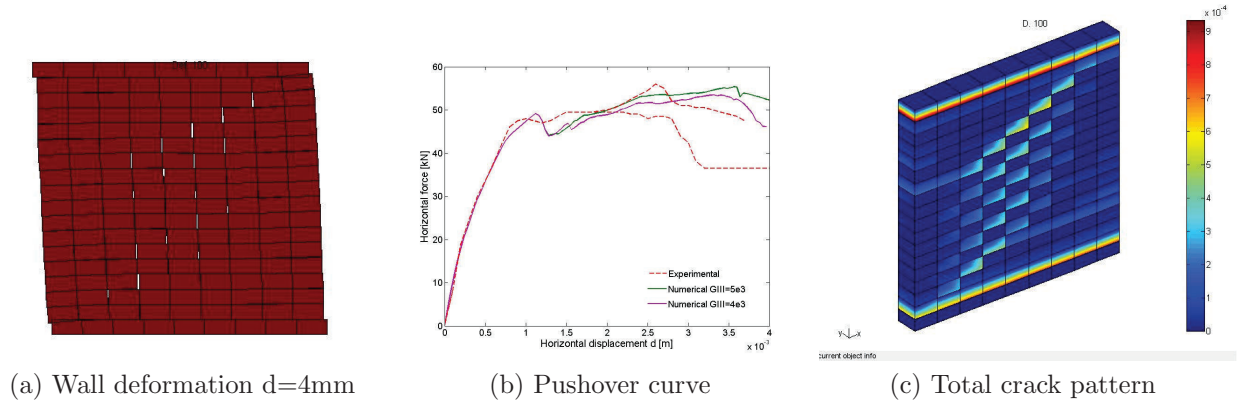


Figure B.24: Shear wall results for $G_{III} = 4E3N/m^2$

- $G_{III} = 7.5E3N/m^2$
- $G_{III} = 1E4N/m^2$

As shown in figure, different fracture energy for mode III results approximately the same crack patterns and the difference between load displacement curves are not great. Diagonal crack pattern, sliding at top and bottom horizontal joints as well as brick tension failure can be seen in these walls. Hence, the value of G_{III} has not great influence on the behavior of shear wall.

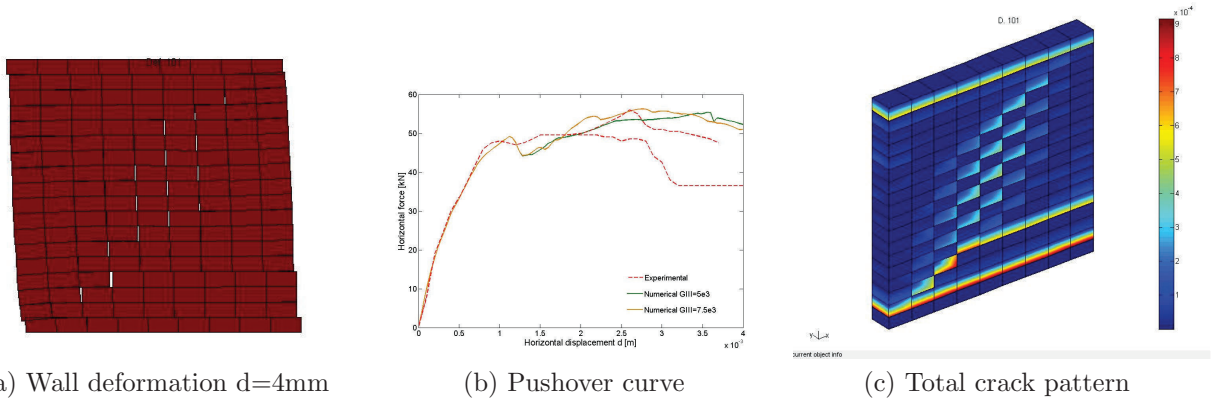


Figure B.25: Shear wall results for $G_{III} = 7.5E3N/m^2$

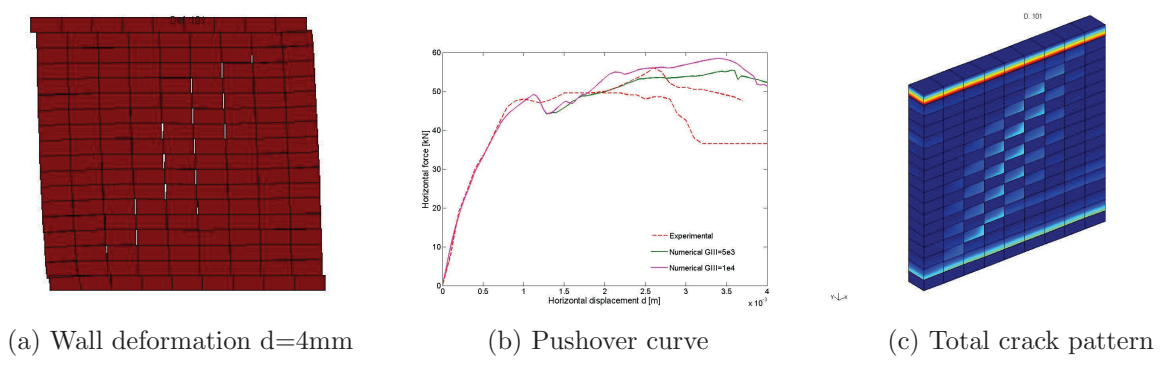


Figure B.26: Shear wall results for $G_{III} = 1E4N/m^2$

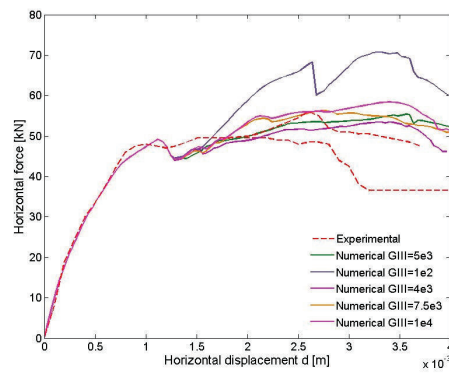


Figure B.27: Pushover curve for the wall with different G_{III}

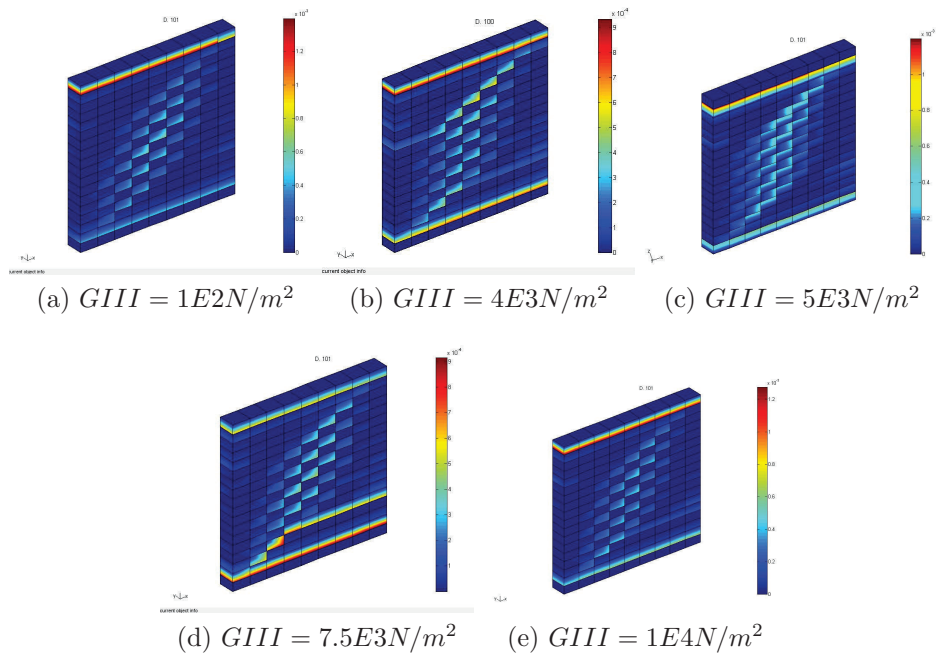


Figure B.28: Profile of cracking in the wall with different $GIII$

Chapter 8

Bibliography

- [1] Abrams D.P., Angel R., Uzarski J., Out-of-plane strength of unreinforced masonry infill panels, *Earthquake Spectra*, (1996).
- [2] ACI, Building Code Requirements for Masonry Structures (ACI 530-88 - ASCE 5-88) and Specifications for Masonry Structure (ACI 530.1-88 - ASCE 6-88), by American Society Of Civil Engineers, November 1, (1988).
- [3] Anthoine A., Derivation of the in-plane elastic characteristics of masonry through homogenization theory, *International Journal of Solids Structures*, 32, p. 137163, (1995).
- [4] Asteris P.G., Finite element micro-modeling of inlled frames, *Electron Journal of Structural Engineering*, 8, p. 111, (2008).
- [5] Asteris P.G., Antoniou S.T., Sophianopoulos D.S., Chrysostomou C.Z., Mathematical macromodeling of infilled frames: State of the art, *Journal of Structural Engineering*, v 137, n 12, p. 1508-1517, December (2011).
- [6] Atkinson R.H., Amadei B.P., Saeb S., Strue S., Response of masonry bed joints in direct shear, *Journal of Structural Engineering*, ASCE, 115, 9, p. 2276-2296, (1989).
- [7] Aubry D., Chouvet D., Modaressi A., Modaressi H., GEFDyn: Logiciel d'Analyse de Comportement Mecanique des Sols par Elements Finis avec Prise en Compte du Couplage Sol-Eau-Air, Manuel scientifique, Ecole Centrale Paris, LMSS-Mat, (1986).
- [8] Aubry D., Modaressi A., GEFDYN, Manuel Scientifique, (1996).
- [9] Belmouden Y., Lestuzzi P., An equivalent frame model for seismic analysis of masonry and reinforced concrete buildings, *Journal of Construction Building Material*, 23, p. 4053, (2009).
- [10] Bertoldi S.H., Decanini L.D., Santini S., Via G., Analytical models in infilled frames, *Proc. of the 10th European Conference in Earthquake Engineering*, Vienna, p. 15331538, (1994).

- [11] Beyer K., Dazio A., Developing force-deformation characteristics of brick masonry spandrels in historic buildings, 15th world conference on earthquake engineering, Lisboa, (2012).
- [12] Calderini C., Lagomarsino S., A micromechanical inelastic model for historical masonry, *Journal of Earthquake Engineering*, 10, 453, (2006).
- [13] Calderini C., Cattari S., Lagomarsino S., In plane seismic response of unreinforced masonry walls: comparison between detailed and equivalent frame models, *COMPDYN2009*, (2009).
- [14] Casolo S., Pena F., Rigid element model for in-plane dynamics of masonry walls considering hysteretic behaviour and damage, *Journal of Earthquake Engineering Structural Dynamics*, 36, p. 102948, (2007).
- [15] Casolo S., Milani G., A simplified homogenization-discrete element model for the non-linear static analysis of masonry walls out-of-plane loaded, *Journal of Engineering Structures*, 32, 8, p. 23522366, (2010).
- [16] Celepa Z., Erkenb A., Taskina B, and Ilkic A, Failures of masonry and concrete buildings during the March 8, 2010 Kovancilar and Palu (Elaz) Earthquakes in Turkey, *Journal of Engineering Failure Analysis*, Volume 18, Issue 3, Pages 868889, (2011).
- [17] Chaimoon K., Attard M., Modelling of unreinforced masonry walls under shear and compression, *Journal of Engineering Structures*, p. 2056-2068, (2007).
- [18] Chen, Yi-Hsin, Seismic Evaluation of RC Buildings Infilled with Brick Walls, PhD thesis, National Cheng- Kung Univ., Tainan, Taiwan, in Chinese, (2003)
- [19] Chiostri S., Vignolia A., Application of a numerical method to study masonry panels with various geometry under seismic loading, *Strema89*, Florence, Italy (1989).
- [20] Chiou Y.J., Tzeng J.Ch., Liou Y.W., Experimental and analytical study of masonry infilled frames, *Journal of structural engineering New York, N.Y.*, 125, 10, p. 1109-1117, (1999).
- [21] Chrysostomou C.Z., Effects of degrading infill walls on the nonlinear seismic response of two-dimensional steel frames, Ph.D. thesis, Cornell University, Ithaca, NY, (1991).
- [22] Chrysostomou C.Z., Gergely P., Abel J.F., A Six-Strut Model for Nonlinear Dynamic Analysis of Steel Infilled Frames, *International Journal of Structural Stability and Dynamics*, 2, 3, p. 335-353, (2002).
- [23] Crisafulli F., Analysis of infilled frame structures, seminar on masonry and earthen structures, Universidade do Minho
- [24] Crisafulli F.J., Carr A.J., Proposed macro-model for the analysis of infilled frame structures, *bulletin New Zealand society earthquake engineering*, 40, 2, p. 6977, (2007).
- [25] Structural masonry: a experimental numerical basis for practical designrules (in Dutch). Report 171, CUR, Gouda, The Netherlands, (1994)

- [26] DAYala D., Worth J., Riddle O., Realistic shear capacity assessment of inll frames: compar-
ison of two numerical procedures, *Engineering Structure Journal*, 31, 8, p. 174561, (2009).
- [27] Decanini L., Mollaioli F., Mura A., Saragoni R., Siesmic performacne of masonry infilled
R/C frames, 13 th World Conference on Earthquake Engineering Vancouver, B.C., Canada,
August 1-6, (2004).
- [28] Drucker D.C., Gibson R.I., Henkel D.J., Soil mechanics and work hardening theories of
plasticity, *Transaction, ASCE*, 122 , p. 338-346, (1957).
- [29] Drysdale R.G., Essawy A.S., Out-of-plane bending of concrete block walls, *Journal of Struc-
tural Engineering, ASCE*, (1998).
- [30] El-Dakhakhni W., Elgaaly M., Hamid A., Three-Strut Model for Concrete Masonry-Infilled
Steel Frames, *Journal of Structural Engineering*, 129, 2, p. 177-185, (2003).
- [31] BRGM, LMT-Cachan, Mss-Mat, Dynamiques concept, CSTB, Une approche mecanique
d'evaluation de la vulnerabilite sismique des maconneries EVSIM, Rapport final, Janvier
(2012).
- [32] FEMA, NEHRP commentary on the guidelines for the seismic rehabilitation of buildings,
FEMA-274, Washington, DC, (1997).
- [33] FEMA, Evaluation of earthquake damaged concrete and masonrywall buildings: Basic pro-
cedures manual, FEMA-306, Washington, DC, (1998).
- [34] Federal Emergency Management Agency , Pre-standard and Commentary for the Seismic
Rehabilitation of Buildings, FEMA356, Washington, D.C., (2000).
- [35] Fouchal F., Lebon F., Titeux I., Contribution to the modelling of interfaces in masonry
construction, *Journal of Construction and Building Materials*, 23, 6, p. 242841, (2009).
- [36] Furtmller Th., Adam Ch., Numerical modeling of the in-plane behavior of historical brick
masonry walls, *Acta Mechanica*, 221, 1-2, p. 65-77, September (2011).
- [37] Gambarotta G., Lagomarsino S., Damage models for the seismic response of brick masonry
shear walls. Part I: The mortar joint model and its applications, *Journal of Earthquake
Engineering & Structural Dynamics*, 26, p. 423-439, (1997).
- [38] Gambarotta L., Lagomarsino S., Damage models for the seismic response of brick masonry
shear walls. Part II: the continuum model and its applications, *Journal of Earthquake En-
gineering and Structural Dynamics*, 26, 4, p. 441-462, (1997).
- [39] Gambarotta K., Lagomarsino S., On dynamic response of masonry panels. In: *Proceedings
of National Conference on Masonry Mechanics between Theory and Practice*, Messina, Italy,
(1996).

- [40] Giambanco G., Rizzo S., Spallino R., Numerical analysis of masonry structures via interface models, *Computer Methods in Applied Mechanics and Engineering*, 190, p. 6493-6511, (2001).
- [41] Goodman R.E., Taylor R.L., Brekke T., A model for the mechanics of jointed rock, *ASCE Journal of soil mechanics and foundation division*, 94, p. 637-59, (1968).
- [42] Gopalaratnam V.S., Shah S.P., Softening response of plain concrete in direct tension, *ACI Journal*, 82, p. 310-323, 1985.
- [43] Griffiths D.V., Numerical modeling of interfaces using conventional finite elements, in. *Proc. 5th conference of Numerical Methods in Geomechanics*, Nagoya, p. 837-844, (1985).
- [44] Griffith M., Vaculik J., Out-of-plane flexural strength of unreinforced clay brick masonry walls, *TMS J*, (2007).
- [45] <http://haitirewired.wired.com/profiles/blogs/one-of-haitis-few-earthquake>
- [46] Hashemi A., M K.M., Seismic Evaluation of Reinforced Concrete Buildings Including Effects of Masonry Infill Walls, *PEER* (2007).
- [47] Herrmann L.R., Finite element analysis of contact problems, *Journal of Engineering Mechanics (ASCE)*, 104, p. 1043-1057, (1978).
- [48] Holmes M., Steel frames with brickwork and concrete infilling, *ICE Proc.*, 19, 4, p. 473478, (1961).
- [49] Ignatakis C., Stavrakakis E., Penelis G., Analytical model for masonry using the finite element method, in *Structural Repair and Maintenance of Historical Buildings*, Computational Mechanics Publications, p. 511-523, (1989).
- [50] Karantoni F.V., Fardis M.N., Effectiveness of seismic strengthening techniques for masonry buildings, *Journal of Structural Engineering*, 1992, 118, 7, p. 1884902, (1992).
- [51] Karapitta L., Mouzakis H., Carydis P., Explicit finite-element analysis for the in-plane cyclic behavior of unreinforced masonry structures, *Journal of Earthquake Engineering & Structural Dynamics*, 40, 2, p. 175193, February (2011).
- [52] Koutromanos I., Stavridis A., Shing P.B., Willam K., Numerical modeling of masonry-infilled RC frames subjected to seismic loads, *Journal of Computers & Structures*, 89, 11-12, p. 1026-37, June (2011).
- [53] Liauw T.C., Kwan K.H., Nonlinear behavior of non-integral infilled frames, *Journal of Computers and Structures*, 18, 3, p. 551-560, (1984).
- [54] Lagomarsino S., Penna A., Galasco A., TREMURI program: Seismic analysis program for 3D masonry buildings, University of Genoa, On Internet: [http://www.stadata.com/Lagomarsino, S., Galasco, A. et Penna, A.](http://www.stadata.com/Lagomarsino,S.,Galasco,A.etPenna,A.), (2004), Pushover and

dynamic analysis of URM building by means of a non-linear macro-element model, Risk-UE project report, (2006).

- [55] Liauw T.C., Kwan K.H., Nonlinear behavior of non-integral infilled frames, *Journal of Computers and Structures*, 18, 3, p. 551-560, (1984).
- [56] Liauw T.C., Kwan K.H., New development in research of infilled frames. In: *Proceedings of the eighth world conference on earthquake engineering*, p. 62330, (1984).
- [57] Lotfi H.R., Shing P.B., Interface model applied to fracture of masonry structures, *Journal of structural engineering* New York, N.Y., 120, 1, p. 63-80, Jan (1994).
- [58] Lourenco P.B., Analysis of masonry structures with interface elements theory and applications, *TNO Building and Construction Research Computational Mechanics*, (1994).
- [59] Lourenco P.B., Rots J.G., On the use of micro-modelling for the analysis of masonry shear walls, in: *Computer Methods in Structural Masonry - 2*, Ed. G.N. Pande, J. Middleton, Books & Journals International, Swansea, UK, p. 1426, (1993).
- [60] Lourenco P.B., Computational strategies for Masonry structures, Ph.D. thesis. The Netherlands: Delft University of Technology, (1996).
- [61] Lourenco P.B., Rots J.G., Multisurface Interface Model for Analysis of Masonry Structures, *Journal of Engineering Mechanics*, 123, 7, p. 660-668, July (1997).
- [62] Lourenco P.B., Rots J.G., Blaauwendraad, Parameter estimation and validation, *Journal of Structural Engineering*, ASCE, 124, 6, p. 64252, (1998).
- [63] Lourenco P.B., Rots J.G., Continuum model for masonry: Parameter estimation and validation, *Journal of structural engineering* New York, N.Y., 124, 6, p. 642-652, Jun (1998).
- [64] Macorini L., Izzuddin B.A., A non-linear interface element for 3D mesoscale analysis of brick-masonry structures, *International Journal for Numerical Methods in Engineering*, 85, 12, p. 1584-608, 25 March (2011).
- [65] Madan A, Reinhorn AM, Mandar JB, Valles RE , Modeling of Masonry Infill Panels for Structural Analysis, *Journal of Structural Engineering* ASCE, 123, 10, p. 1295-1302, (1992).
- [66] Mainstone R.J., On the stiffnesses and strengths of infilled frames, *Proc Inst Civ Eng, Suppl* (iv), p. 57-90, (1971).
- [67] Mainstone R.J., Supplementary note on the stiffness and strengths of infilled frames, *Building Research Station*, Garston, UK, (1974).
- [68] Magenes G., Calvi G.M., In-plane seismic response of brick masonry walls, *Journal Earthquake Engineering and Structural Dynamics*, 26, (1997).
- [69] Magenes G., Della Fontana A., Simplified non-linear seismic analysis of masonry buildings, *Proc Br Masonry Soc*, 8, p. 1905, (1998).

- [70] Magenes G., A method for pushover analysis in seismic assessment of masonry buildings, In: Proc. of 12th world conference on earthquake engineering, (2000).
- [71] Mallick D.V., Severn R.T., The behaviour of infilled frames under static loading, Proc., Instn. Civ. Engrs., 38, p. 639-656, (1967).
- [72] Mallick D.V., Garg R.P., Effect of openings on the lateral stiffness of infilled frames, Proc., Instn. Civ. Engrs., 49, p. 193-209, (1971).
- [73] Mehrabi A.B., Shing P.B., Finite element modeling of masonry-infilled RC frames, Journal of structural engineering New York, N.Y., 123, 5, p. 604-613, May (1997).
- [74] Milania G., Lourencob P.B., Trallia A., 3D homogenized limit analysis of masonry buildings under horizontal loads, Journal of Engineering Structures 29, p. 31343148, (2007).
- [75] Milani G., 3D upper bound limit analysis of multi-leaf masonry walls. International Journal of Mechanical Sciences, 50, p.817836, (2008).
- [76] Mostafaei H., Kabeyasawa T., Effect of Infill Masonry Walls on the Seismic Response of Reinforced Concrete Buildings Subjected to the 2003 Bam Earthquake Strong Motion : A Case Study of Bam Telephone Center, Journal of Bulletin of the Earthquake Research Institute, University of Tokyo, 13 , p.133-156, (2004).
- [77] Mosalam K.M., M.S. Gnay, Chapter 23: Seismic Analysis and Design of Masonry-Infilled Frames,in Structural and Geotechnical Engineering, S.K. Kunnath, Editor, Encyclopedia of Life support Systems (EOLSS) Publishers, Oxford, UK, (2012).
- [78] Masonry standards joint committee, Building Code Requirements and Specification for Masonry Structures, MSJC Code, (2008).
- [79] <http://www.sdtools.com/pdf/datasheet.pdf>
- [80] Oliveira D.V., Lourenco, P.B., Implementation and Validation of a Constitutive Model for the Cyclic Behaviour of Interface Elements, Journal of Computers & Structures, 82, 17-19, p. 1451-1461, (2004).
- [81] Oliveira D.V., Experimental and numerical analysis of blocky masonry structures under cyclic loading. PhD Dissertation, Universidade do Minho, Guimaraes, Portugal, (2003).
- [82] Page A.W., Finite element model for masonry, Journal of Structure Division, ASCE, 104, 8, p. 1267-1285, (1978).
- [83] Pande G.N., Liang J.X., Middleton J., Equivalent elastic moduli for brick masonry, Journal of Computers Geotechnics, 83, p. 243265, (1989).
- [84] Paulay T., Priestley M.J.N, Seismic Design of Reinforced Concrete and Masonry Buildings, JOHN WILEY& SONS, INC.,(1992).

- [85] Pluijm Vd., Material properties of masonry and its components under tension and shear. In: V.V. Neis S, Saskatchewan, editor. Proc 6th Canadian masonry symposium, p. 67586, Canada (1992).
- [86] Pluijm Vd., Shear behavior of bed joints. In: Harris AAHaHG, editor. Proc 6thNorth American Masonry Conf. Drexel University, Philadelphia, Pennsylvania, p. 12536, USA (1993).
- [87] Polyakov S.V., Masonry in Framed Buildings. An Investigation into the Strength and Stiffness of Masonry Infilling, Moscow, (1957).
- [88] Puglisi M., Uzcategui M., Florez-Lopez J., Modeling of masonry of infilled frames Part I: The plastic concentrator Journal of Engineering Structures, 31, 1, p. 113-8, (2009).
- [89] Reinhorn A.M., Mander J.B., Valles R.E., Modeling of masonry infill panels for structural analysis, Journal of structural engineering New York, N.Y., 123, 10, p. 1295-1302, Oct (1997).
- [90] Roca P., Molins C., Mar AR., Strength capacity of masonry wall structures by the equivalent frame method, ASCE, Journal of Structural Engineering, 131, 10, p. 160110, (2005).
- [91] Riddington J.R., Ghazali M.Z., Hypothesis for shear failure in masonry joints, Proc. Instn Civ. Engrs, part2, 89, p. 89-102, (1990).
- [92] Rodrigues H., Varum H., Costa A., Simplified macro-model for infill masonry panels, Journal of Earthquake Engineering, 14, 3, p. 390-416, March (2010).
- [93] Schueremans1 L., Van Rickstal1 F., Ignoul S., Brosens K., Van Balen1 K., Van Gemert1 D., Continuous Assessment of Historic Structures A State of the Art of applied Research and Practice in Belgium.
- [94] <http://www.sdtools.com/pdf/datasheet.pdf>
- [95] Shien-Beygi B., Pietruszczak S., Numerical analysis of structural masonry: mesoscale approach, Computers and Structures, 86, p.19581973, (2008).
- [96] <http://www.staff.city.ac.uk/earthquakes/MasonryBrick/PlainBrickMasonry.htm>
- [97] Smyrou E., Implementation and verification of Masonry panel model for nonlinear dynamic analysis of Infilled RC frames, MSc Thesis, European School for Advanced Studies in Reduction of Seismic Risk (ROSE School), Pavia, Italy, (2006).
- [98] Stafford-Smith B., Carter, A method of analysis for infilled frames, Proceedings of the Institute of Civil Engineers, 44, p. 31-48, (1969).
- [99] Stafford-Smith B., Behavior of Square Infilled Frames, Journal of Structural Division, ASCE, 92(ST1), p. 381-403, (1996).
- [100] Stavridis A., Shing P.B., Finite-Element Modeling of Nonlinear Behavior of Masonry-Infilled RC Frames, Journal of Structural Engineering, 136, 3, p. 285296, (2010).

- [101] Sutcliffe D.J., Yu H.S., Page A.W., Lower bound limit analysis of unreinforced masonry shear walls, *Journal of Computers & Structures*, 79, 14, p. 12951312, June (2001).
- [102] <http://en.wikipedia.org/wiki/Earthquake-engineering>
- [103] Varela-Rivera J.L., Navarrete-Macias D., Fernandez-Baqueiro L.E., Moreno E.I., Out-of-plane behaviour of confined masonry walls, *Journal of Engineering Structures*, 33, p. 17341741, (2011).
- [104] Zucchini A., Loureno P.B., A micro-mechanical model for the homogenisation of masonry, *Int. Journal of Solids Structures*, p. 32333255, (2002).
- [105] Zucchini A., Loureno P.B. , micro-mechanical homogenisation model for masonry: Application to shear walls, *International Journal of Solids and Structures* 46, p. 871886, (2009).